Investigation of Rockburst Mechanisms and Rockburst Prediction Using Numerical Modeling Methods

by

Jun Wang

A thesis submitted in partial fulfillment of the requirements for the degree of

Doctor of Philosophy

in

Mining Engineering

Department of Civil and Environmental Engineering

University of Alberta

ABSTRACT

Rockburst is a sudden rock failure characterized by the breaking up and expulsion of rocks from their surroundings, accompanied by a violent release of energy. Due to its unpredictability and high intensity, rockburst is one of the most hazardous geological disasters. It has caused thousands of injuries and fatalities and significant economic losses to mine enterprises. To date, great efforts have been devoted to the investigation of mechanisms, risk evaluation and prediction, and prevention and mitigation of rockbursts. However, there is no effective way to control rockbursts completely because the phenomenon is very complex and is influenced by many factors. Hence, the rockburst mechanisms in some conditions remain unclear, and current methods and indicators fail to predict rockbursts in many cases.

The objective is to reveal rockburst mechanisms and develop a systematic method and a new stiffness-based indicator for predicting rockburst risks. Compared with other methods, such as physical simulation and field tests, the numerical modeling method has the advantages of low cost, safety, time-saving, and flexibility. More importantly, it can provide more information and simulate the complex mechanical behaviour of rocks and rock masses under different conditions. This can visualize the “real” world in underground mining for researchers and engineers to tackle various rock mechanics problems (e.g., rockburst). Thus, numerical modeling is employed as the primary research approach.

This thesis consists of seven chapters. Chapter 1 presents the research background, problem statement, research objectives and methodologies, and outlines the thesis organization. Chapter 2 provides a literature review of rockburst-related studies based on research objectives. A systematic numerical modeling framework for studying rockburst mechanisms and other rockburst-related problems is established based on the summary and analysis of the literature. In Chapter 3,

following the proposed numerical modeling framework, a three-dimensional (3D) finite difference method (FDM) model is established via fast lagrangian analysis of continua in three dimensions (FLAC3D) using the "5.5" rockburst event in the Zofiówka Coal Mine as a case example to reveal the rockburst source mechanism of driving roadways in close-distance coal seam mining conditions. The results suggest that the superposition of multiple excavation-induced stresses of roadways provides an environment for stress concentration. The side abutment stress induced by mining in the upper coal seam has a "strengthening" effect to rockburst occurrence. The great deviatoric stress induced by complex excavating situations is another important exterior cause. A strict calibration procedure should be implemented before using indicators to predict rockburst potential. Thus, a systematic method that can reasonably select and use rockburst indicators is proposed to predict the location and magnitude of rockbursts. Chapter 4 adopted an improved global-local modeling approach to study strainburst damage mechanisms. The results suggest that the strainburst damage mechanism for the study site combines three types of damage: rock ejection, rock bulking, and rockfall, which agrees well with in situ observations confirming the rationality and capability of the modeling approach. The principles to control and mitigate strainburst damage are also proposed. In Chapter 5, instead of conventional drop tests, the performance of yielding rockbolts (D-bolt and Roofex) during remotely triggered and self-initiated strainbursts was systematically evaluated via building a two-dimensional (2D) distinct element method (DEM) model of a deep roadway using a universal distinct element code (UDEC). The results suggest that the yielding rockbolt with high strength and deformation capacity (e.g., D-bolt) has a better performance in controlling rockburst damage. The support effects can be significantly improved by increasing the bolt number and supplementing cables and surface retaining elements (e.g., steel arch). In Chapter 6, a new rockburst indicator, called strainburst stiffness factor (SSF), is proposed

and developed to predict strainburst risks based on the analysis of stiffness differences. The prediction results of SSF successfully match with the 5.5” rockburst event in the Zofiowka Coal Mine and the “11.28” rockburst event in the Jinping II Hydropower Station, validating the effectiveness of SSF. Chapter 7 presents the thesis summary, conclusions, research contributions, and future work.

This study revealed rockburst mechanisms and developed a systematic method and a new stiffness-based indicator for predicting rockburst risks. The outcomes of this PhD study can contribute to understanding rockburst mechanisms and effectively predicting rockburst risks for improving the safety of workers and production in burst-prone mines.

PREFACE

This thesis is an original work by Jun Wang. It is based on six journal papers that have been published or submitted for consideration of publication.

Chapter 2 is based on the published paper "**Wang, J.**, Apel, D. B., Pu, Y., Hall, R., Wei, C., Sepehri, M. (2021). Numerical modeling for rockbursts: A state-of-the-art review. Journal of Rock Mechanics and Geotechnical Engineering, 13(2), 457-478".

Chapter 3 is based on the published papers "**Wang, J.**, Apel, D. B., Pu, Y., Hall, R., Wei, C., Sepehri, M. (2021). Numerical modeling for rockbursts: A state-of-the-art review. Journal of Rock Mechanics and Geotechnical Engineering, 13(2), 457-478" and "**Wang, J.**, Apel, D. B., Dyczko, A., Walentek, A., Prusek, S., Xu, H., Wei, C. (2021). Investigation of the rockburst mechanism of driving roadways in close-distance coal seam mining using numerical modeling method. Mining, Metallurgy & Exploration, 38(5), 1899-1921".

Chapter 4 is based on the published paper "**Wang, J.,** Apel, D. B., Dyczko, A., Walentek, A., Prusek, S., Xu, H., Wei, C. (2022). Analysis of the damage mechanism of strainbursts by a global-local modeling approach. Journal of Rock Mechanics and Geotechnical Engineering, 14(6), 1671-1696".

Chapter 5 is based on the published papers "**Wang, J.,** Apel, D. B., Xu, H., Wei, C. (2022). Evaluation of the performance of yielding rockbolts during rockbursts using numerical modeling method. International Journal of Coal Science & Technology, 9(87), 1-26" and "**Wang, J.,** Apel, D. B., Xu, H., Wei, C., Skrzypkowski, K. (2022). Evaluation of the effects of yielding rockbolts on controlling self-initiated strainbursts: a numerical study. Energies, 15(7), 2574".

Chapter 6 is based on the submitted paper "**Wang, J.,** Apel, D. B., Wei, C,. Xu, H. (2022). Prediction of strainburst risks based on the stiffness theory: development and verification of a new rockburst indicator. *In preparation for submission*".

This study was supported by the Chinese Scholarship Council (CSC) and the Itasca Educational Partnership (IEP) program from the Itasca Consulting Group, Inc.

In this thesis, my work includes conceptualization, data collection and analysis, methodology development, numerical modeling, theoretical analysis, writing, and editing. Dr. Derek Apel was my supervisor, who contributed to conceptualization, supervision, resources, review, and editing. Dr. Robert Hall was my committee member, who contributed to review and editing. Dr. Stanisław Prusek and Dr. Andrzej Walentek, professors at the Central Mining Institute (Główny Instytut Górnictwa), and Dr. Artur Dyczko, the vice president at the Jastrzębska Spółka Węglowa S.A. Group, provided us with the access to the data of the Zofiówka Coal Mine and reviewed our papers. Dr. Krzysztof Skrzypkowski, a professor at the AGH University of Science and Technology, contributed to review and editing. Dr. Mohammadali Sepehri, Dr. Yuanyuan Pu, Dr. Huawei Xu, and Dr. Chong Wei were my research colleagues, who contributed to review and improving numerical models.

DEDICATION

This thesis is dedicated to:

My Great Parents, Chunhua Wang and Youchang Wang

My Dear Wife Chen Pan

My Lovely Son Hexuan Wang

ACKNOWLEDGEMENTS

I would like to express my sincere gratitude to my PhD supervisor, Dr. Derek Apel, for his continuous support and guidance. I can still remember the first time I met him in Qingdao, China. His sense of humour and extensive rock mechanics and mining engineering knowledge deeply impressed me. He is a very open-minded, enthusiastic, patient, and generous person. We have so many active communications at the University of Alberta. He always inspires me to think and investigate a question in my own way and corrects me when I am not on track. He helps me a lot, not only with my research work but also with my career development. For instance, he always sends information about jobs and scholarships to his graduate students once he receives it. It is so lucky to have a supervisor like him. I want to say really appreciate your work and many thanks to you, Dr. Apel!

I would like to express my gratitude and appreciation to the thesis examining committee members, Dr. Robert Hall, Dr. Yashar Pourrahimian, Dr. Douglas Tomlinson, Dr. Hassan Dehghanpour Hossein Abadi, and Dr. Les Sudak, for their precious time and constructive criticisms and comments. Their suggestions have greatly improved my research work. Thanks.

I would like to acknowledge Dr. Stanisław Prusek and Dr. Andrzej Walentek at the Central Mining Institute (Główny Instytut Górnictwa) and Dr. Artur Dyczko at the Jastrzębska Spółka Węglowa S.A. Group who gave us the access to the data of the Zofiówka Coal Mine.

I would like to thank my parents for their unconditional love and support. Although they are not well educated, they always encourage me to receive higher education and pursue my dreams. All of my achievements owe to you.

I want to say a “special thank you” to my wife, Chen Pan. I will never forget that she came to Canada alone to accompany and support me during the most serious time of the Covid-19

Pandemic. This was the first time that she had gone abroad. How much she loves me makes her risk his life to come here to see me! Moreover, my PhD study has had many ups and downs. My wife always encourages me to treat difficulties positively. She often tells me that sometimes misfortune is a blessing in disguise. She sacrifices a lot, takes care of our baby, and makes our family well-organized. I would also like to thank our lovely baby, Hexuan, for the joy and happiness that he brings to our family. He is doing a great job. I will never forget when he said "baba" for the first time, warming my heart and making me cry. You two make me become a better man and a proud father. I love you all, dear.

I would like to thank my research colleagues, Dr. Yuanyuan Pu, Dr. Huawei Xu, Chong Wei, and Alicja, and my friends, Dr. Xincheng Hu, Dr. Linping Wu, Dr. Guangping Huang, Dr. Xinxiang Yang, Shaosen Ma, Chengkai Fan, Yunting Guo, and Jian Zhao, for their help on my study and daily life. Thank you.

I am grateful to the Chinese Scholarship Council (CSC), which provides me with all the living costs, and to the University of Alberta, which waived my tuition during my PhD period. Thanks.

I would also like to acknowledge the Itasca Consulting Group, Inc. for a software loan within the Itasca Educational Partnership (IEP) and my IEP mentor, Mr. David DeGagné, for helping me by answering my questions about numerical modeling. Thank you.

Thanks for all your encouragement!

TABLE OF CONTENTS

LIST OF FIGURES

LIST OF TABLES

LIST OF ABBREVIATIONS

2D	Two-dimensional
3D	Three-dimensional
3DEC	3D distinct element code
AE	Acoustic emission
ANFO	Ammonium nitrate fuel oil
B	Brittleness coefficient
BBM	Bonded block method
BEM	Boundary element method
BPR	Bursting potential ratio
BPI	Burst potential index
BSR	Brittle shear ratio
CRLDB	Constant-resistance and large-deformation bolt
CSC	Chinese Scholarship Council
CPU	Central processing unit
CY	Continuously yielding joint model
DC-bolt	Deformation-controlled rockbolt
DDA	Discontinuous deformation analysis
DEM	Discrete/Distinct element method
DFN	Discrete fracture network
DY	Double-yield
EPMC	Elastic-perfectly plastic Mohr-Coulomb
ERR	Energy release rate
ESS	Excess shear stress
FAI	Failure approaching index
FEM	Finite element method
FDM	Finite difference method
FDEM	Finite element method/Distinct element method
FLAC	Fast lagrangian analysis of continua
FLAC3D	Fast lagrangian analysis of continua in three dimensions

GRC	Ground reaction curve
GSI	Geological strength index
HMH	Huber, von Mises and Hencky
IEP	Itasca Educational Partnership
ISRM	International Society for Rock Mechanics
IT	Information technology
LERR	Local energy release rate
LMS	Local mine stiffness
LSS	Loading system stiffness
MCS	Mesh convergence study
MCSS	Mohr-Coulomb strain softening
MS	Microseismic
OBI	Out-of-balance index
P and S waves	Primary and secondary waves
PCS	Post-peak characteristic stiffness
PDE	Partial differential equations
PFC	Particle flow code
PPV	Peak particle velocity
REV	Representative elementary volume
RFPA	Realistic failure process analysis
RQD	Rock quality designation
RRE	Representative rock element
SED	Strain energy density
SEDI	Strain energy density index
SHPB	Split-Hopkinson pressure bar
SRM	Synthetic rock mass
SSF	Strainburst stiffness factor
TBM	Tunnel boring machine
UCS	Uniaxial compressive strength
UTS	Uniaxial tensile strength
UDEC	Universal distinct element code

USCB	Upper Silesian Coal Basin
URLERI	Unit time relative local energy release index
USA	United States of America
UTS	Uniaxial tensile strength
VS	Versus

LIST OF SYMBOLS

σ_c	Uniaxial compressive strength
σ_{ci}	Uniaxial compressive strength of intact rock pieces
σ_θ	Maximum tangential stress of surrounding rock
σ_1	Maximum principal stress
σ_3	Minimum principal stress
σ_1'	Maximum principal effective stress at failure
σ_3'	Minimum principal effective stress at failure
σ_t	Uniaxial tensile strength
σ_L	Axial stress of tunnel
C_c	Cohesion force
φ_c	Internal friction angle
σ^t	Tensile cutoff
σ_z	Vertical stress
γ	Unit weight
ν	Poisson's ratio
α	Tao discriminant index
g	Gravity accerlation
D	Diameter; Factor that depends upon the degree of disturbance
E_h	Average deformation modulus of the upper part of the earth's crust measured in a horizontal direction
E_s	Unloading tangential modulus of rock
K	Ratio of the horizontal stress to the vertical stress; bulk modulus
L	Length
T_s	σ_θ/σ_c
Vs	Velocity of secondary wave
Vp	Velocity of primary wave
W_k	Kinetic energy
W_r	Released energy
W_{sp}	Stored elastic energy

W_{st}	Dissipated elastic energy
Z	Depth
m_i	Hoek-Brown material constant for intact rocks
m_b	Hoek-Brown material constant for rock masses
s	Hoek-Brown material constant for rock masses
a	Hoek-Brown material constant for rock masses
ρ	Bulk density of intact rocks
E_i	Young's modulus of intact rocks
v	Poisson's ratio of intact rocks
σ_{cm}	UCS of rock masses
E_m	Deformation modulus of rock masses
h_m	Mining height
h_n	Height of the caved zone
σ	Uniaxial stress applied to the gob material
ε	Strain occurring under the applied stress
E_0	Initial tangent modulus
ε_m	Maximum possible strain of the bulked rock material
b	Initial bulking factor
G	Shear modulus
φ	Internal friction angle
c	Cohesion force
τ_s	Shear stress; prevailing shear stress prior to slip
τ_d	Dynamic shear strength of the plane
f_σ	Rockmass property factor
σ_{sum}	Total stress
σ_0	Initial stress
σ_{final}	Final stress
$\varepsilon_1{}^T$	Strain correspond to the induced stress
W_E	Elastic strain energy accumulated before the failure (peak) point
W_p	Plastic strain energy consumed after rock failure
E	Young’s modulus; seismic energy

ΔF_t	Incremental axial force in a "rockbolt" element
A	Cross-sectional area
L	Length
ε_f	Total strain before peak
ε_b	Total strain after peak
e_c	Elastic strain energy accumulated before the failure (peak) point
U_d	Real time energy
U_0	Utimate capacity of energy storage
I_A	Stability coefficient
k_n	Normal stiffness of contacts
k_s	Shear stiffness of contacts
c^j	Cohesion force of contacts
φ^j	Friction angle of contacts
σ_t^j	Tensile strength of contacts
$\Delta\sigma_n$	Normal stress increment
Δu_n	Normal displacement increment
σ_n	Normal stress
C_p	Speed of p-wave propagation through medium
v_n	Input normal particle velocity
Δu^t	Axial displacement increment
Δu_s^e	Elastic shear displacement increment
cs_{sstiff}	Coupling spring shear stiffness
u_p	Axial displacement of the rockbolt
u_m	Axial displacement of the medium
F_s	Shear force that develops in the shear coupling spring
F_s^{max}	Maximum shear force per length of the rockbolt
cs_{scoh}	Cohesive strength of the shear coupling spring
σ'_c	Average effective confining stress perpendicular to the "rockbolt" element
cs_{sfric}	Friction angle of the shear coupling spring
cs_{nstiff}	Coupling spring normal stiffness
F_n	Normal force that develops in the normal coupling spring

u_p^n	Displacement of the rockbolt perpendicular to the axial direction of the rockbolt
u_m^n	Displacement of the medium (soil or rock) perpendicular to the axial direction of the rockbolt
F_n^{max}	Maximum normal force per length of the rockbolt:
cs_{ncoh}	Cohesive strength of the normal coupling spring
cs_{nfric}	Friction angle of the normal coupling spring
c_r^j	Residual cohesion forces of contacts
φ_r^j	Residual internal friction angle of contacts
σ_{tr}^j	Residual tensile strength of contacts
D_c	Total damage
D_t	Tensile damage
D_s	Shear damage
L_c	Total length of failed contacts
L_t	Length of failed contacts in tensile failure
L_s	Length of failed contacts in shear failure
K_L	Loading system stiffness
K_P	Post-peak characteristic stiffness
K_{LMS}	Local mine stiffness
U	Convergence of tunnel walls after excavation
P_i	In situ stress
P_1	Internal pressure at the tunnel boundary before excavation
P_2	Internal pressure at the tunnel boundary after excavation
d_1	Tunnel diameter before excavation
d_2	Tunnel diameter after excavation
ε_{pl}	Tensile failure strain limit
ε_{pl}^{ax}	Axial plastic strain of rockbolt segment elements
θ_{pl}	Average angular rotation over the rockbolt
d	Rockbolt diameter
M_L	Richter magnitude

W	Total boundary loading work
W_e	Stored strain energy in rock materials
W_j	Dissipated energy in joint shear
W_p	Plastic work of intact rocks
W_r	Released or excess energy
W_d	Cumulative damped energy for all timesteps in the system
t	Time
$\triangle t$	Timestep
$\dot{u}_i$	Velocity of the gridpoint
$F_i^{(t)}$	Resultant of all external forces applied to the gridpoint (from block contacts or otherwise) at time t
m_n	Nodal mass
α	Local damping constant
ψ	Dilation angle
$\sigma_{\theta p}$	Tangential stress of a sampling point in the plastic zone
σ_{rp}	Radial stresses of a sampling point in the plastic zone
$\sigma_{\theta e}$	Tangential stress of a sampling point in the elastic zone
σ_{rp}	Radial stresses of a sampling point in the elastic zone
r_a	tunnel radius
r	Distance from the tunnel boundary to the sampling point
p_0	Initial stress
σ_{R0}	Radial stress at the plastic zone radius
R_p	Plastic zone radius
c_p	Initial cohesion force
φ_p	Initial internal friction angle
c_r	Residual cohesion force
φ_r	Residual internal friction angle
ε_p	Plastic shear strain

k_{PCL}	Post-peak characteristic stiffness of rock masses
k_{LMS}	Local mine stiffness
k_{LMS_x}	Local mine stiffness in the horizontal direction
k_{LMS_y}	Local mine stiffness in the vertical direction
J_r	Joint roughness

1. CHAPTER 1: INTRODUCTION

This chapter is an overview of this thesis. It presents the general research background of the study, the statement of problems, the research objectives and the methodologies used. The organization of the thesis is also outlined at the end of this chapter.

1.1 Research background

Rockburst is a sudden rock failure characterized by the breaking up and expulsion of rocks from their surroundings, accompanied by a violent release of energy (Blake, 1972a). Due to its unpredictability and high intensity, rockburst is one of the most hazardous geological disasters. It damages equipment and facilities and even causes injuries and fatalities (Pechmann et al., 2008; Durrheim, 2010; Zhang et al., 2012a; Naji et al., 2018; Yang and Xiang, 2018; Pu et al., 2019). The statistics of major rockburst accidents in the last 20 years are shown in Figure 1.1.

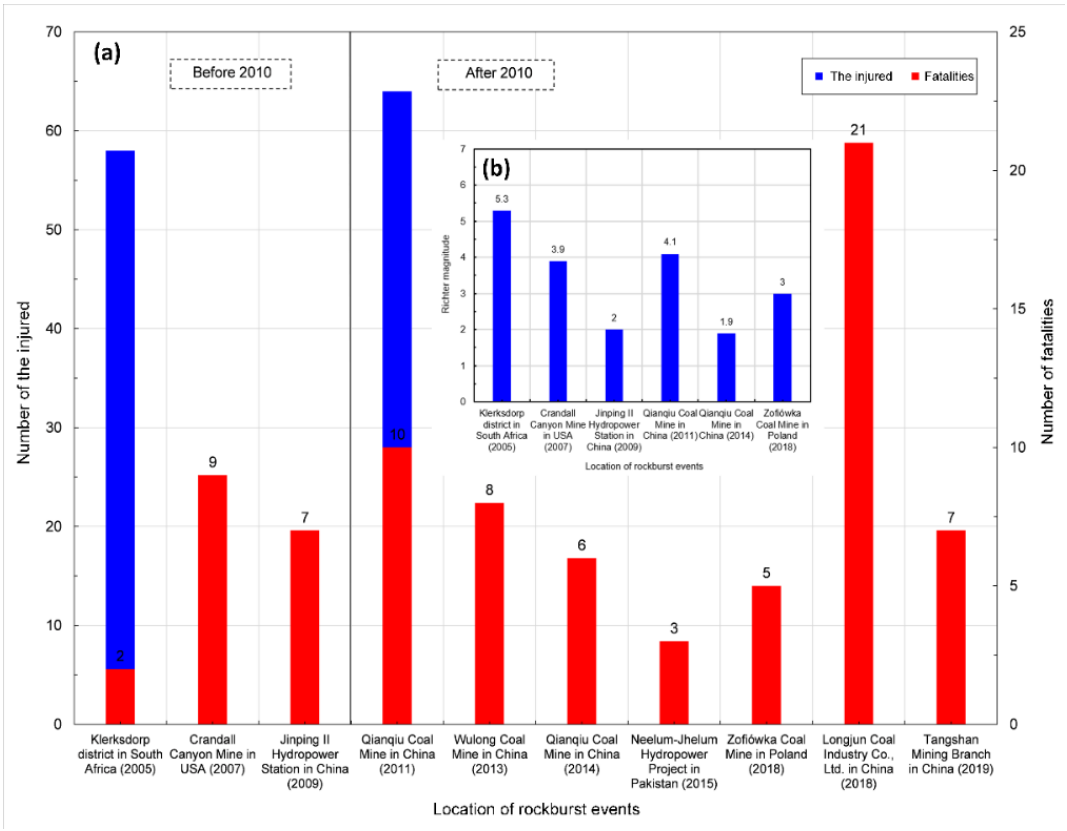

Figure 1.1 Major rockburst accidents in the last 20 years. (a) The number of fatalities and injured. (b) Richter magnitude (Wang et al., 2021b).

To date, rockburst events have been reported in all mining countries (e.g., South Africa, Canada, Australia, USA, Russia, China, India, Poland, and Chile) since the first such events were recorded in South Africa and India at the turn of the 20th century (Blake and Hedley, 2003). Some civil engineering projects, such as deep tunnels in Switzerland, Norway, Iran, Peru, and China also suffered rockburst problems

(Farrokh et al., 2009; Kaiser and Cai, 2012; Zhang et al., 2012a; Dammyr, 2016). Unfortunately, as excavation activities progress to greater depths, the frequency and severity of rockburst events increase due to the higher in-situ stress and more complex geological environments (Kaiser and Cai, 2012; Manouchehriana and Cai, 2018; Gao et al., 2019a). Figure 1.2 shows a historical rockburst map of more than 1100 events from nearly 50 areas from 1995 through 2019. The severity of those incidents and many rockburst events are incontrovertible evidence that rockburst is a universal and serious problem that urges much work to prevent and mitigate rockburst damage.

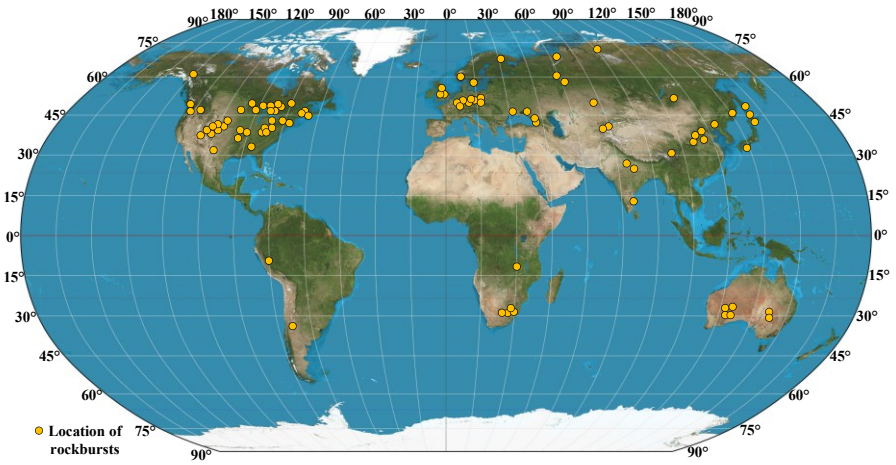

Figure 1.2 A historical rockburst map for 1995-2019 (updated after Bennett and Marshall, 2001).

The core problem of the prevention and mitigation of rockbursts is finding out what caused a rockburst or its mechanism also called the inherent or source mechanism of rockbursts (Ortlepp and Stacey, 1994). The investigation of rockburst source mechanisms can let researchers and engineers reveal the 'nature' of rockbursts and thus help engineers prevent and control rockbursts by choosing the rational location, size, and shape of openings, changing mining methods (e.g., mining protective seams and pillarless mining) and sequences, and using ground conditioning methods (e.g., distress drilling and blasting) (Mitri, 2000; Kaiser and Cai, 2012; Cai, 2013). Besides, understanding rockburst source mechanisms also help researchers and engineers identify different contributing factors required for rockburst occurrence, which provides a theoretical basis for the proposal of various prediction and evaluation indices or indicators of

rockbursts. The rockburst indicators can then predict possible rockburst locations and severity. This can further help engineers improve and optimize project layouts, mining or excavation methods to avoid potential rockbursts during the design phase and adjust construction schemes or adopt distress and support measures during the production stage.

The damage mechanism refers to what types of damage rockburst causes or failure modes (e.g., rock ejection, rock bulking, rockfall, rock buckling, and shear displacement) are induced by rockbursts. The research on rockburst damage can provide insight into the understanding of initiation, development, extent, and types of failure within surrounding rock masses during rockbursts. Furthermore, the rock failure type is one of the essential criteria for selecting rational support elements (e.g., cable bolts or rockbolts), and the damage severity can affect the capacity, extent, and intensity of support systems (e.g., the strength and length of rockbolts). Thus, understanding rockburst damage mechanisms help improve and optimize the design of rock supporting in the burst-prone ground to control and mitigate rockburst risks.

Generally, rockbursts can be classified into three types: strainburst, pillar burst, and fault-slip burst, according to different source mechanisms (Hedley, 1992; Kaiser and Cai, 2012; Cai, 2013). Strainburst is the most common type of rockbursts in mining and civil engineering projects (Zhang et al. 2012a; Cai, 2013). It occurs due to the concentration of excavation-induced tangential stress and the existence of a relatively “soft” loading environment in the rock mass surrounding the fracturing rock (Kaiser and Cai, 2012). A pillar burst is a violent failure in the pillar core or the complete collapse of a pillar. Fault-slip burst is due to the slip along pre-existing faults or newly generated shear ruptures. When the shear stress along a fault or a shear rupture exceeds the shear strength, the fault or shear rupture will slip. The main focus of this study is on strainbursts.

Presently, great efforts have been devoted to investigating the mechanisms, risk evaluation, and prediction of rockbursts. The methodologies of studying these rockburst problems can be generally

summarized into five types: analytical, experimental, empirical, data-based, and numerical (Figure 1.3). Each methodology has its strengths and limitations. Both analytical and experimental methods have the advantages of safety and repeatability. However, they employ many idealized assumptions incapable of matching the real field circumstances. For instance, experimental testing conditions are usually designed to represent field conditions, but the rock behaviour in experimental conditions may be very different from the field conditions due to the different properties of intact rocks and rock masses (Manouchehrian, 2016). Empirical methods such as in-situ monitoring measures can depict rock failure phenomena, but conducting these measures is usually dangerous, time-consuming, and expensive. Finally, data-based methods are reasonable and accurate only if a sized and accessible database and reasonable statistical or machine-learning models are provided (Zhou et al., 2018; Pu et al., 2020).

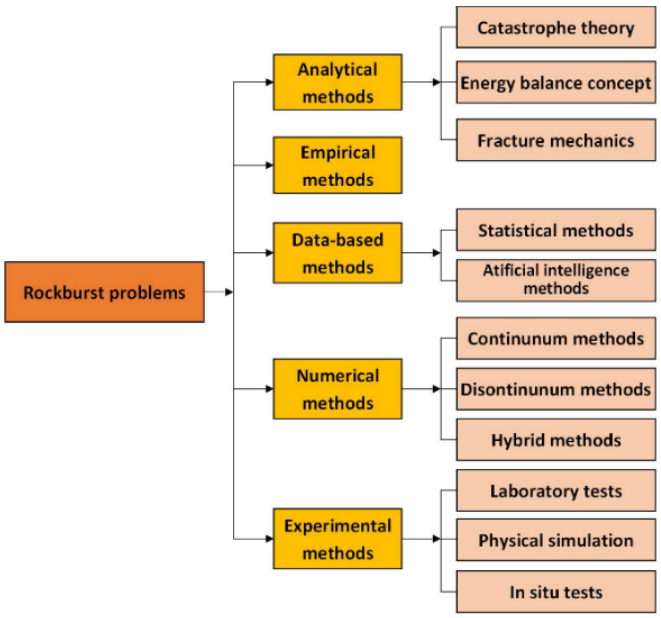

Figure 1.3 A summary of methodologies for studying rockbursts (after Manouchehrian, 2016).

Over the last five decades, with rapid developments in computer software and hardware, significant progress has been made in using numerical modeling to simulate physical phenomena in rock mechanics and rock engineering at various scales (Nikolić et al., 2016; Wang et al., 2021a). Compared with other methods, such as physical simulation and field tests, the numerical modeling method has the advantages

of low cost, safety, time-saving, and flexibility. Also, it can provide more information. Salamon (1993) stated that different aspects of the rockburst problem (e.g., the relationship between mining activities and the related seismicity, source mechanism, and the effects of seismic waves on mining excavations) would benefit from numerical modeling. Numerical simulation methods have been widely used to evaluate complex rock masses' mechanical responses and study rock mass deformation and failure mechanisms. Since the 1970s, these methods have also provided a common and necessary way to study rockburst problems. Therefore, this study employs numerical modeling as the primary research approach.

Currently, there is no effective way to control rockbursts completely because the phenomenon is very complex and is influenced by many factors, e.g., the heterogeneity of rock mass properties, the uncertainty of geological conditions, variations in in-situ and mining-induced stresses, and complex triggering conditions and construction factors. Hence, the rockburst mechanisms in some conditions remain unclear, and current methods and indicators fail to predict rockbursts in many cases (Ahmed et al., 2017). This is why rockburst accidents continue happening, and the rockburst problem has always been a serious threat to the safety of the facilities, equipment, and workers in deep excavations in mining and civil engineering projects. Therefore, the mechanisms and prediction of rockbursts need to be further studied.

1.2 Problem statement

Due to the tireless efforts of researchers and engineers, it has seen significant achievements in rockburst-related studies in the past few decades. However, as mentioned above, rockburst cannot be completely controlled because of the unknown rockburst mechanisms and the failure of rockburst prediction methods and indicators in some conditions. Therefore, after conducting a detailed literature review (see CHAPTER 2), some important but still unsolved problems are summarized as follows:

(1) Owing to the complicated mechanisms and the uncertainty of occurrence, rockburst is different from other rock mechanics problems, such as stable failure modes (e.g., rock spalling and large

deformation) after tunnel excavation and ore extraction. Therefore, many contributing factors should be considered when modeling this complex phenomenon. Thus, it is necessary to establish a systematic and reasonable numerical modeling framework for studying rockburst mechanisms.

(2) Currently, driving roadways underneath mining works in close-distance coal seam mining is common for many underground coal mines. According to some case studies, the mining pressure transferred from the panels or pillars in upper coal seams could play a key role in rockbursts in underlying coal seams. However, current research mainly focuses on the qualitative analysis of stress concentration from some case histories related to close-distance coal seam mining. Limited studies have systematically studied rockburst (source) mechanisms in such conditions using numerical methods (Zhang et al., 2021; Mi et al., 2022). The redistribution and evolution of mining- and excavation-induced stresses in close-distance coal seam mining have not been fully understood. Thus, the influence of close-distance coal seam mining on the rockburst mechanism of driving roadways remains unclear. Therefore, it is essential to reveal the rockburst mechanisms of driving roadways during close-distance coal seam mining using numerical modeling to provide some references and guidelines for controlling rockbursts in underground mines.

(3) In terms of the investigation of strainburst damage mechanisms, most current research belongs to the parametric study (e.g., different factors related to excavation geometry, stress scenario, discontinuity, and material property) without considering the gradual stress concentration or energy accumulation resulted from nearby mining or excavation activities, indicating that the influences of the realistic stress loading path on strainburst occurrence were ignored. Most studies' analyses of rock mass fracturing or damage are qualitative, although using a quantity to describe different damage degrees meticulously is meaningful. Thus, it is worth developing or employing a new modeling approach to capture the realistic stress loading path and investigate rock mass fracturing or damage quantitively during strainbursts.

(4) Using rockburst indicators combined with numerical methods has become an easy, useful, and applicable approach to predict rockburst risks qualitatively and quantitatively for research and engineering projects. However, it should be noted that different prediction and evaluation indicators of rockbursts have their best application conditions and scopes. Furthermore, because most of these indicators are based on specific cases from different regions globally, the geological conditions, rock properties, the geometry of engineering, and excavation-induced effects are very different. Therefore, the rockburst indicators cannot be directly transposed to a particular situation from one region to another. Additionally, although many researchers reported that the effectiveness of rockburst indices had been verified with on-site monitoring results, these indices cannot be popularized casually, even in the same region, due to the small number of rockburst cases and the randomness and complexity of rockburst mechanisms (Mitri, et al., 1999; Qiu et al., 2019; Wang et al., 2021a, b). Therefore, it is necessary and meaningful to develop a comprehensive method in which we can select and use rockburst indicators reasonably.

(5) Most current work focuses on evaluating the effects of traditional rockbolts under dynamic loading, while some researchers try to simulate the dynamic behaviour of yielding rockbolts by reproducing drop tests. Nevertheless, it should be noted that the simulated drop tests employ many idealized assumptions which are difficult to match the real field circumstances. For instance, the dynamic capacity of a rockbolt is not a constant value, and how a rockbolt is loaded will affect its dynamic capacity (Bosman et al., 2018). Therefore, the impact loading from drop tests might not represent rockburst loading, and the rock stress is also absent. Besides, the complex interaction between seismic waves, rockbolts, and reinforced rock masses with explicit rock detachment and ejection (requiring distinct element method (DEM) or DEM-related hybrid methods) is not considered in simulated drop tests. Therefore, it is worthwhile to evaluate the performance (e.g., the capacity of energy-absorption and control of rock damage) of yielding rockbolts during rockbursts with realistic seismic loading.

(6) The loading system stiffness (LSS, also called local mine stiffness (LMS) at the engineering scale) and the post-peak characteristic stiffness (PCS) of rock materials can distinguish stable or unstable failure (rockburst) effectively based on the stiffness theory. If LSS is smaller than PCS, the failure will be unstable and violent, and vice versa. When the research object is a rock sample or rock pillar with a regular shape and obvious loading and bearing systems, obtaining LMS through theoretical equations, numerical modeling, and experimental tests is simple. However, when the focus is a strainburst that usually occurs in a tunnel or roadway, unlike a UCS test, it is even hard to know the extent to which surrounding rock masses can be regarded as a loading system. The determination of LMS becomes a more difficult task (Castro et al., 2012). Thus, the scientific problem of determining the LMS for a tunnel and using it to develop a new indicator for predicting strainburst occurrence has confused researchers for a long time and remains unsolved.

1.3 Research objectives and methodologies

This PhD study aims to reveal rockburst mechanisms and develop a systematic method and a new stiffness-based indicator for predicting rockburst risks. In order to achieve the overall objective, six sub-objectives (see also Figure 1.4) are proposed as follows:

(1) Establish a systematic and reasonable numerical modeling framework for studying rockburst mechanisms after conducting a detailed literature review. The selection of numerical modeling approaches, numerical programs, numerical modeling sequences, material parameters, and model calibration should be included in the framework.

(2) Reveal the rockburst source mechanism of driving roadways during close-distance coal seam mining by building a 3D finite difference method (FDM) model of a case study site via fast lagrangian analysis of continua in three dimensions (FLAC3D) following the established numerical modeling framework. The mining- and excavation-induced vertical stresses will be analyzed in detail, which will

provide a basis to build a conceptual model to explain the source mechanism of the rockburst. Finally, alternative methods will be presented to prevent and mitigate rockburst hazards during close-distance coal seam mining.

(3) Develop a systematic method that can reasonably select and use rockburst indicators to predict the location and magnitude of rockbursts. After reviewing the prediction indicators of rockburst potential, some typical rockburst indicators considering different contributing factors will be selected as the evaluation criteria programmed in the built 3D FDM model to assess the rockburst potential of a case example. The simulation results will be used as motivation and references to develop the systematic rockburst prediction method.

(4) Investigate the damage mechanisms of strainbursts in a typical deep coal roadway by novelly employing an improved global-local modeling approach. The extracted stresses induced by multiple excavations from the three-dimensional (3D) FDM global model are used as boundary conditions for a two-dimensional (2D) DEM local model of the roadway built by universal distinct element code (UDEC). The strainburst damage will be studied quantitively by calculating the "damage degree" and kinetic energy.

(5) Instead of conventional drop tests, evaluate the performance (e.g., the capacity of energy absorption and control of rock damage) of yielding rockbolts during strainbursts via building a 2D DEM model of a deep roadway using UDEC. Two types of yielding rockbolts, namely D-bolt and Roofex, and the traditional rockbolt, resing-grouted rebar (for comparison), will be modelled via the "rockbolt" element in UDEC after a calibration procedure.

(6) Propose a novel method to calculate the LMS for a tunnel. As a result, a new stiffness-based rockburst indicator will be proposed and developed for predicting strainburst risks. The indicator should

successfully predict the possibility and severity of strainbursts and can be easily calculated in numerical programs (e.g., FLAC3D and UDEC).

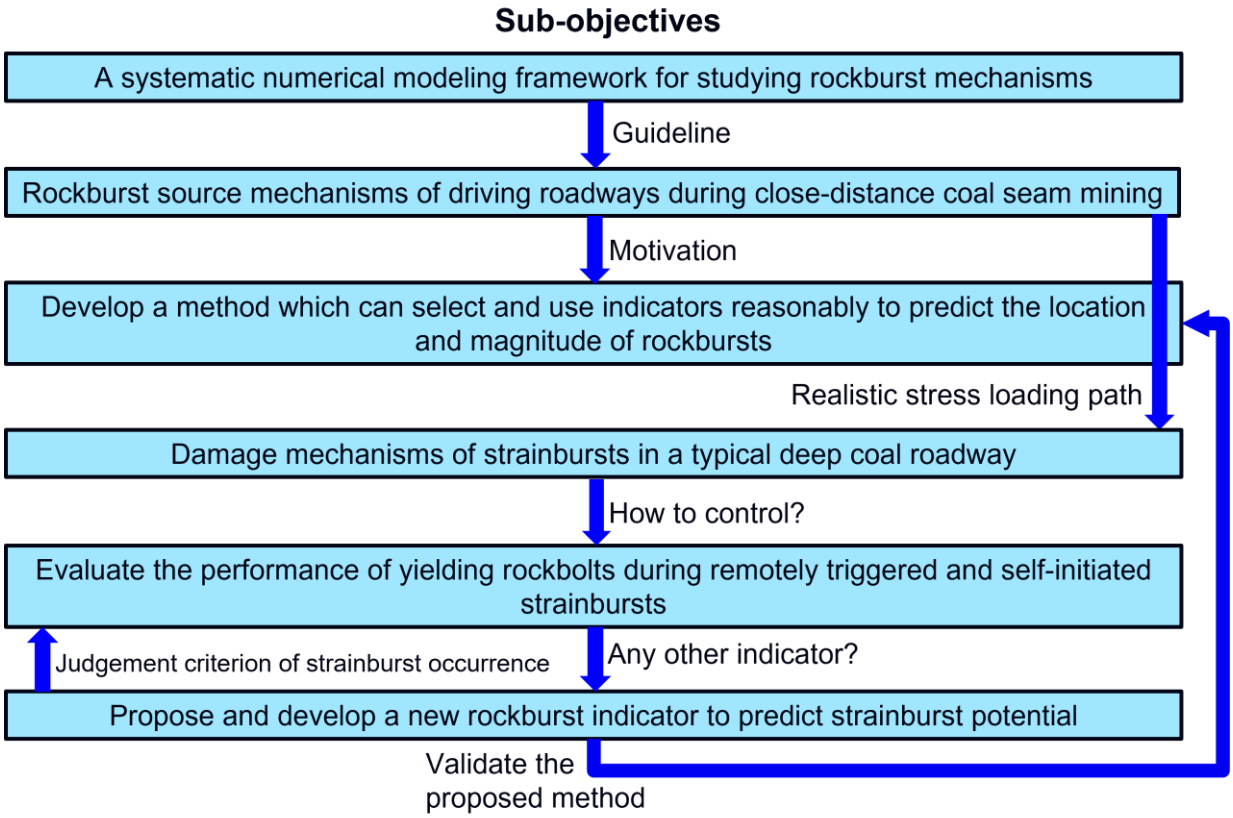

Figure 1.4 Sub-objectives of this study and their connections.

1.4 Organization of the thesis

This thesis consists of seven chapters, presented in a paper-based fashion. Each chapter is summarized as follows.

Chapter 1 is titled *Introduction*. It presents the general research background of the study, the statement of problems, the research objectives and the methodologies used. The organization of the thesis is also outlined.

Chapter 2 is titled *Literature review.* It provides a literature review based on the objectives of this study. The major focuses are on: (i) the definition, type, and mechanism of rockbursts; (ii) the categories, origin, and usage investigation of numerical methods employed in modeling rockbursts; (iii) the application of

numerical modeling in the mechanism study, prediction and evaluation, and prevention and mitigation of rockbursts. Finally, a systematic numerical modeling framework for studying rockburst mechanisms and other rockburst-related problems is established based on the summary and analysis of the literature.

In Chapter 3, following the proposed numerical modeling framework, a 3D FDM model is established via FLAC3D software using the "5.5" rockburst event in the Zofiówka Coal Mine as a case example to reveal the rockburst source mechanism of driving roadways in close-distance coal seam mining conditions. The excavation-induced vertical stresses are analyzed, which provides a basis for building a conceptual model to reveal the rockburst source mechanism. A systematic method that can select and use rockburst indicators reasonably is proposed to predict the location and magnitude of rockbursts. Some alternative measures to prevent and mitigate rockburst hazards in close-distance coal seam mining conditions are also discussed.

Chapter 4 presents an improved global-local modeling approach to study strainburst damage mechanisms. The extracted stresses induced by multiple excavations from a 3D global model established by FLAC3D are used as boundary conditions for a 2D local model of a deep roadway built by DEM software UDEC to simulate realistic stress loading paths and conduct a detailed analysis of rockburst damage from both micro and macro perspectives. The principles to control and mitigate strainburst damage are also proposed.

In Chapter 5, instead of conventional drop tests, the performance of yielding rockbolts (D-bolt and Roofex) during strainbursts was systematically evaluated by building a 2D DEM model of a deep roadway using UDEC. According to the triggering mechanism, strainburst can be classified into two types: remotely triggered and self-initiated. The remotely triggered strainburst is caused by a remote seismic event triggered by large-scale mining activities and high static stress. The self-initiated strainburst occurs due to the concentration of excavation-induced tangential stress and the existence of a relatively "soft"

loading environment in the rock mass surrounding the fracturing rock triggered. There is not a remote seismic event involved in self-initiated strainbursts. Hence, the performance of yielding rockbolts during remotely triggered and self-initiated strainbursts is investigated in parts one and two, respectively.

In Chapter 6, a novel method is first proposed to calculate the LMS for a tunnel. Later, the LMS determined by the proposed calculation method is compared to the PCS of surrounding rock masses with different brittleness to judge strainburst occurrence, which is verified with simulated stable and unstable rock failure occurring in a calibrated deep tunnel model established by UDEC. The reliability and accuracy of the proposed LMS calculation method are further examined by comparing excess energy's analytical and numerical results. Then, a new rockburst indicator, called the strainburst stiffness factor, is proposed to predict strainburst risks based on the analysis of stiffness differences. Finally, the new rockburst indicator is used to predict the rockburst potential of reported strainburst cases by performing the method proposed in Chapter 2 to validate its effectiveness.

In Chapter 7, the thesis summary and research conclusions are presented. The significance and contributions of this research are discussed. Moreover, the chapter also points out future work in investigating rockburst mechanisms and prediction using numerical modeling methods.

2. CHAPTER 2: LITERATURE REVIEW

This chapter reviews the following topics related to rockburst studies:

- *The definition, type, and mechanism of rockbursts*
- *The categories, origin, and usage investigation of numerical methods employed in modeling rockbursts*
- *The application of numerical modeling in the mechanism study, prediction and evaluation, and prevention and mitigation of rockbursts*

*A systematic and reasonable numerical modeling framework for studying rockburst mechanisms and other rockburst-related problems is also presented. This chapter is partially based on the published paper "**Wang, J.**, Apel, D. B., Pu, Y., Hall, R., Wei, C., Sepehri, M. (2021). Numerical modeling for rockbursts: A state-of-the-art review. Journal of Rock Mechanics and Geotechnical Engineering, 13(2), 457-478".*

2.1 Definition, type, and mechanism of rockbursts

Rockburst is a complex, nonlinear, and dynamic rock failure phenomenon governed by many control factors (Feng et al., 2019a; Gao et al., 2019a). Therefore, researchers must understand rockbursts before modeling this special phenomenon for studies and engineering designs. This section summarizes the definition, type, and mechanism of rockbursts.

2.1.1 Rockburst definition

It is important to define the difference between a seismic event and a rockburst, as these two terms are often found in numerous publications and may confuse readers. For example, according to the Chambers of Mines of South Africa (1982):

A seismic event is a transient earth motion caused by a sudden release of potential or stored strain energy in the rock. As a result, seismic energy is radiated in the form of strain waves. The magnitude of a seismic event is usually determined from the peak amplitude of the strain wave using a logarithmic scale (e.g., Richter scale).

A rockburst is a seismic event that causes injury to persons or damage to underground workings. The general and essential feature of rockbursts is their sudden and violent nature.

In summary, a rockburst is a seismic event, but not all seismic events are rockbursts.

There are many definitions of rockbursts, but no universally accepted definition exists. The Ontario Mining Act (1939) (Hedley, 1992) defined rockburst as a phenomenon causing a fall of ground into an excavated area or a movement of the ground in or about an excavated area and characterized/accompanied by a shock or tremor in the surrounding rock. The Canadian Occupational Health and Safety Act (1978) (Hedley, 1992) modified the definition to an instantaneous failure of rock causing expulsion of material at the surface of an opening or a seismic disturbance to a surface or underground mine. Cook (1965a) defined rockburst as an uncontrolled disruption of rock associated with a violent release of energy. Blake

(1972b) suggested that a rockburst is a sudden rock failure characterized by the breaking up and expulsion of rock from its surroundings, accompanied by a violent release of energy. Hoek and Brown (1980) concluded that rockburst results from a shear failure in the surrounding rock masses within high in-situ stress zones. According to the Mine Safety and Health Administration (1984), a rockburst is "a sudden and violent failure of a large volume of overstressed rock, resulting in the instantaneous release of large amounts of accumulated energy."

Lenhardt (1992) suggested that rockburst relates to events generated in mining environments, especially concerning violent rock failure. Kaiser et al. (1996) proposed that a rockburst is a form of damage to an excavation that occurs suddenly or violently and is associated with a seismic event. Qi et al. (2003) concluded that rockburst is a geological hazard involving dynamic instability due to the loosening, splitting, and ejection of rock masses because of suddenly released elastic strain energy after excavation unloading. Tang (2004) proposed that the rockburst development process is static and that rockburst occurrence is dynamic. Zhang et al. (2008) stated that rockburst occurs in hard and brittle intact rock masses. The great depth of excavations or the movement of the crust may cause a large amount of strain energy to accumulate in rock masses, leading to significant initial stresses. When the strain energy is suddenly released during excavation, it is accompanied by loud sounds with many lenticular-shaped rock fragments flying out of the rock wall. Mazaira et al. (2015) reported that rockburst always involves a violent energy release with large rock deformation and rock ejection that can cause severe damage to openings, equipment, and facilities, resulting in fatalities. Ali et al. (2018) found that the term "rockburst" is applied to the damage that occurs as a result of, or is directly associated with, a seismic event that generates sufficient energy to cause the violent failure of the rock mass. Wei et al. (2018) defined a coal burst as a dynamic form of rock failure that usually happens with an audible sound and a large deformation

of roadways. It should be noticed that although none of those definitions is universal, several consensuses are widely recognized by researchers:

(1) *Rockburst is a type of rock failure*. Rock failure modes such as sounds, deformation, fracturing, spalling, bulking, falling, and splitting are often observed in the field when rockbursts occur.

(2) *Rockburst is a dynamic instability failure with suddenly or violently released elastic strain energy and rock ejection, while rock failure without dynamic ejection is recognized as a static brittle failure mode* (Tan, 1991). In addition, a rockburst is always associated with a seismic event, and in some cases, the magnitude of a rockburst is similar to that of a midsize earthquake.

(3) *Rockburst often occurs in hard and brittle rock masses surrounding excavations in high static stress environments*. It should be known that rockburst (coal burst) also occurs in coal masses that belong to a kind of weak and "soft" rock (Ortlepp and Stacey, 1994; Díaz-Aguado and González, 2009; Konicek et al., 2011).

(4) *Rockburst is one of the geological hazards that can damage excavations, equipment, and facilities and can even result in fatalities*. This concept is of great significance when considering rockbursts in different engineering fields. Jiang et al. (2014, 2015) reported that due to the requirements of the roadways or stopes in mining engineering projects are relatively temporary, and it is usually acceptable to moderate even a large deformation or damage to surrounding rock masses, as long as the surrounding rock structure does not destabilize and meets the requirements of safety production. In contrast, only minimal deformation or damage is allowed in civil and geotechnical engineering projects such as tunnels because such projects have a long service life and stringent reliability and security requirements. In addition, the existence of mining-induced stress is another major difference between mining engineering and civil engineering. Therefore, Jiang et al. (2014, 2015) claimed that it should be used as a sign of rockbursts in underground mines that such dynamic phenomena cause "disaster destructiveness" to safe production. For

example, the rockburst described in Norwegian tunnels (Myrvang and Grimstad, 1983) is very different from that described in a deep-level mining situation (Ortlepp, 1978).

2.1.2 Rockburst type

The terms “rockburst type” and “rockburst intensity” describe very different phenomena, but people still confuse them. Rockburst intensity refers to the severity and level of damage caused by a rockburst event. It is generally grouped into three to four types (e.g., minor rockburst, moderate rockburst and major rockburst) based on one or more indicators such as sound, failure shape, damage depth and length, the volume of failed rocks, ejection velocity, and radiated energy. Rockburst type is a classification usually determined by different rockburst mechanisms (Tan, 1991; Zhou et al., 2018). Similar to rockburst definitions, rockburst types are not uniform at present. With the deepening of investigations into and the understanding of rockbursts, researchers have constantly proposed and defined different rockburst types based on intrinsic factors, causes, failure modes, stress states and etc. The main rockburst types proposed in the past 70 years are shown in Table 2.1. According to different classification criteria, rockbursts are usually grouped into two to five types, and the most common classification criteria are based on the source mechanism of rockbursts. In the past, rockbursts with relatively high frequency were classified into five types according to their characteristics and source mechanisms: strainburst, buckling, pillar burst or face crush, shear rupture, and fault-slip burst (Ortlepp 1992). Hedley (1992) and Kaiser et al. (2012) suggested that buckling-type rockbursts can be considered strainbursts, and shear rupture-type rockbursts can be considered fault-slip rockbursts in a broad sense. Therefore, most researchers currently classify rockbursts into three types: strainburst, pillar burst, and fault-slip burst.

Table 2.1 Category of rockbursts

Author (year)	Rockburst type	Number of type	Classification criterion
Colson (1950)	a) Induced burst, b) residual burst, c) inherent burst and d) combination burst	4	Origin of the burst
Brown (1984)	a) Slip-on pre-existing discontinuities and b) fracturing of intact rock	2	Source mechanism

Tan (1991)	a) Horizontal stress type, b) vertical stress type, and c) mixed stress type	3	Stress action pattern
Hedley (1992)	a) Strainburst, b) pillar burst, and c) fault-slip burst	3	Source mechanism
Ortlepp et al. (1994), Ortlepp (1997)	a) Strainburst, b) buckling, c) pillar burst or face crush, d) shear rupture, and e) fault-slip burst	5	Source mechanism
Guo (1996)	a) Splitting and ejection, b) exfoliation, and c) collapse	3	Failure mode
Kaiser et al. (1996)	a) Remotely triggered, and b) self-initiated	2	Triggering mechanism
Kaiser et al. (1996)	a) Bulking, b) ejection and c) seismically-induced fall of ground	3	Damage mechanism
Xu et al., (1996)	a) Gravity stress type, b) tectonic stress type, c) variational stress type, and d) comprehensive stress type	4	Origin of high geostress
Tang (2000)	a) Strainburst, b) fault-slip burst, and c) combined bursts	3	Source mechanism
He et al. (2007)	a) Instant rockburst, b) standard rockburst, and c) delayed rockburst	3	Unloading and the beginning of rockbursts
Qian (2011)	a) Strainburst, b) tectonic rockburst, and c) strain and tectonic hybrid rockburst	3	Source mechanism
He et al. (2012) and (2018)	a) Strainburst, and b) impact-induced burst	2	Triggering mechanisms and physical experimental methods
Cai (2015)	a) Pillar-induced rockburst, b) fold structure-induced rockburst, c) fault-induced rockburst, and d) hard roof induced rockburst	4	Locations and inducing factors
Jiang et al. (2015)	a) Material instability type, b) slip dislocation type, and c) structural instability type	3	Essences of sudden instability and failure
Keneti et al. (2018)	a) Mining-induced, and b) dynamically-induced	2	Source of energy release and damage are co-incident or not
Deng and Gu (2018)	a) Inherent rockburst, b) triggered rockburst, and c) induced rockburst	3	Buckling (instability) problem of structures
Li (2018)	a) Strainburst, and b) seismic rockburst	2	Source mechanism
Tan et al. (2019)	a) Fault-slip burst, b) hard-roof burst, and c) strainburst	3	Rock properties and source mechanism

2.1.3 Rockburst mechanism

Determining rockburst mechanisms is one of the most attractive research topics in the rockburst-related field. Since this phenomenon was discovered at the beginning of the 20th century, numerous researchers have been trying to figure out how a rockburst occurs. Although the mechanisms underlying rockburst are complex and rockburst mechanisms are still unclear at present, scholars have reached an agreement on some mechanisms, especially for a few specific rockburst types.

Ortlepp and Stacey (1994) suggested that it is vital to differentiate the "source mechanism" and the "damage mechanism" for rockbursts because they are often not the exact mechanism and may be located far from each other. The source mechanism is the trigger factor that induces rockbursts. The damage mechanism refers to failure modes induced by rockbursts. In strainbursts and pillar bursts, the rock masses involved in the source and damage mechanisms are generally located in the same place, while in fault-slip bursts, the rock masses involved in the source mechanism are located in shear planes of fractures and of discontinuities, which are often very far from excavation limits (Ortlepp and Stacey 1994; Kaiser and Cai 2012; Cai 2013). This research summarizes rockburst mechanisms based on source and damage mechanisms.

2.1.3.1 Source mechanism

As mentioned above, a rockburst is a rock failure phenomenon that occurs when an excavation- or mining-induced stress exceeds the peak strength of rock masses. Although a part of the intrinsic factors of rockbursts is similar to static rock failure, rockburst mechanisms are unique. As mentioned earlier, the source mechanisms of the most-accepted three types of rockbursts (strainburst, pillar burst, and fault-slip burst, all shown in Figure 2.1) are discussed in this section.

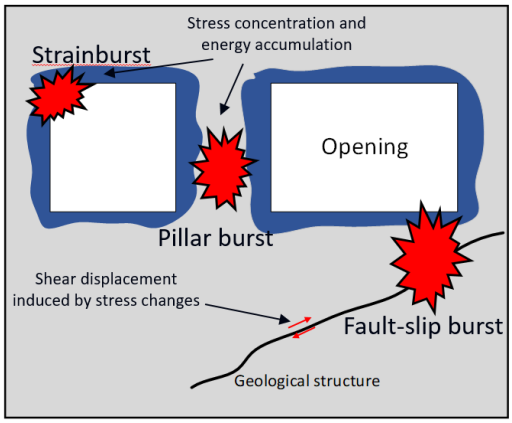

Figure 2.1 Schematic representation of potential for rockbursts (from Castro et al., 2012).

(1) Strainburst: This is the most common type of rockbursts in all underground excavations (Zhang et al. 2012a; Cai, 2013). Two necessary conditions must be met to trigger a strainburst (Kaiser and Cai,

2012). First, the mining- or excavation-induced tangential stress (the maximum principal stress) must exist and be accumulated in the excavation boundary. Second, a relatively "soft" loading environment must be created in the rock mass surrounding the fracturing rock such that the rock can fail locally in an unstable and violent manner, which is very similar to the explanation of rock failure in the uniaxial compressive strength (UCS) test based on stiffness and energy theories (Cook, 1965a; Salamon 1984). Kaiser and Cai (2012) also proposed that strainbursts can be mining-induced due to static stress changes caused by nearby mining, or they can be dynamically induced due to a dynamic stress increase caused by a remote seismic event. In addition, it is worth noting that in some cases, rockbursts occur due to the degradation of rock strength over time, but the maximum principal stress remains constant. This type of rockbursts is called a delayed strainburst (Chen et al., 2012).

(2) Pillar burst: This is a violent failure in the pillar core or the complete collapse of a pillar. After mining or excavating, rock masses surrounding the opening are damaged, and then the high stress and elastic strain energy accumulate gradually in intact rock masses (pillar core area). The pillar burst will occur suddenly when the accumulated elastic strain energy reaches a critical level, which means the released energy is higher than the dissipated energy. As a result, a large volume of failed rocks is released, and the magnitude is usually more significant than a strainburst (Ortlepp and Stacey, 1994). Depending on different trigger factors, pillar burst can also be classified into mining-induced and dynamically-induced (Kaiser and Cai, 2012).

(3) Fault-slip burst: This is due to the slip along pre-existing faults or along newly generated shear ruptures. The faults or shear ruptures can facilitate the storage of stress and elastic strain energy in nearby areas because discontinuity becomes the barrier to the stress redistribution in surrounding rock masses. For example, in mining or tunnelling engineering projects, excavating activities will induce stress redistribution. When the shear stress along a fault or a shear rupture exceeds the shear strength, the fault

or shear rupture will slip. As a result, a large amount of seismic energy will be released suddenly, with high ground vibrations or motions, and may trigger other types of rockbursts. Kaiser and Cai (2012) proposed that the most plausible reason for fault slip is reducing normal stress, which is one of the independent variables of shear strength. However, fault-slip may also be caused by increasing the shear stress, decreasing the normal stress, and increasing the shear stress simultaneously.

2.1.3.2 Damage mechanism

According to Ortlepp and Stacey (1994), Kaiser et al. (1996), Ortlepp (2001), Cai (2012) and (2013), the common types of damage induced by rockbursts are (i) rock ejection; (ii) rock bulking; (iii) rockfall; (iv) rock buckling; and (v) shear displacement (shown in Table 2.2). Table 2.2 shows that different rockburst sources can produce similar rock damage on the excavation surface and that the damage location is not usually limited to a particular area. In addition, for rock ejection, bulking, and rockfall, the location relationship between the rockburst source and damage is not necessarily coincident, while it is coincident for the latter two types of rockburst damage.

Table 2.2 Rockburst damage mechanisms (figures from Ortlepp and Stacey, 1994; Kaiser et al., 1996; Ortlepp, 2001; Kaiser and Cai, 2012; Cai, 2013)

Author (year)	Damage mechanism	Explanation	Damage location (e.g., a tunnel)	Rockburst source	Location relationship between rockburst source and damage	Schematic diagram
Ortlepp and Stacey (1994); Kaiser et al. (1996); Kaiser and Cai, 2012; Cai (2013)	Rock ejection	After the rock fractures, rock is ejected violently because a part of the strain energy stored in the surrounding rock is transferred to the kinetic energy in rock blocks.	Floor, roof, or face	(a) Strainburst (b) Pillar burst (c) Fault-slip burst	Not necessarily coincident	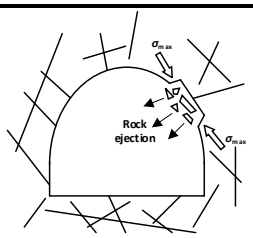
Kaiser et al. (1996); Kaiser and Cai, 2012; Cai (2013)	Rock bulking	The broken rock volume increases as it is fractured and fragmented.	Perpendicular to the excavation wall	(a) Strainburst (b) Pillar burst (c) Fault-slip burst	Not necessarily coincident	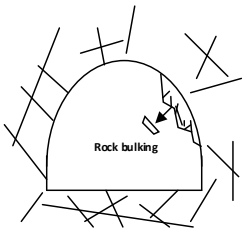

Ortlepp and Stacey (1994); Kaiser et al. (1996); Kaiser and Cai, 2012; Cai (2013)	Rockfall	The seismic wave accelerates the rock, causing forces to overcome the capacity of the support system and thus the rock falls.	Roof and side wall	(a) Pillar burst (b) Fault-slip burst	Not necessarily coincident	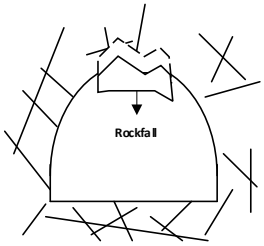
Ortlepp and Stacey (1994)	Rock buckling	Rock deformation and failure of laminated rocks by a buckling mechanism.	Anywhere around the tunnel periphery, including the face	(a) Strainburst (b) Pillar burst (c) Fault-slip burst	Coincident	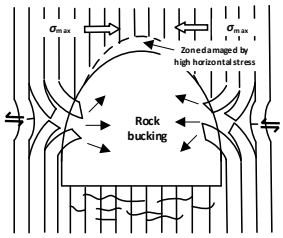
Ortlepp (2001); Cai (2012) and (2013)	Shear displacement	Shear displacement of rocks is due to the activation of faults.	Anywhere around the tunnel periphery, near to faults	(a) Fault-slip burst	Coincident	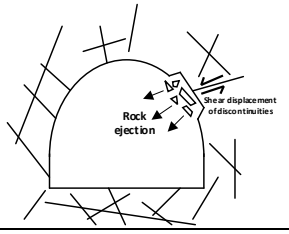

2.2 Numerical methods for modeling rockbursts

2.2.1 Category of numerical methods

With the rapid development of information technology (IT) and computer equipment, the availability of high-powered computer equipment such as supercomputers, cloud computing, and a large number of numerical approaches, as well as a great variety of commercial or academic codes, has opened avenues for the analysis and evaluation of complex problems in rock mechanics and rock engineering. Nevertheless, researchers and engineers must discriminate amongst different numerical approaches and codes before using numerical modeling to tackle rock mechanics problems (Wagner, 2019). According to Jing and Hudson (2002) and Jing (2003), numerical approaches in rock mechanics can be classified into the continuum, discontinuum, and hybrid methods (Table 2.3). The main subtypes and related commercial or research codes at present are also shown in Table 2.3. This literature review is mainly focused on numerical modeling for rockbursts. The detailed discussion of the concepts, principles, advances, and development of various numerical methods used in rock mechanics and rock engineering have been

excellently reviewed by Ryder and Jager (2002), Jing and Hudson (2002), Jing (2003), Brady and Brown (2004), Nikolić et al. (2016), and others.

Table 2.3 Overview of numerical approaches and codes in rock mechanics

Numerical approach	Subtype	Commercial/academic code	Institution/Author (year)
Continuum method	Finite Element Method (FEM)	ABAQUS	Dassault Systèmes
		ADINA	ADINA R&D, Inc.
		ANSYS	ANSYS, Inc.
		GEO5	Fine Software
		LS-DYNA	LSTC
		midas GTS NX	MIDAS IT
		PLAXIS2D; PLAXIS3D	Plaxis
		RFPA2D; RFPA3D	Mechsoft
		RS2 (Phase2); RS3	Rocscience
	Finite Difference Method (FDM)	FLAC; FLAC3D	Itasca Consulting Group, Inc.
	Boundary Element Method (BEM)	Examine	Rocscience
		Map3D Non-Linear	Map3D
Discontinuum method	Distinct Element Method (DEM)	PFC2D; PFC3D	Itasca Consulting Group, Inc.
		UDEC; 3DEC	Itasca Consulting Group, Inc.
	Discontinuous Deformation Analysis (DDA)	DDA codes	Goodman and Shi (1985)
	Discrete Fracture Network (DFN)	FracMan	Golder
		NAPSAC	AEA Technology
Hybrid method	Boundary Element Method/Distinct Element Method (BEM/DEM)	DEM_SRS+BEDA+FNET+BEFA	Wei (1992), Wei and Hudson (1998)
	Boundary Element Method/Finite Element Method (BEM/FEM)	BEM/FEM codes	Zienkiewicz (1977)
	Distinct Element Method/Finite Element Method (DEM/FEM)	CA3	Fakhimi (2009)
		ELFEN	Rockfield
		IRAZU	Geomechanica
		NMM	Shi (1991)
		Y2D	Munjiza (2004)
		Y-Geo	Mahabadi (2012)
	Distinct Element Method/Finite Difference Method (DEM/FDM)	PFC2D/FLAC; PFC3D/FLAC3D	Itasca Consulting Group, Inc.

2.2.2 Origin of numerical methods employed in modeling rockbursts

Employing numerical approaches to investigate rock mechanics problems has been a common practice dating back to the 1960s (Salamon, 1964; Jing and Hudson, 2002; Jing, 2003), while numerical modeling to study rockburst-related problems was introduced a little later, in the 1970s.

The hazard of spalling is an important consideration when rock faces are subjected to dynamic loading induced by blasting or rockbursts near a permanent mine opening. Miranda (1972) first developed a finite-difference computer code to simulate the elastic pulse propagation problem in the Split-Hopkinson pressure bar (SHPB) technique. He found that the computed numerical gage data agreed well with the derived strain and strain rate-time curves of the specimen. In the same year, Blake (1972a) acted as a

pioneer in using the finite element method (FEM) model to study pillar bursts. He found that the areas of high stress concentration could be used as a sign to predict rockburst locations. Brady (1979) developed the boundary element method (BEM) with a proposed complete plane strain concept and first used it to study the unstable failure of pillars (pillar crush). He also proposed a cutting-edge idea: modeling country rock as an elastic continuum by exploiting the efficient BEM and treating pillars as inclusions within more complex constitutive equations. For example, the finite difference method (FDM) might be used in pillars to model the complex behaviour of rock materials. Maybe this is the origin of the hybrid method concept. Board et al. (1980) employed hybrid computer and digital computer models utilizing the displacement discontinuity method (BEM) to study stress and displacement changes. Then he used the calculated energy release rate (ERR) to examine the effect of mining in an underhand fashion on the potential for sill pillar bursting. The results suggested that the ERR was lower when a larger sill pillar remained, but its magnitude was still enough to cause a pillar burst. This shows that a numerical simulation is useful for evaluating rockburst risks and improving mining design. Hart (1980) used the explicit FDM code, STEALTH, and the BEM code, MINAP, to evaluate rock failure and dynamic instabilities (rockbursts) based on the ERR. He concluded that the results between the two codes were close for the elastic simulation, and the BEM model was much easier to formulate and less expensive to run. However, the results also suggested that stored energy simulated by MINAP using the elastic constitutive model was smaller than that using the STEALTH employing a non-linear constitutive model due to the lack of plastic deformation stage. This shows how important it is to select a reasonable constitutive model for geotechnical modeling. Zubelewicz (1983) combined the FEM and a dynamic approach to study rockburst processes in a rock pillars, excavation faces, and tunnels. He also confirmed that the dynamic mode of failure could be numerically studied for any specified configuration and initial conditions.

The usage of the discontinuum method for modeling rockbursts is later than the continuum method since more latter researchers began to notice the significance of discontinuities such as joints, which control and influence the mechanical behaviours of rocks, as well as the requirement of the large displacement of rocks. In contrast, the continuum method is based on the hypothesis of continuous small deformation. The DEM is a discontinuum modeling approach that can, in a straightforward manner, model large displacements, disintegrations, rotations, and general non-linear constitutive behaviours for both rock masses and joints. After the DEM was developed and established (Cundall, 1971, 1979 and 1988), Lemos (1987) was the first researcher to use it to investigate the features of jointed rocks subjected to dynamic loading, such as rockbursts. He stated that the DEM provided a useful tool for understanding various dynamic problems in jointed rock masses. The DFN is a special discrete method that is most useful for studying flow in fractured rock masses (Jing and Hudson, 2002; Jing, 2003). In 2009, Arndt et al. (2009) reported that they used the DFN model to conduct dynamic tests of a heavy support system to investigate the effects of seismic hazards on ground supports. In 2007, Sun et al. (2007) investigated rockbursts in a circular tunnel under unloading conditions by program realistic failure process analysis (RFPA) and DDA. In order to simulate the gestation process of rockbursts, the failure patterns of surrounding rock masses of a circular tunnel were first studied by RFPA, taking into consideration the non-homogeneity of rock materials and different in-situ stresses. The crack lines and some potential cracks in the RFPA model were then imported into a DDA model to simulate a rockburst's dynamic processes. The results suggested that the loss of stability of the surface rock mass was an omen or the beginning of a rockburst. However, Sun et al. (2007) also pointed out that the rock masses had to be discretized artificially in the DDA model and that the released strain energy was ignored in the DDA model. Hence, an improved simulation of rockbursts needs to be further investigated.

Jing (2003) reported that the main influence area of damage is concentrated near the excavation face and that linear material behaviour is exhibited in the far-field region without fractures. Therefore, the discontinuum method is more suitable for near-field analysis, while the continuum method is more suitable for far-field analysis. Thus, it is a good way to combine those two numerical methods, which simultaneously makes full use of their respective advantages and avoids their disadvantages. Daehnke (1999) analyzed the dynamic fracturing due to the interaction of primary (P) and secondary (S) waves with stopes by implementing a parametric study through the FEM/DEM code ELFEN. The results verify that ELFEN can accurately simulate stress wave interactions and dynamic fracturing in underground excavations. After the FDM/DEM coupled method was proposed and developed (Itasca Consulting Group Inc., 2000), Hazzard and Young (2002) adopted it to model microseismic (MS) activities surrounding a deep tunnel. The target area was modeled by an assemblage of particles from particle flow code (PFC) and was then coupled with program fast lagrangian analysis of continua (FLAC). Although the model is clearly a large simplification of realities, the simulation results, such as seismic locations, magnitudes, and mechanisms obtained from the numerical model compared with seismic data in the field, give further confidence that the FDM/DEM coupled model can behave realistically. Later, Cai et al. (2007) employed the FLAC/PFC coupled numerical model to investigate excavation-induced acoustic emission (AE) activities in large-scale underground excavations. In the modeling, PFC was used to simulate AE sensors around surrounding rock masses and FLAC modelled the remaining rock masses. The simulated AE activities were in good agreement with field monitoring results, which confirms that the coupled numerical method as an advanced tool can be applied to the interpretation of monitoring data and stability evaluation of large-scale underground excavations. SPECFEM2D is a powerful software package that can simulate the propagation of acoustic and elastic waves in various media, such as fluids, elastomers, viscoelastic, anisotropic and porous objects, but it cannot analyze excavation stress. By combining

FLAC/SPECFEM2D, Wang and Cai (2017) proposed a coupled numerical method for a non-linear velocity model to study the excavation effect on the ground motion in an excavation boundary. They found that the amplification effect at the excavation surface agreed well with underground field observations, and when the simulated excavation rock was of fair quality, the excavation boundary of the stope had a stronger ground motion and wider seismic response. The coupled numerical method is helpful to better estimate ground motion parameters in dynamic load support design and can provide reasonable ground motion evaluation parameters in an inversion analysis of rockburst damage. Figure 2.2 shows the development process of various numerical methods employed in the history of modeling rockbursts.

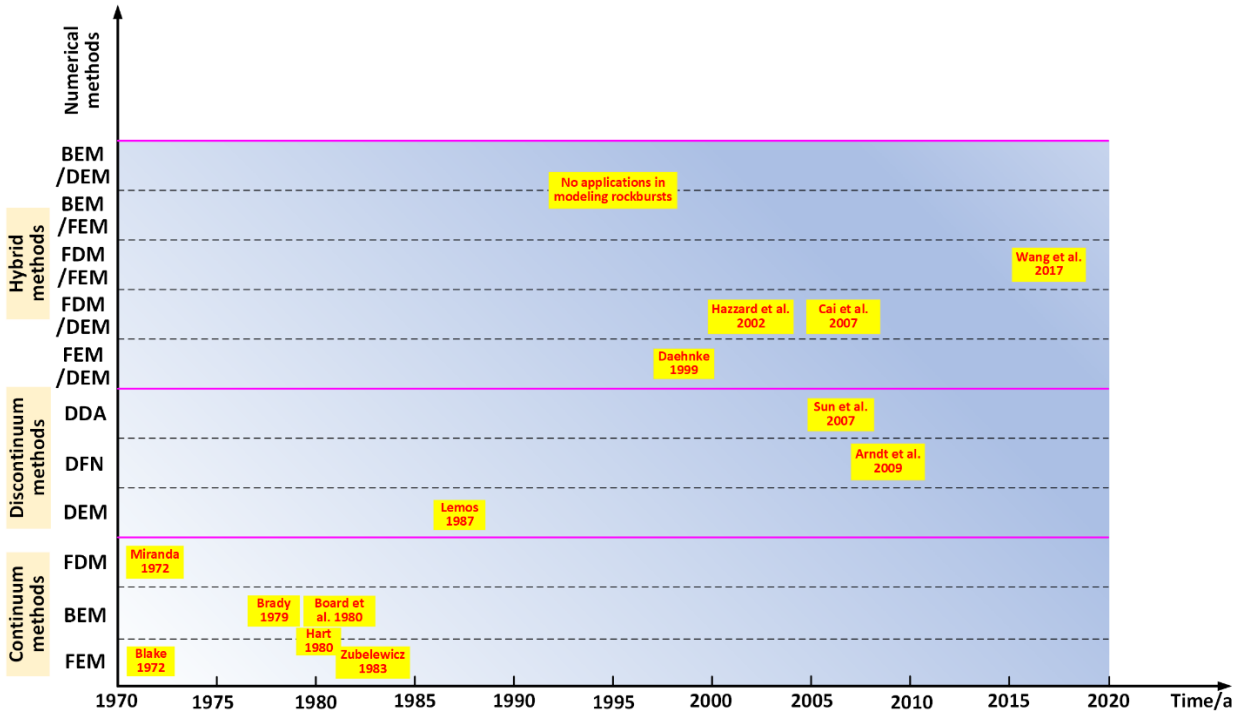

Figure 2.2 History of numerical methods employed in modeling rockbursts.

2.2.3 Usage investigation of numerical modeling for rockbursts

In order to understand the usage of various numerical approaches to model rockbursts, we used "TS=(rockburst* OR rock burst*) AND TS=numerical" as query words in the Web of Science database to investigate literature published during the last 20 years. Unfortunately, it is hard to search all published

literature about this topic due to copyright and access-related issues. However, after reviewing the published literature in this well-accepted and authoritative database and having relatively large amounts of data, we were confident that our investigation reflected the usage situations of various numerical approaches to model rockbursts. The search results are shown in Figure 2.3 to Figure 2.5, and the variation laws are summarized as follows:

(1) Figure 2.3 shows that since 1999, the amount of literature in this field has increased. From 1999 to 2008, the growth was not very apparent, and the number of published articles increased only from three to seven. After 2009, the number of published articles grew rapidly, although they may suffer a decrease in a few years. After 2016, the number of publications was nearly ten times that of 1999. Moreover, most researchers choose the continuum method for addressing rockburst-related problems. After 2014, more researchers began using the discontinuum and hybrid methods.

(2) As shown in Figure 2.4, the most common numerical approach is the continuum method (77.36 %), and the second most common is the discontinuum method (19.54 %). The hybrid method accounts for only 3.10 %. For the continuum method, FEM and FDM are the most popular numerical methods (94.1 % in total). Furthermore, in the FEM, the widely used numerical programs are ABAQUS (13.27 %), ANSYS (11.22 %), and RFPA (22.45 %). Suit3D (14.29 %) and Map3D (35.71 %) are the most popular codes in the BEM, while FLAC (20.72 %) and FLAC3D (76.89 %) account for the largest proportion in the FDM. For the discontinuum method, DEM is the most popular (93.33% in total). There is no DFN in the pie chart because DFN is the built-in function in some programs, such as ABAQUS, FLAC3D, and 3DEC. Thus, we did not show it in a single segment. In the DEM, the most popular codes are UDEC (54.46 %), 3DEC (9.86 %), and PFC2D (17.86 %), respectively. For the discontinuum method, the DEM/FEM (47.37 %) is widely used, and FLFEN (55.56 %) is the most common numerical program.

(3) In reality, rockburst types are various, according to different researchers (Zhou et al., 2018). Therefore, based on loading conditions and seismic waves, we classified the published literature as static simulation and dynamic simulation. As shown in Figure 2.5a, from 1999 to 2008, most numerical modeling of rockbursts was conducted by static simulation, and then there was a rapid growth after 2009, especially after 2015. In 2016, 2017, and 2018, the proportion of dynamic simulation was more than 30 % each year. Figure 2.5b shows that most researchers employ static simulation to investigate rockbursts (71.34 %).

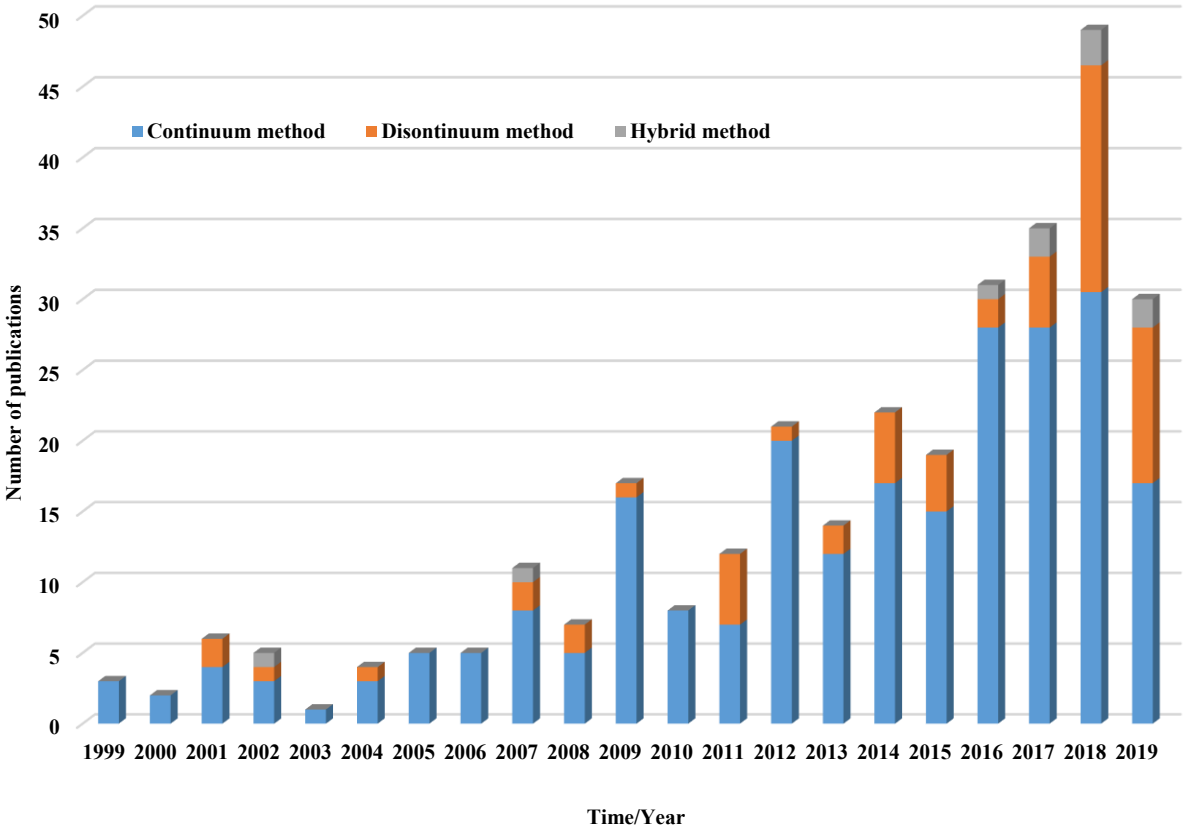

Figure 2.3 Literature about numerical modeling of rockbursts in the last 20 years (the search results in 2019 are incomplete).

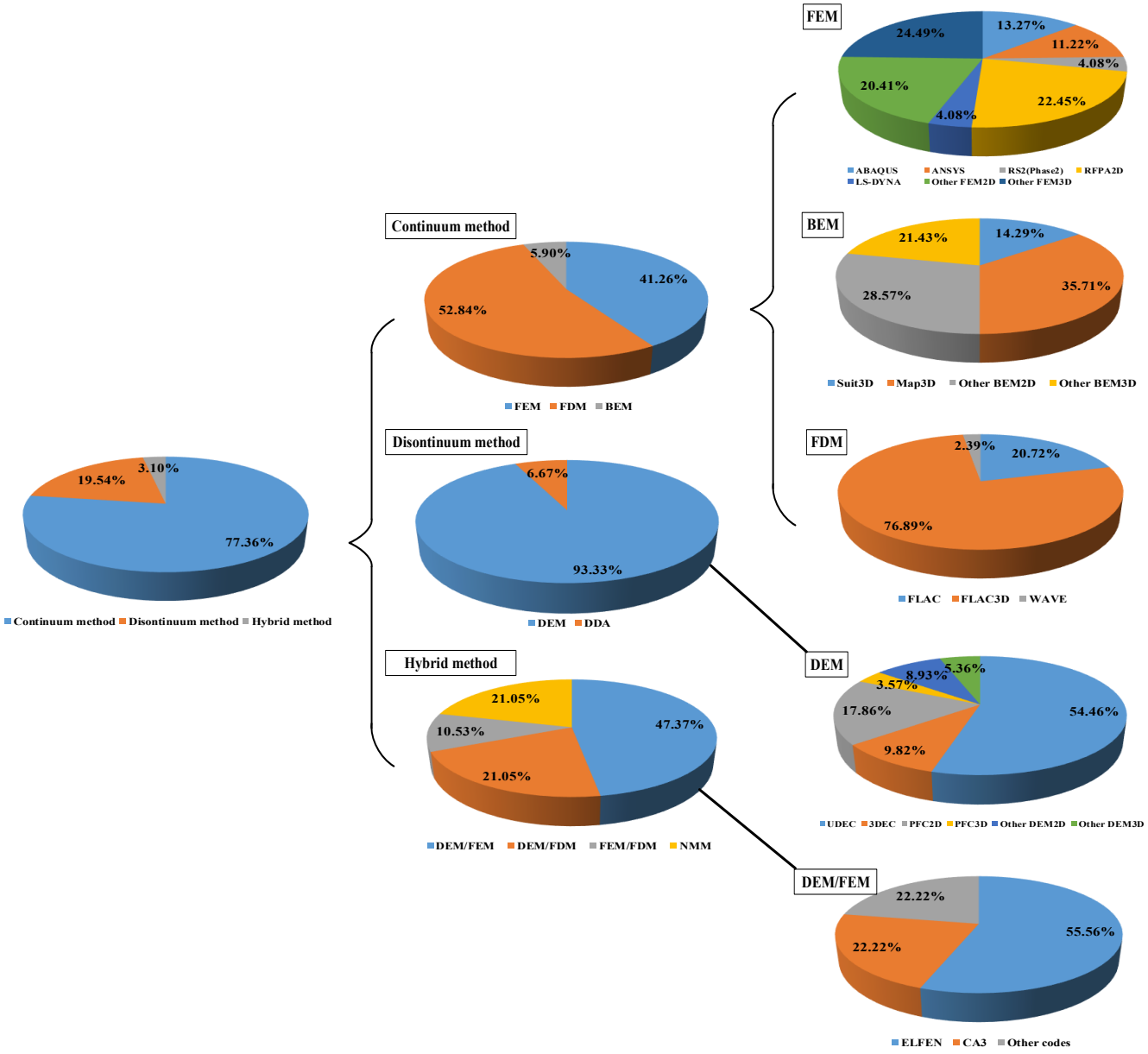

Figure 2.4 Distribution of different numerical methods in modeling rockbursts in the last 20 years (the search results in 2019 are incomplete).

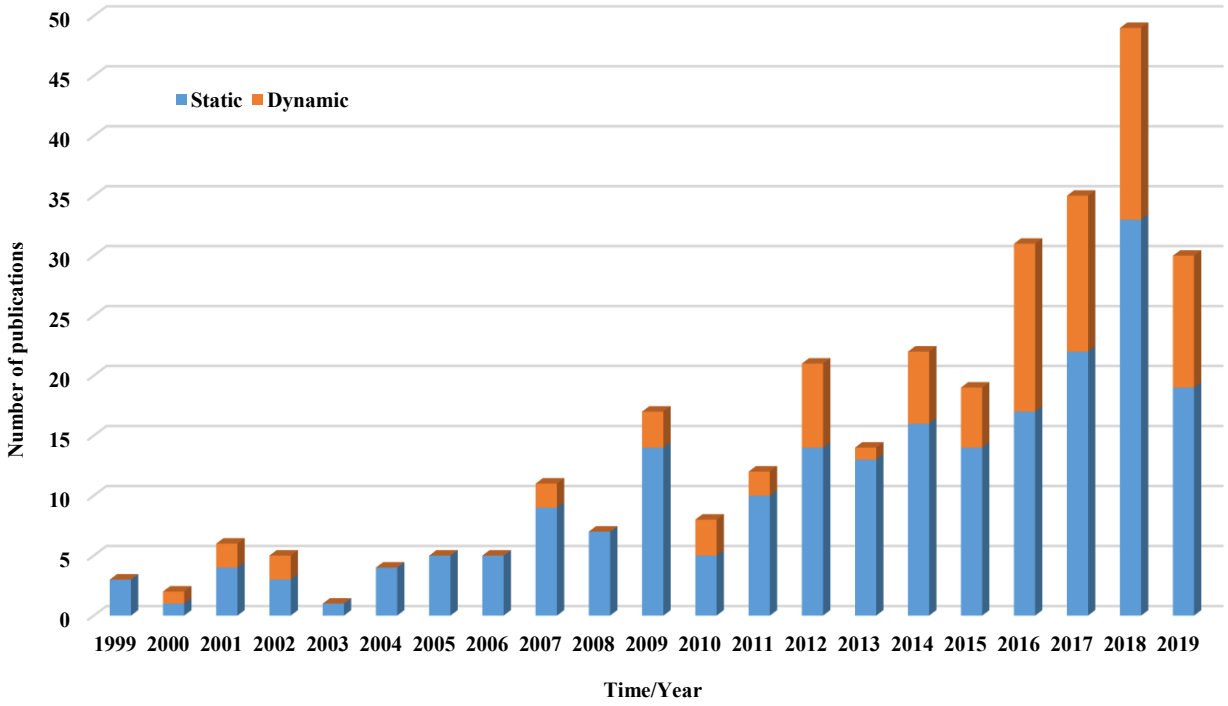

(a) Variation of literature with time

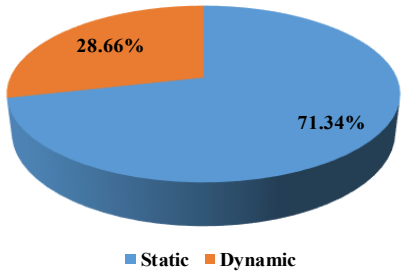

(b) Proportion of literature

Figure 2.5 Literature about the static and dynamic simulation of rockbursts in the last 20 years (the search results in 2019 are incomplete).

2.3 Application of numerical methods in modeling rockbursts

2.3.1 Numerical modeling for rockburst mechanisms

The initial studies of rockburst mechanisms through numerical modeling were based on specific engineering cases. The continuum method, elastic constitutive relationship, and 2D model were often used owing to the lower computation cost and modeling ability at that time. However, many researchers noticed that using elastic-plastic constitutive relationships and 3D models was a better choice. In this stage, researchers tried to reveal rockburst mechanisms by modeling the changes of maximum principal stress,

strain energy, and deformation after mining or excavation activities (Blake, 1972b; Miranda, 1972; Brady, 1979; Board et al., 1980; Napier, 1987; Bardet, 1987, 1990).

After that, with the development of computing capacities and progress in numerical programs for modeling complex geometry and plastic non-linearity, more researchers tended to utilize elastic-plastic constitutive relationships and/or 3D models. The representative studies are listed in Table 4. Rockburst is a type of rock failure phenomenon caused by the initiation, growth, and expansion of micro-fractures, which then develop from the micro-fracture of rocks to a macroscopic fracture (Wang et al., 2006). After confirming that AE parameters are related to the damage variable of rocks, Wang et al. (2003) used RFPA2D to simulate pillar bursts. They found that the simulation results reflect the macroscopic failure evolution process induced by microscopic fractures and the Spatio-temporal distribution characteristics of AE events. Using RFPA2D, Wang et al. also studied the effects of rock heterogeneity on rockburst potential. Then, Wang et al. (2006) employed RFPA2D to study rock pillars' progressive failure process and associated microseismic (MS) behaviour. The simulated results verified that the stiffness of the roof and floor play an essential role in controlling the unstable failure or collapse of rock pillars. Finally, Zhu et al. (2010) used RFPA-Dynamics to simulate the rockbursts triggered by the dynamic disturbance around a deep underground opening and confirmed that the dynamic disturbance is one of the most important contributing factors inducing rockbursts.

As mentioned earlier, most of the work is limited to the study of rock failure based on the small deformation rule. The gestation and development of rockburst is a process from static failure to dynamic failure, transforming from a continuous small deformation into a large discontinuous deformation in a very short time. It is difficult to simulate the discontinuous deformation behaviour of rock masses based on continuum methods such as FEM, BEM, and FDM. To this end, scholars tended to use DEM and other hybrid numerical methods suitable for simulating discontinuous deformation to reproduce rockburst

phenomena. After years of development, the DEM has made great progress in both theories and applied research: 1) from rigid elements to deformable elements; 2) from 2D to 3D modeling; 3) from the simulation of static problems to the simulation of dynamic problems, and 4) from the single mechanical simulation to the simulation of multi-phase media and multi-field coupling problems. The general block DEM considers the rock mass composed of discrete rock masses and joint faces between rock blocks. The rock mass can move, rotate, and deform, and the joint faces can be compressed, slid, and separated to more realistically simulate the continuous and discontinuous deformation of jointed rock masses (Jiang, 2017). Therefore, the DEM and DEM-related hybrid methods are undoubtedly a good choice for the numerical modeling of the continuous-discontinuous deformation behaviour of the rockburst gestation and failure processes. The corresponding studies are also summarized in Table 4. Recently, Vazaios (2018) and Vazaios et al. (2019) used FDEM (FEM/DEM) models through IRAZU to investigate the effect of pre-existing joints on strainburst phenomena in deep hard rock excavation. In order to conduct a parametric study, three numerical model configurations were created. The first configuration did not include any structures (massive rock masses); the other configurations included stochastic joints by integrating a different number of discrete fracture networks (DFNs). In those models, the initiation, propagation, and coalescence of fractures and abrupt rock ejection occurring in the excavation under high-magnitude stresses could be explicitly simulated (part of the results is shown in Figure 2.6). Figure 2.6 shows that rock blocks located around the excavation boundary possess higher velocities than those far away from the excavation wall, which is the reality (Ortlepp and Stacey, 1994; Qiu et al., 2014). Additionally, larger ejected volumes are generated with the increasing number of pre-existing joints, which also govern the shape and size of ejected rock blocks. The FDEM models have made it possible to simulate the change from a continuous deformation to a discontinuous deformation to reproduce the

physical process of rockburst phenomena, which further highlighted the application of the hybrid method in rockburst numerical modeling.

In summary, the employment of various numerical methods, codes, and constitutive models at different dimensions and scales has greatly enriched the understanding of the complex source mechanism and damage mechanism of rockbursts. Compared with continuum methods, the DEM, especially DEM-related hybrid methods, has achieved the explicit simulation of the rockburst process, providing an effective tool for researchers to reveal the nature of rockbursts. This might motivate more researchers to use discontinuum and hybrid methods in this research field. However, it is not true because these methods are not perfect. For example, to eliminate the effects of mesh size on the fracture position within rocks, an excellent mesh resolution is usually needed, which sacrifices the computational efficiency of the model.

Moreover, the calculation time will be significantly extended when the blocks or elements undergo large deformations and are detached from each other (Gao, 2019). For instance, Vazaios et al. (2019) reported that the total run time of the third model configuration is around 100-144 hours. This is an important reason why discontinuum and hybrid methods are less used than continuum methods (see Figure 2.4). Finally, it should be noted that we cannot easily say which numerical method is better to simulate rockburst mechanisms since every method has its advantages and limitations (Table 2.5).

Table 2.4 Summary of the applications of numerical modeling for rockburst mechanisms

Numerical approach	Rockburst type	Study type	Numerical code	Geometry	Constitutive model	Description	Author (year)
Continuum method	Pillar burst	Case study	FLAC	2D	Strain-softening	A cohesion-softening model was utilized to simulate laboratory specimens and then evaluated the shear-fracture rockburst potential for underhand longwall and overhand cut-and-fill stopes in deep mining.	Whyatt and Board (1991)
	Fault-slip burst	Parametric study	FLAC3D	3D	Barton's shear strength, Saeb and Amadei's model	Barton's shear strength model was implemented in FLAC3D using C++ programming language while at the same time considering the change from static friction law to dynamic friction law. The results suggested that the roughness of the fault surface should be considered when estimating the magnitude or the energy of the fault slip. Saeb and Amadei's (1992)'s model was also employed to simulate the fault-slip triggered by the stress wave and the effect of the fault surface asperities on the intensity of seismic waves arising from the fault slip.	Sainoki (2014), Sainoki et al. (2014a, 2014b, 2015)
	Strainburst	Parametric and case study	ABAQUS	2D	Strain-softening	A heterogeneous model was developed in ABAQUS using Python scripts to simulate rockbursts near fault zones in deep tunnels, considering the effect of material heterogeneity on rock failure processes. The simulated results corresponded well with the post-event observation in the "11.28" rockburst in the Jinping II Hydropower Station.	Manouchehrian (2016), Manouchehrian and Cai (2018)
	Fault-slip burst	Case study	FLAC3D	3D	Mohr-Coulomb	Recognizing that the mechanism of intense rockburst induced by nearby small-scale shear zones in deep civil tunnels was unclear, the FLAC3D was applied to simulate the shear zone in a twin-tunnel system.	Naji et al. (2018)
	Strainburst	Parametric study	FLAC3D	3D	Mohr-Coulomb	Numerical simulation was adopted to study the failure laws of the surrounding rocks in the process of rockbursts in roadways with different ratios between principal stresses.	Guo et al. (2019a)
Discontinuum or hybrid method	Pillar burst	Case study	3DEC	3D	Mohr-Coulomb	Two numerical models were built using 3DEC to estimate the pillar stress before failure and to study the rockburst mechanism to investigate a pillar burst event that occurred in a chromite mine.	Dehghan et al. (2013a)
	Strainburst	Parametric study	FEM/DEM	2D	Mohr-Coulomb	The FDEM method was employed to study the effect of unloading rates on granite bursts (strainbursts) at a laboratory scale. A loading/unloading stage was used in the modeling to reproduce the excavation-induced rockburst. The method could accurately and quantitatively manifest the growth, coalescence, and nucleate of microcracks at the whole process of the granite burst.	Li et al. (2015)
	Fault-slip burst	Case study	FEM/DEM	3D	Mohr-Coulomb	In order to investigate the effect of fault surface roughness on fault-slip rockbursts, Grisi et al. (2016) investigated the failure mechanism of a gypsum pillar by comparing the continuum FEM approach with the hybrid FEM/DEM approach. They reported that the FEM/DEM approach could effectively describe the mechanical response of the pillar through fracture propagation, but it requires much more computational cost with increasing errors than the continuum FEM approach.	Grisi et al. (2016)
	Strainburst	Parametric study	CA3	3D	Contact-bond model	CA3 was used to study strainbursts where discrete particles modelled the rock, and finite elements simulated the frame structure. The main contributing factors of the rockburst severity were finally determined.	Hosseini (2016)
	Strainburst	Parametric study	ELFEN	2D	Mohr-Coulomb with rotating crack	Feng et al. (2017) investigated the failure mechanisms of the surrounding rock near a circular hole, taking into consideration the effects of the structural surface through the ELFEN code. The mechanical failure characteristics were studied, as were the crack growth behaviours around the circular hole under the conditions of different locations, lengths, and dip angles of pre-existing flaws.	Feng et al. (2017)
	Strainburst	Parametric study	PFC2D	2D	Parallel-bond model	To investigate the dynamic stress concentration and energy evolution of a circular tunnel under blasting loading, Li et al. (2018) established a numerical model to analyze the distribution of tangential stress and dissipation strain energy around the tunnel under various in-situ stresses and different waveforms.	Li et al. (2018)
	Strainburst	Parametric study	UDEC	2D	Elastic model	A novel distinct-element bonded block method was proposed to simulate strainbursts. In this method, a seismic event induced by dynamic rock cracking is simulated by a strength reduction approach to initiate a dynamic disturbance in a rock pillar, which can produce P and S waves with related seismic wave properties such as velocity, the ratio of Vs/Vp, and frequency that are needed for evaluating strainbursts. Compared with most existing methods, this proposed method overcomes the difficulty of determining the seismic wave properties of the dynamic disturbance input.	Gao et al. (2019a, b)
	Strainburst	Parametric study	ELFEN	2D	Mohr-Coulomb with rotating crack	Different factors such as the dip angle, location, and frictional coefficient of the structural planes and the lateral pressure coefficient were simulated to analyze their effects on the rock failure process and rockburst risks of a circular tunnel under excavation unloading.	Feng et al. (2019b)

Note: In the discontinuum or hybrid method, the contact-bond and parallel-bond models are used for contacts, and other constitutive models are adopted for blocks or elements.

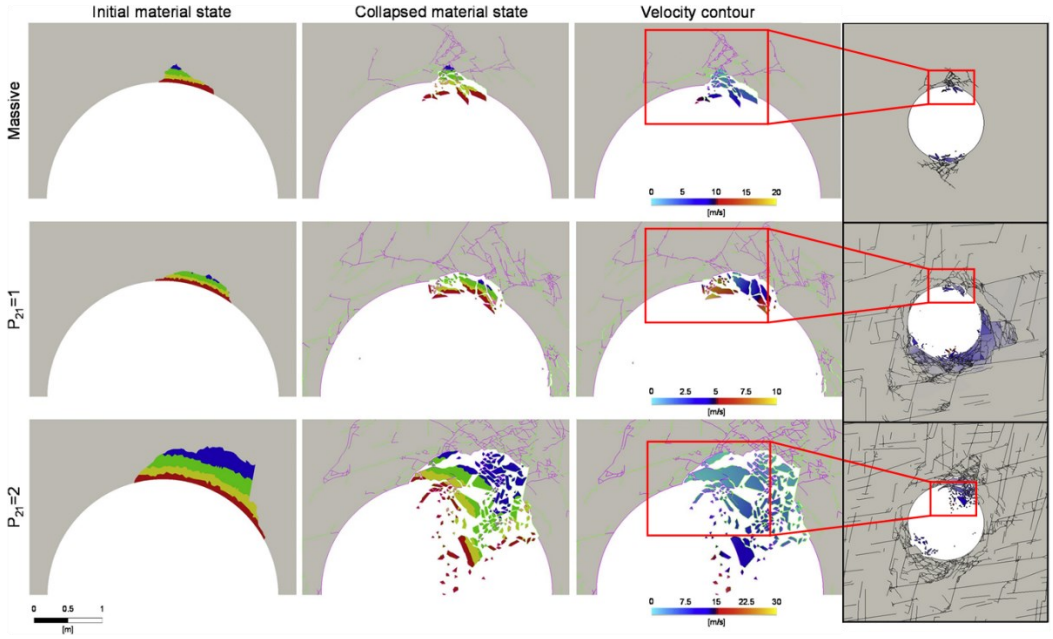

Figure 2.6 Effects of different pre-existing joints on strainburst phenomena (from Vazaios et al., 2019).

Table 2.5 Advantages and limitations of numerical methods in modeling rockburst mechanisms

Numerical method	Advantage	Disadvantage
Continuum method (BEM)	(1) Capability of 3D modeling; (2) Allow the rapid assessment of stress concentration, deformation, and designs	(1) Normally elastic analysis only; (2) Calculation time increases exponentially with the number of elements (Sainoki, 2014)
Continuum method (FEM, FDM)	(1) Capability of 3D modeling; (2) Easily handle material heterogeneity and geometric nonlinearity; (3) Simulate complex behaviour of rock/rock masses with various constitutive models; (4) Allow dynamic loading	(1) Input limitations, e.g. some critical input parameters are difficult to determine; (2) Interfaces can model simple structures but are not suitable for highly jointed-blocky media (Coggan et al., 2012); (3) Rich experience in using numerical analysis is essential; (4) Calculation time increases exponentially with the number of elements
Discontinuum method (DEM)	(1) The capability of 3D modeling; (2) Easy to model jointed rock systems; (3) Able to model complex behaviour of rock/rock masses with various constitutive models; (4) Allow the large deformation and detachment of blocks; (5) Allow dynamic loading	(1) Limited data on joint properties are available, and the calibration of parameters might be needed; (2) Rich experience in using numerical analysis is essential; (3) 2D modeling is usually used due to the great calculation cost of 3D models
Hybrid method (FEM/DEM)	(1) Able to model the extension of existing fractures and creation of new fractures in intact rocks; (2) 3D modeling is possible; (3) Allow dynamic loading	(1) Few data are available for contact properties and fracture mechanics properties; (2) The calibration of parameters is needed; (3) Extremely long run times will require the use of parallel processing for large models (Coggan et al., 2012); (4) 2D modeling is usually used

2.3.2 Numerical modeling for the prediction and evaluation of rockbursts

Researchers agree that it is challenging to accurately predict the occurrence time of rockbursts due to the randomness and complexity of the mechanism of rockbursts (Qian, 2014; Zhou et al., 2018). However,

the occurrence of rockbursts is mainly determined by the change in ground stresses caused by the excavation of deep rock masses. The geological survey technology, ground stress detection technology, rock mechanics theories and methods, and long-term development of numerical simulation have made it possible to perform the qualitative and quantitative prediction of the location and intensity of rockbursts (Qian, 2014). Scholars believe that the era of quantitative prediction of rockbursts has arrived, and such quantitative progress needs to be achieved through a combination of numerical simulation and on-site observation (Stacey, 2013; Cai, 2016).

In the past few decades, scholars have proposed several predictions and evaluation indexes or indicators of rockburst potential based on a variety of rockburst theories and rockburst phenomena from the aspects of strength, stiffness, energy, stability, fracture, damage, etc. (Zhang and Fu, 2008; He et al., 2012; Li et al., 2013; Qian, 2014; Mazaira and Konicek, 2015; Feng et al., 2017; Levile et al., 2017; Zhou et al., 2018; Afraei et al., 2019; Jiang et al., 2019; Pu et al., 2019). At present, the proposed prediction and evaluation indicators of rockbursts can be generally classified into two categories: 1) indicators based on the stress/strength criterion, such as tangential stress, axial stress, UCS, and major principal stress, in which the representative indexes are σ_θ/σ_c (Russenes, 1974), σ_c/σ_1 (Barton et al., 1974), σ_L/σ_c (Turchaninov et al., 1972), σ_c/σ_θ (Hoek and Brown, 1980), σ_c/σ_1 (Tao, 1988), excess shear stress (ESS) (Ryder, 1988), σ_c/σ_t (Peng et al., 1996), $(\sigma_1-\sigma_3)/\sigma_c$ (Castro et al., 2012), etc; 2) indicators based on the energy criterion, such as elastic strain energy and elasto-plastic deformation energy, in which the representative indexes are strain energy storage coefficient (W_{sp}/W_{st}) (Kidybiński, 1981), the ratio of kinetic energy to released energy (W_k/W_r) (Hedley, 1992), energy release rate (ERR) (Salamon, 1984; Kaiser et al., 1996), burst potential index (BPI) (Mitri et al., 1999), local energy release rate (LERR) (Wiles, 2002), loading system stiffness (LSS) (Wiles, 2002), strain energy density (SED) (Wattimena et al., 2012), etc.

Due to the complexity of the geological and construction conditions and mining- or excavation-induced effects, it is challenging to predict and estimate rockbursts based on analytical and experimental methods because many idealized assumptions are employed. By contrast, numerical modeling can simulate rock masses' elastoplastic, non-linear, and post-yield behaviour and the effects of in-situ stresses and geological features on mining or excavation works, which enables researchers to understand the “real world” in underground engineering. Thus, numerical modeling with the prediction and evaluation indexes is a helpful tool for researchers and engineers to estimate rockbursts. The studies about numerical modeling and prediction of rockbursts are summarized in Table 2.6. As shown in Table 2.6, different indicators (stress/strength-based or energy-based) have been widely employed to assess and predict rockburst potential in various engineering projects. In addition to essential variables such as stress and strength, some more complex rockburst indicators, either empirical or user-defined, can be easily obtained by processing the essential variables using the built-in or common programming languages (e.g., FISH language in FLAC3D, C++, Python, etc.) in most numerical programs.

Table 2.6 Summary of the applications of numerical modeling for rockburst prediction

Classi-fication	Rockburst indicator	Research object	Numerical code	Geometry	Constitutive model	Description	Authors (year)
Stress/ strength	Strength factor	Rock pillar	Examine	3D	Hoek-Brown	The strength factor was selected as an indicator for assessing a rock pillar's ground stability and rockburst potential after benching a drift. The in-situ observations further confirmed the predicted results (Figure 2.7).	Apel (2005)
	FAI	Powerhouse and tunnel	FLAC3D	3D	Strain-softening	Failure approaching index (FAI) was proposed to estimate the stress-induced risk based on the stress state, yield surface, and equivalent plastic shear strains. This index successfully predicted the potential rockburst zones in the Jinping II Hydropower Station facilities.	Zhang et al. (2011)
	Pillar stress and strength	Rock pillar	3DEC	3D	Mohr-Coulomb	Compared with the tributary area theory, the numerical model could reproduce the realistic load distribution on pillars. The simulated Domino failure mode of pillars was verified with the observations in a chromite mine.	Dehghan et al. (2013b)
	σ_c/σ_θ	Tunnel and rock pillar	ABAQUS	3D	Mohr-Coulomb	The simulation results suggested that a distinctive ratio of UCS to maximum excavation-induced tangential stress could be determined for the stages of progressive failures, such as rock spalling at tunnel surfaces and pillar crushing.	Kusui et al. (2016)
	Damage risk index	Roadway	FLAC	2D	Mohr-Coulomb	A damage risk index based on the Mohr-Coulomb criterion was proposed to study the rockburst risks and dynamic response characteristics of roadway surrounding rocks under dynamic loading. The potential rockburst zones and severity could be predicted with the proposed index.	Wang et al. (2017)
	Brittle fracture zone	Tunnel	FEM	3D	A self-developed brittle-yield model	After developing a brittle-yield criterion combining damage initiation and spalling limit (Diederichs 2007), Diederichs (2018) successfully predicted the development of the burst potential of a deep tunnel concerning advance through incorporating the criterion in a 3D nonlinear finite element analysis.	Diederichs (2018)
	$(\sigma_\theta+\sigma_L)/\sigma_c$	Tunnel	ABAQUS	3D	Elastic model	An analytical method was developed to investigate the inhomogeneous stress concentration in interbedded strong and weak layers, confirmed by FEM modeling. Numerical results also suggested that rockburst risks change with a mutative orientation of rock layers.	Yang et al. (2018)
	Microseismic events (simulated fractures)	Tunnel	PFC3D	3D	Bonded particle model	Ma et al. (2019) proposed a brittle fracture model and a numerical simulation method of hard rock fracture based on MS information in PFC3D. The simulation results agreed well with field data in tunnel engineering, showing that the proposed method is effective for interpreting and detecting early warning signs of rockburst hazards.	Ma et al. (2019)
Energy	ERR, BPI	Stope	FEM	2D	Elastic	A new indicator, BPI, was proposed based on the energy storage rate and critical energy density. The ERR and BPI were adopted to predict rockburst potentials in a cut-and-fill stope.	Mitri et al. 1999
	LERR	Tunnel	FLAC3D	3D	Elastic-brittle-plastic model	Jiang et al. (2010) proposed a new LERR index considering the difference in energy stored in rock masses before and after brittle failure based on an elastic-brittle-plastic model. The simulation results suggested that the new LERR could successfully predict the intensity and failure depth of rockbursts in deep tunnels.	Jiang et al. (2010)
	URLERI	Tunnel	FLAC3D	2D plane	A self-developed elastoplastic model	A new energy indicator of rockbursts—the unit time relative local energy release index (URLERI), was proposed and used for simulating the rockburst case in the Jinping II Hydropower Station. The simulated results agreed well with the field monitoring results.	Yang et al. (2015)
	Accumulated disturbance energy	Mining level	FLAC3D	3D	—	The accumulated disturbance energy in surrounding rock masses was calculated in FLAC3D, and then was employed to predict the magnitude of rockbursts in each mining level.	Cai (2016)
	σ_θ/σ_c, BPI	Stope and drift	ABAQUS	3D	Mohr-Coulomb (for rock mass) and elastic model (for backfill)	A mine-scale model was established to capture the realistic distribution of in-situ stress and mining-induced stress. σ_θ/σ_c and BPI were adopted as indicators to evaluate the rockburst risks of stopes and drifts in an underground diamond mine (Figure 2.8).	Sepehri (2016), Sepehri et al. (2020)
	Excess energy	Tunnel	UDEC	2D	Strain-softening	A DEM/BEM hybrid model was built to study seismicity and unstable failure in circular excavations using a proposed concept of "excess energy." The results confirmed that a lower horizontal-to-vertical stress ratio resulted in rock masses' more unstable excess energy.	Khademian et al. (2016)
	Elastic deformation energy density	Stope	ABAQUS	2D	Elastic model	The elastic deformation energy density was employed to obtain the factors and conditions that determine the location of the sources and the mechanism of mining-induced tremors. The shear strain energy could be treated as an index of the potential threat of mining-induced tremors.	Cieslik et al. (2017)
	σ_1, SED	Stope	FLAC3D	3D	Mohr-Coulomb	The rockburst proneness of stopes with different mining sequences was analyzed by simulating the variations of maximum principal stress and elastic strain energy accumulation in surrounding rock masses.	Ma et al. (2018)
	SED	Rock pillar	FLAC3D	3D	Mohr-Coulomb	After conducting a series of SHPB tests on rock samples, Li et al. (2019) obtained the formula of stored strain energy by rejecting the fractured dissipative energy based on the fitting of experimental data. The formula was programmed into the FLAC3D as a variable to analyze rock pillars' strain energy and burst potential.	Li et al. (2019)

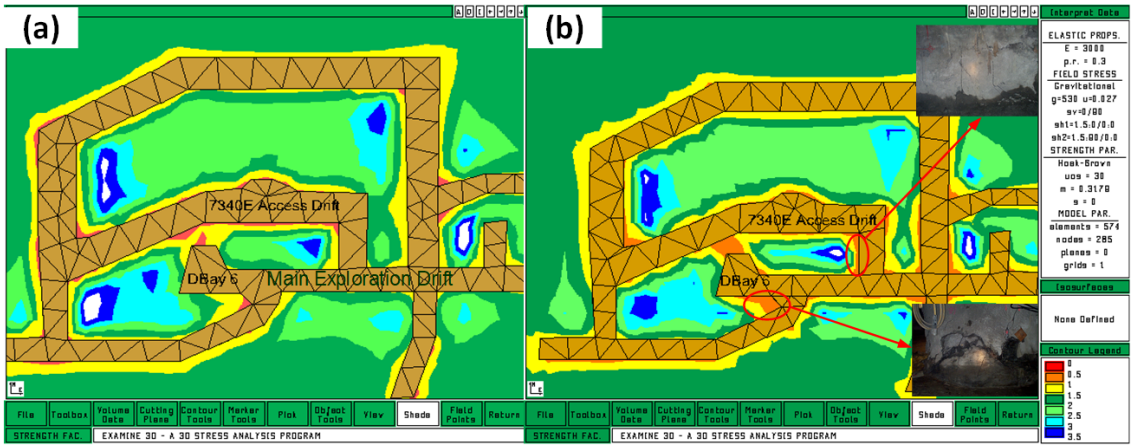

Figure 2.7 Redistribution of the strength factor: (a) Before floor benching and (b) After floor benching (after Apel, 2005).

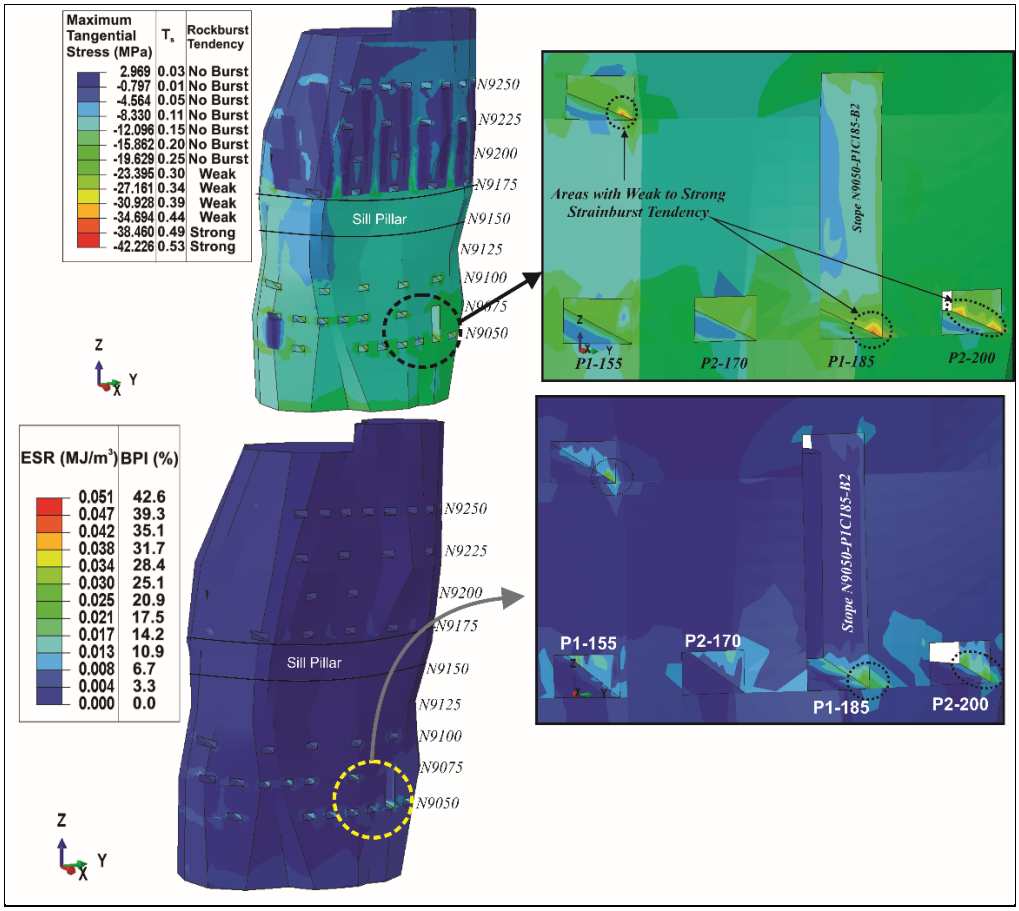

Figure 2.8 Estimation of rockburst tendency with σ_θ/σ_c (T_s) and BPI in a kimberlite pipe (after Sepehri, 2016).

2.3.3 Numerical modeling for the prevention and mitigation of rockbursts

After the burst-prone zones are predicted and evaluated, prevention and mitigation measures should be carried out. Generally, there are three approaches or steps to prevent and mitigate rockbursts, as shown in

Figure 2.9. However, estimating the effects of those measures in the field is very dangerous, time-consuming, and costly. For instance, distress drilling is a widespread technique to mitigate rockburst risks in the field. The design parameters of boreholes, such as diameter, length, position, and pattern layout, are typically determined according to engineers' specialization and experience. However, the design parameters depend on many factors, e.g., the size and shape of excavations, mechanical properties of rocks, in-situ stress, etc. Thus, engineers must spend tremendous time and money to obtain relatively ideal design parameters considering many influence factors of distress drilling. Moreover, conducting experimental schemes of engineers in the field will always expose personnel to a dangerous environment. In contrast, numerical modeling is a cheap, fast, safe, and effective tool for evaluating those three types of measures, especially when optimizing support design and project layout (Mazaira and Konicek, 2015).

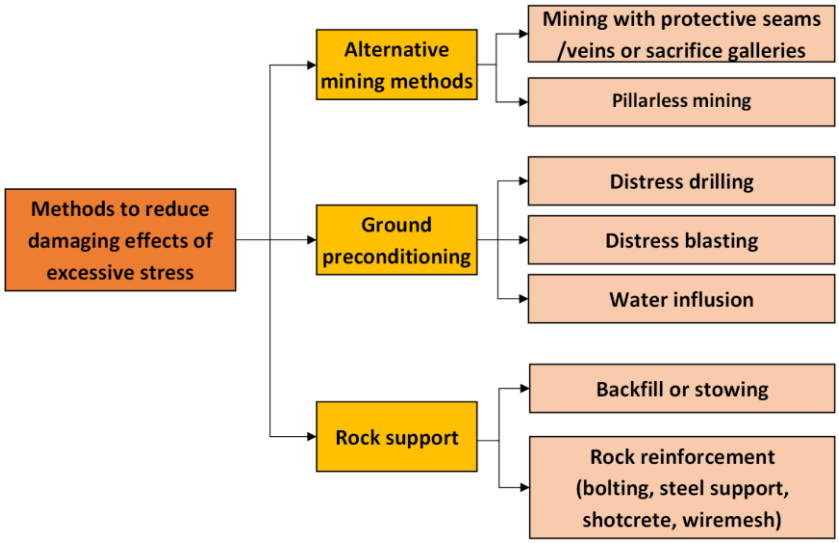

Figure 2.9 Methods to reduce damaging effects of excessive stress in underground mining (after Mitri, 2000).

The studies about numerical modeling of rockburst prevention are summarized in Table 2.7. As shown in Table 2.7, numerical modeling has been widely employed to assess the effects of various techniques on the prevention and mitigation of rockburst risks. For the first type of rockburst prevention approach, the 3D modeling with elastic analysis is a fast and effective method to determine the areas with stress concentration and energy accumulation in the design stage, thereby letting engineers choose rational

project layouts and mining/excavation methods to avoid potential rockbursts. In the production stage, some calibrated rockburst indicators can estimate the rockburst tendency to adjust construction schemes or adopt distress and support measures in time. In contrast, modeling ground preconditioning and rock support is very complex. At present, the main approaches to simulate the effects of destress blasting are reducing the rock properties, such as elastic modulus or adding a stress dissipation factor to model the instantaneous stress drop (Blake, 1972a; Tang and Mitri, 2001; Sainoki et al., 2017; Vennes and Mitri, 2017). Although these methods are straightforward, no actual blastholes exist in the numerical model, which is indeed a type of equivalent approach.

Moreover, specific zones with potential blasting-induced damages must be assumed first to assign parameters that are not real and increase extra efforts. By analyzing a pressure profile of ANFO-type explosive and detonation propagation, Sainoki et al. (2017) proposed an innovative method to simulate a time-varying blast pressure. Using this method, the blasting-induced damage can be simulated more precisely. Nevertheless, the volume dilation of rocks induced by creating and developing fractures was neglected because the continuum method was used in the previous work. Gao (2013) developed a Trigon method that can simulate the apparent dilation phenomenon caused by the generation and propagation of cracks, which can be further adopted to evaluate the blasting-induced damage and the dissipated energy induced by rock fracturing. The numerical modeling of water infusion is less studied due to the infrequent water infusion usage for hard rock engineering. Currently, numerical simulation is mainly utilized to examine the effects of water infusion on mitigating coal burst risks (Li et al., 2005; Fan et al., 2012; Song et al., 2014; Liu et al., 2017; Zhou et al., 2018). Numerical modeling of rock support systems is probably one of the most important and extended applications of numerical methods to underground excavations, and its importance is even more significant when designing support systems in burst-prone grounds

(Mazaira and Konicek, 2015). Numerical analyses in this field mainly focus on support elements such as rockbolts and steel arches under dynamic loading or stress waves produced during rockbursts.

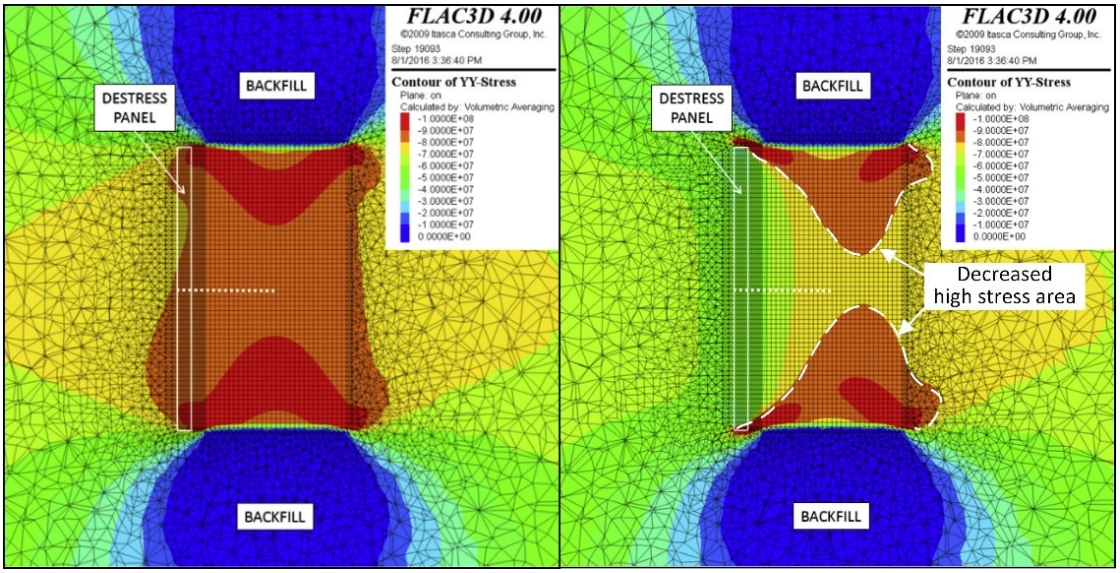

Figure 2.10 Stress state in the pillar before distressing and after distressing (after Vennes and Mitri, 2017).

Table 2.7 Summary of the applications of numerical modeling for rockburst prevention

Rockburst prevention approach	Numerical code	Geometry	Constitutive model	Support element	Description	Author (year)
Alternative mining methods	FLAC3D	3D	Elastic model (for ERR and ESS), and the cohesion weakening and frictional strengthening model (for FAI)		A top pilot tunnel drilling and blasting method was proposed and evaluated using numerical simulation with several prediction indices of rockbursts (FAI, ERR, and ESS). The simulation and field monitoring results showed that the pretreatment aspect of this method could effectively reduce the risks of strainburst and fault-slip rockburst compared with the conventional full-face tunnel boring machine (TBM) excavation method.	Zhang et al. (2012b)
	NFOLD, Map3D	3D	Strain-softening		Numerical modeling was used to assess the effects of mining sequence, advance direction and backfill mining method on mitigating the risks of pillar burst and fault-slip burst.	Castro et al. (2012)
	FLAC3D	3D	Mohr-Coulomb		Zhang et al. (2018) used the FLAC3D simulation to study different-sized sections of tunnels, looking at circumferential and radial stresses, and found that it is possible to reduce the intensity of rockbursts by increasing the size of the excavation inside the tunnel. The statistical data of rockbursts in field tests have also verified the numerical simulation results.	Zhang et al. (2018)
Ground preconditioning	UDEC	2D	Elastic model		UDEC was employed to simulate the effects of fluid injection on the control of fault slip and to model preconditioning the stope by blasting. Results suggested that the injection of high gas into fractured rocks was more likely to be the best preconditioning method.	Lightfoot (1993)
	FLAC3D	3D	Drucker-Prager		FEM modeling was used to examine different layouts of destressed holes under different in-situ stress conditions to reduce rockburst risks.	Zhu et al. (2009)
	FLAC3D	3D	Mohr-Coulomb		Sainoki et al. (2016) compared the simulation results of the traditional modeling approach with the alternative modeling approach. They found that the traditional modeling approach may lead to an overly optimistic indication of destress blasting efficiency.	Sainoki et al. (2016)
	FLAC3D	3D	Elastic model		Numerical modeling was adopted by Vennes and Mitri (2017) to study the stress change and BSR before and after distressing in the pillar. They concluded that the panel destressing method could significantly reduce rockburst risks when mining a highly-stressed ore pillar (see Figure 2.10).	Vennes and Mitri (2017)
Rock support	FEM	2D	Drucker-Prager (for rock) and von Mises (for steel)	Self-developed element	A type of energy-absorption coupling support fashion was proposed by Lv and Pan (2010). The effects of this new support fashion were examined using FEM modeling by comparing a roadway maintained by this fashion with one without it.	Lv and Pan (2010)
	FLAC3D	3D	Mohr-Coulomb (for rock) and elastic model (for rockbolt)	Cable element	Mortazavin and Alavi (2013) studied the behaviour of three types of fully grouted rockbolts (with head plate, without head plate, and yielding rockbolt) under dynamic loading and concluded that the yielding rockbolt was the best choice for absorbing dynamic stress waves and controlling rock mass movement.	Mortazavin and Alavi (2013)
	DDA	2D	Elastic and strain-hardening	Self-developed element	Rockbolt models were developed using DDA to investigate the failure mechanism of an expansion-shell-anchored bolt, the split set, the fully grouted rebar and the D-bolt under static and dynamic loads.	Nie et al. (2014)
	FLAC	2D	Mohr-Coulomb	Beam element	FLAC simulation was used to investigate the effects of the dynamic load on the arch steel support in stress concentration zones. It was found that the higher the peak particle velocity (PPV), the higher the HMH stress (a type of stress developed by Huber, von Mises and Hencky), and that the initial static stress level plays an important role in controlling the failure of arch steel support induced by dynamic loads.	Masny et al. (2017)
	FLAC3D	3D	Elastic-perfectly plastic	Cable element	Numerical modeling was applied for a laboratory-scale test to investigate the behaviour of threadbar in dynamic load testing. The simulation results corresponded well with laboratory observations. However, it was also found that the grout played a secondary role in the system's overall strength, a phenomenon that needs to be further studied in dynamic conditions.	Marambio et al. (2018)
	ABAQUS	3D	Strain-softening	Self-developed element	Sengani (2018) adopted different support fashions under dynamic conditions and conducted a large-scale numerical model for an ultra-deep platinum mine using the ABAQUS Explicit FE solver to study the performance of in-stope pillars. The results indicated that extensive scaling and fracturing occur in most bolt-reinforced in-stope pillars, while in-stope pillars supported by bolt and shotcrete sustain minor or no damage during the dynamic movement.	Sengani (2018)
	DDA	2D	—	Self-developed element	A new energy-absorbing rockbolt, called a deformation-controlled rockbolt (DC-bolt), was proposed by Yokota et al. (2019). The DDA simulated the performance of the DC-bolt, and results suggested that the DC-bolt possessed both high loading capacity and deformation capacity compared with the fully grouted rockbolt.	Yokota et al. (2019)
	UDEC	2D	Elastic model	Rockbolt element	Zhang and Nordlund (2019) employed the UDEC program to investigate the dynamic performances of a fully grouted rebar between the simulated drop tests and seismic loading in the configuration where two slightly separate rock bars were used.	Zhang and Nordlund (2019)

2.4 A numerical modeling framework for studying rockburst mechanisms and other rockburst-related problems

Owing to the complicated mechanisms and the uncertainty of occurrence, the rockburst is different from other rock mechanics problems, such as stable failure modes (e.g., rock spalling) after tunnel excavation and ore extraction. Therefore, many contributing factors for simulating rockbursts should be considered when modeling this complex phenomenon. For instance, the selection of numerical methods should be based on the match between the capabilities of numerical codes and rockburst mechanisms and the specific engineering situation. Thus, it is necessary to establish a systematic and reasonable numerical modeling framework for studying rockburst mechanisms and other rockburst-related problems. The selection of numerical modeling approaches, numerical programs, numerical modeling sequences, material parameters, and model calibration is described in this method. The first step is the preparation which includes problem analysis, selection of numerical methods, and geometry analysis of the research objective. The second step includes five procedures: model establishment and meshing, input of in-situ stress, constitutive models and rock mass parameters, initial and boundary conditions, geostatic step and model calibration, and analysis of simulation results. The details of this framework are shown in Figure 2.11.

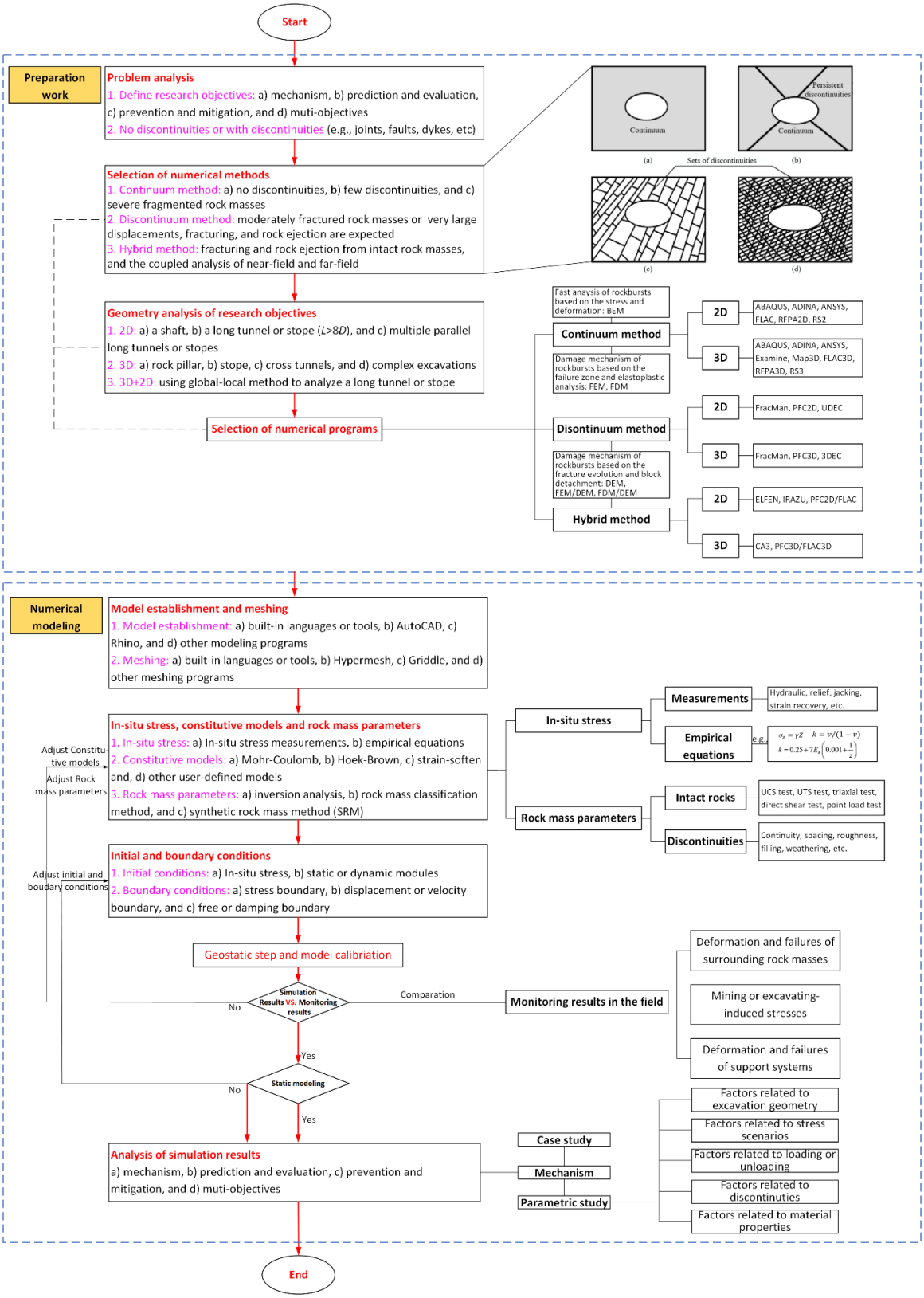

Figure 2.11 Flowchart of a systematic numerical modeling framework for studying rockbursts (after Wang et al., 2021a).

3. CHAPTER 3: INVESTIGATION OF THE ROCKBURST MECHANISM OF DRIVING ROADWAYS IN CLOSE-DISTANCE COAL SEAM MINING USING NUMERICAL MODELING METHOD AND A SYSTEMATIC ROCKBURST PREDICTION METHOD

*In this chapter, a 3D FDM model is established via FLAC3D software using the "5.5" rockburst event in the Zofiówka Coal Mine as a case example to reveal the rockburst source mechanism of driving roadways in close-distance coal seam mining conditions. The excavation-induced vertical stresses are analyzed, providing a basis for building a conceptual model to reveal the rockburst source mechanism. A systematic method that can select and use rockburst indicators reasonably is proposed to predict the location and magnitude of rockbursts. Some alternative measures to prevent and mitigate rockburst hazards in close-distance coal seam mining conditions are also discussed. This chapter is based on the published papers "**Wang, J.**, Apel, D. B., Pu, Y., Hall, R., Wei, C., Sepehri, M. (2021). Numerical modeling for rockbursts: A state-of-the-art review. Journal of Rock Mechanics and Geotechnical Engineering, 13(2), 457-478" and "**Wang, J.**, Apel, D. B., Dyczko, A., Walentek, A., Prusek, S., Xu, H., Wei, C. (2021). Investigation of the rockburst mechanism of driving roadways in close-distance coal seam mining using numerical modeling method. Mining, Metallurgy & Exploration, 38(5), 1899-1921".*

3.1 Introduction

Rockburst is a dynamic rock failure phenomenon usually accompanied by the sudden ejection of rocks from an underground excavation. The ejection of rock materials is violent and associated with a rapid release of energy. Rockburst events have been reported in all mining countries (e.g., South Africa, Australia, Canada, USA, China, India, Poland, Russia, and Chile) since the beginning of the 20th century (Blake and Hedley, 2003). Rockbursts also occur in some civil engineering projects (e.g., deep tunnels) constructed in very complex ground conditions (Zhang et al., 2012a). Due to their unpredictability and high intensity, rockburst has become one of the most hazardous geological disasters. It damages equipment and facilities and even causes fatalities.

The core problem of the prevention and mitigation of rockbursts is to find out what caused a rockburst and its mechanism also called the inherent or source mechanism of rockbursts (Ortlepp and Stacey, 1994). The main methodologies for investigating rockburst mechanisms include analytical, experimental, empirical, data-based, and numerical modeling (Manouchehrian, 2016). The numerical modeling method has the advantages of safety, low cost, time-saving, and flexibility over other methods, such as physical simulation and field tests. It can also provide more information. This method has become a common and even necessary way to investigate rockburst mechanisms since the 1970s (Wang et al., 2021a).

It is generally known that the occurrence of rockbursts is related to the property of rock masses in storing strain energy and bumping when they are damaged, and the environment for generating and storing high stress and strain energy in the surrounding rock system (Park, 1995; Kwasniewski and Wang, 1999; Wang and Park, 2001; Liu et al., 2015; Miao et al., 2016; Guo et al., 2019b). The high-stress concentrations around underground excavations are mainly due to three reasons (Zhao et al., 2018): the high in-situ stress because of great mining depths; geological discontinuities such as faults, dykes, folds and other tectonic areas; the high excavation-induced stress caused by different engineering conditions, such as rock or coal

pillars, remnant working faces, gob, slice mining, multi-coal seam mining, etc. Numerous researchers have studied the effects of the depth and tectonic areas on rockburst mechanisms using numerical modeling methods and have made meaningful achievements in investigating the causes of high-stress concentration and rockburst occurrence (Whyatt and Board, 1991; Castro et al., 2012; Sainoki and Mitri, 2014a; Jiang et al., 2018; Naji et al., 2018; Guo et al., 2019c). For the rockbursts caused by excavation-induced stresses, the scholars mainly focus on the numerical studies of the influence of rock or coal pillars (Apel, 2005; Dehghan et al., 2013a; Kias and Ozbay, 2013; Ahmed et al., 2017; Zhang et al., 2017; Qiu et al., 2019) and remnant working faces (Liu, 2007; Jiang et al., 2012; Wang et al., 2013, 2016; Zhu et al., 2018) on rockburst mechanisms. Their research has achieved many fruitful outcomes that provide good references for understanding rockburst mechanisms under different engineering conditions. Driving roadways underneath mining work in a close-distance coal seam is a common practice for many underground coal mines in the Czech Republic, Poland, and China (Shen et al., 2017; Konicek et al., 2013; Szott et al., 2018). The mining pressure transferred from the panels or pillars in upper coal seams could play a key role in the occurrence of rockbursts in underlying coal seams, according to some case studies (Shen et al., 2017; Konicek et al., 2013; Suchowerska et al., 2013; Zhao et al., 2018). For instance, Zhao et al. (2018) stated that the remnant coal pillars in the No. 13 coal seam (upper mining level) resulted in high excavation-induced stress concentration, a necessary condition for rockburst events occurring in a roadway in the No. 10 coal seam. However, current research mainly focuses on the qualitative analysis of stress concentration from some case histories related to close-distance coal seam mining. Limited studies have systematically studied rockburst mechanisms in such conditions using numerical methods. The redistribution and evolution of excavation-induced stresses in close-distance coal seam mining have not been fully understood. Thus, the influence of close-distance coal seam mining on the rockburst mechanism of driving roadways remains unclear. Hence, it is essential to reveal the rockburst mechanisms of driving

roadways during close-distance coal seam mining using numerical modeling to provide references and guidelines for controlling rockbursts in underground mines.

The presented findings use the back analysis to model the state of excavation-induced stresses before the rockburst occurred at the "Zofiowka" Mine in Poland on May 5, 2018 (Adam, 2018). The investigated rockburst occurred because of a sudden discharge of energy accumulated in the rock mass. The spontaneous shock of the rock mass had an energy of 2×10^9 J, resulting in significant damage to roadways and even fatalities. The mining area where the rockburst took place had a complex geological structure of the deposit with numerous tectonic faults. Therefore, the rock mass had highly concentrated stresses caused by the complex geological and mining situation, which provides a good case example for investigating the mechanism of rockbursts under such conditions. It is well known that most rockburst mechanisms are usually very complex, and one rockburst event might have multiple causes (Zhao et al., 2018). In addition to geological factors (e.g., large faults), the engineering factors (e.g., multi-coal seam mining and excavation schedule) are essential to be considered as they can affect the stress redistribution and further change rockburst potential.

This chapter establishes a 3D FDM model via FLAC3D software using the close-distance coal seam mining conditions in the Zofiówka Coal Mine as a case example. The excavation-induced vertical stresses are then analyzed, which provides a basis to build a conceptual model to explain the rockburst source mechanism of driving roadways during close-distance coal seam mining. After reviewing the prediction indicators of rockburst potential, nine typical rockburst indicators considering different contributing factors are selected as the evaluation criteria to assess rockburst potential. Later, a systematic method is proposed to estimate the location and magnitude of rockbursts combined with numerical modeling, laboratory tests, and field feedback. This chapter also discusses alternative methods to prevent and mitigate rockburst hazards in close-distance coal seam mining conditions.

3.2 Engineering overview

3.2.1 Geology and geotechnical overview

The Zofiówka Coal Mine is located approximately 307 km southwest of Warsaw in Poland (see Figure 3.1). Zofiówka represents one of the largest coal reserves in Poland, having estimated resources of 87 million tonnes of coal. The production is around 3.7 million tonnes per year. The analyzed area of coal seam 409/3 and 409/4 is located in section H in the southern part of Jastrzębie Górne I mining area, and its boundaries are north, Central fault with a throw of 10-11 m/NE; east, Eastern fault with a throw of 15-20 m/E; west, Jastrzębie fault with a throw 15-60 m/W, and south, the border of deposits Bzie-Dębina 1 and O.G. Bzie-Dębina 2-Zachód. The depth of coal seams is 815-990 m.

The thicknesses of coal seam 409/3 and 409/4 are 1.8-2.7 m and 4.0-5.3 m, respectively. The average distance between two coal seams is around one meter. The dip angle of two coal seams is 5-10°. The dip direction is from north to south. Shales and sandstones dominate the lithology of the roof and floor. The rock strata profile is shown in Figure 3.2. The retreating longwall mining method extracts coal seams in the coal mine. The panels H-4 and H-6 in coal seam 409/3 have been mined out successively during 2016-2017. The headgate and tailgate were tunnellings to prepare the Panel H-4 in coal seam 409/4 in 2018 (Figure 3.3). The main support elements in roadways are the yielding steel arch (ŁP12/4/V32) and welded wire mesh with knots.

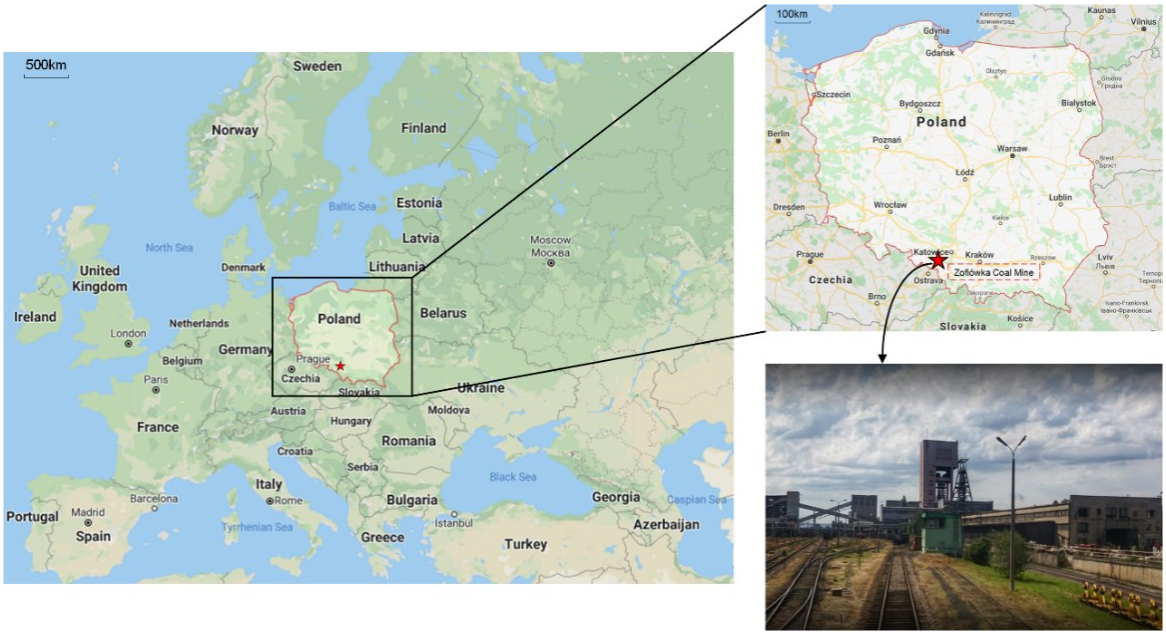

Figure 3.1 Location of the Zofiówka Coal Mine (Photo taken by Fafal, 2017).

Column	Thickness/m	GSI	Lithology
	10.96	45	Clay shale
	17.51	50	Fine-grained sandstone
	1.08	48	Sandy shale
	1.76	45	Clay shale
	1.81	36	Coal seam 409/3
	0.93	45	Clay shale
	4.65	36	Coal seam 409/4
	4.30	48	Sandy shale
	0.95	36	Coal seam
	5.38	48	Sandy shale
	7.43	45	Gritty clay shale

Figure 3.2 Geological column in the study site. (GSI is the geological strength index, Marinos and Hoek, 2000)

3.2.2 Description of the rockbursting event

The "5.5" rockburst event occurred in the intersection area of the H-4 tailgate and H-10 main drift (Figure 3.3). The verified seismic energy of the event is 2×10^9 J, equivalent to an earthquake with a

Richter magnitude of 3.0 according to the classification (see Table 3.1) made by (Bieniawski, 1986). This rockburst event caused a collapse of the H-10 main drift. The surrounding rock masses of the roadway were significantly damaged and deformed (Figure 3.4). The roof-to-floor convergence is from 1 m to the total height of the roadway, with a total length of about 300 m. The pipes in the H-10 main drift were also damaged, and the amount of airflow through this excavation dropped from 2500 m^3/min to 150 m^3/min. The rockburst affected eleven employees staying in the H-10 main drift. Unfortunately, this was a collective accident causing five fatalities and four injuries (Adam, 2018).

Table 3.1 Seismic event classification (Bieniawski, 1986)

Degree of damage	Richter scale	Seismic energy (J)	Seismic event
	-3.5	0.4	Weak shake
Development of joint	-2	63	
	-1	2×10^2	
Exfoliation	0	6.3×10^4	
	1	2×10^6	Weak earthquake
Weak rockburst	2	6.3×10^7	
Strong rockburst	3	2×10^9	
Violent rockburst	4	6.3×10^{10}	

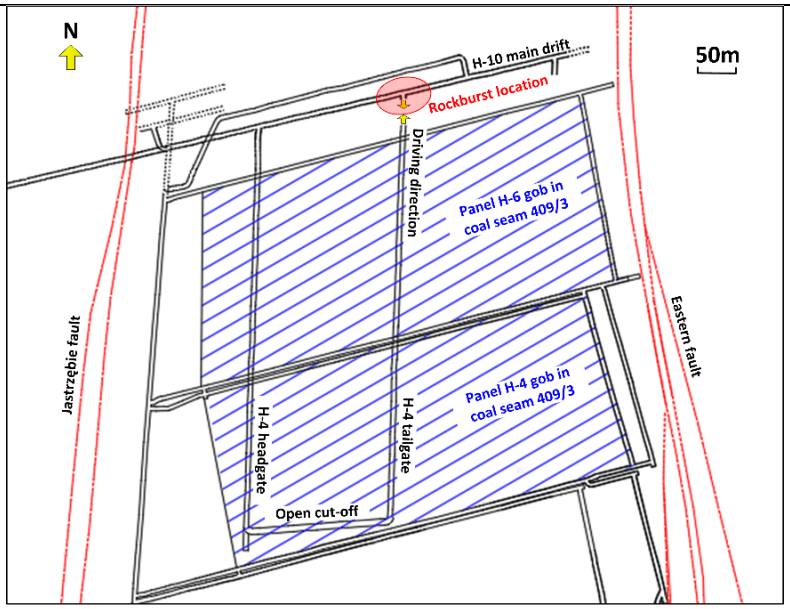

Figure 3.3 Location of the rockburst event and layout of mining works.

Figure 3.4 Field observations of rockburst damage of the "5.5" rockburst event (after Jastrzębska Spółka Węglowa S.A. Group, 2019).

3.3 Numerical modeling

3.3.1 Model setup

3.3.1.1 Finite difference method

The finite difference method (FDM) is a numerical simulation method to approximate the partial differential equations (PDE) of objective functions (e.g., displacement) with finite difference equations while assuming Taylor Series expansion (Jing, 2003; Sainoki, 2014). The domain analyzed is discretized with grid points, based on which the differential equations are solved. Compared with the FEM and BEM, no global system of equations in matrix form needs to be formed and solved in the FDM. The formation and solution of the equations are localized, which is more efficient for memory and storage handling in the computer implementation. No local trial (or interpolation) functions are employed to approximate the PDE in the sampling points' neighbourhoods, as in the FEM and BEM. This also provides the additional advantage of more direct stimulation of complex constitutive material behaviour, such as plasticity and damage, without iterative solutions of predictor-corrector mapping schemes, which must be used in other numerical methods using global matrix equation systems, e.g., the FEM or BEM (Jing, 2003).

FLAC3D is a continuum analysis modeling software. It utilizes an explicit FDM that captures the complex behaviours of models consisting of several stages, shows large displacements and strains, exhibits non-linear material behaviour, or is unstable (including cases of yield/failure over large areas or total collapse). FLAC3D contains null, three elastic, and 20 plastic constitutive models for soil, clay, and

rock (e.g., Mohr-Coulomb, Hoek-Brown, Plastic Hardening, and Strain Softening). It can be applied to the engineering design of civil, mining, and geotechnical excavations (e.g., slopes, tunnels, caverns, stopes, etc.) and constructs (dams, foundations, footings, walls, etc.) in soil, intact rock, and rock masses (e.g., heavily jointed rock). Thus, FLAC3D is used in this research to construct the model of the case study site.

3.3.1.2 Model establishment

A three-dimensional (3D) FDM model was established using FLAC3D software. The main drift, gateroads, and a part of Panel H-6 were included in the model because this study investigates the rockburst mechanism for roadways. The size of the model is 450 m (length) × 300 m (width) × 120 m (height), as shown in Figure 3.5. The upper boundary of the model was free, and vertical stress of 21.87 MPa (assuming the unit weight of overburden is 27 kN/m^3) was applied to the upper boundary to simulate the overburden stress. The roller constraints were applied on the side boundaries, and the bottom boundary was fixed. The horizontal-to-vertical stress (K) ratio is based on in-situ stress measurements at the coal mine. In order to guarantee the calculation accuracy and efficiency, the main drift and gateroads and their surrounding rock masses were divided into small elements with an edge length of one meter. The rest of the elements could be appropriately set up into large sizes. The model was divided into 1066921 elements based on a mesh convergence study (MCS).

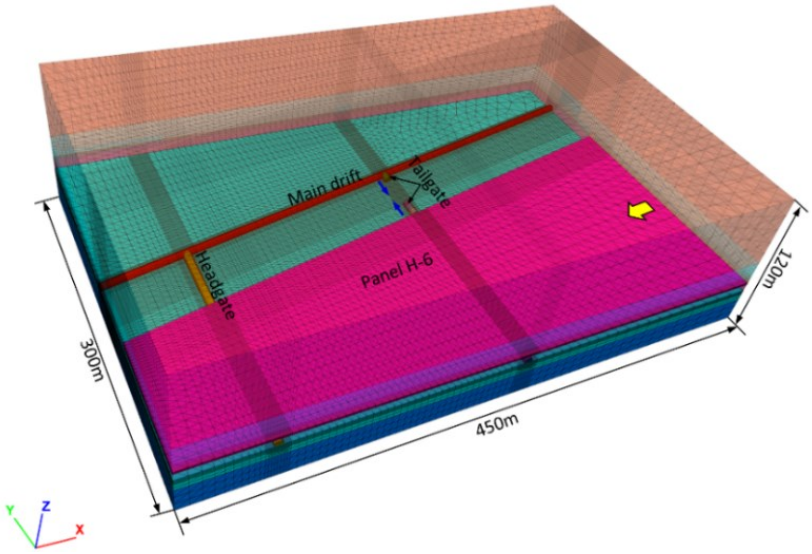

Figure 3.5 Layout of the numerical model.

3.3.1.2 Model assumptions

The built numerical model has following assumptions:

- Rock mass properties are isotropic and uniform.
- The influence of water and temperature on rock mass properties can be ignored.
- The rock mass failure behaviour is governed by Hoek-Brown failure criterion.
- Rock masses in the 3D model are continumm medium. However, the influences of joints on rock mass properties have been considered by using Hoek-Brown failure criterion.
- The unit weitght of the overburden is 27 kN/m^3.

3.3.2 Simulation schemes

In order to evaluate the effects of upper coal seam mining on the rockburst mechanism, two simulation schemes were implemented in this study. Scheme 1 has the following excavation steps: (a) apply the in-situ stress field and reach the geostatic equilibrium, (b) excavate the main drift, (c) excavate the headgate and a part of the tailgate of Panel H-4 in coal seam 409/4, (d) excavate the tailgate with a cycle of five meters per step (11 cycles in total) when it is close to the main drift. In comparison, one more step in Scheme 2: extract the Panel H-6 in coal seam 409/3 along the strike and backfill it with gob materials

before excavating the main drift. The directions of the gateroad development and retreat mining are shown in Figure 3.5. However, this research mainly focuses on investigating rockburst mechanisms from the view of excavation-induced stresses, and the loads from support systems (steel arch and wire mesh) are very small compared to those stresses. Besides, the computation cost will significantly increase when simulating rock support elements in 3D models (Itasca, 2021). Thus, the support systems were not modelled in this study.

3.3.3 Constitutive model and material properties

3.3.3.1 Constitutive model and rock mass properties

The Hoek-Brown failure criterion was selected as the constitutive model to reveal the elastoplastic relation of rock masses. The Hoek-Brown failure criterion is an empirically derived relationship initially developed to estimate the rock mass strength considering the geological conditions (Eberhardt, 2012). Compared with the Mohr-Coulomb failure criterion, the Hoek-Brown failure criterion is a nonlinear envelope, as shown in Figure 3.6. The Hoek-Brown failure criterion for jointed rock masses is expressed as follows (Hoek and Brown, 1997).

$$\sigma_1' = \sigma_3' + \sigma_{ci}\left(m_b \frac{\sigma_3'}{\sigma_{ci}} + s\right)^a \tag{3.1}$$

where σ_1' and σ_3' are the maximum and minimum principal effective stress at failure, respectively; m_b is the value of the Hoek-Brown constant for the rock mass; s and a are constants that depend upon the characteristics of the rock mass; σ_{ci} is the UCS of intact rock pieces. It should be noted that the pore pressure of rocks was not considered in this study.

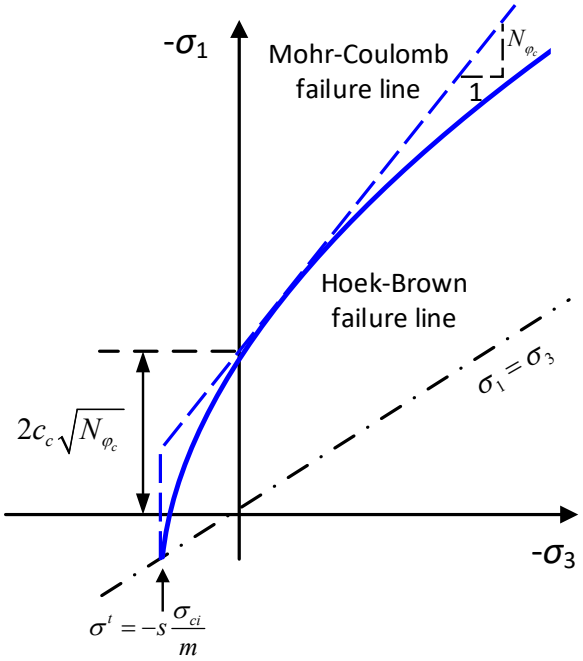

Figure 3.6 Hoek-Brown failure criterion and its Mohr-Coulomb approximation (Itasca, 2019). (C_c is the cohesion force; φ_c is the internal friction angle; $N_{\varphi_c} = (1 + \sin\varphi_c)/(1 - \sin\varphi_c)$; σ^t is the tensile cutoff)

The physical and mechanical parameters of rock masses in adjacent mining areas at the same coal mine were obtained according to the laboratory tests of intact rocks (following the International Society for Rock Mechanics (ISRM) recommended standards, Marinos and Hoek, 2000) and the generalized Hoek-Brown criterion (Marinos and Hoek, 2000) using the GSI system to evaluate rock mass qualities (see Figure 3). Therefore, the rock mass properties used in this study were assumed based on the rock mass parameters from previous research (Małkowski et al., 2017; Szott, 2018; Małkowski and Ostrowski, 2019), as shown in Table 3.2.

Table 3.2 Physical and mechanical parameters of rock masses (Małkowski et al., 2017; Szott, 2018; Małkowski and Ostrowski, 2019)

Lithology	ρ (kg/m^3)	m_b	s	a	σ_{ci} (MPa)	E_i (GPa)	v
Coal	1300	1.729	0.0008	0.5	9.3	1.86	0.30
Clay shale	2500	1.327	0.0022	0.5	29.0	5.62	0.31
Fine-grained sandstone	2580	2.851	0.0039	0.5	90.0	9.52	0.26
Sandy shale	2530	1.877	0.0031	0.5	26.0	5.23	0.25
Gritty clay shale	2440	1.192	0.0022	0.5	47.5	6.98	0.32

Note: ρ is the bulk density of intact rocks. E_i is the Young's modulus of intact rocks. v is the Poisson's ratio of intact rocks.

3.3.3.2 Constitutive model and material properties of the gob

After the coal seam is extracted, the immediate roof collapses and caves rock materials fall into the gob. As a result, rock materials are compacted gradually with the subsidence of upper rock strata. In this process, the overburden stress carried by the mined coal is then supported by the surrounding rock masses and gob materials, resulting in the redistribution of mining-induced stress (Qiu et al., 2019; Wang et al., 2020). Thus, selecting a reasonable gob model to reproduce gobs' mechanical response and capture the realistic redistribution of mining-induced stress is critical.

In the past, the null model in FLAC3D was usually employed to simulate gobs, of which the compaction of caved rock materials was not considered (Jiang et al., 2017a). Therefore, the simulation results were inaccurate. There are two main constitutive models to simulate gob materials: elastic and double yield (DY). Some researchers (Kose and Cebi, 1988; Shabanimashcool and Li, 2012; Cheng et al., 2010; Jiang et al., 2012) used very soft elastic materials (the deformation modulus is small, e.g., 60-100 MPa) to simulate gob materials. Those elastic models are simple and easy to calculate, but the strain-hardening behaviour of compacted gob materials is ignored (Wang et al., 2020). Recently, the DY model has been well employed as it can simulate the strain-stiffening behaviour of rock materials. Furthermore, researchers (Yavuz, 2004; Qiu et al., 2019; Wang et al., 2020) have confirmed that it is reasonable to use the DY model to simulate the real mechanical response of gob materials. Therefore, the DY model in FLAC3D was utilized to simulate the gob response in this study.

The cap pressure and material properties are the required input for the DY model. The Salamon model calculates the cap pressure (Salamon, 1990), and material properties can be obtained based on a back-analysis procedure (Yavuz, 2004; Wang et al., 2020). A flow chart shows the detailed process (Figure 3.7).

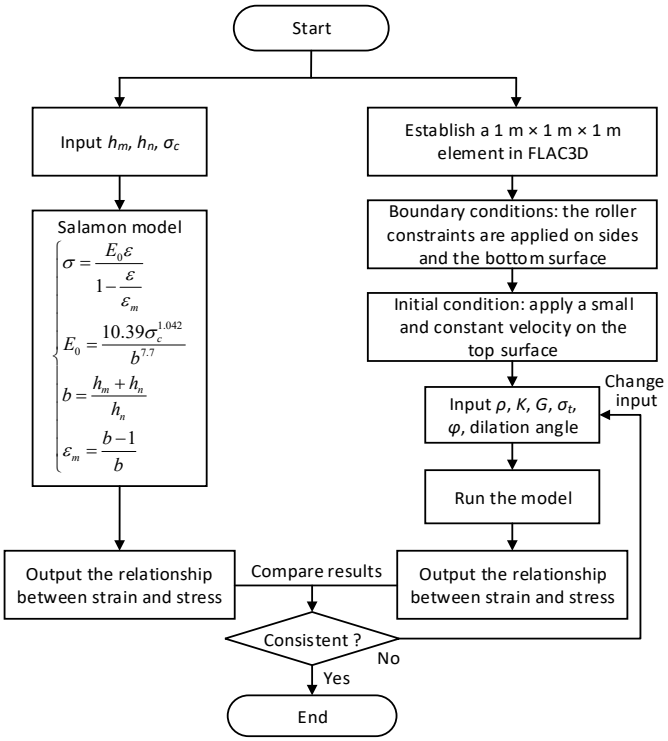

Figure 3.7 Detailed process to obtain the cap pressure and material properties. (h_m is the mining height (2 m for coal seam 409/3 in this case). h_n is the height of the caved zone that can be obtained from the suggested equations given by Peng et al. (1984) and Bai et al. (1985). σ_c is the UCS of the immediate roof. σ is the uniaxial stress applied to the gob material. ε is the strain occurring under the applied stress. E_0 is the initial tangent modulus, and ε_m is the maximum possible strain of the bulked rock material. b is the initial bulking factor. K and G are the bulk and shear modulus. φ is the internal friction angle. σ_t is the uniaxial tensile strength.)

Following the procedures shown in Figure 3.7, the cap pressure and material properties are obtained. It can be seen from Figure 3.8 that there is a good fitting between the numerical model and the Salamon model. The final material properties of the gob are illustrated in Table 3.3.

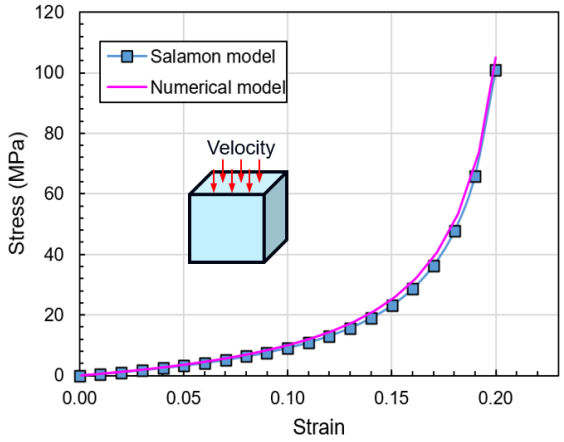

Figure 3.8 Comparison of the stress-strain curves of the numerical model and Salamon model.

Table 3.3 Properties of gob material

ρ (kg/m^3)	K (GPa)	G (GPa)	σ_t (MPa)	φ (°)	Dilation angle (°)
1700	10.0	1.5	0	5	8

3.3.4 Mesh convergence study

The accuracy of simulation results is sensitive to the mesh or element density (Qiu et al., 2019; Wang et al., 2020; Sepehri et al., 2020). Generally, the accuracy of simulation results increases with the growing mesh density. However, more computer capacity and run time will be required if the mesh is refined. Thus, a mesh convergence study is conducted to find an optimal mesh density with accepted accuracy of simulation results and relatively lower computing costs.

In this study, six meshing scenarios are defined (Table 3.4). Figure 3.9 shows the deformation of the main drift in numerical models under different meshing scenarios. In general, there is a positive relationship between mesh densities and simulation results. When the mesh is coarse (less than 889959 elements), the simulation results are susceptible to the mesh density because the roadway deformation increases remarkably with the growth of mesh density. However, the roadway deformation approaches a plateau when the number of elements exceeds 1066921, indicating that the mesh dependency could be negligible. Thus, Model #4 is selected as the optimal model for the subsequent numerical study.

Table 3.4 Meshing scenarios to conduct the MCS

Meshing scenario	Total number of elements	Total number of grid points
Model #1	192099	35059
Model #2	589042	104426
Model #3	889959	153877
Model #4	1066921	182807
Model #5	1496244	254995
Model #6	2034783	346831

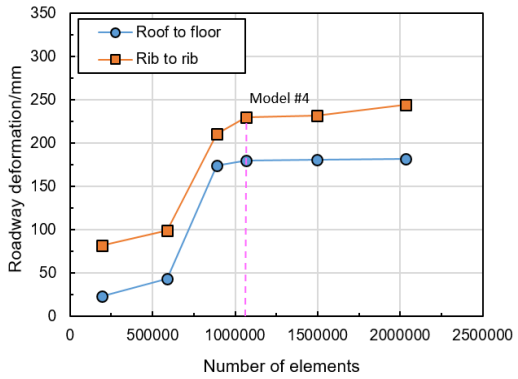

Figure 3.9 Deformation of the main drift with different meshing scenarios.

3.3.5 Validation of the numerical model

3.3.5.1 Validation of gob modeling with previous studies

The vertical stress in the gob and coal seam 409/3 along the dip direction was collected and illustrated in Figure 3.10. The results show that the vertical stress in the gob is minor at the gob edge and then grows gradually with the increasing distance from the gob edge to the gob center. It finally approaches 22.50 MPa (92.59% of the virgin stress) at 196 m (0.22 of the average overburden depth) from the gob edge. Wilson and Carr (1982), and Campoli et al. (1993) stated that the vertical stress would approach the virgin stress state at a distance of 0.2 to 0.3 times the overburden depth based on field measurements. Therefore, the simulated results agree well with previous studies, and the gob's material properties and constitutive model are validated.

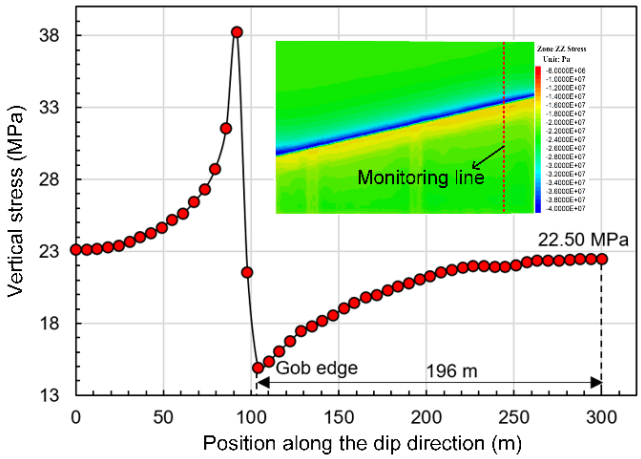

Figure 3.10 Distribution of the vertical stress in the gob and coal seam 409/3.

3.3.5.2 Validation of the whole model with field monitoring

Normally, numerical models can be calibrated by three types of field monitoring data: the deformation or failure of rock masses, mining- or excavation-induced stress, and the deformation or failure of support systems. In this research, the simulated deformation and failure depth of surrounding rock masses of the headgate are compared with the monitoring results obtained by recording roadway convergence (Małkowski et al., 2017) and endoscopic camera investigations (Jastrzębska Spółka Węglowa S.A. Group, 2018) in the field to validate the full model. Figure 3.11a, b shows the numerical model's vertical and horizontal displacement contour. The simulated convergences of roof-to-floor and rib-to-rib are 350 mm and 490 mm, respectively, while the measured roadway deformations are 300~500 mm, and 200~540 mm (Małkowski et al., 2017), respectively. Figure 3.11c, d compares the failure zone in the numerical model and field measurements. The simulated failure depths of the roof and floor are 7.02~7.93 m and 2.64 m, respectively, while the measured failure depths of the roof and floor are 8.2~8.5 m, and 2.7 m, respectively. Therefore, a relatively good agreement between simulated results and field monitoring data was achieved, which validates that the rock mass properties, constitutive models, boundary conditions, and geometries used in the full model are reasonable.

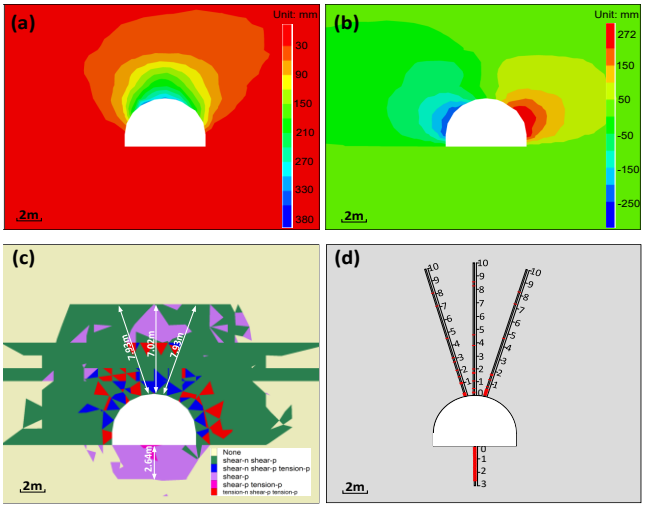

Figure 3.11 (a), (b), and (c) are simulated vertical displacement, horizontal displacement, and failure zone of the headgate. (d) Measured failure depth.

3.4 Results and discussion

3.4.1 Evolution law of mining and excavation-induced stresses

3.4.1.1 After excavating the main drift (Stage 1)

The vertical stress concentration has a significant influence on rockburst occurrence and damage in working faces and roadways (Li et al., 2018). Thus, the excavation-induced vertical stresses were analyzed in this study. As shown in Figure 3.12a and Figure 3.13a, the stress relaxation zones (dark blue areas) are near the excavation wall of the main drift, while stress concentration zones (red and orange areas) are located at the two sides of the main drift. This phenomenon verifies that rock masses surrounding the excavation wall failed because their strength is smaller than the high excavation-induced stress, which is then transferred into the deeper rock masses on roadway sides. The distance from the excavation wall to the edge of the stress concentration zones is about 4.2 m. When the distance is greater than 4.2 m, the excavation-induced effect is increased first and then decreased, and the surrounding rock stress gradually approaches the in-situ stress level. As shown in Figure 3.12b and Figure 3.13b, the main drift's distribution of surrounding rock stress is partly similar to Scheme 1. The difference between the two schemes is that the surrounding rock stress in the right side of the main drift in Scheme 2 has been influenced by the side abutment stress (red areas in Figure 3.13b) of Panel H-6.

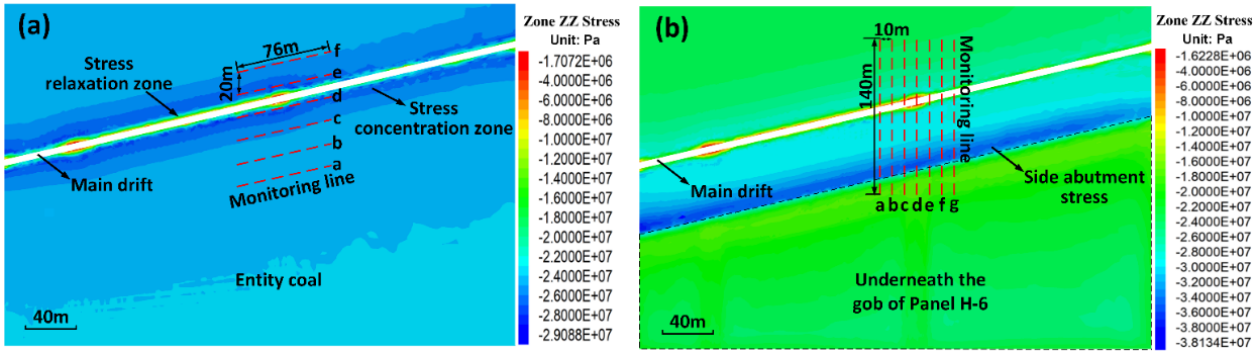

Figure 3.12 Distribution of the vertical stress (plane view). (a) Scheme 1. (b) Scheme 2.

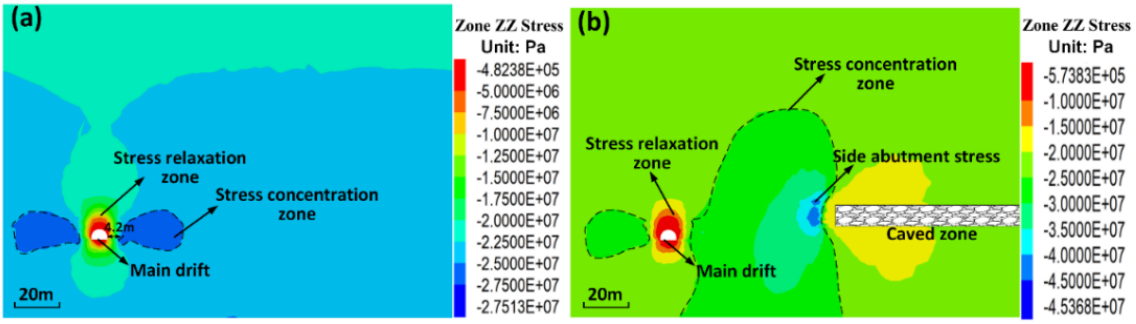

Figure 3.13 Distribution of the vertical stress (section view). (a) Scheme 1. (b) Scheme 2.

In order to further investigate the distribution of surrounding rock stresses, seven (along the dip direction) and six monitoring lines (along the strike direction) were arranged in models in the both schemes, as shown in Figure 3.12 and Figure 3.13. The simulation results are shown in Figure 3.14. Figure 3.14a shows that the distribution of surrounding rock stress is uniform along the strike direction. This is because there are no other excavation activities nearby at this stage. In Figure 3.14a, the average values calculated by monitoring lines d and e are 26.78 MPa and 26.58 MPa, respectively, greater than others, as monitoring lines d and e are located at stress concentration zones induced by excavating the main drift. In Figure 3.14b, the average value for monitoring line a is much smaller than others because it is located at stress relaxation zones underneath the edge of Panel H-6's gob. The average value for monitoring line b is the greatest due to the influence of the side abutment stress of Panel H-6. In addition, the gap between different monitoring lines in Figure 3.14b is more significant than that in Figure 3.14a, indicating that the extraction of Panel H-6 changes the normal distribution of surrounding rock stress of the main drift.

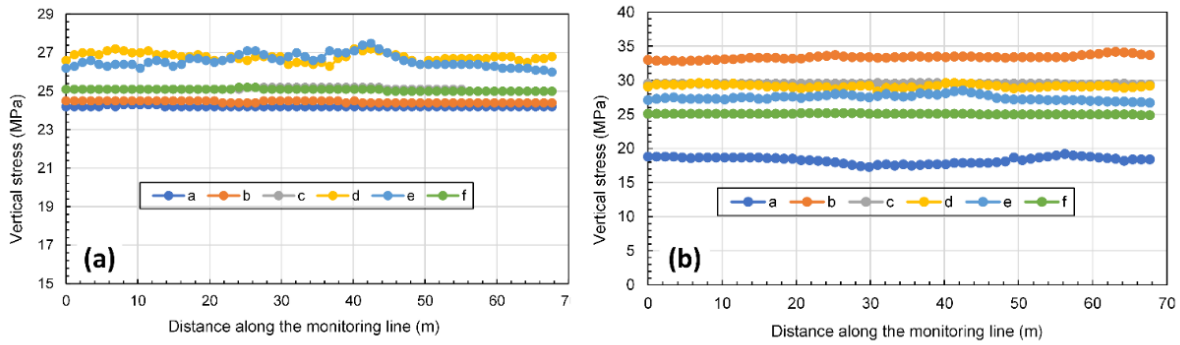

Figure 3.14 Distribution of the vertical stress along the strike direction. (a) Scheme 1. (b) Scheme 2.

The distribution of surrounding rock stress in the dip direction is shown in Figure 3.15. As shown in Figure 3.15a, the stress distribution is symmetrical along the axis of the main drift. There are three zones: stress relaxation, concentration, and in-situ stress on each side of the main drift. The average peak stress is 27.09 MPa, and the stress concentration coefficient (peak stress divided by in-situ stress) is 1.11. This peak stress area is around 7.77 m away from the excavation wall. In addition, the range of the stress concentration zone (green area in Figure 3.15a) is about 25 m. By contrast, the distribution of surrounding rock stress is asymmetrical when the extraction of Panel H-6 is considered (see Figure 3.15b). There are two peak stresses on the right side of the main drift. Peak stress 1 is caused by excavating the main drift, and peak stress 2 is produced by overburden movement and local coal-rock deformation after mining Panel H-6.

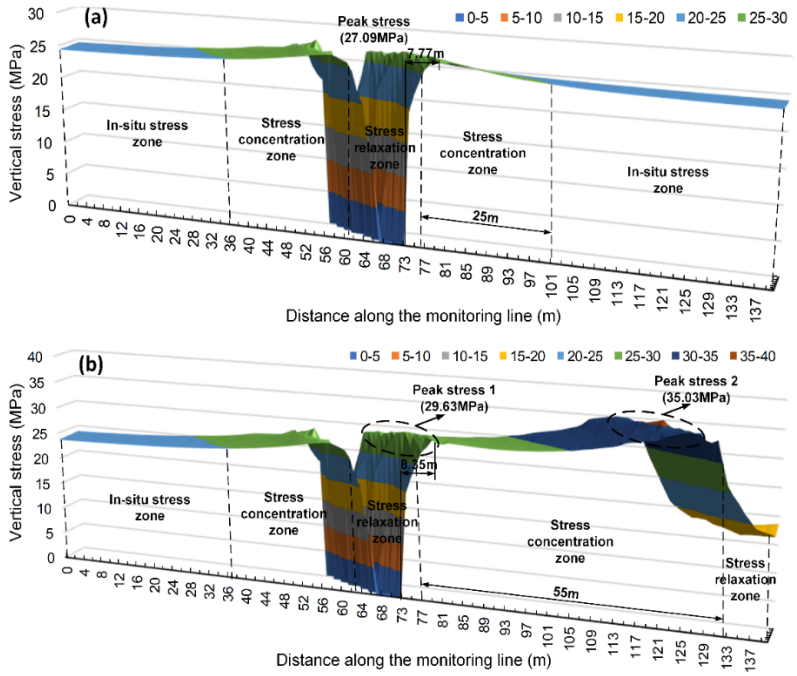

Figure 3.15 Distribution of the vertical stress along the dip direction. (a) Scheme 1. (b) Scheme 2.

It should be noted that there are still three zones on the left side of the main drift, but there is no in-situ stress zone on the right side. The peak stress and the range of stress concentration zone in the left side are almost the same as in Scheme 1, suggesting that the main drift cut off the transfer of the side abutment

stress of Panel H-6. However, the peak stress 1 is 29.63 MPa, and the stress concentration coefficient is 1.22, which increased by 9.90%. The peak stress is around 8.35 m away from the excavation wall. Additionally, on the right side of the main drift, the range of the stress concentration zone is about 55m, which is much greater than that of Scheme 1. Compared with rock properties (internal factor), the high excavation-induced stress is the critical exterior factor contributing to rockbursts. Therefore, the range of potential rockburst area is expanded because of the redistribution of excavation-induced stresses from the extraction of panels in the upper coal seam.

3.4.1.2 After excavating the headgate and a part of the tailgate of Panel H-4 (Stage 2)

After excavating the headgate and a part of the tailgate of Panel H-4, the stress distribution is shown in Figure 3.16 and Figure 3.17. Figure 3.16 and Figure 3.17 show that stress relaxation zones near the excavation wall of two gateroads are located at their sides, similar to those of the main drift. As shown in Figure 3.17a, a large stress concentration zone is produced near the cross area of the main drift and the headgate. This is due to the superposition of stress concentration zones induced by excavating the main drift and the headgate. However, a similar stress concentration zone is mainly near the cross area of the headgate and the unmined coal seam beneath Panel H-6's gob (Figure 3.16b). In this case, the phenomenon is caused by the superposition of the stress concentration zone induced by excavating the headgate and the side abutment stress of Panel H-6. Additionally, it can be observed that a small stress concentration zone is in front of the tailgate (Figure 3.17), which is the advanced abutment stress produced by tunnelling.

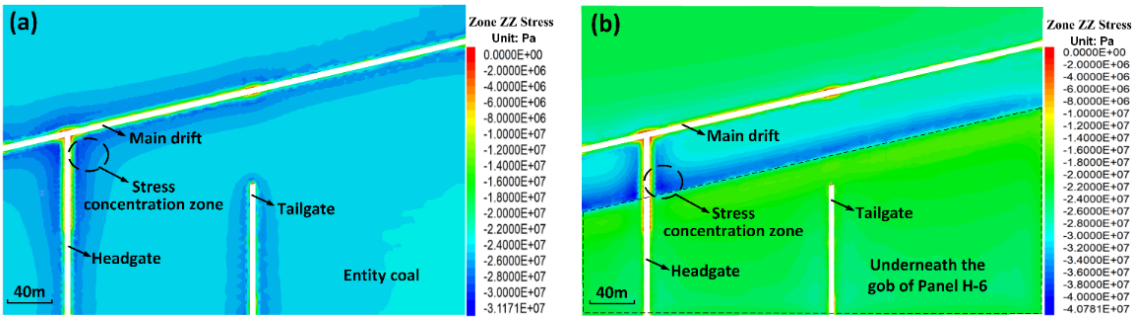

Figure 3.16 Distribution of the vertical stress (plane view). (a) Scheme 1. (b) Scheme 2.

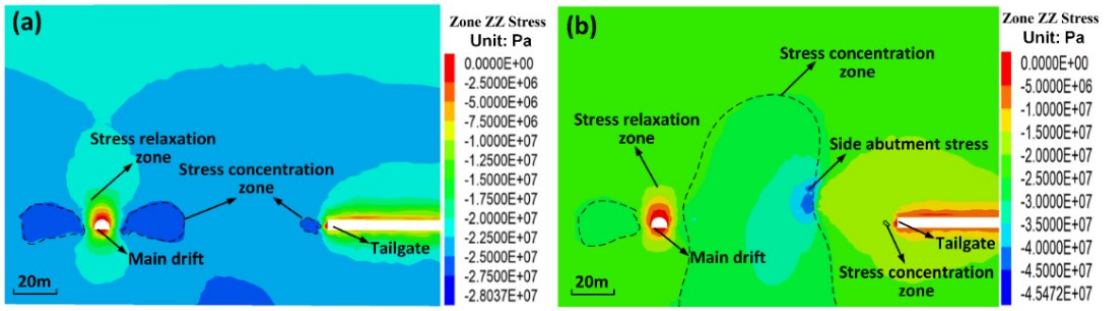

Figure 3.17 Distribution of the vertical stress (section view). (a) Scheme 1. (b) Scheme 2.

The distribution of surrounding rock stress along the strike direction is shown in Figure 3.18. The stress distribution is also uniform along the strike direction. There are a few differences between the results of excavating the tailgate and without excavating it, suggesting that the effects of excavating the tailgate are minor in this stage. The distribution of surrounding rock stress along the dip direction is shown in Figure 3.19. In Scheme 1, the average peak stress is 27.30 MPa, which is 0.21 MPa greater than before. The range of stress concentration zone barely changes. In scheme 2, the average peak stress (peak stress 1) near the main drift is 29.66 MPa (increased by 0.03 MPa), and the range of the stress concentration zone also changes little. The small increments of peak stress might be due to the influence of the advance abutment stress caused by tunnelling. Nevertheless, the range of potential rockburst area is limited in this stage.

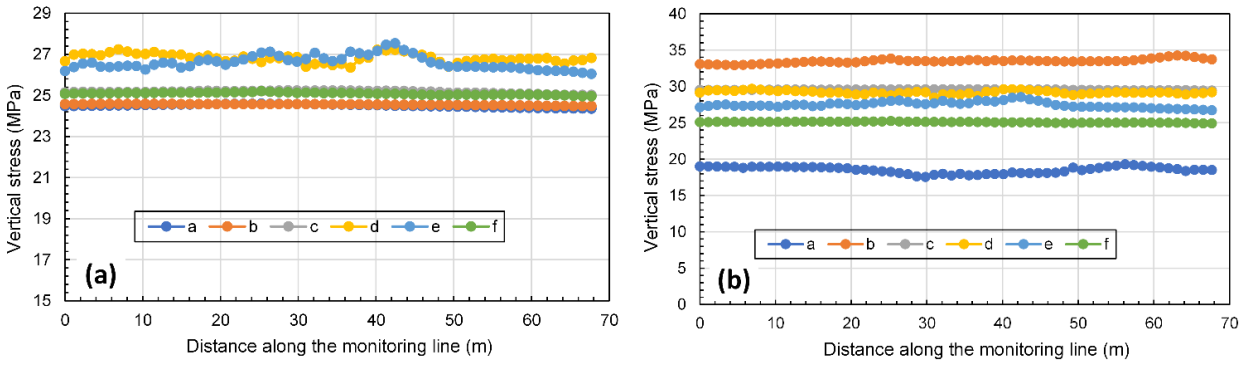

Figure 3.18 Distribution of the vertical stress along the strike direction. (a) Scheme 1. (b) Scheme 2.

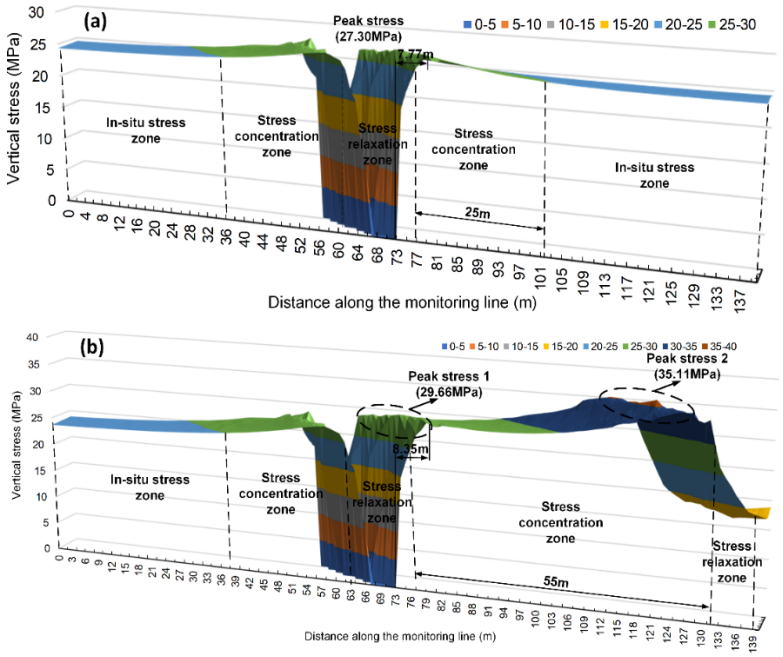

Figure 3.19 Distribution of the vertical stress along the dip direction. (a) Scheme 1. (b) Scheme 2.

3.4.1.3 Completion of the tunnelling of the tailgate (Stage 3)

After the tunnelling of the tailgate was finished, the stress distribution is shown in Figure 3.20 and Figure 3.21. Compared with the last stage, a large stress concentration zone is produced between the two heading faces of the tailgate (see Figure 3.20). This is due to the intersection of three stress concentration zones induced by excavating the main drift and the tailgate (two heading faces). There is an advance abutment stress for each heading face. Besides, the distance from the main drift to the tailgate also decreases with further tunnelling; thus, their stress concentration zones could be merged. As shown in Figure 3.21, a similar phenomenon can also be observed in Scheme 2. However, the range of the stress concentration zone in Scheme 2 is greater than that in Scheme 1. In addition to the combined effect of the excavation-induced stresses of the main drift and the tailgate, the "strengthening" effect of the side abutment stress of Panel H-6 is the crucial contributing factor.

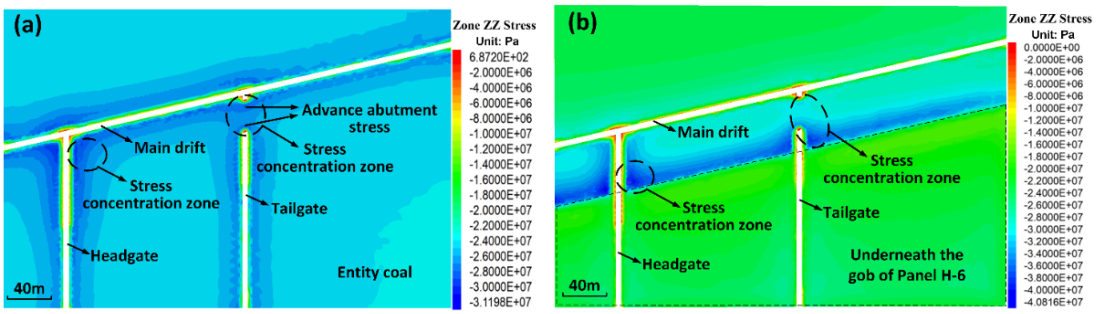

Figure 3.20 Distribution of the vertical stress (plane view). (a) Scheme 1. (b) Scheme 2.

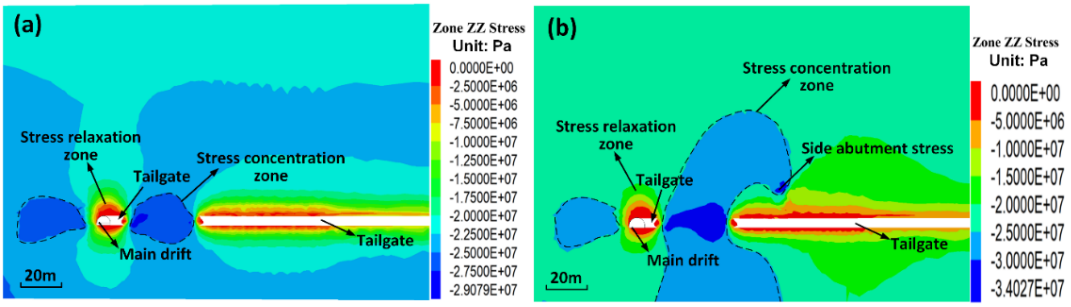

Figure 3.21 Distribution of the vertical stress (section view). (a) Scheme 1. (b) Scheme 2.

The distribution of surrounding rock stress along the strike direction is shown in Figure 3.22. For monitoring lines a and b (Figure 3.22a), there is a zero-stress zone in the middle of the chart, while the stress in two sides is increased to the peak first and then gradually approaches the in-situ stress. This is due to the distribution of excavation-induced stress. The data of monitoring lines c and d are different from those in previous stages, indicating that the stress distribution is no longer uniform, especially for the areas between the main drift and the tailgate. The stress distribution along the monitoring line c is like an "arch," while it was approximately a straight line in previous stages. The maximum stress is 26.63 MPa, increasing by 1.38 MPa (5.5%) to stage 2. There is an apparent pit of the stress distribution along the monitoring line d, suggesting that the surrounding rock stress in this region is released. This indicates that the rock masses in this area have failed due to higher stress, which confirms that stress concentration zones induced by excavating the main drift and the tailgate are intersected. Thus, the range of potential rockburst area is expanded, and rockburst risks are also increased.

Additionally, there is no obvious change in surrounding rock stress on the left side of the main drift. As shown in Figure 3.22b, the stress distribution in Scheme 2 is similar to that in Scheme 1. The main difference between the two schemes is the higher stress magnitude in Scheme 2. The high peak stresses along the monitoring line b can be owing to the superimposition of the stress concentration zone near the tailgate and the side abutment stress of Panel H-6.

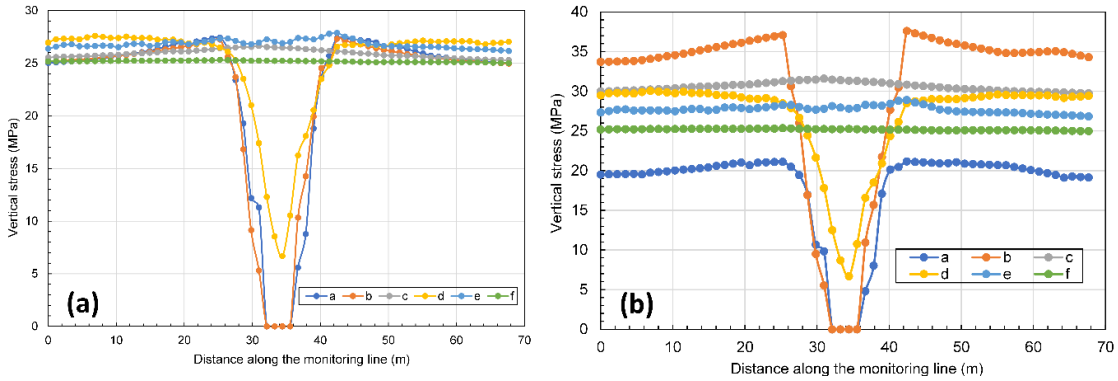

Figure 3.22 Distribution of the vertical stress along the strike direction. (a) Scheme 1. (b) Scheme 2.

The distribution of surrounding rock stress along the dip direction is shown in Figure 3.23. As shown in Figure 3.23a, there are still three zones on the left side of the main drift, but there is no in-situ stress zone on the right side compared with previous stages, consistent with Figure 3.21a. More importantly, two more peak stresses occurred after the tunnelling finished. This peak stress 1 and 3 are induced by excavating the main drift and tailgate, while peak stress 2 is caused by tunnelling the tailgate in the other direction. The values of those peak stresses are 27.49 MPa, 28.15 MPa, and 27.19 MPa, respectively, and stress concentration coefficients are 1.13, 1.16, and 1.12, respectively. The distances from peak stresses to the main drift are 7.89 m, 9.07 m, and 26.19 m, respectively. In addition, the range of the stress concentration zone is about 60 m which has been expanded greatly.

Similarly, there is no in-situ stress zone in the right side of the main drift in Scheme 2 (see Figure 3.23b). However, four peak stresses occurred after the tunnelling was finished. The peak stress 4 could be owing to the intersection of the stress concentration zone near the tailgate and the side abutment stress of

Panel H-6. The values of those peak stresses are 30.08 MPa, 31.25 MPa, 33.43 MPa, and 38.34 MPa, respectively, and stress concentration coefficients are 1.24, 1.29, 1.38, and 1.58, respectively. The distances from peak stresses to the main drift are 8.73 m, 9.05 m, 28.20 m and 51.88 m. The peak stress and the range of stress concentration zone in the left side of the main drift are almost the same as in Scheme 1. The peak stress 1 increases by 9.73% compared with Scheme 1 in stage 3 and increases by 11.71 % compared with Scheme 1 in stages 1 and 2. In addition, on the right side of the main drift, the range of the stress concentration zone is around 58 m, which is smaller than Scheme 1. This is because a part of the tailgate is beneath the gob of Panel H-6, a stress relaxation zone. Compared with previous stages, the range of potential rockburst area is expanded, and rockburst risks are further increased.

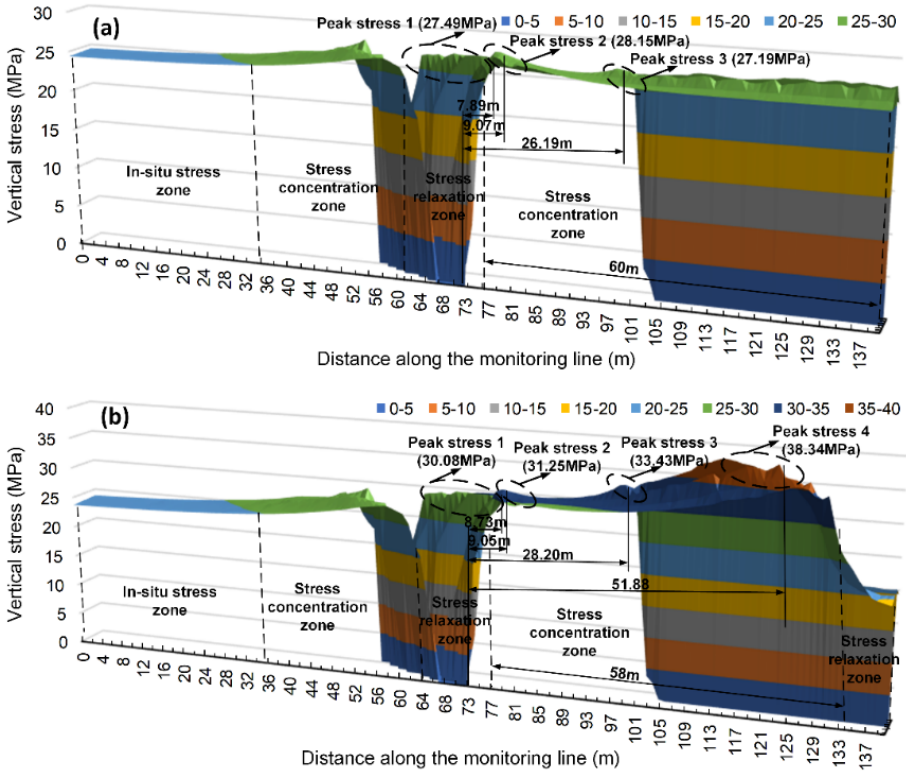

Figure 3.23 Distribution of the vertical stress along the dip direction. (a) Scheme 1. (b) Scheme 2.

As shown in Figure 3.20, a banded "pillar" (a stress concentration zone, Dehghan et al., 2013; Kias and Ozbay, 2013; Zhang et al., 2017; Ahmed et al., 2017; Qiu et al., 2019) between the main drift and the tailgate was produced after the tunnelling finished. To further investigate the stress evolution pattern inside

the “pillar”, the stresses along the pillar axis are collected and analyzed during the final stage. The stress evolution of the “pillar” concerning different driving distances is shown in Figure 3.24. Figure 3.24a shows two peak stresses near the two ends of the “pillar”. Before the last driving cycle finished, peak stress 1 slowly grew with the increasing driving distance. Because the tunnelling reduces the size of the “pillar”, and the stress concentration is strengthened. There are almost no changes for peak stress 2. This is due to the great distance from peak stress 1 to peak stress 2, and the negligible excavation-induced effect. When the last driving cycle is finished, there is a surge for peak stress 2, and the increment is 0.66 MPa, which suggests that the rockburst risks suddenly increase in the last tunnelling procedure. Similar to Scheme 1, there are two peak stresses near the two ends of the “pillar” when the heading face of the tailgate is not underneath Panel H-6’s gob (Figure 3.24b). Before the last driving cycle was finished, peak stress 1 decreased gradually with the increasing distance from the heading face to the side abutment stress of Panel H-6, while peak stress 2 increased slightly. When the last driving cycle is finished, a leap for peak stress 2 is also observed, and the increment is 1.01 MPa. This is because the size of the “pillar” is further decreased, and the side abutment stress of Panel H-6 and excavation-induced stresses of the tailgate could be intersected. Therefore, it can be concluded that driving the H-4 tailgate into the “pillar” (stress concentration zone) and the reduction of the “pillar” size with excavation raise the stress concentration level, increasing rockburst potential.

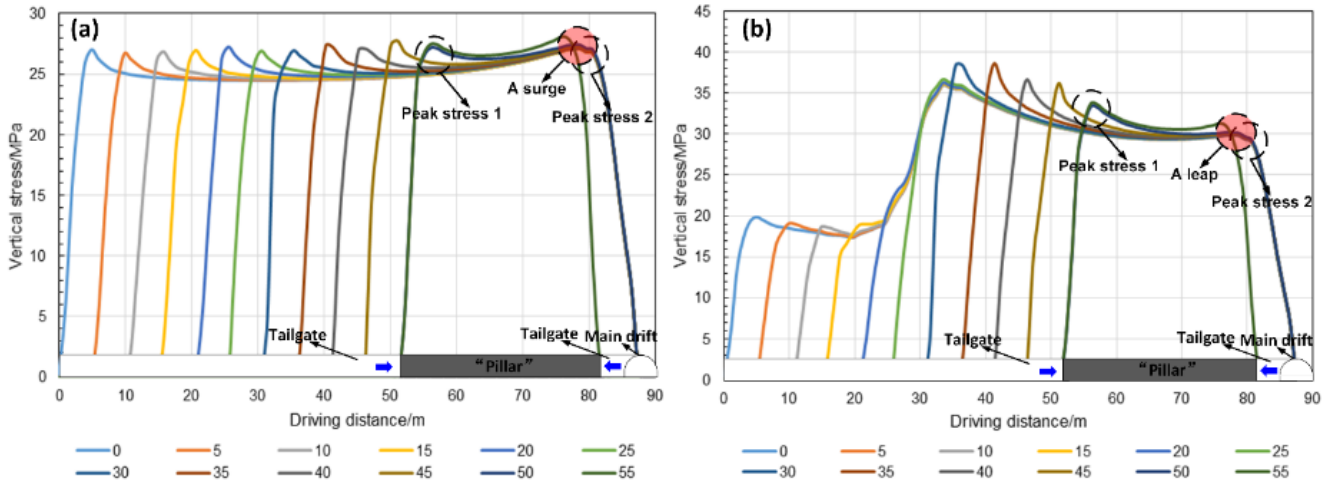

Figure 3.24 Stress evolution concerning different driving distances. (a) Scheme 1. (b) Scheme 2.

3.4.2 Rockburst source mechanism

Based on the previous analysis of the excavation-induced stress distribution, a conceptual model was built to explain the possible rockburst mechanism (Figure 3.25). As shown in Figure 3.25a, there are two types of excavation-induced stresses after the tunnelling of the main drift is finished: the side abutment stress induced by mining in the upper coal seam and the excavation-induced stress of the main drift. Each has a single peak due to the overburden movement and the deformation and failure of surrounding rock masses. After those stresses intersected, a stress field with a "double-peak" was produced (Figure 3.25b). It can be seen from Figure 3.25b that there is an increase in the peak stress induced by excavating the main drift.

In contrast, the peak of the side abutment stress changes little because of the greater distance from the main drift to the gob and the smaller excavation-induced effect compared with the mining-induced effect. In this stage, the range of potential rockburst areas is expanded, and rockburst risks are increased. When the heading face of the tailgate is underneath the gob, there are no changes in the stress field shown in Figure 3.25b, which does not contribute to the rockburst occurrence. Hence, this stage is not illustrated in the conceptual model. When the heading face of the tailgate is underneath the side abutment stress zone (Figure 3.25c), its excavation-induced stress and the side abutment stress are superimposed, and thus

higher peak stress is produced, while there is a minimal increase of the peak stress induced by excavating the main drift. With the further tunnelling of the tailgate, the high peak stress moves to the main drift gradually, but its value is reduced because the heading face of the tailgate is far away from the side abutment stress zone (Figure 3.25d).

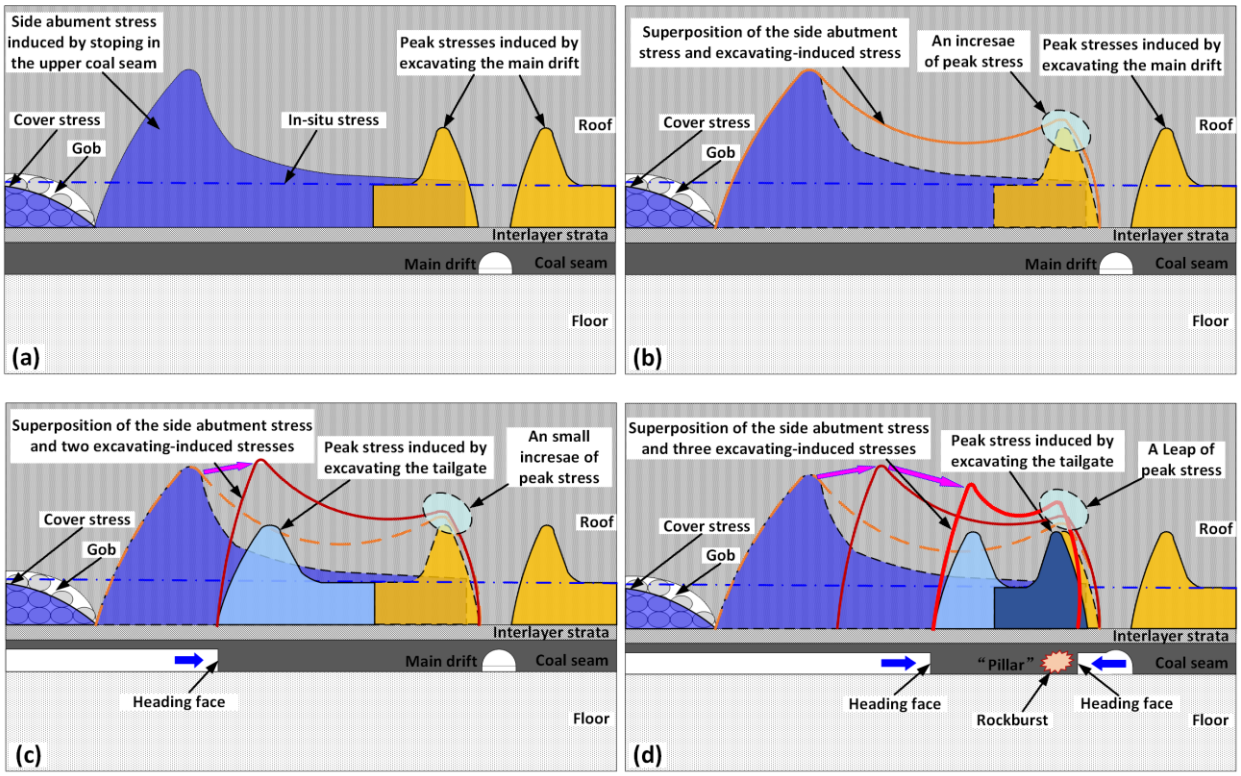

Figure 3.25 Conceptual model of the rockburst mechanism. (a) Before the superposition of the side abutment stress and excavation-induced stress. (b) Superposition of the side abutment stress and excavation-induced stress. (c) Superposition of the side abutment stress and two excavation-induced stresses. (d) Superposition of the side abutment stress and three excavation-induced stresses.

Meanwhile, the tunnelling of the tailgate was operated from the main drift in the opposite direction. New excavation-induced stress joins the superposition of the side abutment stress of Panel H-6 and excavation-induced stresses (main drift and the tailgate toward it). Therefore, a leap of peak stress occurred near the heading face of the tailgate. As mentioned above, a banded "pillar" was produced after the tunnelling was finished, which is prone to stress concentration. The higher concentrated stress results in the continuous deformation of surrounding rock masses, and thus, more strain energy is expected to be accumulated. The rockburst could occur when the accumulated strain energy reaches a critical level

(higher than the dissipated energy) (Ortlepp and Stacey, 1994). In this case, the side abutment stress induced by mining in the upper coal seam has a "strengthening" effect on excavation-induced stresses and energy accumulation, increasing rockburst potential and risks. It might be argued that there is also peak stress near the tailgate in the other direction, but the rockburst event did not occur in this zone. This problem was further investigated and explained in the next section.

3.4.3 Alternative measures to prevent and mitigate rockburst hazards

To prevent and mitigate rockburst hazards, engineers need to consider the possible superposition of concentrated stresses induced by multiple excavations during the design stage. A good choice is to select a reasonable mining method (e.g., pillarless mining and extracting protective seams), excavation sequence, and advance rate. For instance, the excavation-induced stress magnitude positively correlates with the opening width (Apel, 2005; Singh et al., 2011; Liu et al., 2021a). In the case study site, the up-dip panel recovery sequence (extracting Panel H-4 first, then Panel H-6) was used, which creates a great opening width. Hence, the stress concentration is high near the outer edge of Panel H-6 gob.

In contrast, the rockburst hazard would be reduced using the down-dip recovery sequence. For example, panel H-6 could be mined first, followed by driving the H-4 tailgate in coal seam 409/4. Then, Panel H-4 could be extracted. This operation can lower the stress concentration level because of the remarkable reduction of the opening width when driving the H-4 tailgate. Besides, the driving direction of the H-4 tailgate could be changed to mitigate rockburst potential. For example, if the H-4 tailgate were only tunnelled from the main drift to the down-dip, the heading face would soon enter into the stress shadow of the overlying Panel H-6 gob, a stress relaxation zone (see Figure 3.10). Hence, the rockburst risks can be significantly reduced. The effects of these measures on controlling rockbursts can be assessed using numerical modeling.

Additionally, the layout of panels and roadways should avoid high-stress areas underneath the outer edge of gobs and remnant pillars in upper mining levels. When it is difficult to avoid areas with high-stress concentration, the length of roadways and working faces under high-stress areas should be as small as possible to reduce the magnitude of the accumulated strain energy and mitigate the rockburst level risks.

In the mining phase, the rockburst risks can be mitigated by improving the properties of surrounding rock masses, stress relief and stress transfer, and using backfill mining and yielding supports. Rock masses can be made soft in operations by spraying water on the tunnelling face or using water infusion technology (Wang et al., 2021a). Distress drilling and blasting are two common techniques to relieve and transfer concentrated stresses to rock masses in-depth (Konicek et al., 2011; Jiang et al., 2012; Zhu et al., 2018). Backfill mining technology can also mitigate rockburst risks (Castro et al., 2012). This is because backfill materials can significantly reduce the subsidence of rock strata, thereby reducing the abutment stress magnitude.

Additionally, some types of yielding or energy-abortion rockbolts, e.g., D-bolt, Roofex, and He-bolt, have been verified that they can control rockbursts effectively (Wang et al., 2021a). Hence, the yielding rockbolts should be installed in burst-prone roadways.

Numerical modeling is suggested to evaluate the effects of these measures on controlling rockbursts as it is a cheap, safe, and effective tool.

3.5 A systematic rockburst prediction method

Over the past several decades, researchers have proposed many indicators to predict and evaluate rockburst potential based on various rockburst theories and phenomena from the aspects of stiffness, strength, energy, fracture, damage, etc (Wang et al., 2021a). Currently, the proposed rockburst indicators can be generally classified into two categories: 1) indicators based on the stress/strength criterion, such as major principal stress, tangential stress, axial stress, and UCS; 2) indicators based on the energy criterion,

such as elastic strain energy and elastoplastic deformation energy. A table shows the rating systems of some typical rockburst indicators (see Table 3.5). To utilize those indicators more reasonably and conveniently, they are classified according to different scales: lab (intact rock) and engineering scale (rock mass).

According to the laboratory test results, the σ_c and σ_t of coal materials are 9.3 MPa and 0.6 MPa, respectively. Hence, the rock brittleness coefficient (B) is 15.5, showing that the coal inherently possesses a moderate rockburst proneness. However, this indicator only depends on mechanical properties at a laboratory scale which is insufficient for large-scale excavations (Ahmed et al., 2017). More importantly, many factors contribute to the occurrence and severity of rockbursts, which can be classified into internal and external factors (Park, 1995; Kwasniewski and Wang, 1999; Miao et al., 2016). Keneti and Sainsbury (2020) also summarized those factors into two main categories: stress conditions, including stress direction and magnitude, excavation direction and rate, and the geometry of the opening; rock mass characteristics, including mineralogical properties, geomechanical properties and geological intensifiers. Hence, noticing that the occurrence and severity of rockbursts also depend on a favourable geo-stress environment, nine typical indicators are selected as the rockburst criteria in this study. The strength properties of the rock and environment factors (e.g., mining-induced stress or energy) are both considered in those criteria (see bold texts in Table 3.5).

Table 3.5 Rating system of different prediction and evaluation indicators of rockburst potential

Classification criterion	Scale	Indicator	Equation	Rockburst tendency				Author (Year)
				No	Weak	Moderate	Strong	
Stress /strength	Lab	Rock brittleness coefficient (B)	σ_c/σ_t	> 40	40-26.7	26.7-14.5	<14.5	Peng et al. (1996)
	Engineering	Barton criterion	σ_c/σ_1	> 10	10-5	5-2.5	<2.5	Barton et al. (1974)
	Engineering	**Barton criterion**	σ_t/σ_1	> 0.66	0.66-0.33	0.33-0.16	<0.16	Barton et al. (1974)
	Engineering	**Russenes criterion**	σ_θ/σ_c	≤0.2	0.2-0.3	0.3-0.55	>0.55	Russenes (1974)
	Engineering	The criterion of tangential stress	σ_θ/σ_c	0.34	42	0.56	0.7	Hoek and Brown (1980)
	Engineering	**Tao discriminant index (α)**	σ_c/σ_1	>14.5	5.5-14.5	2.5-5.5	<2.5	Tao (1988)
	Engineering	Excess Shear Stress (ESS)	τ_s-τ_d	<5	5-15	>15	—	Ryder (1988)

	Engineering	**Competency factor (C_g)**	$(f_\sigma\sigma_c)/\sigma_\theta$	>2.5	2.5-1	1-0.5	<0.5	Palmström (1995)
	Engineering	RQD	—	<25	25-50	50-70	>70	Li et al. (2008)
	Engineering	**Brittle shear ratio (BSR)**	$(\sigma_1-\sigma_3)/\sigma_c$	<0.45	0.45-0.6	0.6-0.7	>0.7	Castro et al. (2012)
	Engineering	**Stability coefficient (I_A)**	σ_{sum}/σ_c	<1.5	1.5-2	2-2.5	≥2.5	Jiang et al. (2017b)
Energy	Lab	Impact property (R)	W_E/W_p	—	>1	—	—	Neyman et al. (1972)
	Lab	Strain energy storage coefficient (F)	W_{sp}/W_{st}	≤2	2-3.5	3.5-5	≥5	Kidybiński (1981)
	Lab	Linear elastic energy (W_E)	$\sigma_c^2/2E$ (unit: KJ/m^3)	<40	40-100	100-200	>200	Kwasniewski et al. (1994)
	Lab	k	$\sigma_c\varepsilon_f/\sigma_t\varepsilon_b$	<20	20-75	75-130	>130	Tang and Wang (2002)
	Engineering	**Energy released rate (ERR)**	$\frac{1}{2}\int \varepsilon_1^T(\sigma_{final}-\sigma_0)dV$	<15	15-30	30-55	>55	Jaeger and Cook (1979)
	Engineering	**Burst potential index (BPI)**	$(ESR/e_c)100$ (unit: %)	<25	25-50	50-75	75-100	Mitri et al. (1999)
	Engineering	**Strain energy density index (SEDI)**	U_d/U_0	0.3	0.4	0.5	0.7	Chen et al. (2009)

The FISH language embedded in FLAC3D was used to fulfill the expression of those criteria, and the simulation results are shown in Figure 3.26. The Barton criterion gives values between 0.014 to 0.20, showing moderate or strong rockburst potential for all areas. The Russenes criterion shows that all areas have a strong rockburst tendency because the values are greater than 0.55. Similarly, the Tao discriminant index (α) and Competency factor (C_g) reflect a violent rockburst liability for all areas, which fail to discriminate zones with different rockburst risks. On the other hand, the Stability coefficient (I_A) and three energy-based indices are also incapable of predicting rockburst potential, which is overestimated in this case. The distribution of rockburst tendency estimated by those four indicators is similar to the vertical stress distribution (Figure 3.20b). Fortunately, we found that the brittle shear ratio (BSR) can recognize the zones with different burst potentials. As shown in Figure 3.26, the zones with high BSR (1.4 to 1.7) are consistent with the actual area of the "5.5" rockburst event in the field, while there is a "no" or "weak" rockburst tendency for other areas.

For BSR, the main contributing factor is the deviatoric stress when the UCS of the coal seam is uniform. As mentioned above, two peak stresses near the tailgate's facing face in different directions can trigger a rockburst. However, the BSR in those two zones is 0.59 and 1.54, indicating a weak and strong rockburst

potential. This finding suggests that deviatoric stress plays an important role in creating a rockburst which has also been confirmed by other researchers (Castro et al., 1997; Castro, 1996; Diederichs, 1999; Martin et al., 1999). Thus, it can be concluded that one of the possible external causes of the "5.5" rockburst event is the superposition of concentrated stresses and great deviatoric stress induced by complex excavation situations.

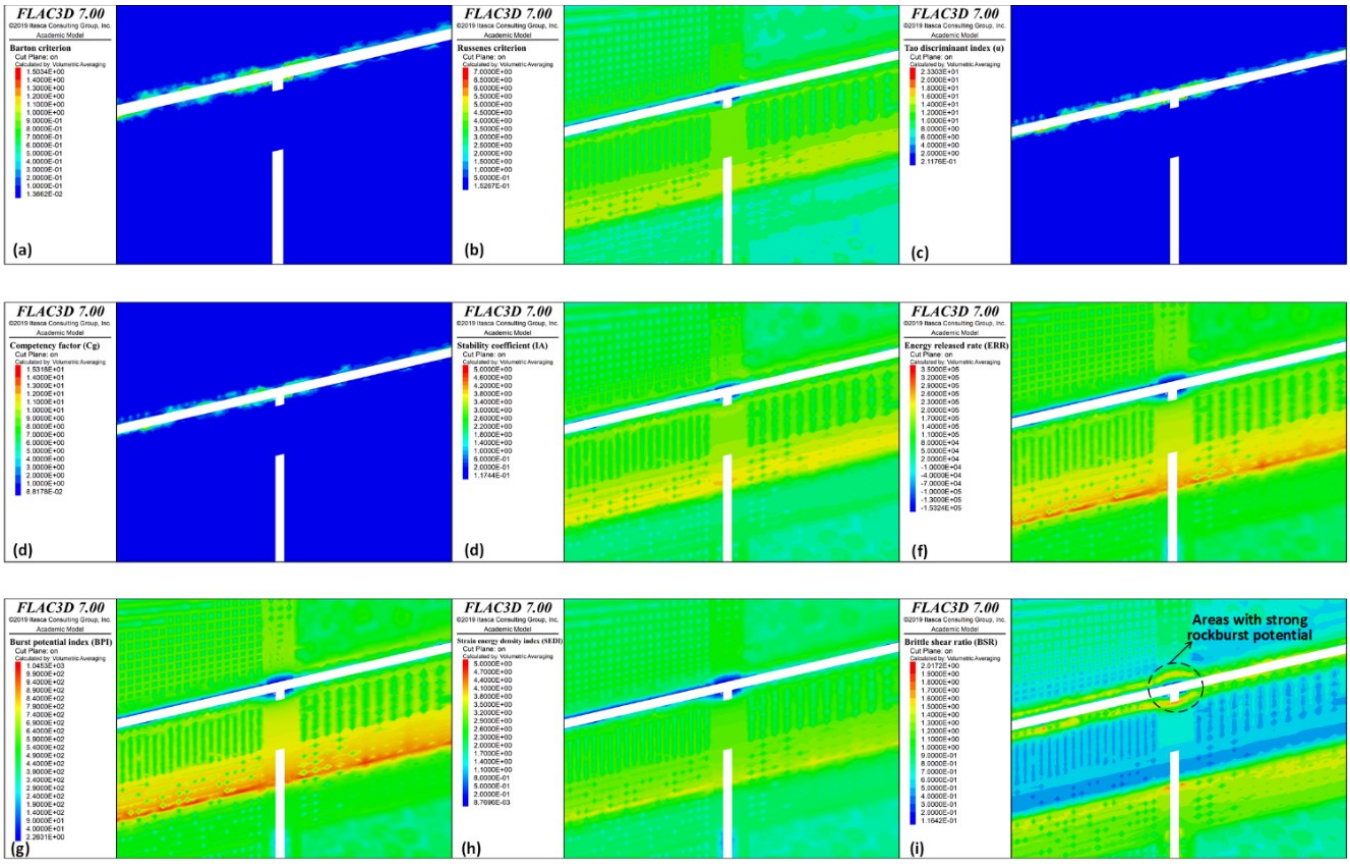

Figure 3.26 Evaluation of rockburst tendency with different indicators.

Most of those indicators are based on specific cases from different regions in the world, of which the geological conditions, rock properties and excavation-induced effects are different. Similarly, Mitri et al. (1999) pointed out that ERR values in a Canadian mine are much lower than those leading to rockburst problems in South African mines. Thus, the rockburst indicators cannot be directly transposed to a particular situation from one region to another. Therefore, a strict calibration procedure should be implemented before using indicators to predict and estimate rockburst tendency.

Hence, a systematic method that can reasonably select and use rockburst indicators is proposed to predict and evaluate rockburst potential using numerical modeling combined with laboratory tests and feedback from the field. A flowchart shows the proposed method (Figure 3.27). The first step is to evaluate the rockburst proneness of rocks based on indicators at a laboratory scale. If the rock does not possess rockburst proneness, rockbursts will not occur during rock mass engineering in this type of rock (Cai, 2016; Leveille et al., 2017; Zhou et al., 2018). The second step is to initially choose indicators (engineering scale) and predict rockburst tendency using numerical simulation. The selection of rockburst indicators can refer to a summary made by Zhou et al. (2018): FAI (failure approaching index, Zhang et al., 2011), BSR (brittle shear ratio, same as $(\sigma_1-\sigma_3)/\sigma_c$, Castro et al., 2012), ERR (Salamon, 1984; Kaiser et al., 1996), BPI (Mitri et al., 1999), and LERR (Wiles, 2002; Jiang et al., 2010) can be used for evaluating strainbursts; and ESS (excess shear stress, Ryder, 1988), BPR (bursting potential ratio, Simon, 1999) and OBI (out-of-balance index, Simon, 1999) are suitable for assessing fault-slip bursts. However, Zhou et al. (2018) did not mention what indicators could be adopted to estimate pillar burst risks. Some researchers (Wiles, 2002; Castro et al., 2012; Kusui et al., 2016; Vennes and Mitri, 2017; Li et al., 2019) suggested that the ERR (Salamon, 1984; Kaiser et al., 1996), LSS (Wiles, 2002), σ_c/σ_θ (Hoek and Brown, 1980), BSR (Castro et al., 2012), and SED (Wattimena et al., 2012) could be employed for the assessment of pillar burst potential. Then, the selected indicators can be calculated in numerical programs, thereby initially determining or updating the indicators by comparing the occurrence area and intensity of a rockburst case in the field. In the third step, reasonable indicators are finally obtained after the calibration with more rockburst cases or a rockburst database of this region. Following these three steps, engineers will be confident to use some indicators as rockburst criteria to predict risks quantitatively and take appropriate rockburst prevention and mitigation measures.

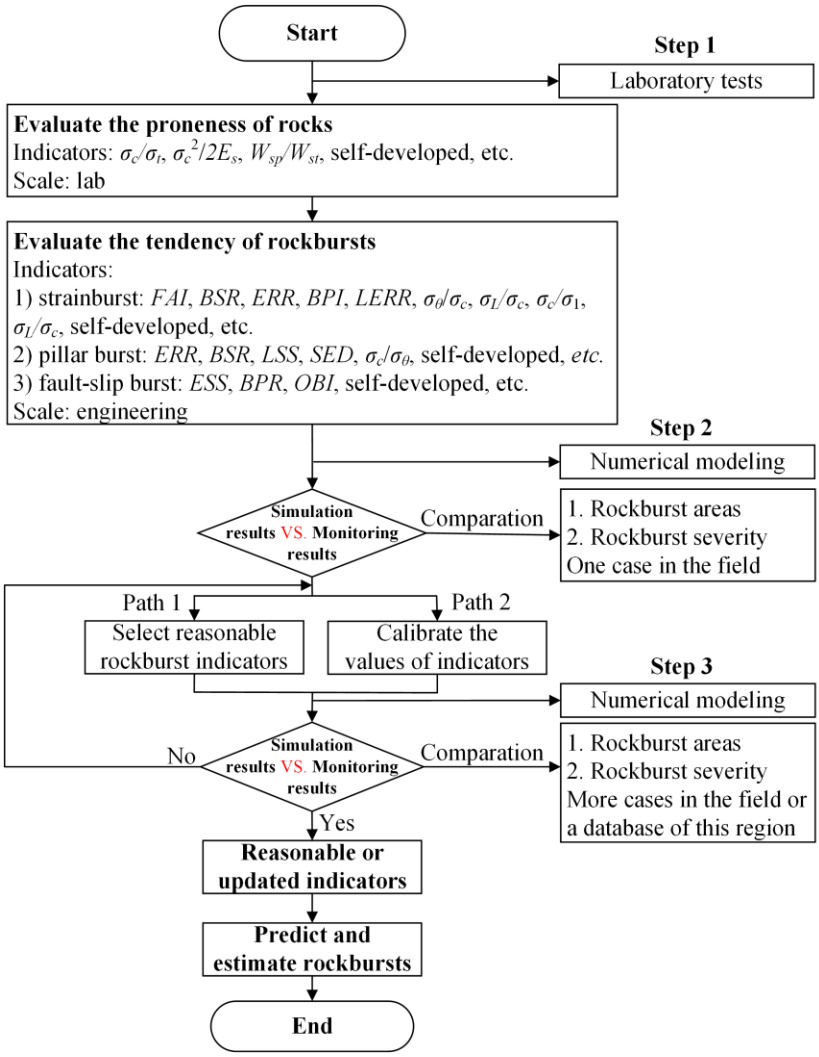

Figure 3.27 A systematic method to predict and evaluate rockburst potential.

3.5. Conclusions

In this chapter, taking the "5.5" rockburst event in the Zofiówka Coal Mine as a case example, the rockburst source mechanism of driving roadways during close-distance coal seam mining is thoroughly investigated the view of excavation-induced stresses using a numerical modeling method. Furthermore, a systematic rockburst prediction method is also proposed. The main conclusions are as follows:

1) After excavating the main drift (Stage 1), rock masses surrounding the excavation wall failed because their strength was smaller than the high excavation-induced stress, which was then transferred into the deeper areas. The extraction of Panel H-6 changes the main drift's normal distribution of surrounding rock stress. There are three zones: stress relaxation, stress concentration

and in-situ stress on each side of the main drift, but there is no in-situ stress zone on the right side when the mining of Panel H-6 is considered. The range of potential rockburst area is expanded because of the redistribution of excavation-induced stresses from the extraction of panels in the upper coal seam.

2) With the further tunnelling of the tailgate (Stage 3), a large stress concentration zone is produced between the two heading faces of the tailgate. The peak stress 1 increases by 9.73% compared with Scheme 1 in stage 3 and increases by 11.71 % compared with Scheme 1 in stages 1 and 2. As a result, the range of potential rockburst area is expanded, and rockburst risks are further increased. A banded "pillar" between the main drift and the tailgate is produced after the tunnelling is finished, and there are two peak stresses near the two ends of the "pillar". Before the last driving cycle is finished, peak stress 1 decreases gradually with the increasing distance from the heading face to the side abutment stress of Panel H-6, while peak stress 2 increases slightly. When the last driving cycle is finished, a leap for peak stress 2 is observed, and the increment is 1.01 MPa.
3) The rock brittleness coefficient is 15.5, showing that coal inherently possesses a moderate rockburst proneness. The superposition of multiple excavation-induced stresses of the main drift and tailgate provides an environment for stress concentration and energy accumulation. The side abutment stress induced by mining in the upper coal seam has a "strengthening" effect. The great deviatoric stress induced by complex excavation situations is another critical exterior cause. The rockburst indicators cannot be directly transposed to a particular situation from one region to another. A systematic method that can select and use rockburst indicators reasonably is proposed to predict the location and magnitude of rockbursts.

4. CHAPTER 4: ANALYSIS OF THE DAMAGE MECHANISM OF STRAINBURSTS BY A GLOBAL-LOCAL MODELING APPROACH

*In this chapter, an improved global-local modeling approach was developed to study strainburst damage mechanisms. The extracted stresses induced by multiple excavations from a 3D global model established by FLAC3D are used as boundary conditions for a 2D local model of a deep roadway built by UDEC to simulate realistic stress loading paths and conduct a detailed analysis of rockburst damage from both micro and macro perspectives. The principles to control and mitigate strainburst damage are also proposed. This chapter is based on the published paper "**Wang, J.,** Apel, D. B., Dyczko, A., Walentek, A., Prusek, S., Xu, H., Wei, C. (2022). Analysis of the damage mechanism of strainbursts by a global-local modeling approach. Journal of Rock Mechanics and Geotechnical Engineering, 14(6), 1671-1696".*

4.1 Introduction

Ortlepp and Stacey (1994) suggested that it is essential to distinguish the "source mechanism" and the "damage mechanism" of rockbursts because they are often not the same mechanism and might have different locations. The source mechanism is the trigger factor that induces rockbursts. In general, rockbursts can be grouped into three types: strainburst, pillar burst, and fault-slip burst, based on different source mechanisms (Hedley, 1992; Kaiser and Cai, 2012; Cai, 2013). Strainburst is the most common rockburst type (Zhang et al., 2012a; Cai, 2013). It happens because of the excavation-induced stress concentration and a "soft" loading environment around fractured rock masses (Kaiser and Cai, 2012). As a result, the rock can fail locally at excavation boundaries in an unstable and violent manner. The damage mechanism refers to failure modes (e.g., rock ejection, rock bulking, rockfall, rock buckling, and shear displacement) induced by rockbursts. The research on rockburst damage can provide insight into the understanding of initiation, development, and extent and types of failure within surrounding rock masses during rockbursts. The rock failure type is an essential criterion for selecting rational support elements (e.g., cable bolts or rockbolts), and the damage severity can affect the support system's capacity, extent, and intensity (e.g., strength and length of rockbolts). Thus, understanding rockburst damage mechanisms help improve and optimize the rock support design in the burst-prone ground to control and mitigate rockburst damage. The focus of this study is on strainburst damage mechanisms.

Significant efforts have been made to study strainburst damage mechanisms by experimental, field surveying, and numerical methods. Various engineering disciplines have employed numerical modeling, ranging from bioengineering (Apel et al., 2021) to mining engineering. Compared with field surveying and experimental tests, numerical methods have the advantages of low cost, safety, time-saving, and flexibility. Numerical modeling can also obtain more information (Salamon, 1993). In the past few decades, many numerical methods and programs have been developed to deal with various rock mechanics

problems (Wang et al., 2021a). These methods have become a useful and frequently used way to study the damage mechanism of strainbursts. Zhang et al. (2011, 2013) proposed the FAI and then programed it in FLAC3D to estimate the potential rockburst damage zones in deep powerhouses and tunnels. Hosseini (2016) used the CA3 program to study the strainburst damage where discrete particles modelled the rock, and finite elements simulated the frame structure. Feng et al. (2017, 2019b) employed ELFEN to analyze the effects of structural planes and stress regimes on the process of rockbursts occurring in a circular opening. Manouchehrian and Cai (2018) built a heterogeneous model in ABAQUS via Python programming and then simulated rockburst damage near faults in deep excavations. Gao et al. (2019a, b) proposed a novel bonded block method in UDEC to model strainbursts and studied rockburst damage by monitoring failed cracks. Vazaios et al. (2019) employed IRAZU (FEM/DEM program) to study the effect of a different number of pre-existing joints (DFNs)) on strainburst phenomena in a hard rock excavation under high magnitude stresses. Guo et al. (2019) adopted FLAC3D numerical simulation to investigate the failure laws of the roadway surrounding rocks during rockbursts considering different ratios between principal stresses. The research work of those scholars has made many significant achievements and provided good references for understanding the damage mechanisms of strainbursts under different conditions.

However, most current research belongs to the parametric study (e.g., different factors related to excavation geometry, stress scenario, discontinuity, and material property) without considering the gradual stress concentration or energy accumulation resulting from nearby mining or excavation activities, indicating that the influences of the realistic stress loading path on strainburst occurrence were ignored. Furthermore, most studies' analyses of rock mass fracturing or damage are qualitative, although using a quantity to describe different damage levels meticulously is meaningful. Therefore, it is worth developing or employing a new modeling approach to capture the realistic stress loading path and investigate rock

mass fracturing or damage quantitively during strainbursts. For example, Edelbro (2008) developed the global-local modeling approach as an efficient and effective method to study the failure and deformation of roadways. In this approach, the various stresses from excavating multiple openings can be extracted accurately from an overall 2D/3D model and then used as boundary conditions for 2D local models of roadways.

Besides, the computational efficiency is significantly enhanced because of the usage of elastic properties in the global model, and the detailed analysis of 2D local models can be accomplished with a high mesh resolution and elastoplastic relationships. Hence, this approach might have great potential to investigate the damage mechanism of rockbursts, especially the strainbursts, since they usually occur in tunnels or roadways. However, to the authors' knowledge, no studies in the literature have been reported to use this approach to analyze strainburst damage.

The presented research used back analysis to simulate the state of mining- or excavation-induced stresses before the rockburst event at the Zofiowka Coal Mine in Poland on May 5, 2018 (Adam, 2018). The rockburst event had seismic energy of 2×10^9 J, causing tremendous roadway damage and even fatalities. The rockburst location had a complex geological structure with many faults. The complex geological and mining environments resulted in high concentrated stresses in the roadway surrounding rock masses, which provides a good case example for studying strainburst damage mechanisms.

This study first employs an improved global-local modeling approach to study strainburst damage mechanisms. First, a 3D finite-difference numerical model is built via FLAC3D software. Next, the elastoplastic constitutive relationship of rock mass materials is used in 3D modeling to capture the actual and accurate mining- or excavation-induced stress distribution. Then, the extracted stresses induced by multiple excavations from the 3D global model are used as boundary conditions for a 2D local model of a deep roadway built by a DEM code UDEC. The damage mechanism of strainbursts is investigated from

both micro and macro perspectives. Finally, the effects of the current support system are initially evaluated, and the control principles of rockburst supporting are proposed according to the analysis of strainburst damage mechanisms. This study presents a systematic framework to investigate strainburst damage mechanisms using the improved global-local modeling approach.

4.2 Engineering overview

4.2.1 Geology and geotechnical overview

The "5.5" rockburst event reported in the Zofiówka Coal Mine was used as a case example to investigate strainburst damage mechanisms. The detailed information about the geological and geotechnical characteristics of the case study site has been provided in Chapter 3 (see section 3.2).

4.2.2 Rock mass properties

The UCS test and Brazilian tension test were conducted to determine the mechanical parameters of intact rocks (following ISRM standards, Fairhurst and Hudson, 1999). Then, the rock mass properties were obtained by scaling the mechanical parameters of intact rocks using the generalized Hoek-Brown criterion (Marinos and Hoek, 2000) and the GSI system (Figure 3.2). The values of GSI were determined from the quantitative GSI chart (Marinos and Hoek, 2000) according to the inspection of rock mass structures and the surface condition of discontinuities. The rock mass properties used in numerical modeling are listed in Table 4.1, which can also be referred to in the literature (Małkowski et al., 2017; Szott, 2018; Małkowski and Ostrowski, 2019). The UCS and deformation modulus (E_m) of rock masses were estimated from the following equations (Hoek et al., 2002; Hoek and Diederichs, 2006):

$$\sigma_{cm} = \sigma_{ci} \frac{(m_b+4s-a(m_b-8s))\left(\frac{m_b}{4+s}\right)^{as-1}}{2(1+a)(2+a)} \tag{4.1}$$

$$E_m = E_i \left(0.02 + \frac{1-D/2}{1+e^{((60+15D-GSI)/11)}}\right) \tag{4.2}$$

where m_b, s, and a are constants for rock masses; σ_{ci} is the UCS of intact rocks; E_i is Young's modulus of intact rocks; σ_{cm} is the UCS of rock masses; E_m stands for the deformation modulus of rock masses, and

D is a factor representing the disturbance level of rock masses caused by different tunnelling methods. For the study site, D is assumed to be zero considering that the mechanical tunnelling results in minimal disturbance to confined rock masses (Hoek et al., 2002). The calculated results of UCS and E_m of rock masses are also summarized in Table 4.1.

Table 4.1 Physical and mechanical parameters of rock masses (Małkowski et al., 2017; Szott, 2018; Małkowski and Ostrowski, 2019)

Lithology	Constant				Intact rock				GSI	Rock mass	
	m_i	m_b	s	a	ρ (kg/m^3)	σ_{ci} (MPa)	E_i (GPa)	v		σ_{cm} (MPa)	E_m (GPa)
Coal	17	1.729	0.0008	0.5	1300	9.3	1.86	0.30	36	2.50	0.23
Clay shale	9	1.327	0.0022	0.5	2500	29.0	5.62	0.31	45	7.93	1.26
Fine-grained sandstone	17	2.851	0.0039	0.5	2580	90.0	9.52	0.26	50	24.53	2.92
Sandy shale	12	1.877	0.0031	0.5	2530	26.0	5.23	0.25	48	7.11	1.42
Gritty clay shale	8	1.192	0.0022	0.5	2440	47.5	6.98	0.32	45	13.03	1.56

Note: m_i is a material constant for intact rocks. ρ is the bulk density of intact rocks. v is the Poisson's ratio of intact rocks.

4.3 Numerical modeling

4.3.1 Global-local modeling approach

The global-local modeling approach was initially proposed to study the brittle failure of footwall drifts in an underground hard rock mine (Edelbro, 2008; Edelbro et al., 2012). In this approach, stresses induced by mining multiple stopes were extracted from an overall 2D model and then were input into 2D local models of drifts as boundary conditions. Owing to the employment of elastic properties in the global 2D model, the computational efficiency is significantly enhanced, and the detailed analysis of 2D local models can be accomplished with a high mesh resolution and elastoplastic relationships. Edelbro et al. (2012) reported that the simulated failure of drifts agreed well with the in situ observations, indicating that the used approach is an efficient and robust way to analyze the damage and stability of tunnels. After that, the approach was used to analyze the stress and deformation of gateways in longwall panels. Basarir et al. (2019) established a 3D global model by FLAC3D to extract the mining-induced stresses implemented into 2D local models built by RS2 (Rocscience, 2015) for the stability analysis of gateways. The modelled

deformation of gateways in 2D local models matched well with the monitored roadway convergences, which further verified the effectiveness of this modeling approach.

The global-local modeling approach might have great potential to investigate the damage mechanism of rockbursts, especially the strainbursts, which usually occur in tunnels or roadways. First, the 3D global model can capture the realistic stress loading path before a strainburst occur. Second, rock mass fracturing or damage during strainbursts can be investigated quantitively and in detail in 2D local models with the employment of elastoplastic relationships and high mesh resolution. Hence, this approach was employed in this study.

However, there are two significant improvements in the used modeling approach. First, the elastoplastic constitutive relationships of rock masses rather than elastic models are used in 3D modeling to capture the redistribution of mining- or excavation-induced stress more realistically and accurately. The employment of elastoplastic constitutive relationships might increase the calculation cost significantly. Nevertheless, over the last two decades, the calculation speed of numerical programs (e.g., FEM and FDM codes) has been significantly increased with rapid developments in computer equipment. For instance, it takes around 0.15 s for the FLAC3D Version 7.0 (Itasca, 2019) to process 624000 zones in 100 timesteps on a computer with an Intel i9-9820 central processing unit (CPU) at 3.30 GHz (10 cores) due to better multi-threading and improved algorithms (Hazzard, 2020). Thus, using elastoplastic properties for global 3D modeling is no longer an inefficient and luxury thing at present.

Second, a 2D DEM code UDEC (Version 7.0, Itasca, 2020) was employed in this research, while the 2D FEM code RS2 was used in the previous studies. Rockburst failure is a process in that rock masses suffer a continuous small deformation first and then a large discontinuous deformation in a very short time. However, continuum methods, such as BEM, FEM, and FDM, are unbale to model the discontinuous deformation behaviour of rock masses. Hence, researchers preferred to adopt DEM and DEM-related

hybrid methods to model the discontinuous deformation of rock masses during rockbursts (Grisi et al., 2016; Feng et al., 2017, 2019b; Li et al., 2018; Vazaios et al., 2019; Gao et al., 2019a, b). The rock mass consists of distinct blocks and contacts in the block DEM. The blocks will slide or separate from each other when the stress exceeds the contact's strengths. Besides, the blocks can move, rotate, and deform according to Newton's second law and related constitutive relationships (Jiang, 2017). Thus, the DEM is suitable for modeling the discontinuous deformation of rock masses to reproduce rockburst damage processes (Wang et al., 2021a). It might be argued that only a single 3D DEM code can solve this problem. However, the main concern is that the calculation speed of current 3D DEM codes (e.g., 3DEC) is much slower than that of 3D FEM, FDM, and 2D DEM codes (Yang et al., 2018). Thus, the combination of 3D FDM and 2D DEM (global-continuous and local-discontinuous) can be accepted as a more efficient and rational approach to the current investigation of strainburst damage mechanisms.

4.3.2 Global model

4.3.2.1 Model setup

A 3D finite-difference numerical model was established using FLAC3D software, as shown in Figure 4.1. Instead of all coal basins, only the most critical parts, including H-4 headgate, H-4 tailgate, H-10 main drift, and a part of Panel H-6 were built in the model, as this study aims to investigate the strainburst damage mechanism for a roadway. It could be argued that the major faults, e.g., the Central fault, Eastern fault, and Jastrzębie fault, may contribute to the redistribution of stress surrounding the main drift. Tsesarsky et al. (2013) stated that the discontinuities could be assumed continuous over areas much greater than any excavation. The study site's scale of excavations (tunnelling faces of the gateway) is much smaller than that of main faults, with a few hundred meters to more than one kilometre. Therefore, it is assumed that faults are not included in the 3D global model, which significantly reduces the size and zone number of the model and saves the computational cost. The model's top boundary was free, and vertical stress of

21.87 MPa was applied to it to model the overburden weight. This value is determined by multiplying the unit weight of overburden (assuming 0.027 MN/m^3) and the distance from the model's top boundary to the ground surface (810 m). The horizontal displacement on the model's side boundaries is not allowed. Both horizontal and vertical displacements are constrained on the bottom boundary. The initial stresses were set based on in situ measurements from the study site. To ensure the efficiency and accuracy of computation, the roadways and surrounding rock masses were discretized into small zones with a side length of one meter and the remaining domain was set with larger sizes. The model has 1066921 zones in total, which is determined according to a mesh convergence study (see Section 3.3.4).

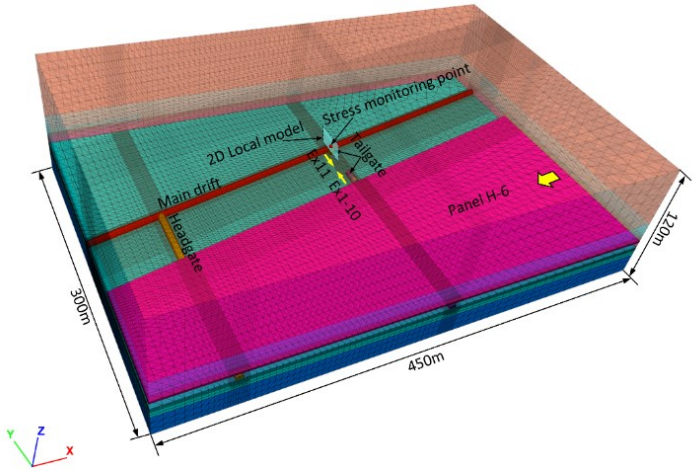

Figure 4.1 The layout of the numerical model.

4.3.2.2 Constitutive model and material properties

(a) Constitutive model of rock masses

The Hoek-Brown failure criterion is suitable for modeling the mechanical behaviour of jointed rock masses (Hoek and Brown, 1997), and it has been widely used in numerical modeling for the stress and deformation analysis in many Polish coal mines (e.g., Małkowski et al., 2017; Małkowski and Ostrowski, 2019). Besides, the brittle failure behaviour of rock masses (e.g., spalling and rock ejection) during strainbursts was studied in UDEC modeling rather than FLAC3D. Therefore, the mechanical behaviour

of rock masses in FLAC3D is governed by the Hoek-Brown failure criterion, which is expressed as follows (Hoek and Brown, 1997):

$$\sigma_1 = \sigma_3 + \sigma_{ci}\left(m_b \frac{\sigma_3}{\sigma_{ci}} + s\right)^a \tag{4.3}$$

where σ_1 and σ_3 are the major and minor principal stresses, respectively. It should be noted that the pore pressure of rocks was not considered in this study.

(b) Constitutive model and material properties of the gob

In coal mining, the overburden stress carried by the mined coal is then supported by surrounding rock masses and gob materials, resulting in the redistribution of mining-induced stresses. Hence, it is essential to choose a suitable constitutive model to simulate the mechanical behaviour of gob materials and reproduce the realistic state of mining-induced stresses.

The null and elastic models were often used to simulate gobs (Kose and Cebi, 1988; Cheng et al.,2010; Jiang et al., 2012; Basarir et al., 2015, 2019). However, the gob materials are not even simulated when using the null model, and the elastic model cannot capture the strain-hardening behaviour of compacted gob materials. Recently, some research work has verified that the double yield (DY) model can simulate the strain-stiffening behaviour of gob materials (Yavuz, 2004; Qiu et al., 2019; Wang et al., 2020). This study also adopted the DY model to simulate the gradual compaction of caved rock materials in the gob.

The DY model requires the cap pressure and material parameters of the gob. The Salamon model can calculate the cap pressure (Salamon, 1990). The gob material parameters can be obtained according to a detailed calibration procedure (see Figure 3.7). Following this procedure, the cap pressure and gob material parameters are finally determined. Figure 4.2 shows that simulated gob stress agrees well with the cap pressure calculated by the Salamon model. The used gob material parameters are listed in Table 4.2.

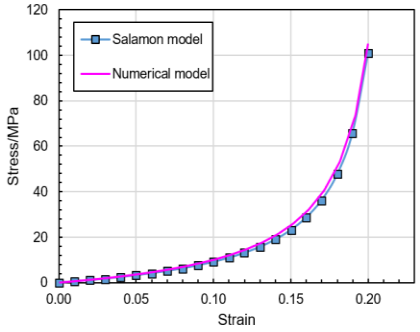

Figure 4.2 Stress-strain curves of the numerical model and Salamon model.

Table 4.2 Gob material parameters in numerical modeling

ρ (kg/m^3)	K (GPa)	G (GPa)	σ_t (MPa)	φ (°)	Dilation angle (°)
1700	10.0	1.5	0	5	8

Note: φ and σ_t are the internal friction angle and tensile strength, respectively.

4.3.2.3 Validation of the global model

(a) Validation of gob modeling

As shown in Figure 4.3, a stress monitoring line is arranged in the gob and coal seam 409/3 to plot the vertical stress distribution. The vertical stress in the gob gradually rises to 92.59 % of the in situ vertical stress at 196 m (0.22 times the average depth of coal seam 409/3) from the edge to the center. The vertical stress in the gob will be recovered to the in situ stress level at a distance of 0.2-0.3 times the mining depth according to field measurements (Wilson and Carr, 1982; Campoli et al., 1993). Hence, the simulated results agree with field measurements, verifying the effectiveness of the DY model and gob material parameters.

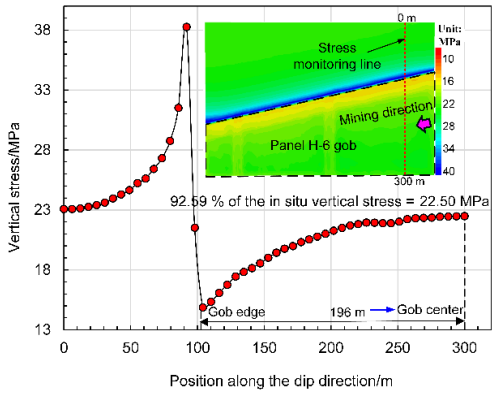

Figure 4.3 Vertical stress distribution in the gob and coal seam 409/3.

(b) Validation of the full model

In this research, the full model was verified by comparing the simulated deformation and failure depth of surrounding rock masses of the headgate with field measurement data (Małkowski et al., 2017; Jastrzębska Spółka Węglowa S.A. Group, 2018). As shown in Figures 4.4a and b, the simulated convergences of roof-to-floor (350 mm) and rib-to-rib (490 mm) are within the measured roadway deformation range (Wang et al., 2021b). Additionally, Figures 4.6c and d show that the simulated failure depths of the roof (7.02-7.93 m) and floor (2.64 m) match well with the monitored rock damage depths (8.2-8.5 m and 2.7 m). Thus, the material properties, constitutive relationships, and boundary conditions in the global model and the model geometry are validated.

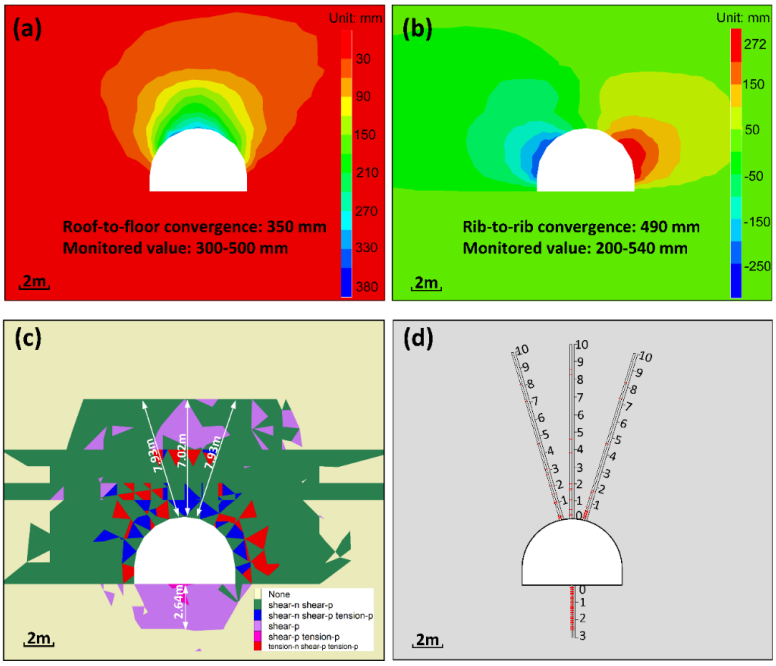

Figure 4.4 (a), (b), and (c) are simulated vertical and horizontal displacement contours and failure zone of the headgate, respectively; and (d) Monitored damage depth.

4.3.2.4 Mining- and excavation-induced stresses

The global model has calculation steps as follows: (1) initial stress equilibrium; (2) mine out Panel H-6 and conduct gob modeling; (3) tunnel H-4 headgate and a part of H-4 tailgate; and (4) tunnel H-4 tailgate 5 m/step with 11 excavation steps in total when it is near to H-10 main drift. Figure 4.3 shows the

excavation directions of the panel and roadways. The normal and shear stresses at the monitoring point (see Figure 4.1) of the main drift in the global model were recorded at different excavation steps. The extracted stresses are shown in Figure 4.5, whose orientations have been transferred for further usage in the 2D local model. The excavation of Panel H-6 and a significant part of gateroads remarkably influence the redistribution of the stresses in the main drift. After that, the stresses increase slowly with the driving of the tailgate. This is because the distance from the tunnelling face to the monitoring point is great, and the influence of the excavation-induced effect on stress concentration is smaller than that of the mining-induced effect. Finally, there is a sudden surge of stresses, and the direction of shear stress is also deflected when the last excavation step (Ex11) is finished. This is due to the tunnelling of the tailgate from the main drift. It should be noted that the plane strain assumption for the main drift in the 2D local model is no longer valid during the Ex11 excavation step. Therefore, the extracted stresses in this step were not considered for subsequent simulation in the local model.

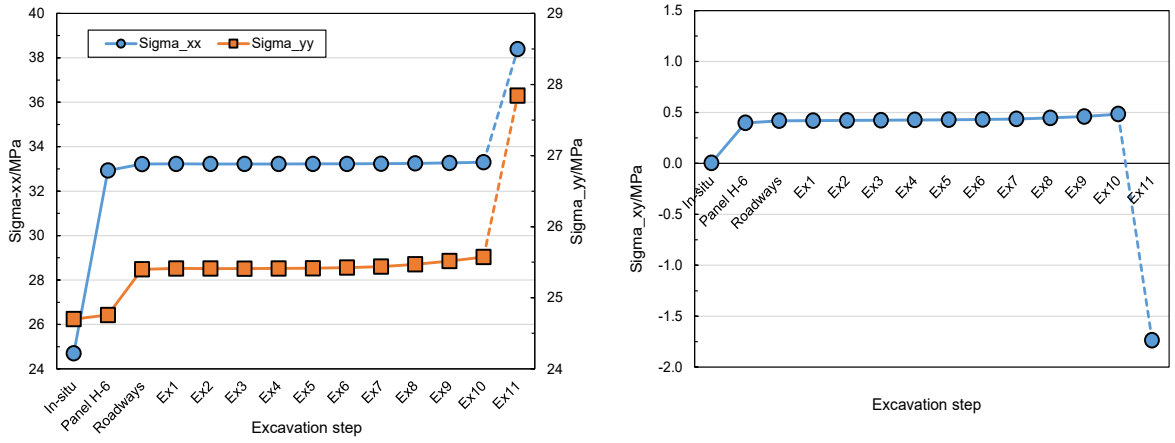

Figure 4.5 Extracted stresses at the location of the main drift during different excavation steps (Sigma_xx and Sigma_yy are normal stresses in horizontal and vertical directions, respectively. Sigma_xy is the shear stress).

4.3.3 Local model

4.3.3.1 Distinct element method

In the DEM, a rock mass is represented as an assembly of discrete blocks. Joints are viewed as interfaces between distinct bodies (e.g., the discontinuity is treated as a boundary condition). The contact

forces and displacements at the interfaces of a stressed assembly of blocks are found through a series of calculations that trace the movements of the blocks. Movements result from the propagation through the block system of disturbances caused by applied loads or body forces. This is a dynamic process in which the speed of propagation depends on the physical properties of the discrete system. The calculations performed in the DEM alternate between applying a force-displacement law at all contacts and Newton's second law at all blocks. The force-displacement law is used to find contact forces from known (and fixed) displacements. Newton's second law gives the motion of the blocks resulting from the known (and fixed) forces acting on them. If the blocks are deformable, motion is calculated at the grid points of the triangular finite-strain elements within the blocks. Then, applying the block material constitutive relations gives new stresses within the elements.

UDEC is a 2D numerical program that simulates the quasi-static or dynamic response to loading media containing multiple intersecting joint structures. It has been used in various engineering and scientific analyses, including stability analysis of jointed rock slopes or underground excavations; fluid or gas flow through jointed rock; stability of masonry structures, dams, and foundations; blasting, earthquakes, and microseismicity; among many more applications. UDEC can model large displacements, disintegrations, rotations, and general non-linear constitutive behaviours for both rock masses and joints in a straightforward manner. Also, it can simulate the dynamic responses of rock masses during seismic loading. Thus, UDEC is selected as a tool to build the local model of a deep coal roadway for studying rockburst damage mechanisms.

4.3.3.2 Model setup

The 2D local model was extracted from the global model's Y-Z plane along the tailgate axis, as shown in Figure 4.1. A widely used 2D DEM code UDEC was adopted to construct the local model for conducting a detailed analysis of the damage mechanism of strainbursts. Figure 4.6 shows the local model, which is built according to the lithology (see Figure 3.2) and the designed size of the main drift. A Trigon

approach (Gao and Stead, 2014) was applied to generate blocks, as this approach can reproduce the natural fracturing processes and dynamic mechanical behaviour of rock masses without adopting complicated constitutive models (Stavrou et al., 2019). In the Trigon approach, a rock mass comprises triangular blocks and contacts (Gao et al., 2015). The fracturing process can be exhibited by sliding or opening contacts. In the 2D local model, the average blocks' edge lengths in two coal seams and nearby clay shale between them are set to 0.3 m. The block size with a range of 0.2-0.5 m was sufficiently fine to model the failure behaviour of surrounding rock masses for a 2D model (Gao, 2013; Gao and Stead, 2014; Zang et al., 2020). The average blocks' edge lengths in the upper clay shale, sandy shale, and fine-grained sandstone were set to 0.5 m, 0.5 m, and 1 m, respectively. The average blocks' edge lengths in the floor are 0.3 m and 1 m. A graded increasing edge length of blocks can avoid the resulting loss of simulation accuracy and enhance the calculation's reliability. The horizontal displacement on the model's side boundaries is not allowed. Both horizontal and vertical displacements are constrained on the bottom boundary. The normal and shear stresses shown in Figure 4.5 were applied to model boundaries.

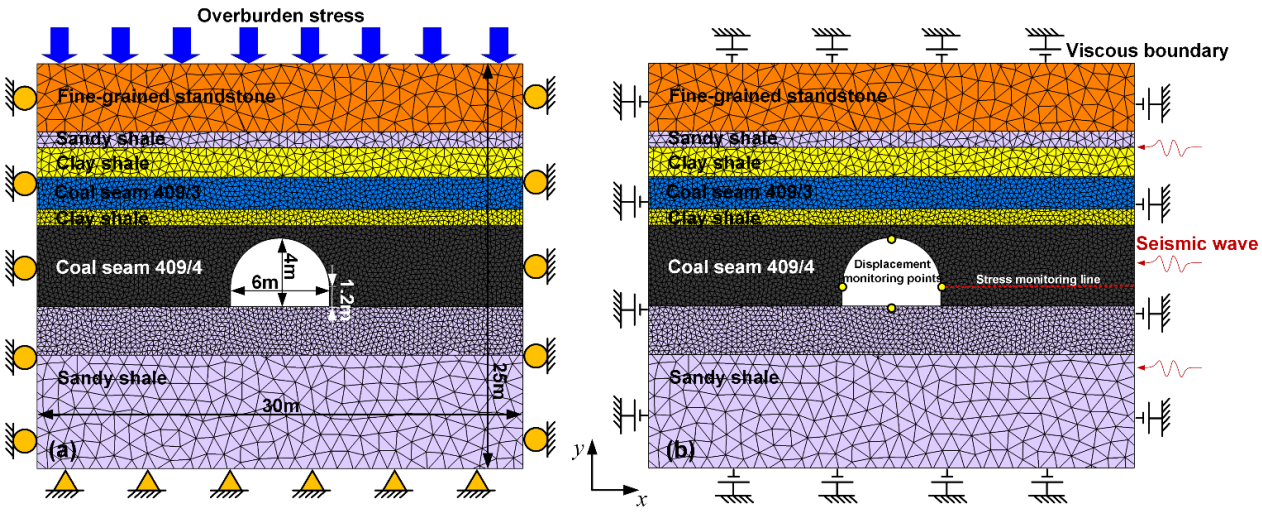

Figure 4.6 2D local model. (a) Static stage. (b) Dynamic stage.

4.3.3.3 Constitutive model and material parameters

The elastic constitutive model was chosen for blocks composed of finite-difference zones. The Coulomb slip model was used for contacts. A spring-rider simulates the behaviour of contacts, and the

model deformation occurs when the contact stress is smaller than the contact strength, which is governed by the elastic modulus of blocks and contact stiffness; contact failure occurs when the stress exceeds its shear or tensile strength, and then blocks will slide or separate with each other (Chen et al., 2016). The constitutive behaviour of contacts is shown in Figure 4.7.

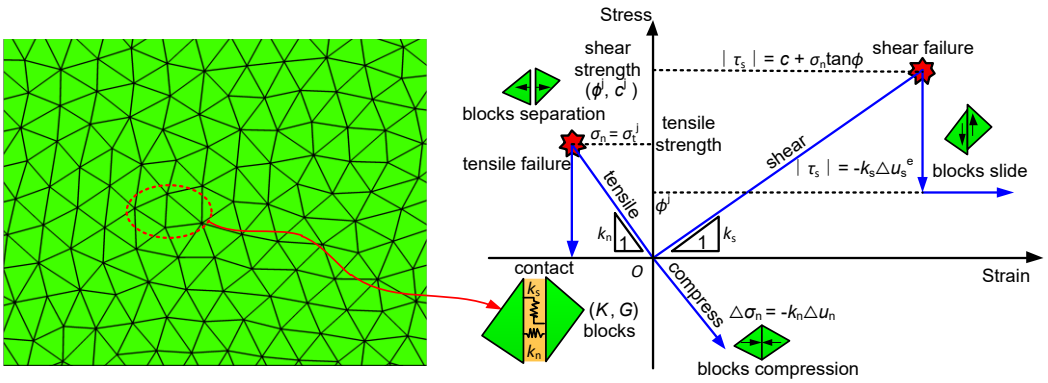

Figure 4.7 Constitutive behaviour of contacts (after Yang et al., 2017). (K and G are the bulk and shear moduli. c^j; φ^j, and σ_t^j are the cohesion force, internal friction angle, and tensile strength. K_n and K_s are the normal and shear stiffness. $\Delta\sigma_n$ and Δu_n are the effective normal stress increment and normal displacement increment. σ_n and τ_s are the normal and shear stresses. Δu_s^e is the elastic shear displacement increment.)

In the Trigon approach, the macro properties of rock masses (e.g., UCS and E_m) depend on the micro parameters (e.g., contact strength and stiffness) of blocks and contacts (Gao, 2013; Gao et al., 2015). In this research, these micro parameters were calibrated with rock mass properties (see Table 1) via a series of simulated UCS tests (Gao et al., 2015). To eliminate block size's effects on simulation accuracy, the UCS test model had a large scale (4 m×8 m) (Yang et al., 2017) and identical block size to the main drift model. However, there is a problem in that different block sizes were employed for the rock strata with the same lithology (e.g., block size of 0.3 m and 0.5 m for clay shale, and 0.3 m, 0.5 m and 1 m for sandy shale), which means that different material parameters might be used even for the same lithology. A sensitivity study has shown that block size's effect on simulated rock mass properties can be negligible (see Figure 5.5). Test loading was simulated by applying a velocity of 0.1 m/s to the top platen's surface (Figure 4.8). This loading rate is slow enough to avoid the dynamic responses of models (Hu et al., 2020; Gao et al., 2019b). The initial micro parameters were first assumed according to rock mass parameters.

Then, the modeling of UCS tests was conducted iteratively with adjusting micro parameters until simulated results were identical to targeted material properties. Gao (2013) and Tan and Konietzky (2014) gave a detailed calibration process of micro parameters. The simulated failure modes and stress-strain curves of rock mass samples are illustrated in Figure 4.8. The main failure modes of rock mass samples are tensile (axial splitting) and tensile-shear failure, which is consistent with typical failure modes of rock masses under no or low confining pressures (Diederichs, 2007). Table 4.3 shows the calibrated micro parameters of blocks and contacts. The errors between the targeted and simulated E_m and UCS are all less than 3% (Table 4.4), suggesting that the targeted values match well with calibrated rock mass parameters. Thus, the calibrated micro parameters in Table 4.3 could be used for further numerical analysis of the damage mechanism of strainbursts.

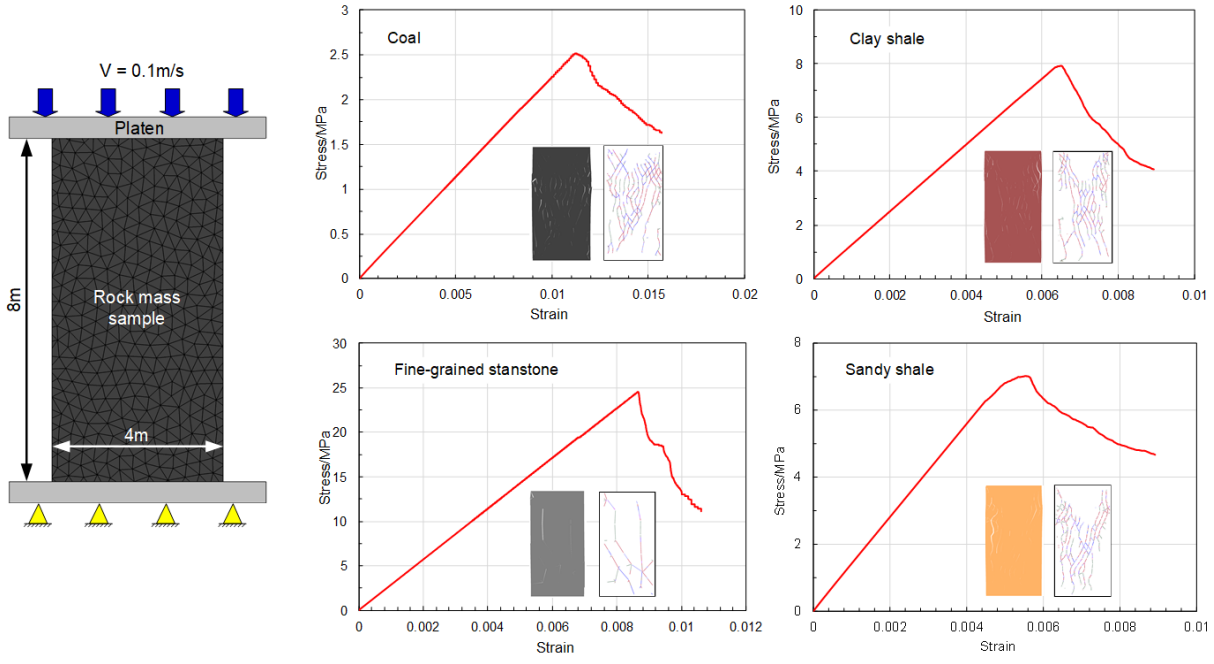

Figure 4.8 Simulated failure modes and stress-strain curves of rock mass samples.

Table 4.3 Calibrated micro parameters of blocks and contacts

Lithology	Block property			Contact property				
	ρ (kg/m^3)	K (GPa)	G (GPa)	k_n (GPa/m)	k_s (GPa/m)	c^j (MPa)	φ^j (°)	σ_t^j (MPa)
Coal	1300	0.16	0.09	18.7	7.5	0.99	33	0.25
Clay shale	2500	0.85	0.50	108.5	40.6	2.96	35	0.79
Fine-grained sandstone	2580	1.91	1.17	69.4	27.8	8.11	36	2.15
Sandy shale	2530	0.94	0.57	113.3	45.3	2.95	36	0.85

Table 4.4 Comparison between the targeted and simulated rock mass parameters

Lithology	E_m (GPa)			UCS (MPa)		
	Target	Simulation	Error (%)	Target	Simulation	Error (%)
Coal	0.23	0.226	0.09	2.50	2.51	0.48
Clay shale	1.26	1.234	-1.82	7.93	7.91	-0.29
Fine-grained sandstone	2.92	2.852	-2.48	24.53	24.52	-0.05
Sandy shale	1.42	1.39	-2.11	7.11	7.02	-1.27

4.3.3.4 Model assumptions

The built numerical model has following assumptions:

- Rock mass properties are isotropic and uniform.
- The influence of water and temperature on rock mass properties can be ignored.
- Rock mass damage can be represented by the failure of contacts. Blocks are elastic based on this assumption.
- Plane strain condition is valid.
- The unit weitght of the overburden is 27 kN/m^3.
- Seimic wave is a P wave.

4.3.3.5 Simulation schemes

The modeling of the damage mechanism of strainbursts was performed using three stages.

Stage I (static stage): The in situ stress field was applied to the model, and the geostatic equilibrium was achieved. Then, the main drift was excavated by deleting the blocks. Finally, adequate calculation steps were run to ensure the surrounding rock stresses' gradual and slow release (Gao et al., 2015).

Stage II (static stage): The varied normal and shear stresses extracted from the 3D global model (Figure 4.8) were applied to local model boundaries. Adequate calculation steps were run to stabilize the model.

Stage III (dynamic stage): The dynamic mode was activated. Studies have shown that the sudden release of elastic energy stored in rock masses is often caused by dynamic loads, which can result in severe rockburst accidents (Ortlepp and Stacey, 1994; Lu et al., 2015; Masny et al., 2017; Kong et al., 2019; Ji et al., 2021). Zhu et al. (2010) reported that the disturbance of the external dynamic load is one of the key

factors to trigger rockbursts. Kaiser and Cai (2012) proposed that strainbursts can be mining-induced due to static stress changes caused by nearby mining, or they can be dynamically induced due to a dynamic stress increase caused by a remote seismic event. Diederichs (2018) stated that many rockburst damages in mining environments were based on the primary mechanism of a remote seismic event triggered by large-scale mining activities. The primary rockburst source is the roadway surrounding rock mass in geotechnical engineering projects. The source mechanism of rockbursts associated with seismic waves and high static stress is currently the most common in Polish underground coal mines (Mutke et al., 2015). Therefore, it is necessary and meaningful to study the effects of dynamic loads on strainburst damage mechanisms. The dynamic load is exerted on mining works in a fashion of vibration waves or stress waves which are resulted from rock fracturing, fault-slip, blasting, mechanical vibration, etc. A seismic wave caused by fault-slip was assumed to be the dynamic load source because post-event observations show the activation of the Jastrzębie fault and Eastern fault. Mutke et al. (2015) and Kong et al. (2019) reported that the rockburst potential of roadways is positively correlated to the peak particle velocity (PPV) of vibration waves and buried depths, as shown in Table 4.5. The statistical analysis of rockbursts in the Upper Silesian Coal Basin (USCB) suggests that PPVs are mainly within 0.05-1.0 m/s (Figure 4.9a, b). Additionally, rockbursts are usually related to seismic waves characterized by low frequencies from 10 Hz to 30 Hz (Figure 4.9c). Therefore, seven PPVs of 0.2 m/s, 0.4 m/s, 0.6 m/s, 0.8 m/s, 1.0 m/s, 1.2 m/s and 1.4 m/s are adopted to simulate different dynamic loads ($\sigma_n=2(\rho C_p)v_n$), Itasca, 2020).

Table 4.5 Evaluation of the influence of seismicity on rockburst potential (Mutke et al., 2015; Kong et al., 2019)

Rockburst risk	PPV (m/s)	Depth of roadway(D) (m)
Lack of hazard	PPV ≤ 0.05	D ≤ 0.05
Minor	0.05 < PPV ≤ 0.2	300 < D ≤ 500
Moderate	0.2 < PPV ≤ 0.4	500 < D ≤ 700
Major	PPV＞0.4	D＞700

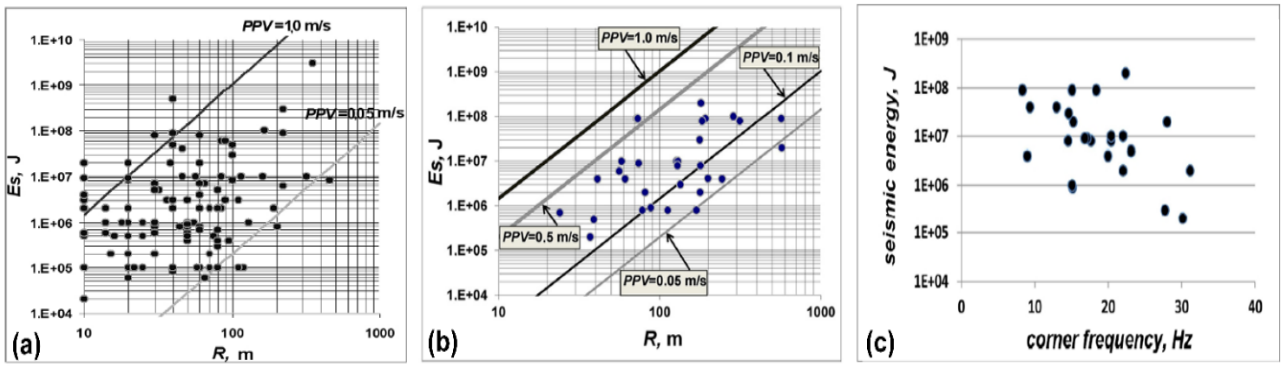

Figure 4.9 (a) 120 seismic events associated with rockbursts in USCB (1988–2006). (b) 32 seismic events associated with rockbursts in Polish coal mines (2003–2012). (c) The relationship between frequencies and the seismic energy of rockbursts (seismic events which caused significant roadway failure) in USCB during 1998-2006 (R is the distance from damaged working to seismic sources, and E_s is the seismic energy). (from Mutke, 2008; Mutke et al., 2016).

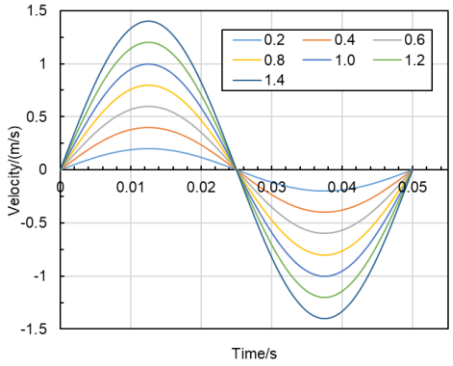

Figure 4.10 Waveforms of different seismic waves.

The frequency is assumed to be 20 Hz, and the time is 120 ms (a vibration period plus a quiet time of 70 ms). The seismic waveform is simplified to be a sine wave since any complex stress wave can be obtained by the Fourier transform of simple sine waves (Liu, 2017). The waveforms with different PPVs are shown in Figure 4.10. The dynamic calculation used the viscous boundary to avoid propagating waves' reflection and allow the necessary energy radiation. A recommended Rayleigh damping of 0.5 % was used (Itasca, 2020). This value is suitable for dynamic analyses that involve large block deformation or great joint displacement. Then, a series of seismic waves were applied to the model's right boundary to investigate the dynamic responses of the roadway. Ideally, the dynamic mechanical properties of rock masses and joints and related constitutive relationships should be employed (Gao et al., 2019b). Considering that those data are unavailable, and the research's objective is to show the effectiveness and

advance of the global-local modeling approach in studying strainburst damage mechanisms, the properties of rock masses and joints and constitutive relationships were therefore not changed. The simulation procedures are shown in Figure 4.11.

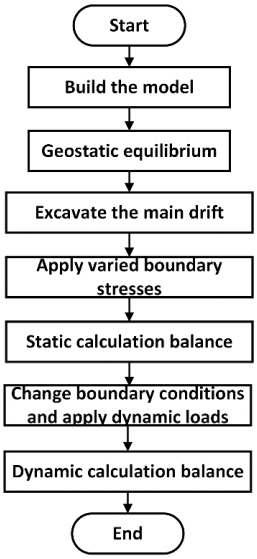

Figure 4.11 Flow chart of the simulation process

4.4 Results and discussion

4.4.1 Static stage

4.4.1.1 Displacement analysis

The deformation of surrounding rock masses of the main drift during different excavation steps is shown in Figures 4.12 and 4.13. Severe roadway deformation is observed when the main drift is not supported. The primary deformation forms of the main drift are roof subsidence and the shrinkage of two sidewalls. After excavating the main drift, the roof subsidence and deformation of two sidewalls are 510.5 mm, 361 mm, and 347.3 mm, respectively. The minimum deformation (102.9 mm) appears in the floor due to the relatively high strength of the floor stratum. The extraction of Panel H-6 creates a superposition of the mining-induced stress and initial surrounding rock stress induced by excavation. Thus, the main drift suffers severer deformation during this stage. The displacement of the roof, two sidewalls and floor are 610 mm, 571.2 mm, 350.7 mm, and 104.6 mm, respectively, and the growth rates are 19.49 %, 58.22 %,

1.37 %, and 1.65 %, respectively. A considerable increment of roof subsidence and deformation of the left sidewall is observed. The difference of deformation between two sidewalls is great (220.5 mm), indicating an asymmetric convergence phenomenon. When a part of the gateways was excavated, the deformation of the roof, two sidewalls and floor were 674.7 mm, 709.9 mm, 359.7 mm, and 104.6 mm, respectively, and the growth rates were 10.61 %, 24.28 %, 2.57 %, and 0 %, respectively, indicating a moderate increase of deformations. This is because the main drift is very far from the tailgate's tunnelling face and the excavation-induced effects are much smaller than mining. After the tunnelling of the tailgate was finished, the final deformation of the roof, two sidewalls and floor were 683.9 mm, 709.9 mm, 382.2 mm, and 104.6 mm, respectively.

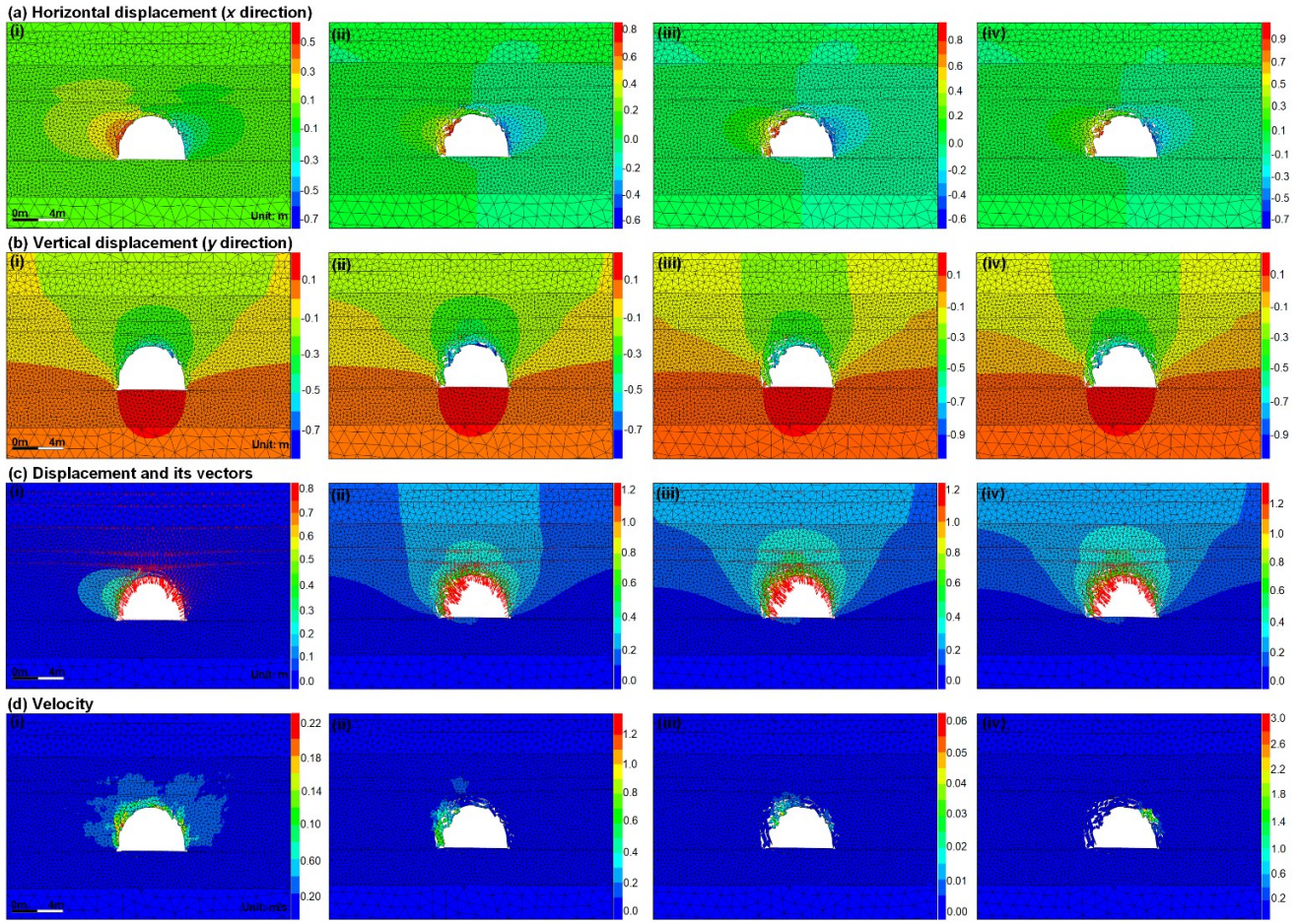

Figure 4.12 Distribution of displacement and velocity of the main drift during four excavation steps. (i), (ii), (iii), and (iv) are four excavation steps: excavation of the main drift, Panel H-6, a part of roadways and 10th excavation step (Ex10) of the tailgate.

Figure 4.13 shows that the roadway deformation gradually increases with different excavation steps, especially the surface displacements in the roof and sidewalls. This is due to the growth of surrounding rock stress resulting from the superposition of mining- or excavation-induced stress of the panel and roadways. Panel H-6's extraction has the most significant influence on the roadway deformation, suggesting that the deformation values are related to the magnitude of mining- or excavation-induced stress. Besides, the deformation becomes more uneven (also see displacement vector maps in Figure 4.12). The roof and left sidewall suffer more deformations than the right sidewall and floor. The nearby excavations result in the least influence on floor deformation. The surrounding rock masses of the main drift will lose their stability if no control measures are adopted in time.

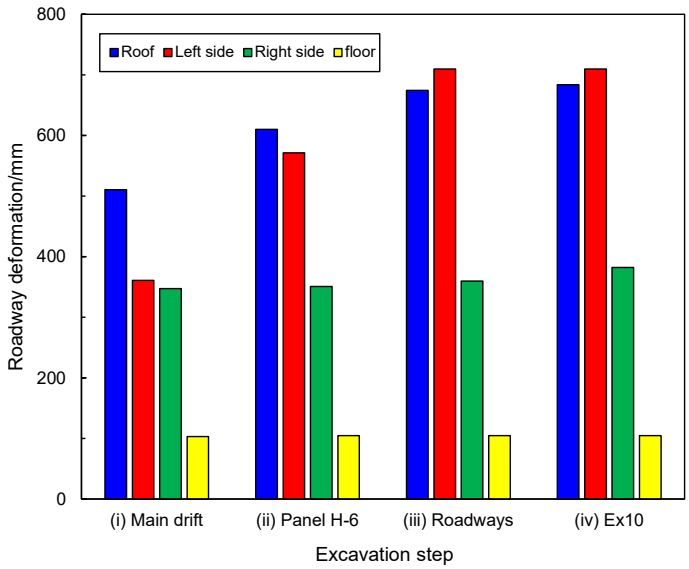

Figure 4.13 Comparison of the deformation at different positions of the main drift during four excavation steps.

4.4.1.2 Fracture evolution and failure process

Studies have shown that many rock engineering accidents, including rockbursts, are due to the weakening of rock mass strengths resulting from the initiation and development of internal fractures (Esterhuizen et al., 2011; Chen et al., 2016; Gao et al. 2019a, b; Wu et al., 2019; Zang et al., 2020). The fracture evolution and failure process were analyzed to study roadway damage surrounding rock masses during static and dynamic stages. A function was developed using FISH language programming in UDEC

to record the length and number of failed contacts (including tensile and shear failure) in the local model. A damage variable was then defined in the self-developed FISH function according to the ratio of failed contacts' length to the total contact length in the local model (Gao et al. 2015):

$$D_c = \frac{L_t+L_s}{L_c}, D_t = \frac{L_t}{L_c}, D_s = \frac{L_s}{L_c} \tag{4.4}$$

D_c, D_t, and D_s are the total, tensile, and shear damage levels, respectively. L_c, L_t, and L_s are the total contact length and the length of failed contacts in tensile and shear failure, respectively.

Figure 4.14 illustrates the cracks' development in surrounding rock masses during four excavation stages. Figure 4.15 shows the variation in the damage levels of the main drift. The comparison of different damage levels is shown in Figure 4.16. As shown in Figure 4.14a, tensile cracks are mainly observed in the opening periphery, owing to the release of radial stress and the concentration of tangential stress after excavation (Yu et al., 2015). The depth of tensile cracks is 0.3-1.3 m. The shear cracks are well distributed and extend deeper into rock masses, indicating that rock blocks' slipping gradually develops from the roadway surface to depth. The depth of shear cracks is 0.8-1.8 m. Both tensile and shear damage undergo a rapid increase. Figure 4.16 shows that the shear damage (1.70 %) is the dominant failure mode, accounting for 80.95 % of the total damage, while the tensile damage (0.40 %) accounts for 19.05 %. The ratio of shear to tensile damage is 4.25. After the extraction of Panel H-6, the extent of shear and tensile cracks increased significantly while the damage depth grew slightly. The shear and tensile damage levels are 1.96 % and 0.55 %, with growth rates of 15.29% and 37.5%, respectively. The ratio of shear to tensile damage is 3.56, suggesting that the tensile failure gradually plays a key role in the stability of surrounding rock masses. The depth of shear cracks is 1.0-1.9 m, increased by 0.1-0.2 m, and the depth of tensile cracks is 0.4-1.5 m, increased by 0.1-0.2 m. The extent and depth of tensile and shear cracks grow little in the next stage. The evolution of shear and tensile damage gradually becomes steady. The ratio of shear (2.0 %) to tensile damage (0.6 %) is decreased to 3.33. When the tunnelling of the tailgate is finished, the extent

of shear and tensile cracks further increases, and the failure depth reaches the maximum values (1.4-2.8 m for shear cracks and 0.7-2.0 m for tensile cracks). The ratio of shear (2.12 %) to tensile damage (0.62 %) is 3.41, indicating a slightly decreased ratio of tensile damage.

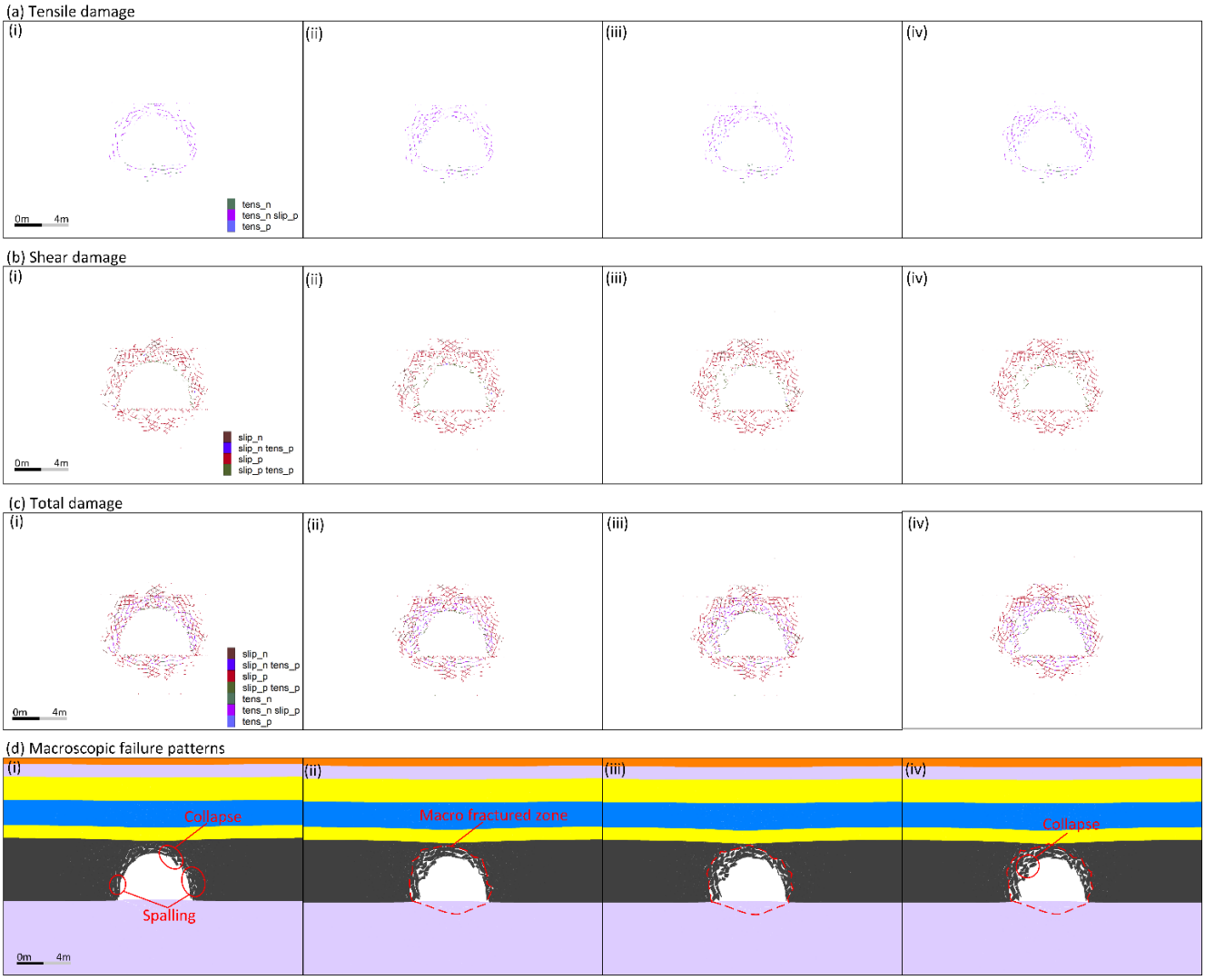

Figure 4.14 Evolution of cracks and macroscopic failure patterns of the main drift during four excavation steps. (i), (ii), (iii), and (iv) are four excavation steps: excavation of the main drift, Panel H-6, a part of roadways, and the 10th excavation step of the tailgate (Contact state flag: slip_n—shear failure now, slip_p—shear failure in the past, tens_n—tensile failure now, and tens_p—tensile failure in the past).

As shown in Figure 4.14d, macroscopic fractures are observed around the periphery of the main drift after the initiation, growth, and expansion of micro cracks. The main failure mechanisms are the collapse of the roof and spalling of sidewalls. When the extraction of Panel H-6 influenced the main drift, more rock blocks were detached from failed rock masses, and a huge fractured zone was produced. During the

last two stages, macro fractures continue to grow and expand due to the further development of micro cracks in depth. However, the failure mechanism changes from the roof collapse and sidewall spalling to the continuous fall of detached rock blocks. Therefore, the rock and coal masses beyond the fractured zone are still intact, capable of continuous stress concentration and energy accumulation for the subsequent occurrence of strainbursts.

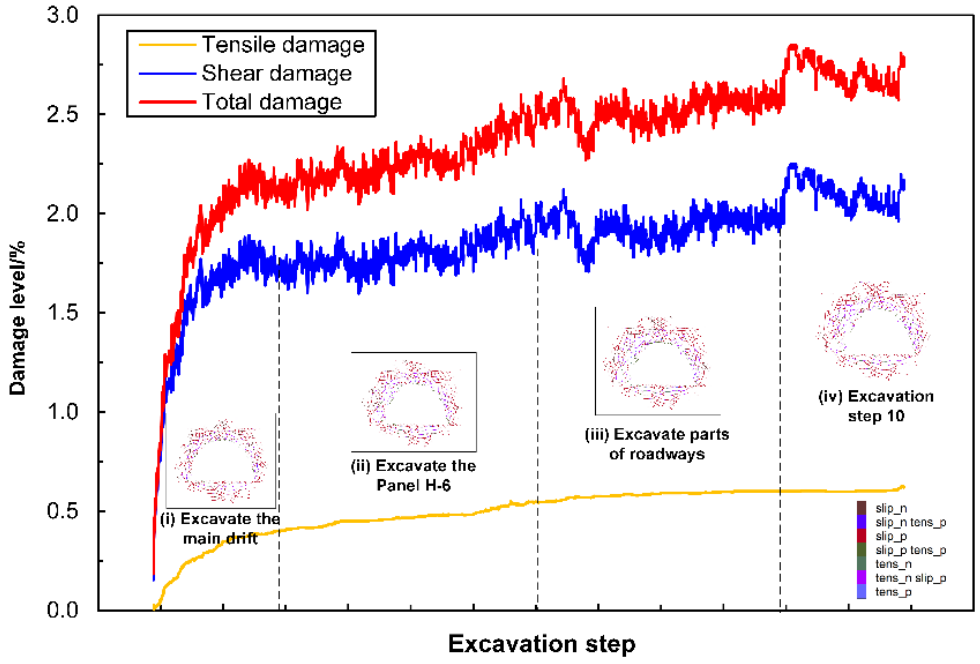

Figure 4.15 Simulated damage evolution of the main drift during four excavation steps.

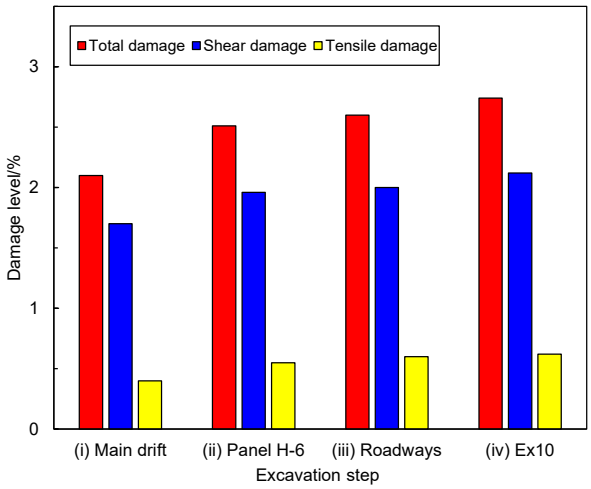

Figure 4.16 Comparison of the damage levels of the main drift during four excavation steps.

4.4.1.3 Stress analysis

The concentrated stress significantly influences rockburst occurrence and damage in underground openings (Li et al., 2018). Thus, the maximum principal stress surrounding the main drift induced by excavation and mining was analyzed in this study. Figure 4.17 shows the contour of maximum principal stresses during different excavation steps. After excavation, there is an apparent stress relaxation zone (red and orange areas in Figure 4.17a) around the main drift. This is because surrounding rock masses fail due to the release of radial stress and the concentration of tangential stress. The stress concentration (green areas) mainly occurs around the stress relaxation zone, and the significant stress concentration (blue areas) is observed in two bottom corners and the roof of the main drift. When Panel H-6 was extracted, the range of the stress relaxation zone is enlarged as more rock blocks were detached from failed rock masses owing to the influence of mining-induced stress. Compared with the previous stage, the range of stress concentration zone (green areas) is also enlarged because of the superposition of mining- and excavation-induced stresses. After excavating a part of roadways, stress relaxation and concentration zone are further expanded. When the tunnelling of the tailgate was finished, the distribution of maximum principal stresses is similar to that in the former stage, and the range of the stress relaxation zone increased a little due to minor excavation-induced effects.

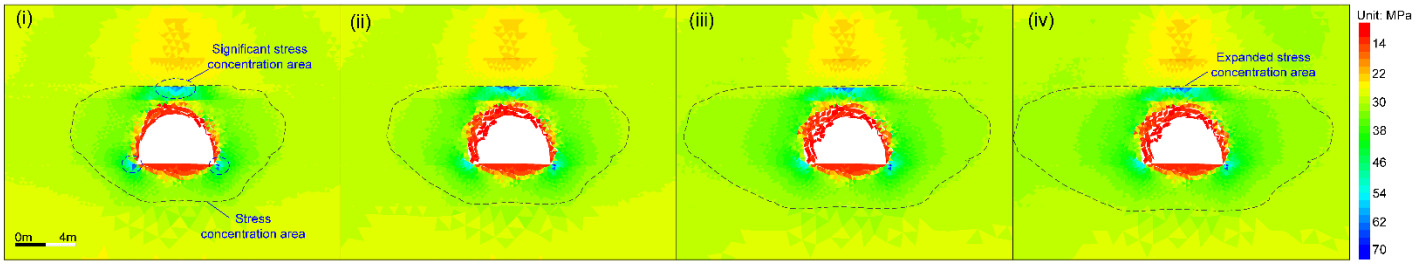

Figure 4.17 Distribution of the maximum principal stress surrounding the main drift during four excavation steps. (i), (ii), (iii), and (iv) are four excavation steps: excavation of the main drift, Panel H-6, a part of roadways, and the 10th excavation step of the tailgate.

To further study the evolution law of mining- and excavation-induced stress concentration around the main drift, a monitoring line was arranged on main drift's right sidewall to record maximum principal

stresses' variation (Figure 4.6). The simulation results are illustrated in Figure 4.18. Stress relaxation and increased areas (Figure 4.18a) are produced due to the failure of rock masses and the superposition of excavation- and mining-induced stresses, respectively. The average values of maximum principal stresses in the stress-increased area during the four stages are 30.48 MPa, 30.64 MPa, 31.68 MPa, and 31.88 MPa (Figure 4.18b), respectively, showing the gradual increase of surrounding rock stresses in deep zones. The peak stresses during the four stages are 37.46 MPa, 37.95 MPa, 39.22 MPa and 39.56 MPa, respectively, and the stress concentration coefficients (peak stress over in situ vertical stress) are 1.54, 1.56, 1.61 and 1.63, respectively. The growth rates are 1.30 %, 4.55 %, and 5.84 %, respectively, compared with that in the first stage, suggesting an increasing peak stress trend (Figure 4.18b). The significant increase of surrounding rock stresses will result in more accumulated strain energy in two sidewalls, providing a necessary condition for the strainburst occurrence in the dynamic stage.

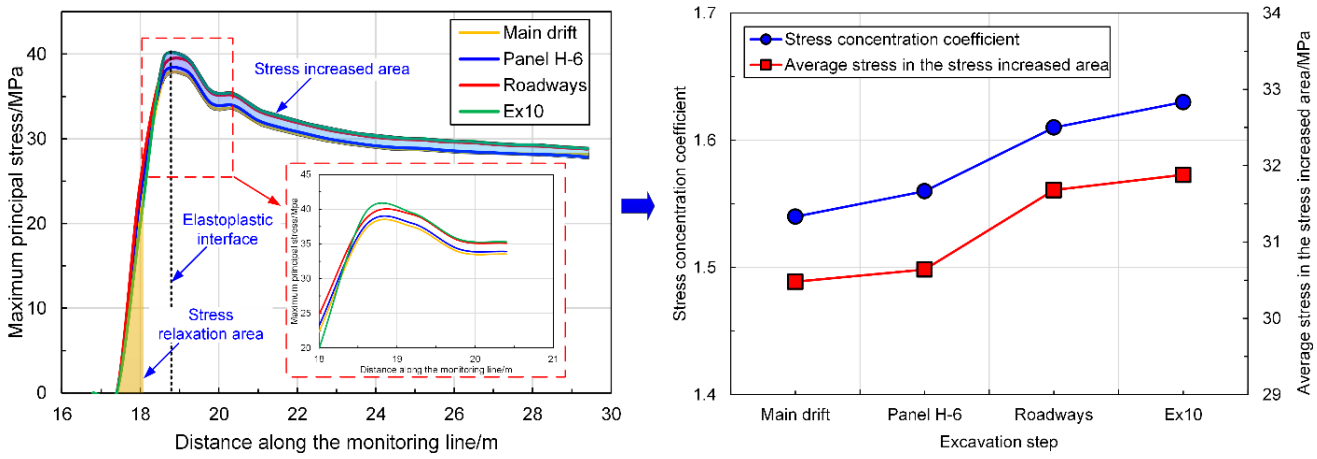

(a) (b)

Figure 4.18 (a) Variation of surrounding rock stresses during four excavation steps. (b) Variation of stress concentration coefficient and the average stress in the stress-increased area during four excavation steps.

4.4.2 Dynamic stage

4.4.2.1 Occurrence process of a strainburst

The configuration with a PPV of 1.4 m/s was used as an example to demonstrate the occurrence procedure of a strainburst caused by a seismic wave. The simulated velocity vectors of rock blocks during

the strainburst are shown in Figure 4.19. When the time was 20 ms, the rock masses in main drift's right sidewall were initially influenced by the incident seismic wave, while the main drift has not been affected by dynamic stresses. When the time was 40 ms, the surrounding rock masses in the right sidewall and roof were suddenly influenced by dynamic stresses and ejected. The maximum velocity of ejected rock blocks is around 20-28 m/s. When the time was 60 ms, the rock masses in all directions were affected by the seismic wave, and some rock blocks were ejected from the floor with a velocity of 20-30 m/s. From 60 to 80 ms, more rock blocks were ejected from the roof, and a few were initially ejected from the left sidewall. When the time was 80 ms, the range of the velocity of new ejected rock blocks is 30-39 m/s, which is greater than before. It can also be observed that the rocks in the floor, having a velocity of 15-20 m/s, were moving into the opening. When the time was 100 and 120 ms, more rock blocks were ejected from the roof and sidewalls, and the maximum velocity is 35-45 m/s. The red arrows in Figure 4.21f present the movement direction of most rock blocks: from the right top sidewall, roof, left sidewall, and floor to the roadway center.

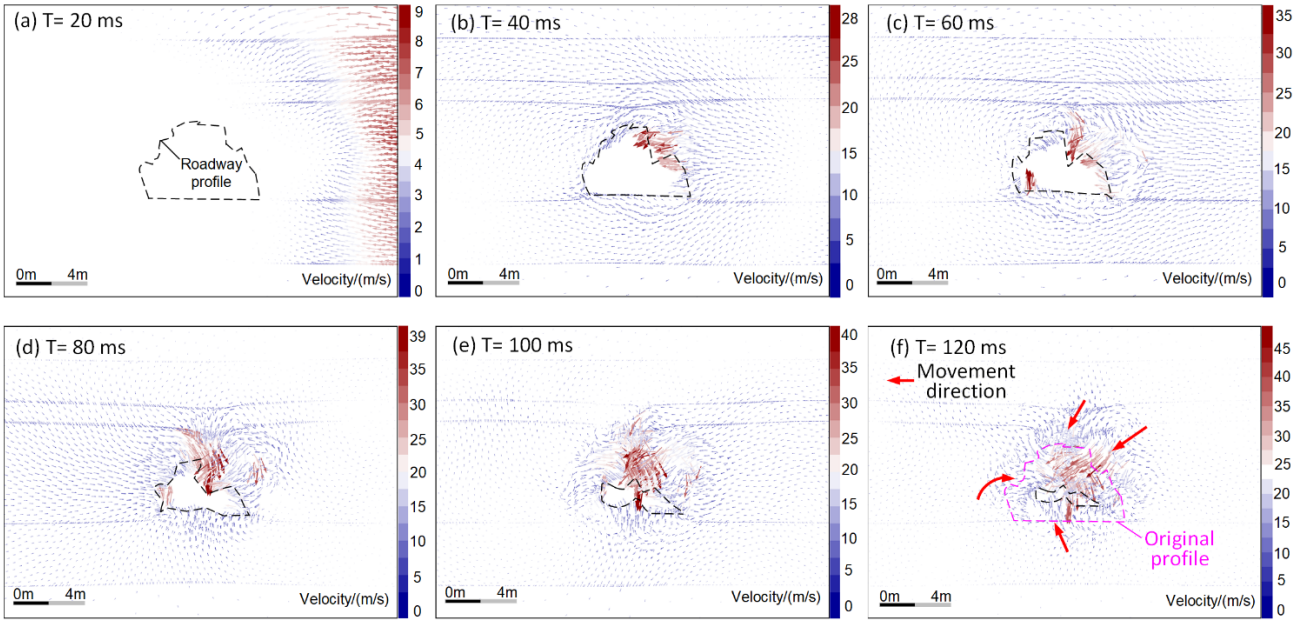

Figure 4.19 Simulated velocity vectors of rock blocks during the occurrence process of a strainburst.

It might be argued that the simulated velocity of some ejected rocks is higher than that (typically lower than 10 m/s) observed in the field. This can be partly attributed to the fact that no supporting systems were considered in the current simulation. Thus, the deformation energy of rock masses can be sufficiently released and transferred to the kinetic energy of ejected rocks. The ejection velocity is also positively correlated to PPVs. The higher the PPV is, the greater the ejection velocity is (Qin and Mao, 2008). Besides, considering that the seismic data are unavailable, and the research's objective is to show the effectiveness and advance of the global-local modeling approach in studying the damage mechanism of strainbursts, the seismic loading in this study is thus a simplified situation. The seismic waves were directly applied to the model's right boundary. The distance from the seismic source to the excavation boundary is very small compared to the cases on sites. Hence, the attenuation of seismic waves in numerical modeling is weaker than in the field. Another cause is no energy dissipation when two contact faces are splitted.

Further studies (e.g., setting residual values of contacts or selecting more representative constitutive models) will be done to address this problem. However, it should be noted that the average velocity of ejected rocks is 16.6 m/s after conducting a statistical analysis. In addition, some researchers have confirmed that the ejection velocity with an order of 10 m/s or greater is not unusual (Ortlepp and Stacey, 1994; McGarr, 1997).

In summary, the rock blocks with a high velocity during a strainburst might be ejected from all directions oriented to the roadway profile, and even the seismic wave originates from a specific direction. In addition, the rapid bulking or heaving of the floor can occur, which needs to be paid much attention to since the treatment of the floor is usually the most overlooked part in rockburst supporting.

Figure 4.20 shows the evolution of cracks and macroscopic failure patterns during the strainburst. Figure 4.21 shows the variation of damage levels with the dynamic calculation time. When the time was

20 ms, there was no noticeable increase in tensile and shear damage than in the static stage. From 20 ms to 40 ms, the tensile damage suffered rapid growth while the shear damage decreased slightly because some shear cracks disappeared due to the detachment of rock blocks. When the time was 40 ms, tensile cracks in the floor continued to initiate, propagate, and develop and gradually formed more macroscopic fractures. Besides, tensile and shear damage also developed into deep areas within the roof and floor. Some ejected rock blocks from the right sidewall were observed. After 40 ms, both tensile and shear damage increased rapidly. From 40 ms to 60 ms, the tensile damage increased from 1.17 % to 1.49 %, with a growth rate of 27.35 %. The shear damage increased from 1.71 % to 3.14 %, with a growth rate of 83.62 %. When the time was 60 ms, more rock blocks were ejected from the right sidewall, macroscopic fractures began to occur in deep areas, and the floor was more fractured than before. After that, the tensile damage continued to increase almost linearly, while the shear damage also grew significantly, although it might suffer a few fluctuations. When the time was 80 ms, new macroscopic fractures were observed in the roof with the propagation and development of micro cracks and some rock blocks were ejected from the left sidewall. When the time was 120 ms, tensile and shear damage levels were 2.57 % and 4.68 %, increased by 119.66 % and 173.68 %, respectively, compared with that in 40 ms. As shown in Figure 4.22d (vi), the damage mechanism for this case is the combination of three types of damage: rock ejection, rock bulking, and rockfall, which is consistent with the complexity of damage mechanisms of many violent rockburst events (Cai, 2013; Manouchehrian and Cai, 2018; Lu et al., 2019; Vazaios et al., 2019). Hence, rock-supporting systems must possess multiple functions, such as dissipating kinetic energy and retaining ejected rock fragments to resist and mitigate different rockburst damage.

Additionally, it is interesting to note that the range of the macroscopic failure zone is the same as that of the tensile damage (see Figure 4.20a and d). Thus, the initiation, propagation, and development of tensile cracks play a key role in controlling the macroscopic failure of surrounding rock masses, although

the shear crack always accounts for the main proportion of damage levels during the entire occurrence process of the strainburst. This finding agrees that the wave impedance of rock masses and air differ greatly in that most stress waves are reflected at the surface, resulting in the tensile failure of surrounding rock masses (Wu et al., 2019).

It is also interesting that many shear cracks (see purple cracks in Figure 4.20) accumulate within clay shale. This can be attributed to the great difference in wave impedance between coal seams (409/3 and 409/4) and clay shale. The greater the contrast in wave impedance, the smaller the seismic energy transmitted through the rock layer interface. Besides, because of the constraint of two coal seams, the "trapped" seismic energy in clay shale is difficult to be transferred to the kinetic energy of ejected rocks, as is observed near the excavation boundary. Thus, the shear sliding of contacts consumes the seismic energy in clay shale.

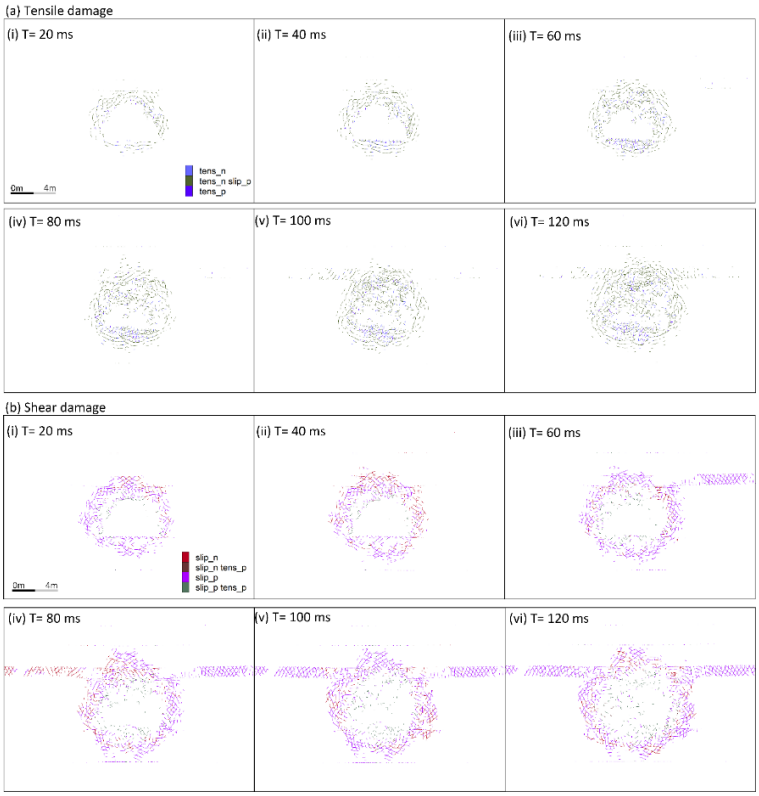

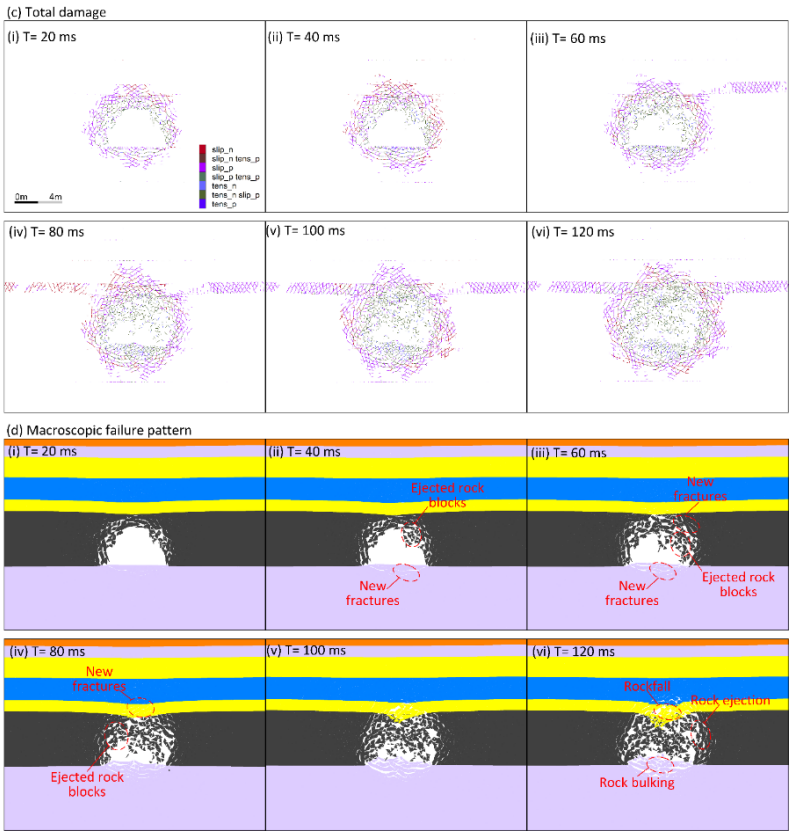

Figure 4.20 Evolution of cracks and macroscopic failure patterns of the main drift during the occurrence process of a strainburst.

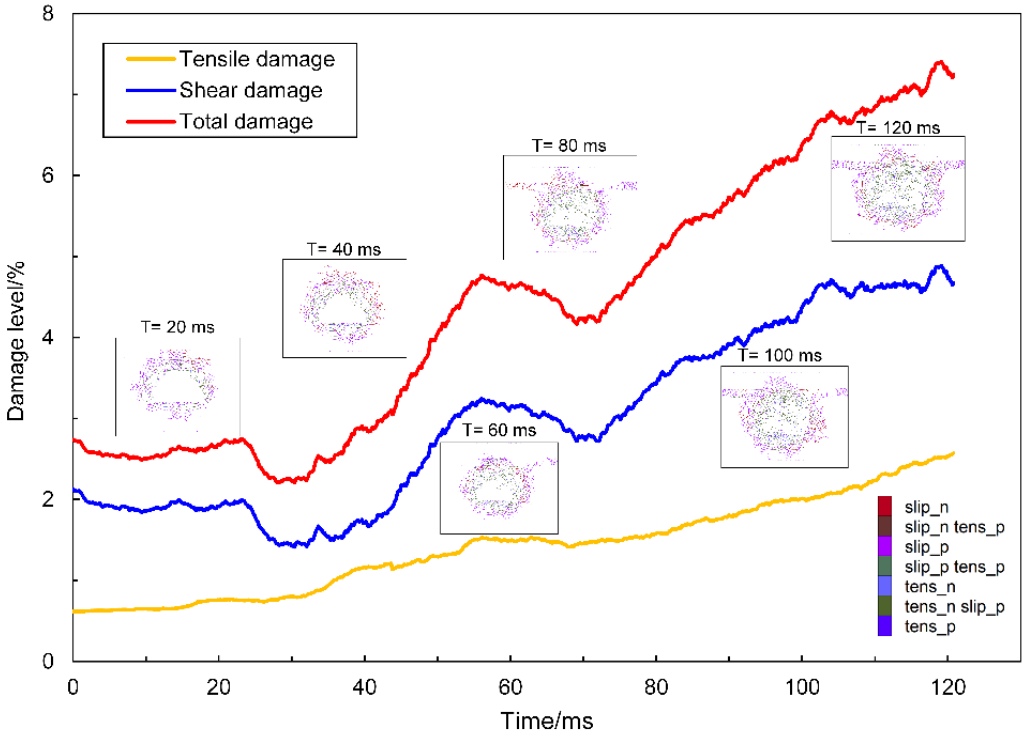

Figure 4.21 Simulated damage evolution of the main drift during the occurrence process of a strainburst.

The comparison between the simulated failure patterns and in situ observations is shown in Figure 4.22. It can be seen that the rockfall and floor heaving induced by the strainburst can be realistically captured by the local model, suggesting the rationality and capability of the method used in modeling strainburst damage. However, it should also be noted that much more rocks are ejected from the simulation roof and sidewalls than in the field. This is because no support (steel arch and mesh) was modelled at this stage. Thus, the stress can be fully released from the roof and ribs and ejected any support elements that do not hold rock materials.

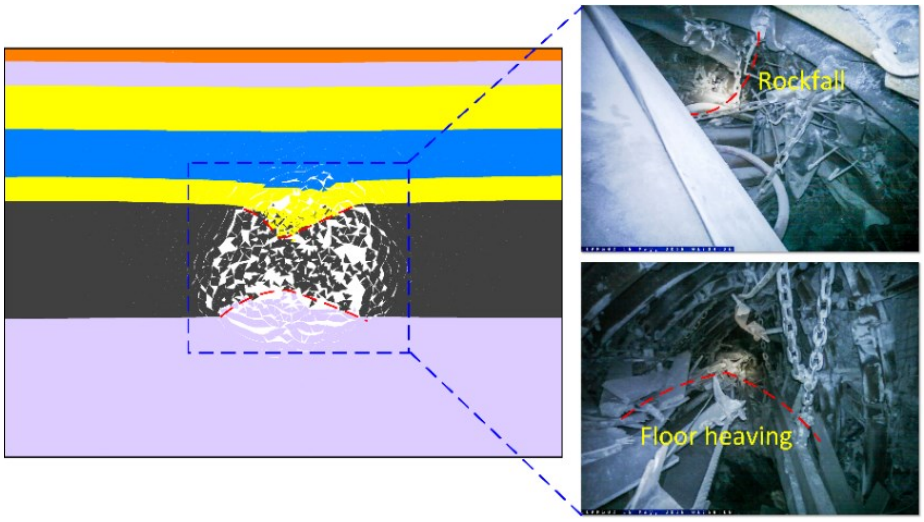

Figure 4.22 Simulated failure patterns of a strainburst and field observations of rockburst damage (after Jastrzębska Spółka Węglowa S.A. Group, 2019).

Figure 4.23 shows the contour of maximum principal stresses during the strainburst. The significant stress concentration (blue areas) mainly appeared in the two bottom corners and the roof of the main drift when the time was 20 ms. There were no significant stress distribution changes compared to the static stage. This is because most surrounding rock masses were not affected by dynamic stresses during the early stage of the strainburst process. When the time was 40 ms, the significant stress concentration zone (blue areas) in the roof and bottom corners was enlarged because clay shale and sandy shale have relatively high strength, and a part of the strata did not fail in this stage which is prone to stress concentration. After that, significant stress concentration was no longer observed in the roof with the further development of

cracks and fractures, while it gradually developed in deep floors surrounding fractured zones. When the time was 120 ms, a large stress relaxation zone (orange and red areas) was produced owing to the ejection, bulking, and fracturing of rock masses. The significant stress concentration mainly occurred on the floor and has a "u" shape. Therefore, it can be concluded that the stress concentration gradually transfers from the roof and bottom corners to the floor. As shown in Figure 4.23, the macroscopic fracturing mainly happened in the floor's shallow part. Thus, the rock masses in deep areas of the floor were competent, which provided an environment for further stress concentration. Hence, it can be anticipated that the rapid rock bulking in the floor will continue to develop if the dynamic time is sufficient or the floor is not hard. This anticipation agrees with many facts that significant floor heaving (up to 2 m) is often observed in rockburst events induced by seismic waves (Mutke et al., 2009; Stacey and Rojas, 2013; Prusek and Masny, 2015).

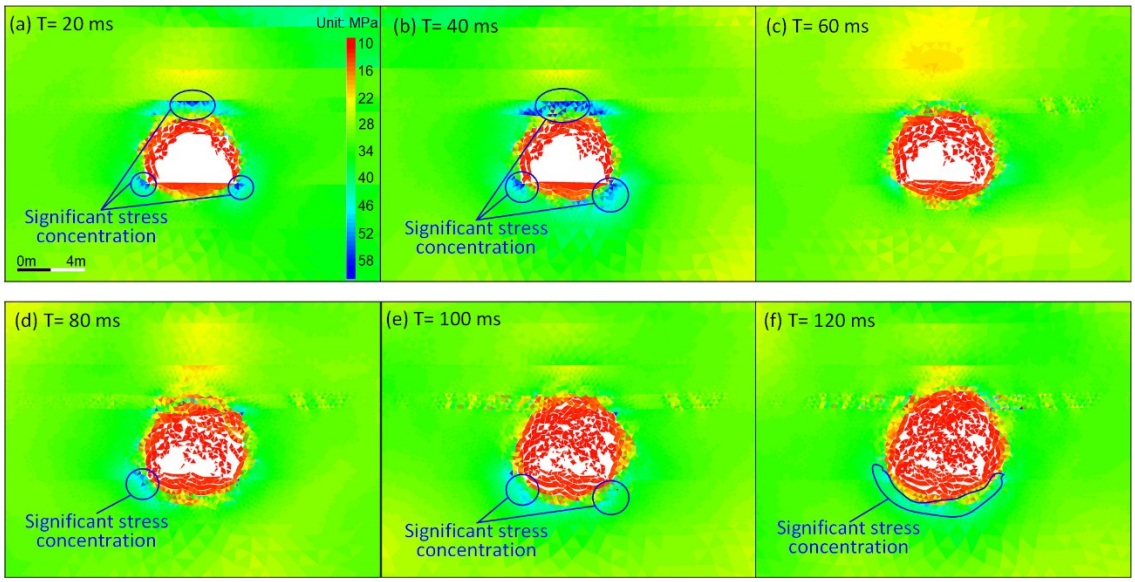

Figure 4.23 Distribution of the maximum principal stress surrounding the main drift during a strainburst.

The microscopic mechanism of crack initiation and development can be further explained based on the stress analysis. Rock masses fail predominantly by extensile fracturing (e.g., spalling) under no or low confining pressure (Gao et al., 2019b). Hence, during the early stage of the strainburst, the tensile failure of cracks mainly occurs surrounding the opening boundary because of the stress relaxation after

excavation (see orange and red areas in Figure 4.23). The initiation of tensile cracks is constrained at depth due to the increasing confining pressure (stress concentration zone, see blue and green areas in Figure 4.23), but the shear fracturing of rock masses happens under high confining pressures. Thus, the shear damage depth is greater than tensile damage. With the stress relaxation zone's expansion, much more cracks fail in tension in this area. The range and depth of shear cracks also grow because the stress concentration zone transfers to deep areas around the tensile failure zone.

4.4.2.2 Influence of PPVs

(a) Displacement analysis

Figures 4.24 and 4.25 show the displacement patterns of the main drift affected by different PPVs. The roadway deformation was aggravated due to dynamic stresses. The magnitude of floor heaving and sidewall convergence rise significantly with the growth of PPVs, while the roof subsidence keeps relatively constant. However, the primary deformation forms are roof subsidence and the shrinkage of two sidewalls when the PPV is less than 0.8 m/s. After that, the floor heaving accounts for an essential part of the deformation. The floor heaving value is increased from 528 mm (PPV=0.8 m/s) to 920 mm (PPV=1.4 m/s), and the ratio of floor heaving to the total deformation is increased from 12.6 % to 18.5 %, with a growth rate of 46.8 %. Hence, the rock support should consider the data of seismic activities in this area. Treatment might not be adopted in the floor when the PPV is low. However, additional support should be conducted on the floor when the roadway is located in areas where active seismic events often have a great magnitude. Two alternative measures are rockbolting the floor and using inverted arches (Yang et al., 2017). In this regard, numerical modeling is suggested for evaluating the performance of support measures during the design stage as it has the benefits of low cost, safety, time-saving, and flexibility.

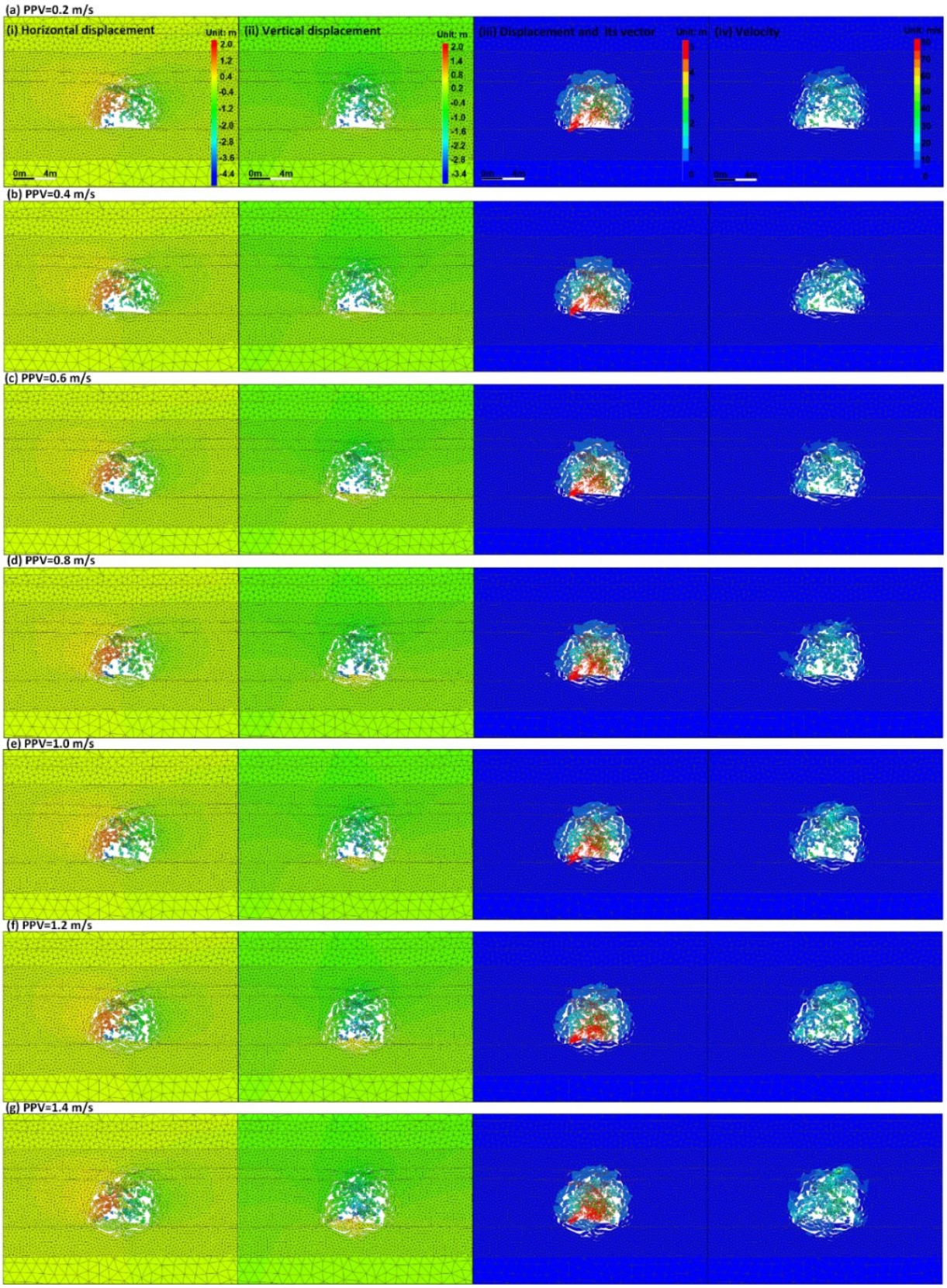

Figure 4.24 Distribution of displacement and velocity of the main drift affected by different PPVs.

Moreover, it can also be observed that the difference between the displacement in two sidewalls is more significant with the increasing PPVs. For instance, the displacement in the right sidewall is 905 mm more than that in the left sidewall (PPV=1.4 m/s), while the displacement difference between the two sidewalls is 690 mm (PPV=0.2 m/s), suggesting that a more non-uniform-displacement pattern occurs when the seismic event has a large magnitude. This phenomenon also indicates that the sidewall deformation is strongly correlated with seismic waves' incident direction if the PPV is great. It can be noted that there are several fluctuations in the variation of roadway deformations (Figure 4.25). This can be attributed to the fact that some monitoring points are located at rock blocks that have been detached and might be collided by others. Nevertheless, the roadway profile continuously shrinks with increasing seismic magnitudes (Figure 4.26). Therefore, the support strength should be high enough to resist the large deformation induced by dynamic stresses in areas where seismic activities occur frequently.

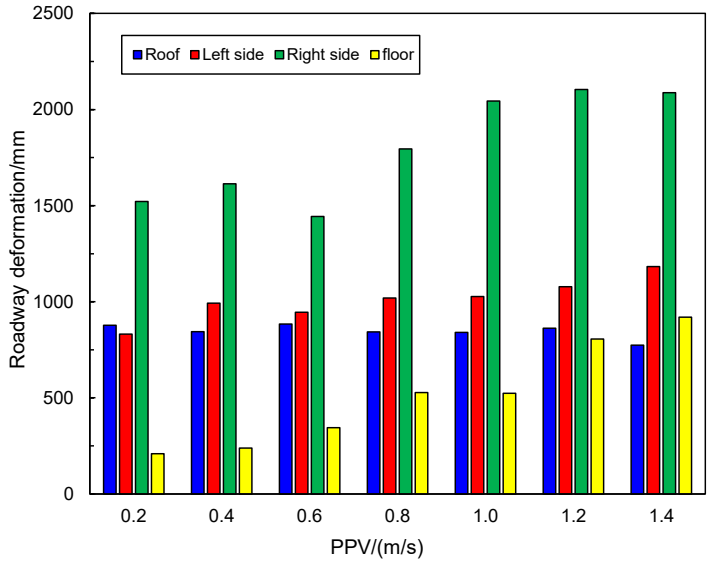

Figure 4.25 Comparison of the deformation in different positions of the main drift affected by different PPVs.

Figure 4.24d shows the velocity distribution of rock blocks. The velocity of some rock blocks can reach 20-40 m/s even when the PPV is 0.2 m/s. These rock blocks are mainly located at the right sidewall. With the increase of PPVs, the range of the region with high velocities grows. Additionally, this region is gradually enlarged from the right sidewall to the roof and the left sidewall, suggesting that the areas with

high rockburst risks are more significant with the increasing PPVs. Thus, it can be concluded that the asymmetric support scheme could be used when the seismic source is known (e.g., a nearby minor fault) and the monitored PPVs are usually low. However, if the monitored PPV is often great or the seismic source is unknown, equal support strength should be adopted in both sidewalls.

(b) Fracture evolution and damage analysis

Figure 4.26 shows cracks in the roadway surrounding rock masses concerning different PPVs. The comparison of damage levels is shown in Figure 4.27. Both the extent and level of damage grow with the increasing PPVs. The tensile damage mainly occurs in the roof and two sidewalls when the PPV is small (less than 0.6 m/s). Tensile cracks are concentrated in the floor's shallow part, and the failure depth is less than 1.2 m. When the PPV is more significant than 0.6 m/s, tensile cracks begin to appear in deep areas of the floor, and the damage depth can reach 2.4 m (PPV=1.4 m/s). Compared with tensile damage, the shear damage occurs in the roof, floor and two sidewalls, and its extent and depth are large. For instance, when the PPV is 1.4 m/s, the tensile cracks' depth in the roof is about 4.3 m, while the shear cracks' depth is 5.5 m. The tensile cracks' depth in the floor is 2.4 m, while the shear cracks' depth is 3.7 m. As shown in Figure 4.29, the shear damage is always the dominant failure mode and increases significantly with the growth of PPVs. The tensile damage decreases first and then grows. The ratio of shear to tensile damage increases from 1.25 to 1.82, suggesting that more slipping of rock masses occurs with the increasing dynamic stresses. This is because the roadway deformation becomes more un-uniform (see displacement vector maps in Figure 4.24). Therefore, the cable bolt is recommended in burst-prone areas since it can provide high pre-tension stress to strengthen fractured rocks, thereby resisting the shear deformation and having a greater control extent than regular rockbolts.

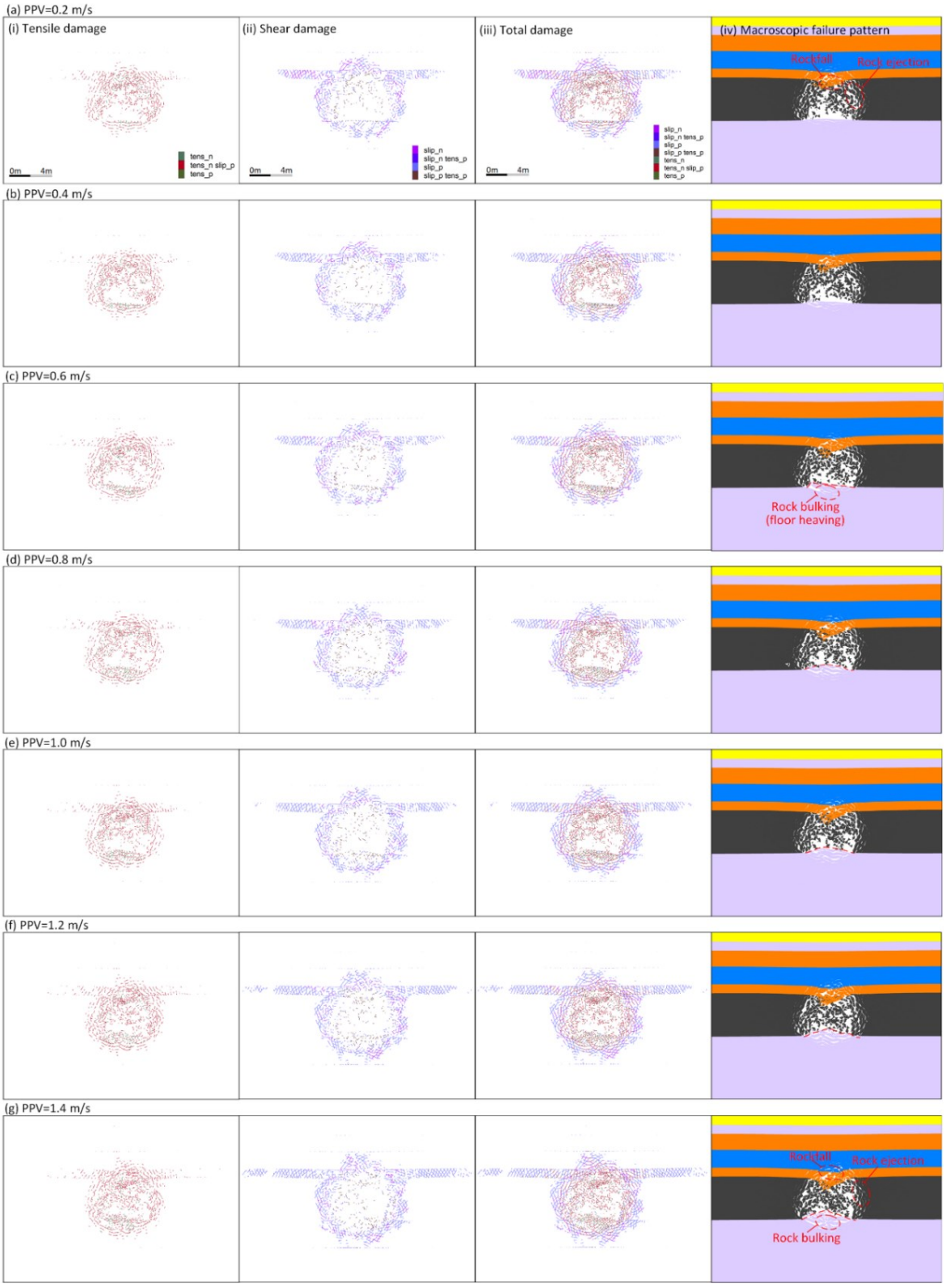

Figure 4.26 Distribution of cracks and macroscopic failure patterns of the main drift affected by different PPVs.

Figure 4.26 also shows the macroscopic failure patterns of the main drift. When the PPV is less than 0.6 m/s, macroscopic fractures are mainly observed in the roof and two sidewalls. With the growth of PPVs, more macroscopic fractures appear in the floor and gradually extend into deep areas. The floor heaving is more obvious if the PPV is higher. In conclusion, the damage mechanism of the strainburst is the combination of three types of damage: rock ejection, rock bulking, and rockfall when the PPV is high, while there is no obvious rock bulking when the PPV is low. Therefore, the objects of rock support can be adjusted according to the analysis and summarization of a large amount of seismic data in a specific area. However, it is always conservative and safe for engineering practices to consider all the damage mechanisms for support designs. Additionally, the macroscopic failure fashion of surrounding rock masses is still the tensile failure, and it mainly occurs in shallower areas compared with the shear failure. Hence, the rockbolts and cable bolts with enough pre-stress should restrain the initiation and development of tensile cracks, thereby reducing the level of damage during a strainburst.

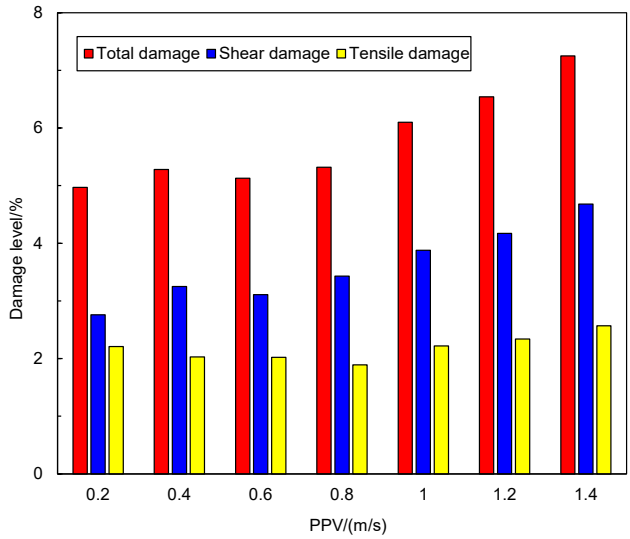

Figure 4.27 Comparison of the damage levels of the main drift affected by different PPVs.

(c) Energy evolution

The severity of strainbursts is related to the magnitude of the kinetic energy of ejected rock materials. The kinetic energy is one part of the total released energy that the whole supporting system (e.g., rockbolt,

cable bolt, liner and steel mesh) must absorb to reduce rockburst risks (Raffaldi et al., 2017). Therefore, the influence of PPVs on the change and distribution of kinetic energy was investigated in this study. The kinetic energy of rock blocks was captured by the FISH language programming in UDEC using the following formula:

$$W_k = \sum \frac{1}{2} m v^2 \tag{4.5}$$

where m and v are the mass and velocity of rock blocks at the current time step.

Figure 4.28 shows the variation of kinetic energy with time influenced by different PPVs. The peak kinetic energy positively correlates with PPVs, indicating that seismic waves with higher PPVs cause severer rockbursts. However, the variation of kinetic energy with time depends on PPV values. The kinetic energy increases linearly with time from 0 ms to 87 ms and is gradually stable (PPV= 0.2 m/s). When the PPV is higher than 0.2 m/s, the kinetic energy grows to a peak value and then gradually decreases to a certain extent over time. The kinetic energy drops because some initially ejected rock blocks have been settled on the floor. It can also be observed that the higher the PPV is, the less time is needed to reach the peak kinetic energy, which is reasonable because of the equal distance from the seismic source to the main drift. This phenomenon suggests that rock ejection influenced by higher PPVs is sudden and violent, while that influenced by lower PPVs is relatively slow.

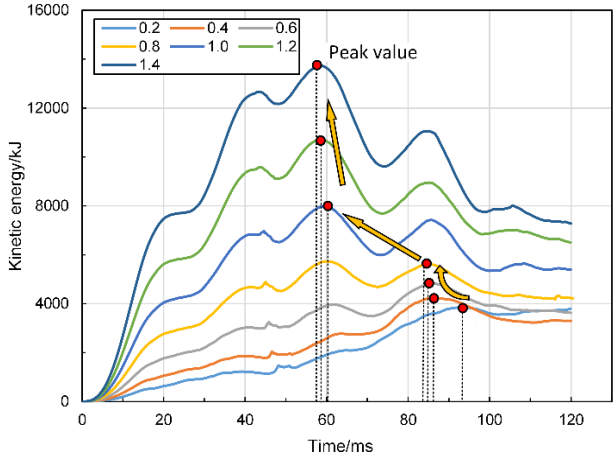

Figure 4.28 Comparison of the kinetic energy of the whole rock system influenced by different PPVs.

The distribution of kinetic energy influenced by different PPVs is shown in Figure 4.29. The kinetic energy pattern is similar to velocity (see Figure 4.24). The kinetic energy of some rock blocks can exceed 14 kJ even when the PPV is 0.2 m/s. These rock blocks are mainly ejected from the right sidewall. This phenomenon matches some local strainburst damage observed in the field (e.g., ejected rocks and rockbolts from a limited area (Zhang et al., 2012a, 2013). With the increase of PPVs, the range of the region with great velocities grows; thus, more rock blocks possess high kinetic energy. Besides, this region is also gradually enlarged from the right sidewall to the roof and the left sidewall, which indicates that the areas with high rockburst risks are expanded with the increasing PPVs. Assume that the tensile yield force of resin-grouted rebar is 160 kN and the maximum allowed deformation is 25 mm (Stillborg, 1994). The energy absorption capacity for this rebar is only 4 kJ, which is 17 % of the kinetic energy (23.4 kJ) of a 0.3 m× 0.3 m× 1 m coal block with an ejection velocity of 20 m/s. Thus, the ejected coal block has a velocity of 16.6 m/s, which is still very harmful to mine workers and equipment. Therefore, yielding support elements (e.g., He-bolt, Roofex, and D-Bolt) is essential and should be used to effectively absorb the ejected rocks' kinetic energy.

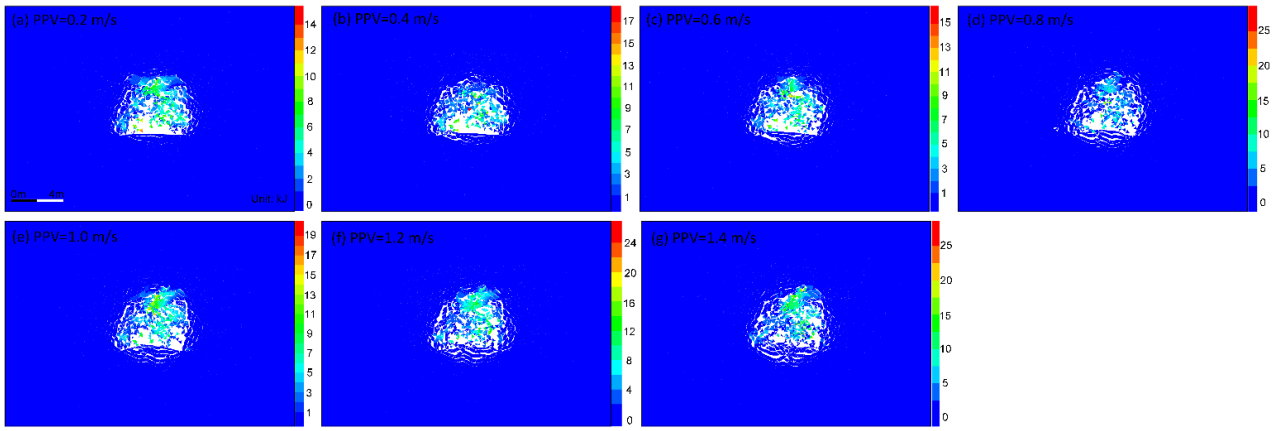

Figure 4.29 Kinetic energy distribution of the whole rock system influenced by different PPVs.

It should be noted that the detached blocks might penetrate too far into one another in numerical modeling, especially in the dynamic stage, which can cause too great an overlap of contacts. Some alternative approaches to handle this problem can be referred to Itasca (2020).

4.5 Suggestions for rockburst supporting

4.5.1 Evaluation of the current support system

Rockburst support systems are required to resist dynamic loads and great deformation caused by rock fracturing, dilation, and ejection, which are different from conventional or standard supports aiming to control gravity-induced rockfalls and manage loose rocks in shallow areas (Kaiser and Cai, 2012). Kaiser and Cai (2012) and Cai (2013) summarized three key and indispensable functions of rockburst supporting: reinforcement, retaining, and holding. The aims of reinforcement (e.g., employing fully grouted rebar and cable bolts) are to prevent the propagation and expansion of fractures and to strengthen rock masses by increasing their cohesion force and friction angle, thereby producing a bearing structure or anchorage body to support itself and outside rock masses (Gao et al., 2009). Retaining elements (e.g., wire mesh, steel arch, and shotcrete) are used to avoid unravelling fractured rocks. The holding function can be fulfilled by tying retaining elements and loose rocks back to stable areas in depth to dissipate the kinetic energy induced by rock ejection and to prevent gravity-induced rockfall. Yielding support elements should be used since they can accommodate great deformation and absorb kinetic energy.

The main drift was supported by yielding steel arches and welded wire mesh. These support elements can accomplish the retaining function, and the shrink characteristic of the yielding steel arch (fulfilled by the frictional sliding between connecting pieces and steel arches) can absorb kinetic energy (Horyl and Snuparek, 2012). However, the steel arch and wire mesh combination is a passive support fashion. The high stiffness of steel arches can limit roadway convergence to a certain extent, but the excavation-induced fracturing is not effectively restrained due to the lack of active compressive force and reinforcement acting on fractured and deteriorated surrounding rock masses (see Figure 4.14). Although steel arches and wire meshes can retain the loose rocks, the bearing load of these elements is significantly increased because they are subject to the loads of loose rocks that are not held with deeper stable rock masses. Therefore,

the capacity of energy absorption of the yielding steel arch might not be sufficient enough to dissipate kinetic energy during a rockburst when a part of the capacity has been consumed owing to the large deformation and loads of fractured rocks because of high in situ stresses, mining-induced stresses, and poor rock conditions (Gao et al., 2009). The kinetic energy from ejected rocks will then be transferred to the high-strain energy accumulated in yielding steel arches that might be overloaded and lose their functions. This is why severe rockburst damage is widespread in many deep roadways that use yielding steel arches and wire meshes as the main support elements (Figure 4.30).

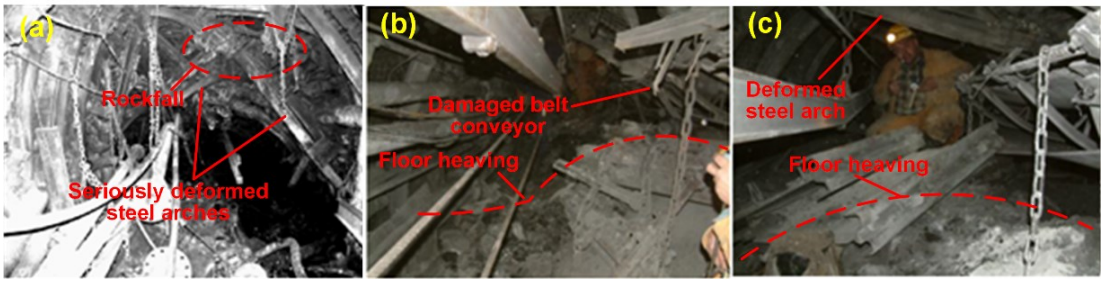

Figure 4.30 Pictures showing severe failure of steel arches, damaged belt conveyer, rockfall, and floor heaving in deep roadways after rockbursts ((a) is from Horyl and Snuparek, 2012; (b) and (c) are from Mutke et al., 2009).

4.5.2 Principles of rockburst supporting

It is also imperative to determine the possible rockburst damage mechanisms to select reasonable support elements for accomplishing three critical functions of rockburst support (Kaiser and Cai, 2012). The modeling approach used in this study can anticipate the damage mechanisms of strainbursts (the type, location or range, level, and energy) from both micro and macro perspectives, improving and optimizing the support design. Based on the case study site as an example, the following principles of rockburst supporting are proposed according to the analysis of the simulation results of strainburst damage mechanisms (see also Figure 4.31):

1) Support area. The seismic activities in planned construction areas should be recorded and analyzed in advance. If the seismic source is known (e.g., a nearby minor fault) and monitored PPVs are usually low, treatment might not be adopted in the floor, and the asymmetric support scheme could be used.

Although the asymmetric support scheme is a common practice in entries or drifts in longwall mining, it should be used with caution, considering the greater risk and more uncertainties in the burst-prone ground. The feasibility and effectiveness of this strategy need to be verified with more cases. In contrast, when the roadway is located in areas where seismic events are active and often have a great magnitude, or the seismic source is unknown, equal support strength should be used in both two sidewalls, and the floor needs to be treated with additional support measures to avoid rapid bulking or floor heaving.

2) Using yielding rockbolts. Kaiser et al. (1996) reported that in rockburst-prone mines, ejection velocities below 1.5 m/s could be handled by standard ground support, but additional support is required for higher velocities. Therefore, yielding rockbolts with high strengths (e.g., D-bolt) are recommended. These yielding rockbolts can bear high loads and accommodate large deformations during rockbursts. Also, it can absorb more kinetic energy than those with low strength and conventional rockbolts (Figure 4.32). Enough pre-stress should be applied to surrounding rocks when installing rockbolts to control separation and fracturing induced by the development of tensile cracks and to increase the confining pressure, which has been proven effective in improving the physical and mechanical performance of fractured rocks (Yang et al., 2017). In addition, the yielding rockbolts can fulfill reinforcement and a part of the holding function.

3) Using cable bolts. The cable bolts with high strengths and pre-stress should be used to restrain the development of cracks and resist large deformations, thereby strengthening surrounding rock masses and maintaining their integrity (reinforcement function). Cable bolts usually have a great length, holding retaining elements and shallow rocks back to stable areas in depth. Besides, the cable bolts also have a relatively high elongation rate (4%-7%, Kang et al., 2009) to absorb the deformation energy induced by rock bulking.

4) High-strength retaining elements. The wire mesh with high tensile strength is recommended since this mesh type can deaccelerate ejected rocks and absorb kinetic energy effectively because of its strength and flexibility (Roth et al., 2007).

5) Improving the connection between rockbolts and meshes. Cai (2013) proposed that the support system often loses its effectiveness due to the weakness of the bolt-mesh linkage rather than the insufficient capacity of rockbolts. Thus, he recommended that the relatively large plates (minimum 150 mm × 150 mm) should be used to connect rockbolts to wire meshes.

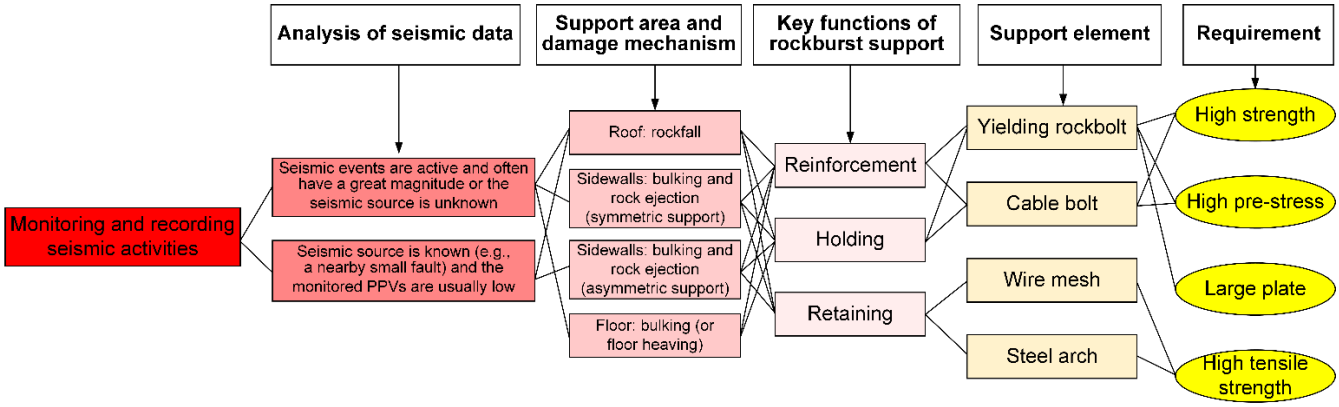

Figure 4.31 Principles of rockburst supporting based on the analysis of strainburst damage mechanisms.

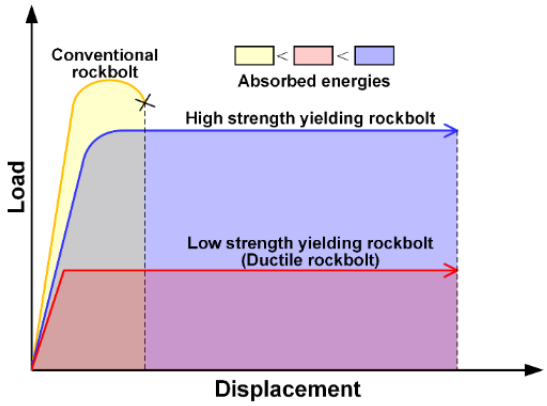

Figure 4.32 Comparison between the conventional and yielding rockbolts with low and high strength (after Li, 2021).

4.6 Conclusions

This chapter presents an improved global-local modeling approach to study strainburst damage mechanisms. The extracted stresses induced by multiple nearby excavations from a calibrated 3D FDM

global model are used as boundary conditions for a 2D DEM local model of a roadway. The damage mechanism of strainbursts is investigated from both micro and macro perspectives. The main conclusions are as follows:

(1) The used approach provides a more insightful understanding of the influences of the realistic stress loading path on strainburst occurrence. The roadway surrounding rock stress increases significantly because of the superposition of excavation-induced stresses of nearby panels and roadways. This results in more accumulated strain energy in two sidewalls, providing a necessary condition for the strainburst occurrence in the dynamic stage. A better understanding of the realistic stress loading path can also help identify stress concentration zones and adopt distress measures in time to mitigate rockburst risks.

(2) The strainburst damage mechanism of a violent rockburst event in the Zofiówka Mine, including rock ejection, rock bulking, and rockfall, is successfully captured in the local model, which confirms the rationality and capability of the modeling approach. The rock mass fracturing or damage during the strainburst is investigated quantitively using a self-defined damage variable in UDEC. During the strainburst, tensile cracks' initiation, propagation, and development play a crucial role in controlling the macroscopic failure of surrounding rock masses, although the shear crack always accounts for the main proportion of damage levels. Therefore, the rockbolts and cable bolts with enough pre-stress should be used to restrain the initiation and development of tensile cracks, thereby reducing the level of damage.

(3) The roadway's deformation and damage level during the strainburst positively correlate with the increasing PPVs. A more non-uniform displacement pattern occurs when the seismic event has a large magnitude. The asymmetric support scheme is an alternative strategy when the known seismic source and the monitored PPVs are usually low.

(4) The yielding steel arch might not dissipate kinetic energy and mitigate strainburst damage effectively owing to the limited energy absorption capacity. Based on the findings in this chapter, the principles (Figure 4.31) to control and mitigate strainburst damage are proposed.

5. CHAPTER 5: EVALUATION OF THE PERFORMANCE OF YIELDING ROCKBOLTS DURING STRAINBURSTS USING NUMERICAL MODELING METHOD

*In this chapter, instead of conventional drop tests, the performance (e.g., the capacity of energy absorption and control of rock damage) of yielding rockbolts (D-bolt and Roofex) during strainbursts was systematically evaluated via building a 2D DEM model of a deep roadway using UDEC. According to the triggering mechanism, strainburst can be classified into two types: remotely triggered and self-initiated. The remotely triggered strainburst is caused by a remote seismic event triggered by large-scale mining activities and high static stress. The self-initiated strainburst occurs due to the concentration of excavation-induced tangential stress and the existence of a relatively "soft" loading environment in the rock mass surrounding the fracturing rock triggered. There is not a remote seismic event involved in self-initiated strainbursts. Hence, the performance of yielding rockbolts during remotely triggered and self-initiated strainbursts is investigated in parts one and two, respectively. Part one is based on the published paper "**Wang, J.,** Apel, D. B., Xu, H., Wei, C. (2022). Evaluation of the performance of yielding rockbolts during rockbursts using numerical modeling method. International Journal of Coal Science & Technology, 9(87), 1-26". Part two is based on the published paper "**Wang, J.,** Apel, D. B., Xu, H., Wei, C., Skrzypkowski, K. (2022). Evaluation of the effects of yielding rockbolts on controlling self-initiated strainbursts: a numerical study. Energies, 15(7), 2574".*

PART ONE: EVALUATION OF THE PERFORMANCE OF YIELDING ROCKBOLTS DURING REMOTELY TRIGGERED STRAINBURSTS

The assessment of yielding rockbolts' performance during rockbursts with actual seismic loading is essential for rockburst supporting designs. In this part, two types of yielding rockbolts (D-bolt and Roofex) and the fully resin-grouted rebar bolt are modelled via the "rockbolt" element in UDEC after an exact calibration procedure. A 2D model of a deep tunnel is built to fully evaluate the performance (e.g., the capacity of energy absorption and control of rock damage) of yielding and traditional rockbolts during remotely triggered rockbursts. The influence of different rockburst magnitudes is also studied. This study highlights the effectiveness of numerical modeling methods in assessing the complex performance of yielding rockbolts during rockbursts, which can provide some references to improve and optimize the design of rock supporting in burst-prone grounds.

5.1 Evaluation of the performance of yielding rockbolts during remotely triggered strainbursts

5.1.1 Introduction

It is always the best choice to prevent rockburst occurrence rather than to control and mitigate rockburst damage afterward. Methods that can avoid rockburst include choosing the rational location, size, and shape of openings, changing excavation methods and sequences, and using ground conditioning methods (e.g., distress drilling and blasting) (Mitri, 2000; Kaiser and Cai, 2012; Cai, 2013). However, despite prevention measures being applied successfully in many cases, rockbursts can still occur due to the lack of sufficient geotechnical data and the complexity of rockburst mechanisms (Cai, 2013; Ghorbani et al., 2020). Hence, the rock support system is usually required as the last defence line to control and mitigate rockburst damage. The rockburst support elements (e.g., rockbolts) in burst-prone grounds must resist dynamic loads and accommodate large deformations caused by rock fracturing, dilation, and ejection (Kaiser and Cai, 2012). Kaiser et al. (1996) reported that, generally, ejection velocities below 1.5 m/s could be handled by standard ground supports, but additional supports were required for higher velocities. Thus, support elements should allow yielding to absorb more kinetic energy and have higher displacement capacities than conventional support elements. This demand promotes the emergence and development of yielding or energy-absorption rockbolts. Figure 5.1 shows the typical load-displacement characteristics of yielding and conventional rockbolts.

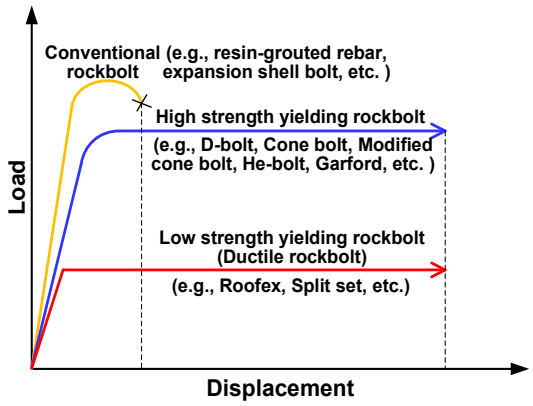

Figure 5.1 Load-displacement characteristics of conventional and yielding rockbolts (after Li et al., 2014).

As shown in Figure 5.1, various types of yielding rockbolts have been invented due to the tireless efforts of researchers and engineers (Li et al., 2014; Sharifzadeh et al., 2020). Although the energy absorption mechanism (shank stretching, e.g., D-bolt; ploughing of anchors, e.g., cone bolt; extrusion of shanks, e.g., Roofex) might be different, some types of yielding rockbolts, e.g., Cone bolt (Ortlepp, 1992), Roofex (Charette and Plouffe, 2007; Atlas Copco Construction Mining Technique, 2009), Garford bolt (Varden et al., 2008), D-Bolt (Li, 2011; Normet, 2021), Yield-Lok (Wu et al., 2011), and He-bolt (He et al., 2012) have been shown that they can control rockbursts effectively.

A critical task is to evaluate the performance (e.g., deformation, strength, control of rock damage and capacity of energy absorption) of rockbolts before being widely used. The methodologies to study rockbolt behaviour mainly include field tests (Kang et al., 2009; Li, 2011; Wu et al., 2019), laboratory tests, and numerical modeling. Field test methods can obtain real-time data and assess the in situ performance of rockbolts, but they are usually time-consuming, expensive, and dangerous, especially in burst-prone grounds. Compared with field tests, experimental methods have the advantages of repeatability, safety, and flexibility (Zhang and Nordlund, 2019). At present, significant efforts have been made to evaluate the static and dynamic performances of conventional and yielding rockbolts via laboratory tests, mainly including pull-out, shear, and drop tests (Stillborg, 1994; Stjern, 1995; Charette and Plouffe, 2007; Cai et al., 2010; Li, 2011; Li and Doucet, 2011; Skrzypkowski et al., 2020; Skrzypkowski, 2021). The research has achieved many positive outcomes, providing excellent references for understanding rockbolt behaviour under different conditions.

Nevertheless, it should be noted that experimental methods employ many idealized assumptions which are incapable of matching the actual field circumstances (Manouchehrian, 2016). For instance, Bosman et al. (2018) stated that the dynamic capacity of a rockbolt is not a constant value, and the loading mode of a rockbolt will affect its dynamic capacity. Therefore, the impact loading from conventional drop tests

might not represent rockburst loading. Wu et al. (2019) also pointed out that the impact load in drop tests cannot represent the impact of ground pressure load, and the existing test system generally cannot reproduce the complex ground support/rock mass interaction that exists in an underground environment. Besides, original rock stress is not considered in tests. Therefore, the performance of yielding rockbolts during rockbursts with actual seismic loading is worth evaluating.

With the rapid development of IT and computer equipment, various numerical methods and codes have been developed and employed to simulate complex physical phenomena in rock mechanics and engineering (Wang et al., 2021a). The numerical simulation methods have been acknowledged as effective research and engineering design tools as they can represent the realistic mechanical behaviour of rock masses and support elements with rational input data (e.g., excavation size and shape, material properties, and boundary conditions) and calibration procedures (Manouchehrian, 2016). Hence, the actual engineering problems can be simulated and analyzed in detail and depth. Mortazavi and Tabatabaei Alavi (2013) employed FLAC3D software to study the behaviour of fully grouted rebar rockbolts (with and without head plates) and the yielding rockbolt under dynamic loading. They concluded that the yielding rockbolt had the best performance in absorbing dynamic stress waves and controlling rock movement. Nie et al. (2014) developed rockbolt models using DDA to investigate the failure mechanism of an expansion-shell bolt, fully grouted rebar, split set, and D-bolt in simulated pull-out and drop tests. Marambio et al. (2018) modelled a laboratory-scale test via FLAC3D to study the performance of threadbar in dynamic loading. The simulation results matched well with laboratory observations. Yokota et al. (2019) assessed a self-developed deformation-controlled rockbolt (DC-bolt)'s behaviour in tunnel support via DDA simulation. Zhang and Nordlund (2019) employed UDEC to investigate the differences of dynamic performances of a fully grouted rebar between the simulated drop tests and seismic loading in the configuration where two slightly separated rock bars were used. Zhao et al. (2021) studied the influence

of structure element position on the anchoring effect of energy absorption bolts via simulating pull-out tests.

In summary, most current work focuses on evaluating the effects of traditional rockbolts under dynamic loading, while some researchers try to simulate the dynamic behaviour of yielding rockbolts by reproducing drop tests. However, to the authors' knowledge, few numerical studies have been reported to assess yielding rockbolts' performances during rockbursts with actual seismic loading. Furthermore, as mentioned above, the impact loading in drop tests might not be able to represent rockburst loading because there is a complex interaction between seismic waves, rockbolts, and reinforced rock masses during rockbursts with explicit rock detachment and ejection (requiring distinct element method (DEM) or DEM-related hybrid methods). Therefore, the influence of realistic rockburst loading on the performance of yielding rockbolts remains unclear. Hence, it is essential to evaluate the performance of yielding rockbolts during rockbursts using DEM to provide some references to improve and optimize the design of rock supporting in burst-prone grounds.

This study uses a numerical modeling method to evaluate the performance of yielding rockbolts during rockbursts with actual seismic loading. Two types of yielding rockbolts, D-bolt and Roofex, are modelled via the "rockbolt" element in a DEM software UDEC after an exact calibration procedure. D-bolt is a typical representative of a type of yielding rockbolts with high strengths and deformation capacity, while Roofex stands for the other type of yielding rockbolts having low strengths but excellent deformation capacity (Figure 2). The fully resin-grouted rebar bolt is also simulated to demonstrate the differences between yielding and traditional rockbolts. Instead of conventional drop tests, a two-dimensional (2D) model of a deep tunnel in an underground coal mine is built to fully evaluate the performance (e.g., the dynamic capacity of energy-absorption and control of rock damage) of yielding and traditional rockbolts during the simulated rockbursts. The influence of different rockburst magnitudes is also studied.

5.1.2 Numerical modeling

5.1.2.1 Model setup

A widely used 2D DEM software UDEC was used to construct the model of a deep tunnel (more than 600 m, He et al., 2015) for conducting the detailed analysis of the effects of yielding rockbolts on controlling rockbursts. The shape of the tunnel cross-section is a semicircular arch, with a width and height of 6 m and 4 m, respectively. Noticing that the model size might affect simulation results, two models with different dimensions (small model: 30 m × 25 m, and large model: 60m × 50 m) were established to examine the effect of model size on the failure depth in surrounding rock masses and the peak stresses in two sidewalls. Table 5.1 shows that the differences between the two models are minor, e.g., the errors of peak stresses are less than 3%. However, the run time for the initial equilibrium and tunnel excavation in the two models are 3.22 h and 7.65 h, respectively, when using a regular computer with an Intel i7-3770 CPU at 3.40 GHz (8 cores). The small model can save 57.90 % on computation costs and is chosen as the final model to conduct a subsequent simulation. Figure 5.2 shows the geometry of the used model, based on the lithology and designed size of a deep tunnel in an underground coal mine.

Table 5.1 Comparison between the simulation results of small and large models

Model	Failure depth (m)				Peak stresses in two sidewalls (MPa)		Run time (hour)
	Roof	Floor	Left rib	Right rib	Left side	Right side	
Large model	1.78	2.19	1.31	1.64	39.56	38.62	7.65
Small model	1.75	1.92	1.32	1.44	39.53	39.57	3.22
Error (%)	-1.69	-12.33	0.76	-12.20	-0.08	2.46	—

A Trigon approach developed by Gao et al. (2015) was used to generate blocks in the model, as this approach can be capable of reproducing the natural fracturing processes (e.g., crack initiation, propagation, and coalescence) of rock masses without adopting complicated constitutive models (Chen et al., 2016; Yang et al., 2017; Hu et al., 2020; Stavrou et al., 2019;). In the Trigon approach, a rock mass represents an assembly of triangular blocks bonded by contacts (Gao et al., 2015). The fracturing process can be

exhibited by sliding or opening contacts. In the model, the average edge length of the blocks in two coal seams and nearby clay shale was set to 0.3 m. The block size with a range of 0.2-0.5 m was sufficiently acceptable to simulate the failure behaviour of surrounding rock masses for a 2D model (Gao et al., 2015; Chen et al., 2016; Yang et al., 2017). The average edge length of the blocks in the upper clay shale, sandy shale, and fine-grained sandstone was set to 0.5 m, 0.5m, and 1 m, respectively. The average edge length of the blocks on the floor was set to 0.3 m and 1 m. A graded increasing edge length of blocks can avoid the resulting loss of simulation accuracy and enhance the calculation's reliability. The upper boundary of the model was free and vertical stress of 24.3 MPa (assuming the unit weight of overburden is 0.027 MN/m^3 and the buried depth is 900 m) was applied to the upper boundary to simulate the overburden weight. The roller constraints were applied on lateral boundaries, and the bottom boundary was fixed during the static stage (Figure 5.2a). The ratio of horizontal to vertical stress (K) was assumed to be one since the hydrostatic stress state is a general situation of the in situ stress in many deep excavations (Dai et al., 2021).

Generally, rockburst can be classified into two types: remotely triggered and self-initiated (Kaiser et al., 1996). Studies have shown that many rockbursts in mining environments are caused by the combination of a remote seismic event triggered by large-scale mining activities and high static stress, while the primary source of rockbursts is the rock mass itself around the tunnel in civil engineering projects (Diederichs, 2018; Mutke et al., 2015). This research specifically focuses on evaluating the performance of yielding rockbolts during remotely triggered rockbursts. A seismic wave caused by the nearby fault slip was assumed to be the dynamic load source to trigger a rockburst in the tunnel (Gao et al., 2021; Zhang and Nordlund, 2019). Mutke et al. (2015) and Kong et al. (2019) reported that the rockburst potential of tunnels has a positive correlation with the PPV of seismic waves and buried depths. The statistical data of rockbursts suggest that PPVs were mainly in the range of 0.05 m/s to 1.0 m/s, and

rockbursts are usually related to seismic waves characterized by low frequencies from 10 to 30 Hz (Mutke et al., 2009; Mutke, 2016;). Therefore, two PPVs of 0.2 m/s and 0.8 m/s were adopted to simulate different dynamic loads ($\sigma_n=2(\rho C_p)v_n$, Itasca, 2020). The frequency is assumed to be 20 Hz and the busy time is 120 ms (a vibration period plus a quiet time of 70 ms). The seismic waveform was simplified to be a sine wave since any complex stress wave can be obtained by the Fourier transform of several simple sine waves (Liu, 2017). A series of seismic waves were applied to the model's right boundary to investigate the tunnel's dynamic responses. The boundary conditions (e.g., fixed boundaries) used in the static stage can cause the reflection of outward propagating waves back into the model and do not allow the necessary energy radiation. Thus, the viscous boundary developed by Lysmer and Kuhlemeyer (1969) was used in the dynamic calculation (Figure 5.2b). A recommended Rayleigh damping of 0.5 % was applied (Itasca, 2020). This value is suitable for many dynamic analyses that involve large block deformation or large joint displacement.

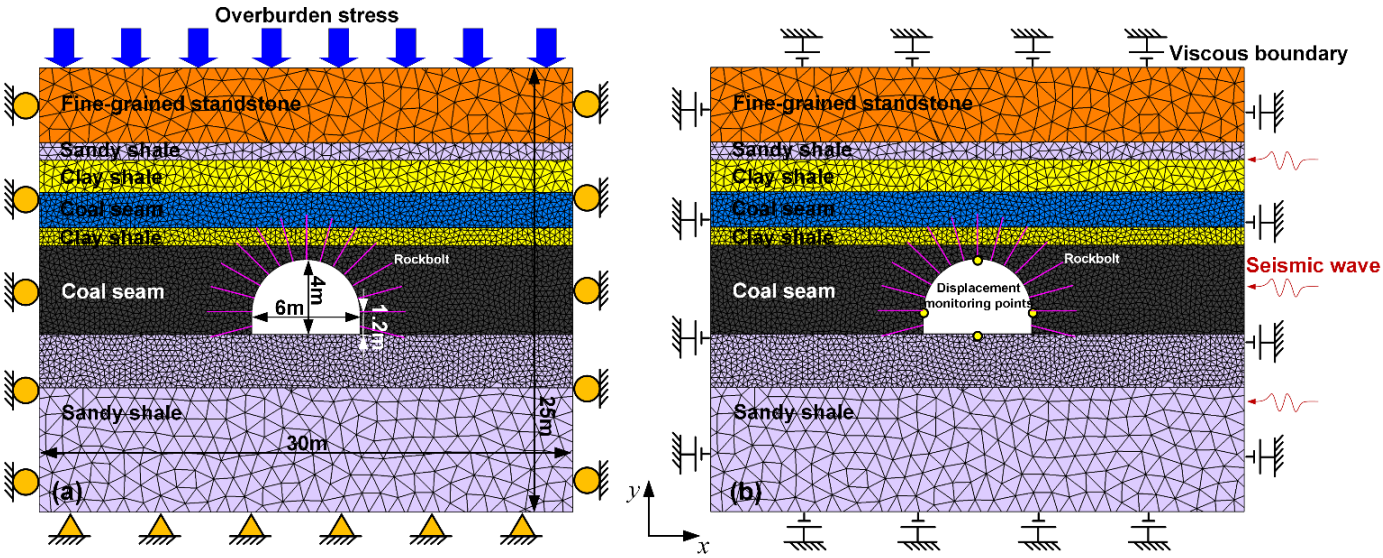

Figure 5.2 2D numerical model of a deep tunnel. (a) Static stage (b) Dynamic stage.

5.1.2.2 Constitutive model and rock mass properties

The properties of rock masses (see Table 5.2) around the tunnel were obtained according to the laboratory tests of intact rock pieces (following ISRM recommended standards, Fairhurst and Hudson,

1999) and the generalized Hoek-Brown criterion (Marinos and Hoek, 2000) using the GSI system to evaluate rock mass qualities (Małkowski et al., 2017; Szott et al., 2018; Małkowski and Ostrowski, 2019). The UCS and deformation modulus of rock masses were estimated from the following equations (Hoek et al., 2002; Hoek and Diederichs, 2006):

$$\sigma_{cm} = \sigma_{ci} \frac{(m_b + 4s - a(m_b - 8s))\left(\frac{m_b}{4+s}\right)^{as-1}}{2(1+a)(2+a)} \tag{5.1}$$

$$E_m = E_i \left(0.02 + \frac{1 - D/2}{1 + e^{((60+15D-GSI)/11)}}\right) \tag{5.2}$$

where D is a factor that depends upon the degree of disturbance to which the rock mass has been subjected by blast damage and stress relaxation. In this study, the value of D is assumed to be zero considering that the mechanical tunnelling results in minimal disturbance to confined rock masses (Hoek et al., 2002). The calculated results of UCS and deformation modulus of rock masses are also summarized in Table 5.2.

Table 5.2 Physical and mechanical parameters of rock masses (Małkowski et al., 2017; Szott, 2018; Małkowski and Ostrowski, 2019)

Lithology	Constant				Intact rock				Rock mass	
	m_i	m_b	s	a	ρ (kg/m^3)	σ_{ci} (MPa)	E_i (GPa)	v	σ_{cm} (MPa)	E_m (GPa)
Coal	17	1.729	0.0008	0.5	1300	9.3	1.86	0.30	2.50	0.23
Clay shale	9	1.327	0.0022	0.5	2500	29.0	5.62	0.31	7.93	1.26
Fine-grained sandstone	17	2.851	0.0039	0.5	2580	90.0	9.52	0.26	24.53	2.92
Sandy shale	12	1.877	0.0031	0.5	2530	26.0	5.23	0.25	7.11	1.42
Gritty clay shale	8	1.192	0.0022	0.5	2440	47.5	6.98	0.32	13.03	1.56

Note: m_i is a material constant for intact rocks. m_b, s, and a are constants for rock masses. ρ is the bulk density of intact rocks. σ_{ci} is the UCS of intact rocks. E_i is the Young's modulus of intact rocks. v is the Poisson's ratio of intact rocks. σ_{cm} is the UCS of rock masses and E_m stands for the deformation modulus of rock masses.

The elastic constitutive model was chosen for blocks that are composed of finite-difference zones. The coulomb slip model was used for contacts. The constitutive behaviour of contacts is shown in Figure 5.3. A spring-rider simulates the behaviour of contacts, and the model deformation occurs when the contact stress is smaller than the contact strength, which is governed by the elastic modulus of blocks and contact

stiffness; contact failure occurs when the stress exceeds its shear or tensile strength, and then blocks will slide or separate with each other (Chen et al., 2016).

In the Trigon approach, the deformation and failure of rock masses depend on the properties of blocks and contacts (Gao et al., 2015; Chen et al., 2016) ;). Thus, the micro parameters of blocks and contacts were calibrated against the rock mass properties (Table 5.2). A series of simulated uniaxial compression tests were conducted to calibrate the micro parameters (Gao et al., 2015). To eliminate the effect of block size on simulation accuracy, the calibration model had a large scale (4 m×8 m) (Yang et al., 2017) and an identical block size to the tunnel model. However, there is a problem in that different block sizes were employed for the rock strata with the same lithology (e.g., block size of 0.3 m and 0.5 m for clay shale, and 0.3 m, 0.5 m, and 1 m for sandy shale), which means that different material parameters might be used even for the same lithology. A sensitivity study showed that the block size effect on simulated rock mass properties could be negligible (Figure 5.4). A displacement loading mode was used in the simulation by applying a constant velocity of 0.1 m/s to the surface of the top platen, and the bottom platen was fixed. This loading rate of 0.1-0.15 m/s is slow enough to avoid the dynamic responses of models because UDEC automatically selects very small time steps (e.g., 10^{-7} s) in static analysis (Hu et al., 2020; Gao et al., 2019b). The initial micro parameters were first assumed based on the macro parameters of rock masses. Then, uniaxial compression tests were modelled iteratively with adjusting micro parameters until the simulated results were consistent with the targeted material properties. Tan and Konietzky (2014) describe micro parameters' detailed calibration process. The simulated failure modes and stress-strain curves of rock mass samples are shown in Figure 5.5. The calibrated micro parameters of rock masses are listed in Table 3. The errors between the targeted and simulated deformation modulus and UCS are all less than 3 % (Table 5.4), suggesting that the targeted values agree well with calibrated rock mass parameters. Thus,

the calibrated micro parameters in Table 5.3 could be used for further numerical analysis to evaluate the performance of yielding rockbolts during rockbursts.

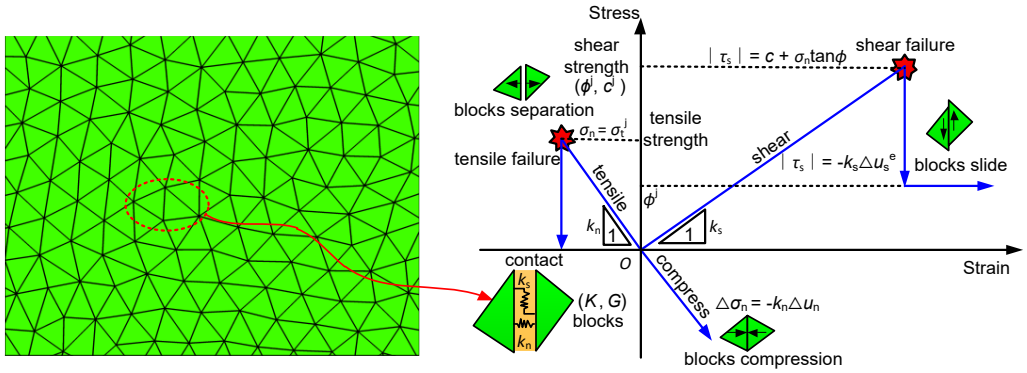

Figure 5.3 Constitutive behavior of contacts (after Yang et al., 2017).

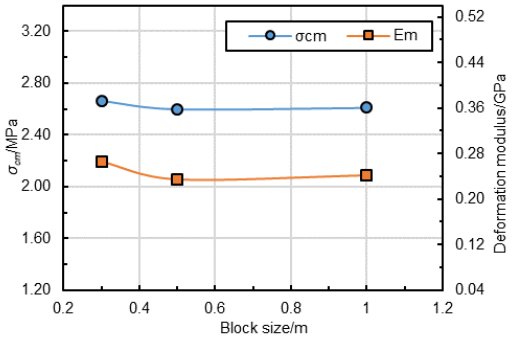

Figure 5.4 Influence of different block sizes on simulated material properties. (The block edge length of 0.3 m, 0.5 m, and 1 m were used in the sensitivity study)

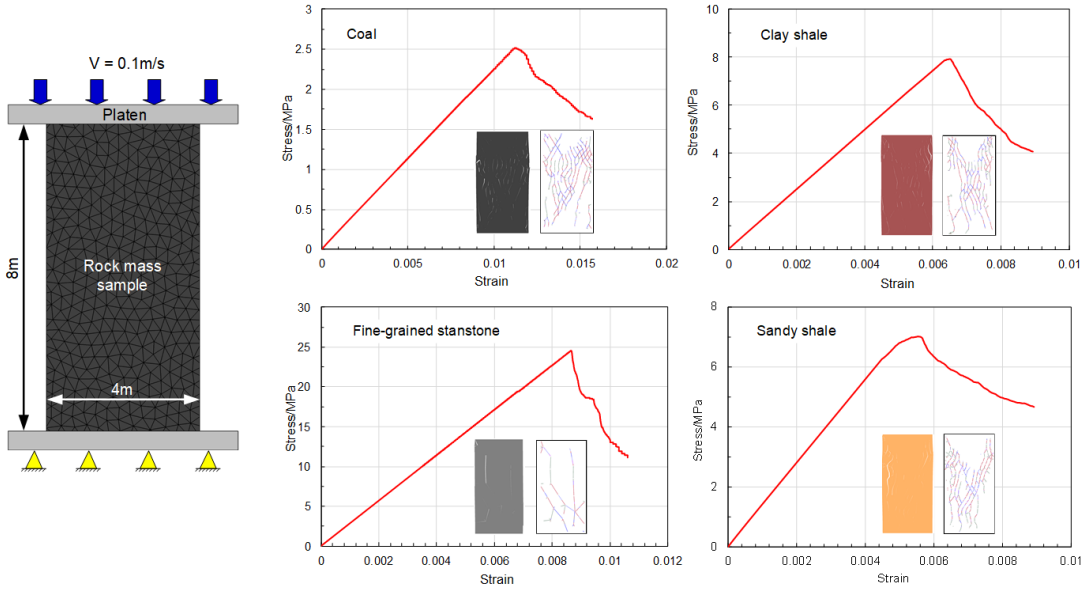

Figure 5.5 Simulated failure modes and stress-strain curves of rock mass samples.

Table 5.3 Calibrated micro parameters of rock masses in the model

Lithology	Block properties			Contact properties				
	ρ (kg/m^3)	K (GPa)	G (GPa)	k_n (GPa/m)	k_s (GPa/m)	c^j (MPa)	φ^j (°)	σ_t^j (MPa)
Coal	1300	0.16	0.09	18.7	7.5	0.99	33	0.25
Clay shale	2500	0.85	0.50	108.5	40.6	2.96	35	0.79
Fine-grained sandstone	2580	1.91	1.17	69.4	27.8	8.11	36	2.15
Sandy shale	2530	0.94	0.57	113.3	45.3	2.95	36	0.85

Table 5.4 Comparison between the targeted and simulated rock mass parameters

Lithology	E_m (GPa)			UCS (MPa)		
	Target	Simulation	Error (%)	Target	Simulation	Error (%)
Coal	0.23	0.226	0.09	2.50	2.51	0.48
Clay shale	1.26	1.234	-1.82	7.93	7.91	-0.29
Fine-grained sandstone	2.92	2.852	-2.48	24.53	24.52	-0.05
Sandy shale	1.42	1.39	-2.11	7.11	7.02	-1.27

5.1.2.3 Properties of rockbolts

(a) Introduction of rockbolt element

In the past, the "cable" element in UDEC was more popular used than the "rockbolt" element to model a mechanically anchored or grouted cable or rockbolt, although both elements can simulate the shearing resistance along their length, which is provided by the shear bond between the grout and either the cable/rockbolt or the host rock (Bahrani and Hadjigeorgiou, 2017). This could be owing to more understandable input parameters and the more straightforward calibration process for using the "cable" element. Figure 5.6 shows the conceptual mechanical representation of "cable" and "rockbolt" elements. It can be seen that two types of elements are composed of several segments and nodal points located at segment ends. Nevertheless, the "rockbolt" element has both shear and normal coupling springs, which are connectors that transfer forces and motion between the "rockbolt" element and the grid points associated with the block zone, while the "cable" element only has sliders (similar to shear coupling springs). Therefore, the "cable" element provides little resistance to bending, and thus it is more suitable for modeling cable bolts.

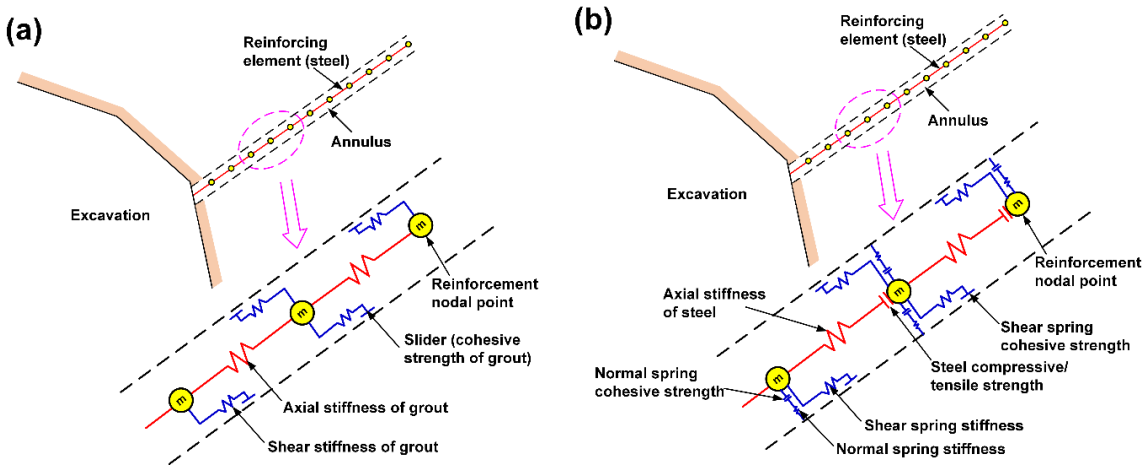

Figure 5.6 Conceptual mechanical representation of the global reinforcement: (a) "cable" element, which accounts for shear behavior of the grout annulus, and (b) "rockbolt" element, which accounts for shear behavior of grout annulus and bending resistance of the reinforcement (after Itasca 2020).

In contrast, the "rockbolt" element can provide sufficient resistance for shearing and bending, which is appropriate for simulating rockbolts such as rebar bolts (Tomasone et al., 2020). The other strength of the "rockbolt" element is that it can explicitly model the rockbolt breakage according to a user-defined tensile failure strain limit (Itasca, 2020), providing a more accurate and realistic approach to reproducing rockbolt performances. Thus, the "rockbolt" element was used in this study to simulate the mechanical behaviour of both yielding and conventional rockbolts. In addition, the "rockbolt" element has a linearly elastic material behaviour in UDEC that it can yield both tension and compression in the axial direction (Figure 5.7). The incremental axial force in a "rockbolt" element, $\triangle F_t$, can be obtained by the calculation of the incremental axial displacement:

$$\Delta F_t = -\frac{EA}{L}\Delta u^t \tag{5.3}$$

where $\triangle u^t = \triangle u_i t_i = \triangle u_1 t_1 + \triangle u_2 t_2 = (u_1^{[b]} - u_1^{[a]})t_1 + (u_2^{[b]} - u_2^{[a]})t_2$; $u_1^{[b]}$, $u_1^{[a]}$, etc. are the displacements at the bolt nodes associated with each "rockbolt" element. Subscript 1 and 2 represent the x-direction and y-direction, respectively; the superscripts [a], [b] stand for bolt nodes. The direction cosines t_1, t_2 refer to the tangential (axial) direction of the "rockbolt" element.

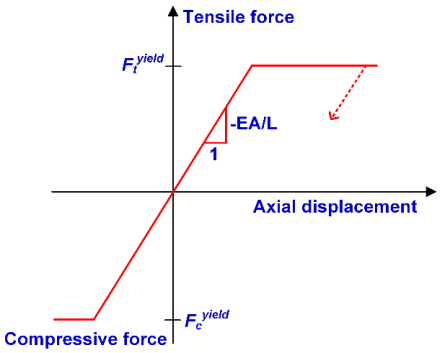

Figure 5.7 Mechanical behaviour of the "rockbolt" element in the axial direction (Itasca 2020).

The shear and normal behaviour of the "rockbolt" element were briefly introduced in this study. The shear behaviour of the rockbolt/gridpoint interface is represented as a spring-slider system at the rockbolt nodal points. This behaviour during relative displacement can be described numerically by the coupling spring shear stiffness (cs_{sstiff} in Figure 5.8a):

$$\frac{F_s}{L} = cs_{sstiff}\left(u_p - u_m\right) \tag{5.4}$$

where F_s represents the shear force that develops in the shear coupling spring (e.g., along with the interface between the rockbolt element and the gridpoint); cs_{sstiff} is the coupling spring shear stiffness; u_p is the axial displacement of the rockbolt; u_m is the axial displacement of the medium (soil or rock); and L is the contributing element length.

The maximum shear force that can be developed along the rockbolt/gridpoint interface is a function of the cohesive strength of the interface and the stress-dependent frictional resistance along with the interface (Figure 5.8b). The following equation can be used to determine the maximum shear force per length of the rockbolt:

$$\frac{F_s^{max}}{L} = cs_{scoh} + \sigma_c' \times tan\left(cs_{sfric}\right) \times perimeter \tag{5.5}$$

where cs_{scoh} is the cohesive strength of the shear coupling spring; σ'_c is the average effective confining stress perpendicular to the "rockbolt" element; cs_{sfric} is the friction angle of the shear coupling spring, and perimeter is the exposed perimeter of the element.

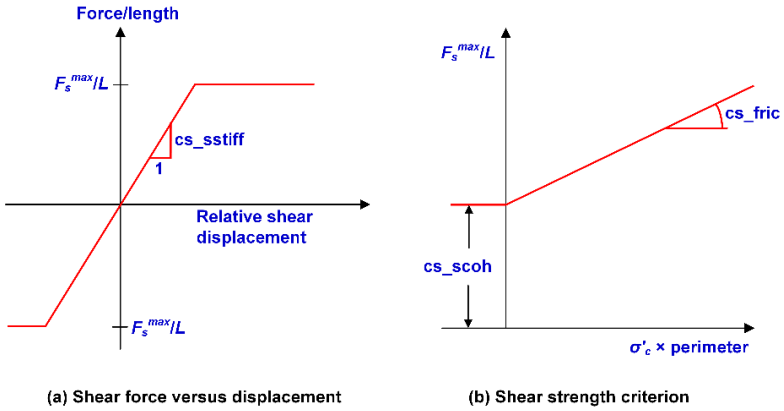

Figure 5.8 Mechanical behavior of shear coupling spring for the "rockbolt" element (Itasca, 2020).

The normal behaviour of the rockbolt/gridpoint interface is represented by a linear spring with a limiting normal force that is dependent on the direction of movement of the rockbolt node. The expected behaviour during the relative normal displacement between the rockbolt nodes and the gridpoint can be described numerically by the coupling spring normal stiffness (cs_{nstiff} in Figure 5.9a):

$$\frac{F_n}{L} = cs_{nstiff}\left(u_p^n - u_m^n\right) \tag{5.6}$$

where F_n represents the normal force that develops in the normal coupling spring (e.g., along with the interface between the rockbolt element and the gridpoint); cs_{nstiff} is the coupling spring normal stiffness; $u_p{}^n$ is the displacement of the rockbolt perpendicular to the axial direction of the rockbolt; $u_m{}^n$ is the displacement of the medium (soil or rock) perpendicular to the axial direction of the rockbolt, and L is the contributing element length.

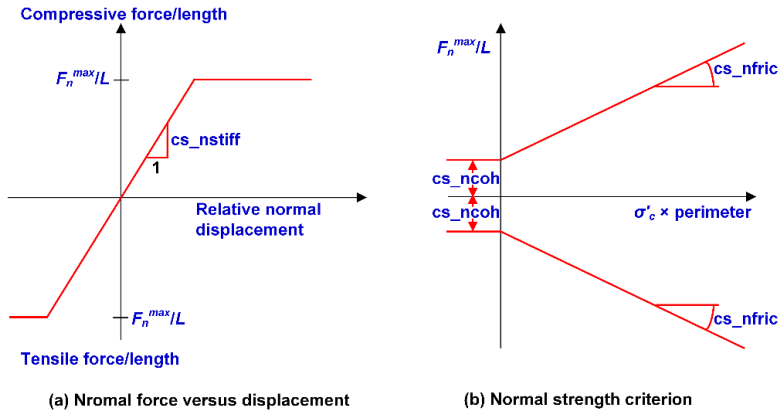

Figure 5.9 Mechanical behaviour of normal coupling spring for the "rockbolt" element (Itasca, 2020).

A limiting normal force can be prescribed to stimulate the localized three-dimensional effect of the rockbolt pushing through the grid (e.g., the soil being squeezed around a single rockbolt). The limiting normal force is a function of normal cohesive strength and a stress-dependent frictional resistance between the rockbolt and the gridpoint (Figure 5.9b). The following equation can be used to determine the maximum normal force per length of the rockbolt:

$$\frac{F_n^{max}}{L} = cs_{ncoh} + \sigma_c' \times tan\left(cs_{nfric}\right) \times perimeter \tag{5.7}$$

where cs_{ncoh} is the cohesive strength of the normal coupling spring, which depends on the loading direction; σ'_c is the average effective confining stress perpendicular to the rockbolt element; cs_{nfric} is the friction angle of the normal coupling spring, and perimeter is the exposed perimeter of the element.

(b) Calibration of rockbolt properties

The hypothesis of this study is that the drop test could not be representative of rockburst loading and the real performance of yielding rockbolts is complex, which should be evaluated during rockbursts with actual seismic loading. The pull-out test is a well-recognized test, and it can represent the static load-displacement characteristics of rockbolts before rockbursting and the performance of rockbolts during rockbursts will be initially confirmed by in situ observations (Cai et al., 2010, 2019; Charette and Plouffe, 2007; Li, 2021) and others' experimental (Hyett et al., 1996) and numerical simulation results (Lisjak et al., 2020; Ma et al., 2014). Hence, only the simulated pull-out tests were conducted to calibrate the input parameters of the "rockbolt" element with the comparison of the laboratory test results from Charette and Plouffe (2007), Stillborg (1994), and Li (2011). The model size is 2×1 m, and the bolt length is 2 m. This model size is almost identical to that of Bahrani and Hadjigeorgiou (2017). The model has Young's modulus of 7.5 GPa and a Poisson's ratio of 0.25 to represent an elastic rock mass because it has been confirmed that the elastic properties of the rock mass do not influence the load-displacement response of the "rockbolt" element (Tomasone et al., 2020) which can significantly save computation time. The

rockbolt was divided into 40 segments and 41 nodes to ensure that at least one node fell into each block zone (Bahrani and Hadjigeorgiou, 2017). The upper boundary of the model was free, and a vertical upward velocity of 0.08 m/s was applied to the end node of the bolt to simulate a pull action (Zhu et al., 2020). The roller constraints were applied on the side boundaries and the bottom boundary. A function was developed using the FISH language (built-in programming package) in UDEC to monitor the axial force of the last segment of the rockbolt.

Pull-out tests were modelled iteratively to adjust input parameters (e.g., tensile yield strength, tension failure strain, shear coupling spring stiffness, and shear coupling spring cohesion, Itasca, 2020) until the simulated results were consistent with the targeted properties of rockbolts. Other input parameters (e.g., the diameter, length, density, and elastic modulus of rockbolts) are the same as that used in laboratory tests. The simulated load-displacement curves and axial force of rockbolts and the block displacement are shown in Figure 5.10. The calibrated input parameters of rockbolts are listed in Table 5.5. The applied load is axial in an ideal pull test as simulated in this study. Thus, the parameters regarding resistance to bending are not employed. The errors between the targeted and simulated ultimate load, rupture displacement, and static energy-absorption capacity of rockbolts are less than 5 % (Table 5.6), indicating that the targeted values agree well with calibrated input parameters. Thus, the calibrated parameters in Table 5.5 could be used to further the numerical analysis of the performance of yielding and conventional rockbolts (Zhang and Nordlund, 2019). However, it should be noted that the sliding or extraction of Roofex was not simulated explicitly in the pull-out test, and its energy-absorption mechanism was simplified to the deformation or stretch of bolt shanks. This equivalent approach could be regarded as a relatively good selection at this stage since the complexity of simulating bolt sliding was ignored, and the time cost was thus significantly reduced.

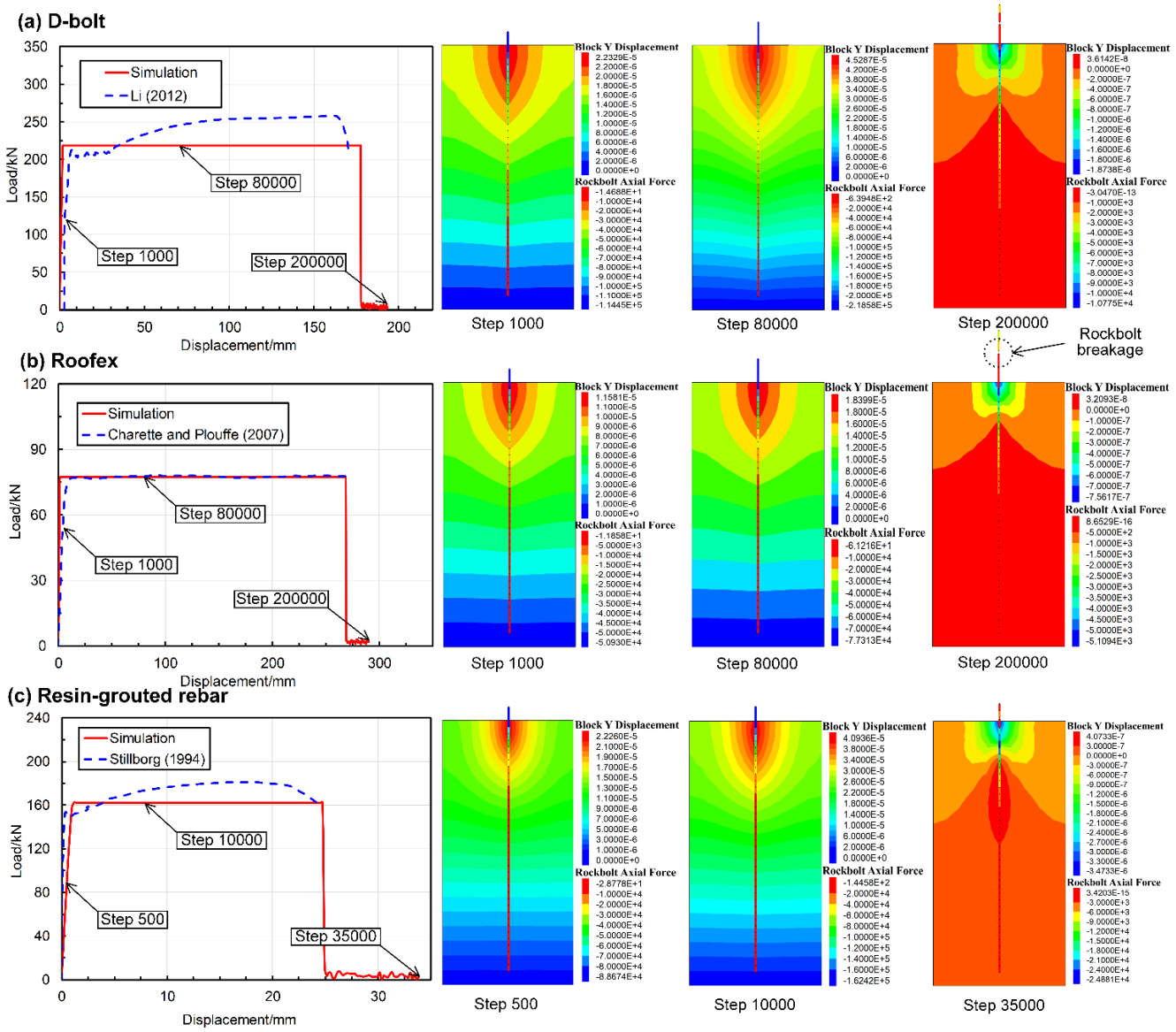

Figure 5.10 Simulated load-displacement curves and axial forces of rockbolts and deformation of rock masses. (Rockbolt axial force in N and block Y displacement in m.)

Table 5.5 Calibrated input parameters of rockbolts

Rockbolt type	Cross-sectional area (m^2)	Moment of inertia (m^4)	Perimeter of borehole (m)	Density (kg/m^3)	Elastic modulus (GPa)	Tensile yield strength (kN)	Tension failure strain	Shear coupling spring stiffness (GN/m/m)	Shear coupling spring cohesion (kN/m)	Shear coupling spring friction angle (°)
Resin-grouted rebar	3.14×10^{-4}	7.85×10^{-9}	0.08	7500	200	517	0.33	0.31	400	45
D-bolt	3.80×10^{-4}	1.15×10^{-8}	0.10	7500	200	575	1.36	0.29	438	45
Roofex	1.23×10^{-4}	1.20×10^{-9}	0.08	7500	200	630	1.66	0.21	353	45

Table 5.6 Comparison between the targeted and simulated rockbolt properties

Rockbolt type	Ultimate load (kN)	Rupture displacement (mm)	Static energy-absorption capacity (kJ)

	Laboratory test	Simulation	Error /(%)	Laboratory test	Simulation	Error /(%)	Laboratory test	Simulation	Error /(%)
Resin-grouted rebar	162	162	0.0	24.1	24.9	3.3	4.15	3.96	-4.6
D-bolt	212	219	3.3	170	178	4.7	40.23	38.65	-3.9
Roofex	77.6	77.3	-0.4	274	269	-1.8	20.94	20.71	-1.1

5.1.2.4 Simulation process and schemes

The following stages and schemes simulated the performance of yielding rockbolts during rockbursts.

Stage I (static stage): The in situ stress field was applied to the model, and the geostatic equilibrium was achieved. Then, the tunnel was excavated by deleting the blocks. Adequate calculation steps were run to ensure the surrounding rock stresses' gradual and slow release (Gao et al., 2015). The installation of rockbolts was conducted immediately after the excavation of the tunnel.

Stage II (dynamic stage): The dynamic mode was activated in this stage. Rockbursts having different magnitudes were produced by exerting a series of seismic waves with varied PPVs (0.2 m/s and 0.8 m/s, representing weak and strong rockbursts, Mutke et al., 2015). The pattern layout of rockbolts in the tunnel is shown in Figure 5.2. The roof and two ribs of the tunnel were supported by 15 rockbolts in total, while the floor remained unsupported, as is a common practice. The roof and rib bolts have a length of 2.5 m and row spacing of 0.7 m. The out-of-plane spacing of rockbolts is one meter by setting the “spacing” parameter in UDEC. Besides, D-bolt, Roofex, and fully resin-grouted rebar were simulated in each scheme.

5.1.3 Analysis of simulation results

5.1.3.1 Displacement and velocity analysis

The simulated displacement patterns of the tunnel supported by different rockbolts are shown in Figure 5.11. When the PPV is 0.2 m/s (see Figure 5.11a), large deformation only occurs in a local tunnel area that D-bolts support. In contrast, noticeable roof subsidence and sidewall shrinkage are observed when the tunnel is supported with Roofex and resin-grouted rebar. When the PPV is 0.8 m/s, the deformation of the tunnel surrounding rock masses aggravates due to more significant dynamic stresses. In addition to roof subsidence and sidewall shrinkage, severe floor heaving occurs in all three support schemes. This

phenomenon agrees with many facts that significant floor heaving is often observed in rockburst events with high seismic magnitudes (Mutke et al., 2009; Prusek and Masny, 2015). To further investigate the effects of different rockbolts on controlling rockbursts, four monitoring points were arranged at the roof, floor, and two sidewalls of the tunnel to record the tunnel deformation induced by rockbursts (Figure 5.2). The comparison of the tunnel deformation in three support schemes is shown in Figure 5.12. When the PPV is 0.2 m/s (Figure 5.12a), the tunnel supported by D-bolts suffers minor deformation (only 273 mm in total). However, the total deformations of the tunnel supported with Roofex and resin-grouted rebar are 1767 mm and 1086 mm, respectively, which are 6.47 and 3.98 times that of the tunnel supported by D-bolts. The most severe deformation is found when Roofex supports the tunnel. This is because the Roofex possesses the lowest strength (77 kN) compared to the D-bolt (219 kN) and resin-grouted rebar (162 kN). Thus, the Roofex fails to restrain the large deformation induced by rockbursts. When the PPV is 0.8 m/s (Figure 5.12b), the tunnel deformations in three support schemes all experienced significant growth. For instance, the total deformation of the tunnel supported by D-bolts increases from 273 mm to 2310 mm, with a growth rate of 746 %.

The tunnel deformation in this scenario is still the least compared to the other two support schemes. However, it can be found that the tunnel supported by resin-grouted rebar rather than Roofex suffers the most severe deformation. Although the resin-grouted rebar has relatively high strength, its elongation rate is low and easy to break during dynamic shocks. As shown in Figure 5.13a (iii), b (iii), many resin-grouted rebar bolts are broken during the rockburst; therefore, they cannot control rapid rock bulking or ejection effectively. Some in situ observations can confirm this phenomenon (Figure 5.14). In summary, the tunnel profile continuously shrinks with increasing seismic magnitudes. All three rockbolts fail to control the large deformation induced by dynamic stresses during the violent rockburst (PPV = 0.8 m/s).

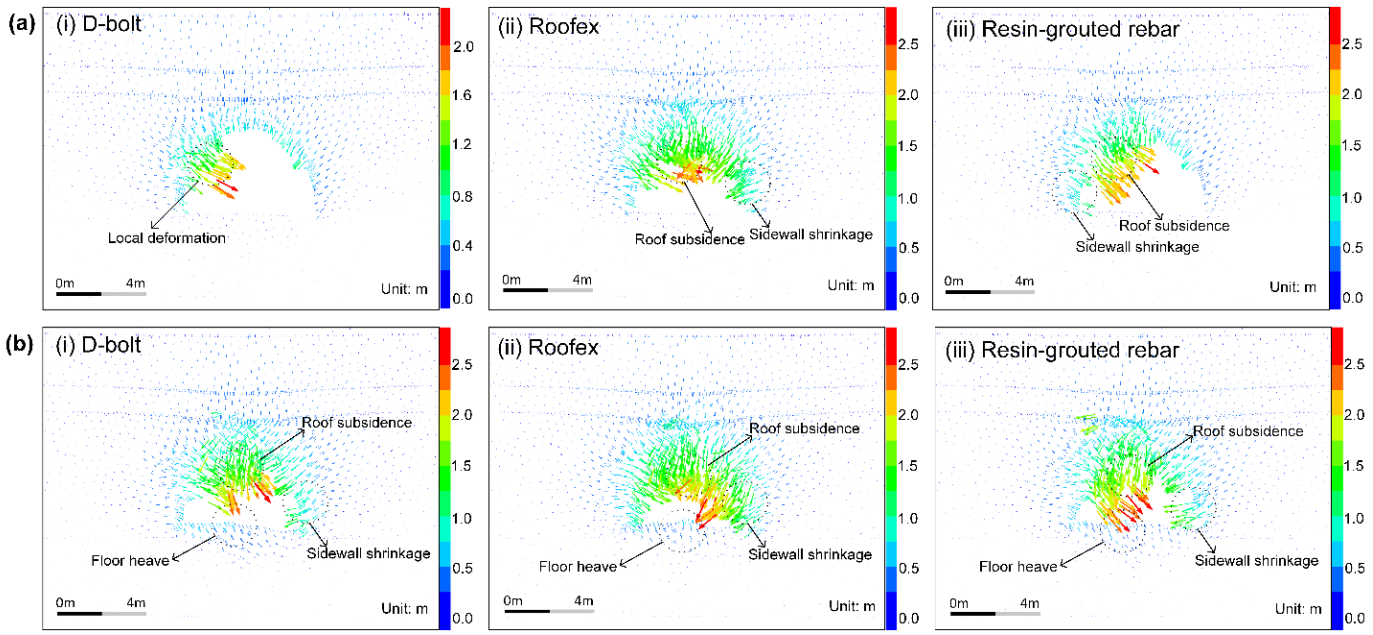

Figure 5.11 Simulated displacement vectors of the surrounding rock masses along the tunnel supported by different types of rockbolts. (a) PPV = 0.2 m/s. (b) PPV = 0.8 m/s.

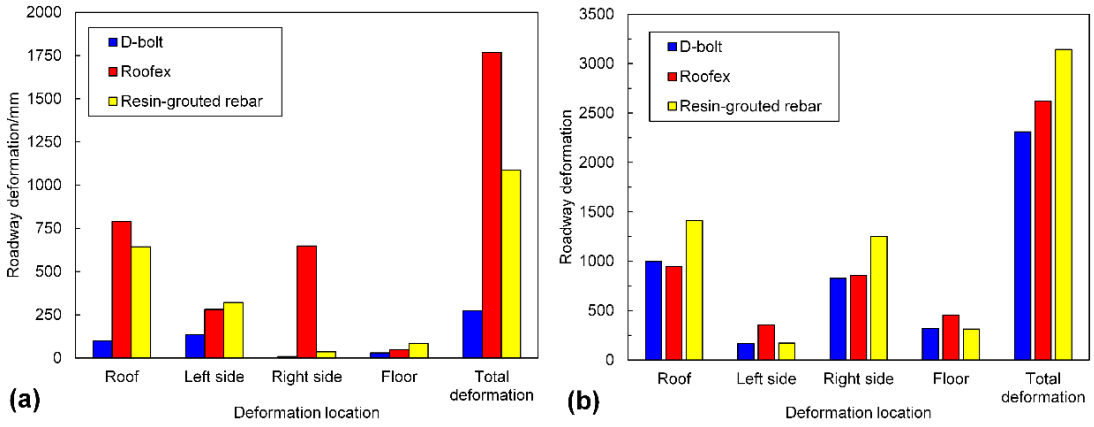

Figure 5.12 Comparison of the deformation of the tunnel supported by different types of rockbolts. (a) PPV = 0.2 m/s. (b) PPV = 0.8 m/s.

The velocity distribution of tunnel surrounding rock masses in three support schemes is shown in Figure 5.13. It can be seen from Figure 5.13a that only a few rock blocks are ejected from a local zone when the D-bolt is adopted. For the tunnel supported by Roofex and resin-grouted rebar, much more rock blocks are ejected from the roof and sidewalls. With the increase of PPVs, the range of the region with high velocities grows (see Figure 5.13b). A large quantity of ejected rock blocks is observed no matter which type of rockbolts is used. To further study the effects of different rockbolts on mitigating rockburst

damage, a function was developed using FISH language in UDEC to record the velocity and volume of all the detached rock blocks in the model. The statistical analysis results are illustrated in Figure 5.15. As shown in Figure 5.15a, the average velocity of rock blocks in the tunnel supported by D-bolts is only 1.20 m/s, although a few blocks may have a relatively high velocity (e.g., 10-18 m/s). By comparison, the average velocities of rock blocks in the tunnel supported with Roofex and resin-grouted rebar are 9.07 and 6.65 m/s, respectively.

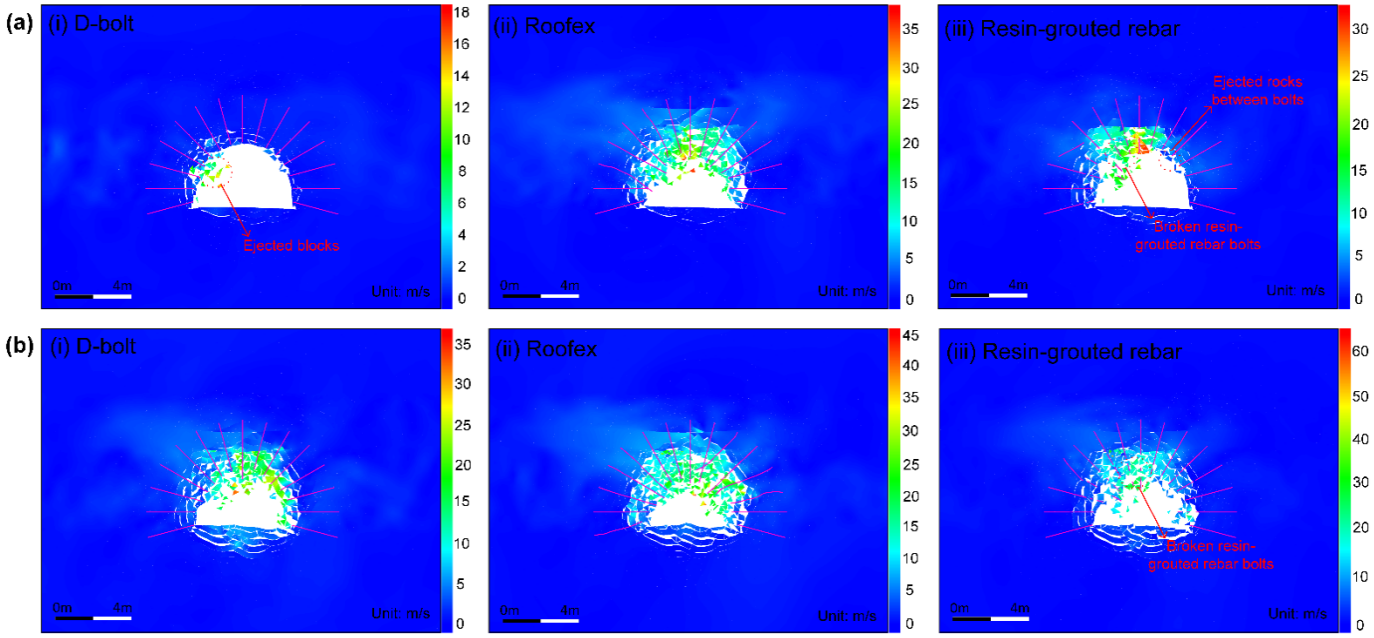

Figure 5.13 Simulated velocity distribution of the surrounding rock masses along the tunnel supported by different types of rockbolts. (a) PPV = 0.2 m/s. (b) PPV = 0.8 m/s.

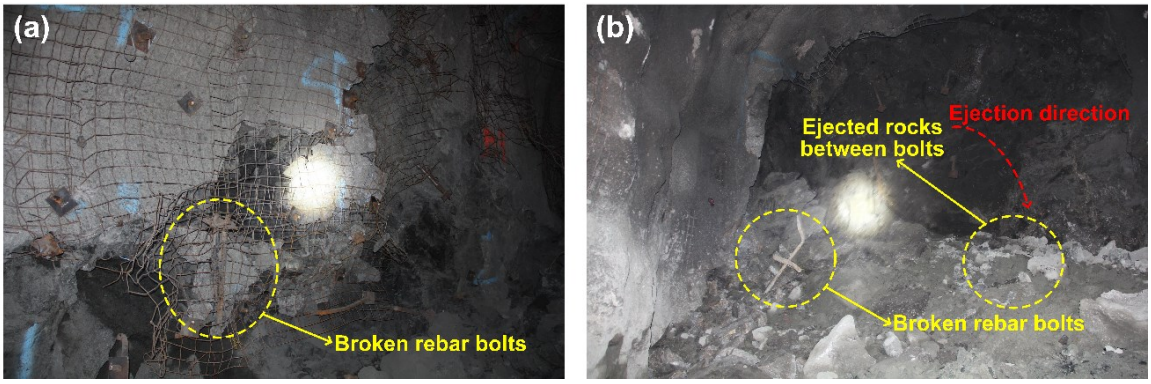

Figure 5.14 (a) and (b) are in situ observations of broken rebar bolts after rockbursts in deep tunnels in Canada (photographs taken by authors).

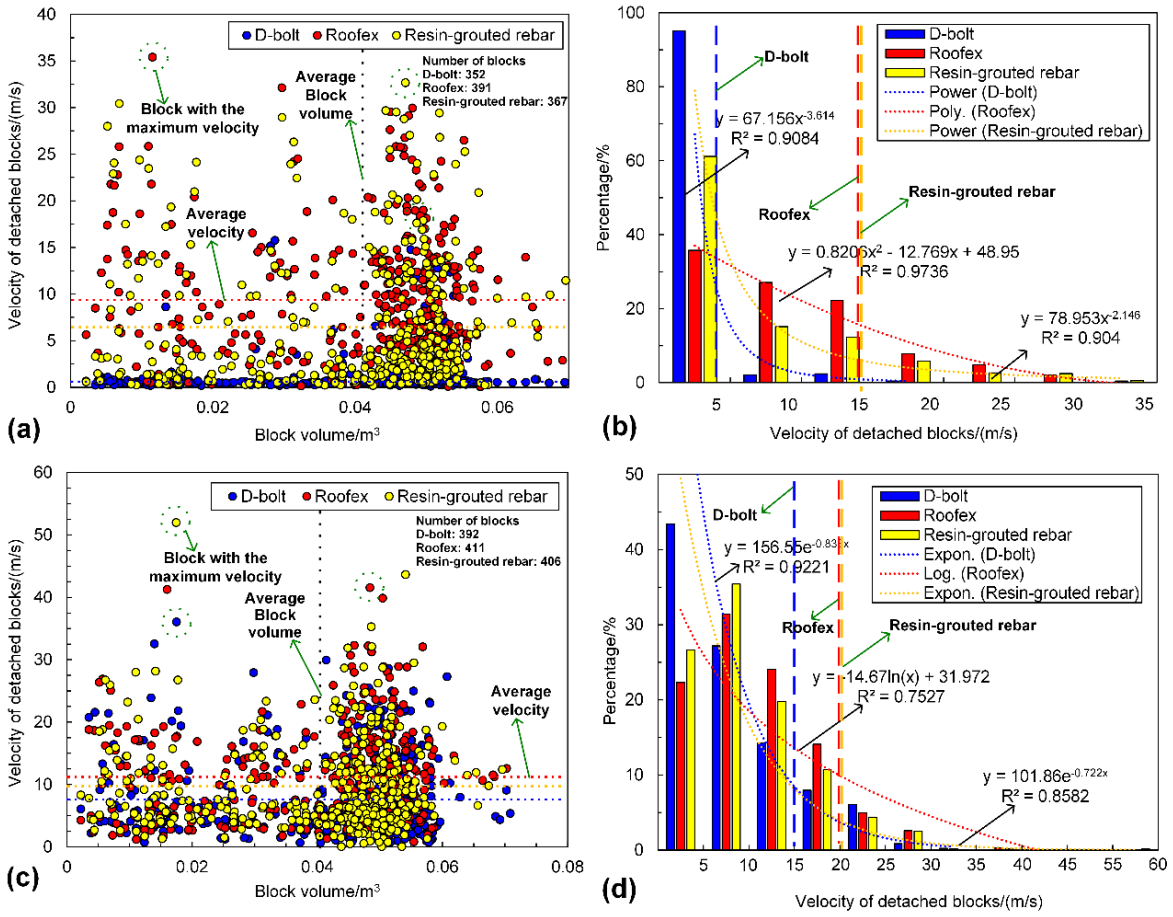

Figure 5.15 (a) and (c) is the velocity of all detached blocks versus block volume when the PPVs are 0.2 m/s and 0.8 m/s, respectively. (b) and (d) is the velocity distribution of all detached blocks when the PPV is 0.2 m/s and 0.8m/s, respectively.

Additionally, the velocity distributions of rock blocks in these two scenarios are more extensive than those in the tunnel using D-bolts. Figure 5.15b shows that 95.1% of rock blocks in the tunnel supported by D-bolts possess a velocity lower than 5 m/s, while the velocities of most rock blocks in the other two scenarios (85.1 % for Roofex and 88.6 % for resin-grouted rebar) are within the range of 0-15 m/s. Many rock blocks focus on the volume range of 0.04-0.055 m^3 due to the setting of the edge length of blocks (0.3 m) within the tunnel surrounding rock masses. When the PPV is 0.8 m/s (Figure 5.15c), the average velocities of rock blocks in the three support schemes undergo growth. For example, the average velocity of rock blocks in the tunnel supported by D-bolts increases from 1.20 to 8.34 m/s, with a growth rate of 595 %. It is also found that the velocity distributions of rock blocks in the three support schemes are more

extensive than in the tunnel during the weak rockburst. As shown in Figure 5.15d, 84.8 % of rock blocks in the tunnel supported by D-bolts possess a velocity of 0-15 m/s, while the velocities of most rock blocks in the other two scenarios (91.9 % for Roofex and 88.6 % for resin-grouted rebar) are within the range of 0-20 m/s. Another finding is that more rock blocks are detached or ejected when the PPV is 0.8 m/s. For instance, the number of detached rock blocks in the tunnel supported by D-bolts increases from 352 to 392, with a growth rate of 11.36 %. These results suggest that the rockburst is more violent when the PPV is high and further confirm that supporting three types of rockbolts are unable to control violent rockbursts.

5.1.3.2 Rockburst damage analysis

Studies have shown that many rock engineering accidents, including rockbursts, are due to the weakening of rock mass strengths resulting from the initiation and development of internal fractures (Chen et al., 2016; Gao et al., 2015; Yang et al., 2017). To investigate the influences of different rockbolts on mitigating rockburst damage, the crack distribution, macroscopic failure pattern, and damage degree of the tunnel induced by rockbursts was analyzed. A function was developed using the FISH language in UDEC to record the model's length and the number of failed contacts (representing cracks, including tensile and shear failure). A damage variable was then defined in the self-developed FISH function according to the ratio of the length of failed contacts to the total contact length in the model (Gao et al., 2015):

$$D_c = \frac{L_t + L_s}{L_c}, D_t = \frac{L_t}{L_c}, D_s = \frac{L_s}{L_c} \tag{5.8}$$

D_c, D_t, and D_s are total, tensile, and shear damage degrees, respectively. L_c, L_t, and L_s are the total contact length and the length of failed contacts in tensile and shear failure. The severity of rockburst damage can also be evaluated by the failed rock volume (Cai, 2013). Therefore, the volume of ejected rock blocks is recorded using another self-developed FISH function in the UDEC model.

Figure 5.16 shows the distribution of cracks and macroscopic failure patterns of the tunnel supported by different types of rockbolts. It is interesting to note that the range of the macroscopic failure zone is the same as that of the tensile damage. This suggests that the initiation, propagation, and development of tensile cracks play a key role in controlling macroscopic failures of surrounding rock masses. The finding agrees that when the stress wave reaches the tunnel surface, the difference in wave impedance between rock and air is excellent. Hence, most stress waves are reflected at the surface, causing tensile spalling of the tunnel surrounding rock masses (Wu et al., 2019). As shown in Figure 5.16a, when D-bolts are adopted in the tunnel, the extent of rockburst damage is smaller than that of the tunnel supported with Roofex and resin-grouted rebar. Only a few rock blocks are ejected between bolts, and the tunnel surrounding rock masses is overall stable. However, for the tunnel using Roofex and resin-grouted rebar, many more ejected rock blocks are found, and rockfall occurs.

The tunnel tends to be unstable. The comparison of damage degrees of the tunnel is shown in Figure 5.17a, b. It should be noted that the tunnel damage in the excavation stage was excluded since this study focuses on assessing the performance of yielding rockbolts during rockbursts. When the PPV is 0.2 m/s (Figure 5.17a), the total damage degrees of the tunnel supported by D-bolt and resin-grouted rebar is 0.91 % and 0.74 %, respectively, which are lower than that of the tunnel using Roofex supporting (1.14 %). When the rockburst is violent, the tunnel damage is more serious (Figure 5.16b). For example, the total damage degree of the tunnel using D-bolts is increased from 0.91 % to 1.42 %, with a growth rate of 56 % (Figure 5.17b).

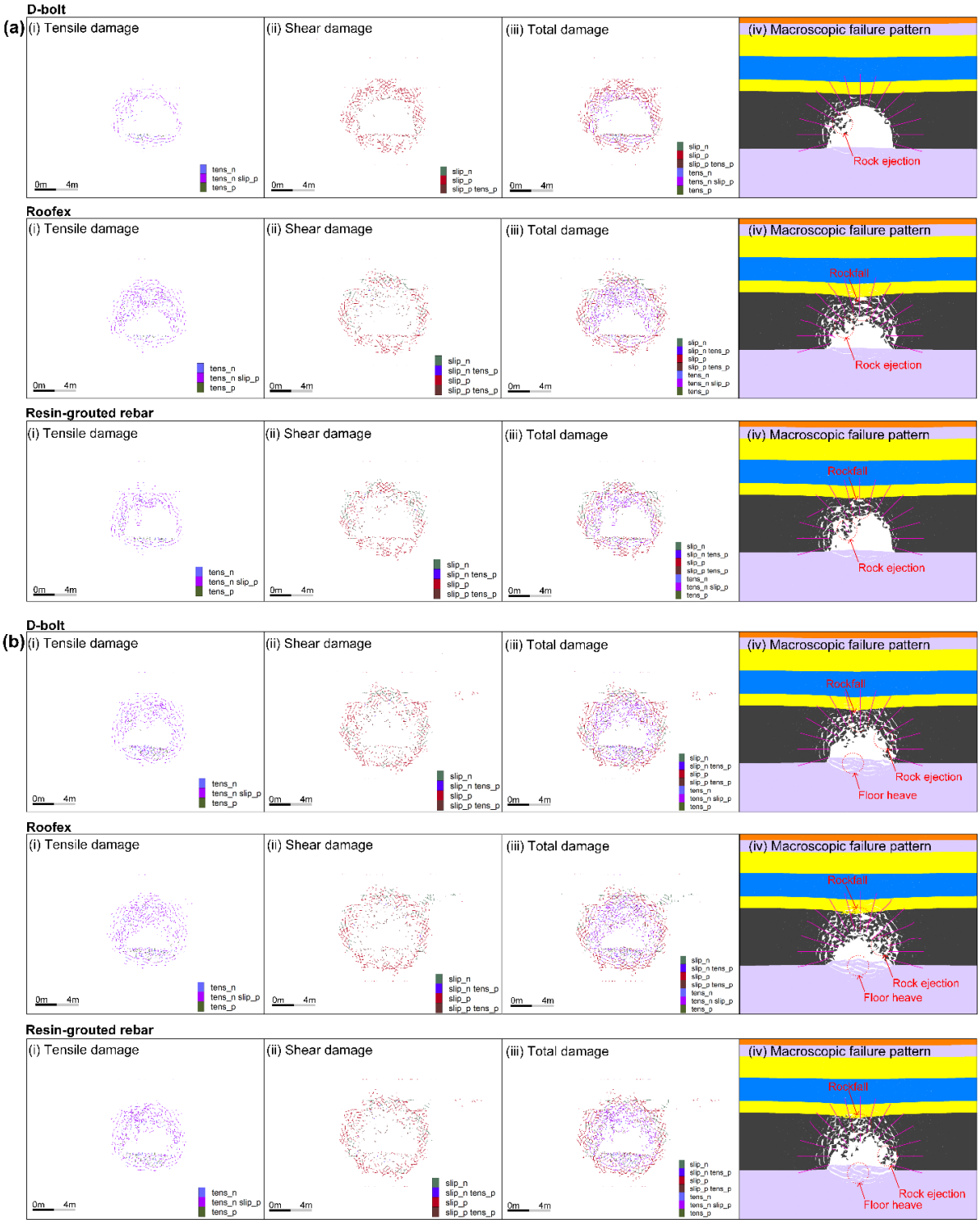

Figure 5.16 Distribution of cracks and macroscopic failure patterns of the tunnel supported by different types of rockbolts. (a) PPV = 0.2 m/s. (b) PPV = 0.8 m/s.

Nevertheless, minor rockburst damage is found when the tunnel adopts D-bolt support, while the total damage degree of the tunnel supported with Roofex and resin-grouted rebar is 1.63 %. Some results seem

confusing, especially when the PPV is 0.2 m/s. In this scenario, the resin-grouted rebar is better in mitigating rockbursts damage over D-bolt and Roofex. This is because the resin-grouted rebar is a stiff support fashion. It can effectively restrain the initiation and development of cracks (Yang et al., 2017) and reduce damage degrees. However, many resin-grouted rebar bolts are broken when the rockburst is violent due to more significant dynamic stresses. The resin-grouted rebar bolts lose their functions to prevent the development of fissures, and therefore the rockburst damage degree is high.

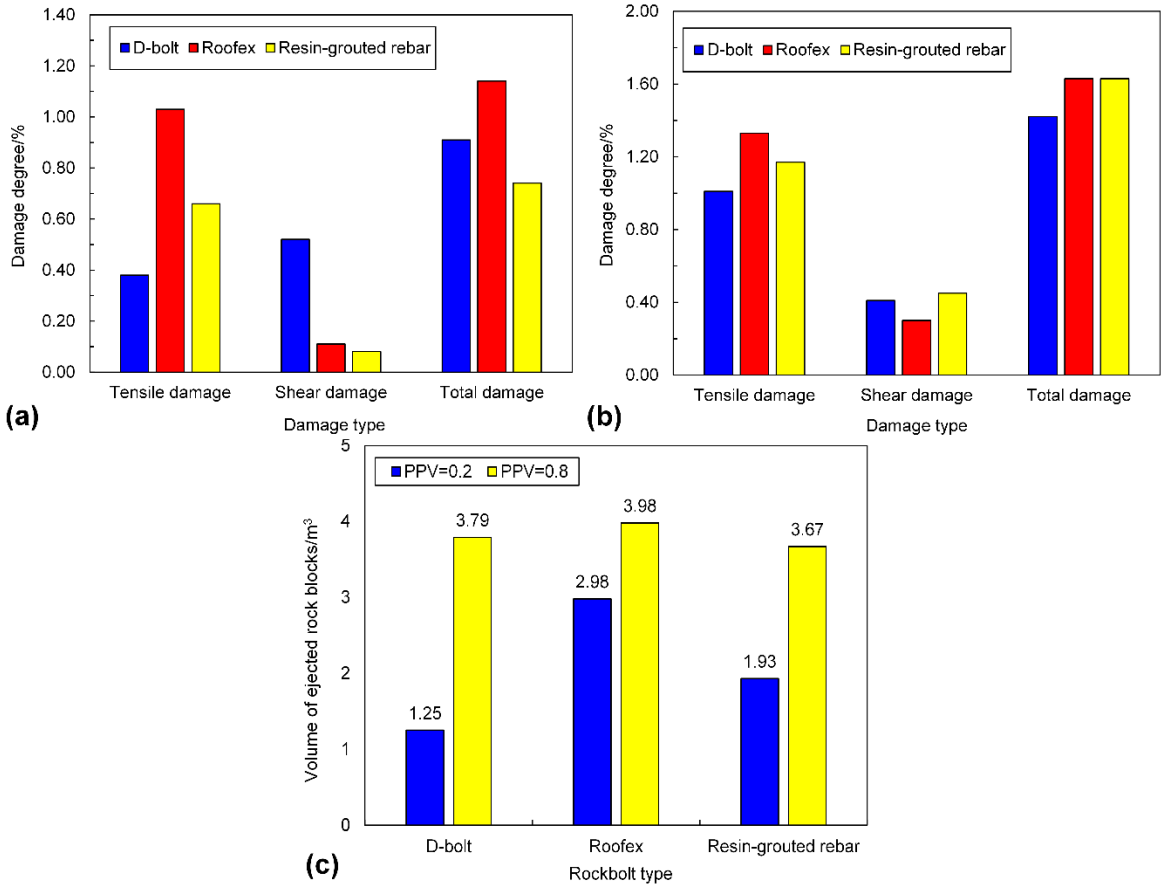

Figure 5.17 (a) and (b) are the damage degrees of the tunnel when the PPVs are 0.2 and 0.8 m/s, respectively. (c) is the volume of ejected rock blocks of the tunnel induced by rockbursts.

Comparing the volume of ejected rock blocks of the tunnel in three support schemes is shown in Figure 5.17c. The volume of ejected rock blocks is the least (1.25 m^3) when the tunnel uses D-bolt supporting during a weak rockburst (PPV = 0.2 m/s). However, the volume of ejected rock blocks of the tunnel supported with Roofex and resin-grouted rebar is 2.98 m^3 and 1.93 m^3, respectively, which are 2.38 and

1.54 times that of the tunnel supported by D-bolts. The rockburst damage is the most serious when Roofex supports the tunnel due to its lower strength to limit rock deformations and damage. When the PPV is 0.8 m/s, the volume of ejected rock blocks in three support schemes undergoes significant growth. For example, the volume of ejected rock blocks of the tunnel supported by Roofex increases from 2.98 to 3.98 m^3, with a growth rate of 33.56 %. The ejected block volume in this scenario is still the greatest compared to the other two support schemes. The difference between D-bolt and resin-grouted rebar is very little (only 0.12 m^3). It can also be found that the difference in the ejected block volume between different rockbolt types is similar to that of tunnel deformations and damage degrees, which suggests that the volume of ejected rock blocks is a clear and straightforward variable to evaluate rockburst damage severity.

5.1.3.3 Energy evolution analysis

The severity of rockbursts is related to the magnitude of the kinetic energy of ejected rock materials (Cai, 2013; Gao et al., 2019b). The kinetic energy is one part of the total released energy that the supporting system (e.g., rockbolt, cable bolt, liner, and wire mesh) must absorb to reduce rockburst risks (Raffaldi et al., 2017). Therefore, the influences of rockbolt supporting the distribution and change of kinetic energy were investigated in this study. The kinetic energy of ejected rock blocks was captured by the FISH language programming in UDEC using the following formula:

$$W_k = \sum \frac{1}{2} m v^2 \tag{5.9}$$

where *m* and *v* are the mass and velocity of ejected rock blocks at the current time step.

The distribution of kinetic energy of ejected rock blocks in three support schemes is shown in Figure 5.18. It can be seen that the kinetic energy pattern is very similar to that of velocity (see Figure 5.13). As shown in Figure 5.18a, only a few rock blocks have relatively high kinetic energy when the D-bolt is adopted. Much more rock blocks possess higher kinetic energy for the tunnel supported by Roofex and resin-grouted rebar. With the increase of PPVs, the range of the region with great velocities grows (see

Figure 5.13b), and thus more rock blocks possess high kinetic energy (Figure 5.18b), which suggests that the rockburst damage is severe. The variation of kinetic energy with time influenced by different rockbolt types is illustrated in Figure 5.19a, b. When the PPV is 0.2 m/s, the evolution of kinetic energy in three support schemes can all be divided into two stages. For D-bolt, the kinetic energy increases slowly to the peak value from 0 to 84 ms and then gradually declines. For Roofex, the kinetic energy experiences fast growth, especially after 52 ms, and reaches the peak value at 105 ms. Then, the kinetic energy drops with time but is still at a high level. When the tunnel is supported by resin-grouted rebar, the kinetic energy first increases slowly to a plateau from 0 to 97 ms and then suffers a sudden surge.

In contrast, the kinetic energy of ejected rock blocks in three support schemes increases almost linearly with time when the PPV is 0.8 m/s, although they may experience several fluctuations. In summary, when the PPV is 0.2 m/s, D-bolts effectively absorb the kinetic energy of ejected rock blocks, and the rockburst is controlled. However, they cannot absorb sufficient kinetic energy to control a violent rockburst successfully. Roofex and resin-grouted rebar fail to effectively reduce the kinetic energy of ejected rock blocks and cannot solely control weak and strong rockbursts.

To further evaluate the dynamic energy-absorption capacity of three types of rockbolts, the tunnel without adopting any supports during rockbursts (PPVs are 0.2 and 0.8 m/s) was simulated. Then, a new variable was defined as the reduced kinetic energy, the difference between the final kinetic energy of ejected rock blocks in the tunnel without and using rockbolts. It should be noted that the calculation of the energy-absorption magnitude of rockbolts is not feasible because the action of rockbolts during rockbursts is very complex and is no longer a simple pull-out test or drop test (Zhang and Nordlund, 2019). Thus, the indirect calculation method used in this study can be accepted as a relatively rational estimation to assess the dynamic energy-absorption capacity of rockbolts. Figure 5.19c compares the reduced kinetic energy of ejected rock blocks in the tunnel supported by different rockbolts. When the tunnel uses D-bolt support,

the reduced kinetic energy is the highest (673.19 and 1485.44 kJ for PPV = 0.2 and 0.8 m/s). By comparison, the reduced kinetic energy is the lowest (22.91 and 829.71 kJ) for the tunnel supported by Roofex, while the performance of resin-grouted rebar on reducing kinetic energy is in between the D-bolt and Roofex. It might be argued that the Roofex, a yielding rockbolt, has a higher energy-absorption capacity than resin-grouted rebar (20.94 vs. 4.15 kJ, see Table 5.3), and should reduce more kinetic energy than resin-grouted rebar. This could be because Roofex has a lower strength, and its sliding mechanism can be easily activated. Thus, it is too "soft" or "smooth" to limit ejected rocks' movement compared to the resin-grouted rebar and D-bolts. It can also be seen that the reduced kinetic energy grows with the increasing PPVs. This law is consistent with some published simulation results (Raffaldi et al., 2017; Raffaldi and Loken, 2016). Therefore, it can be concluded that the dynamic energy-absorption capacity of rockbolts is affected by rockburst magnitudes, which should be considered in rockburst support designs. This finding also verifies the hypothesis that the performance of rockbolts during rockbursts is complex, while the dynamic energy-absorption capacity of rockbolts obtained from drop tests is usually a constant value (Bosman et al., 2018).

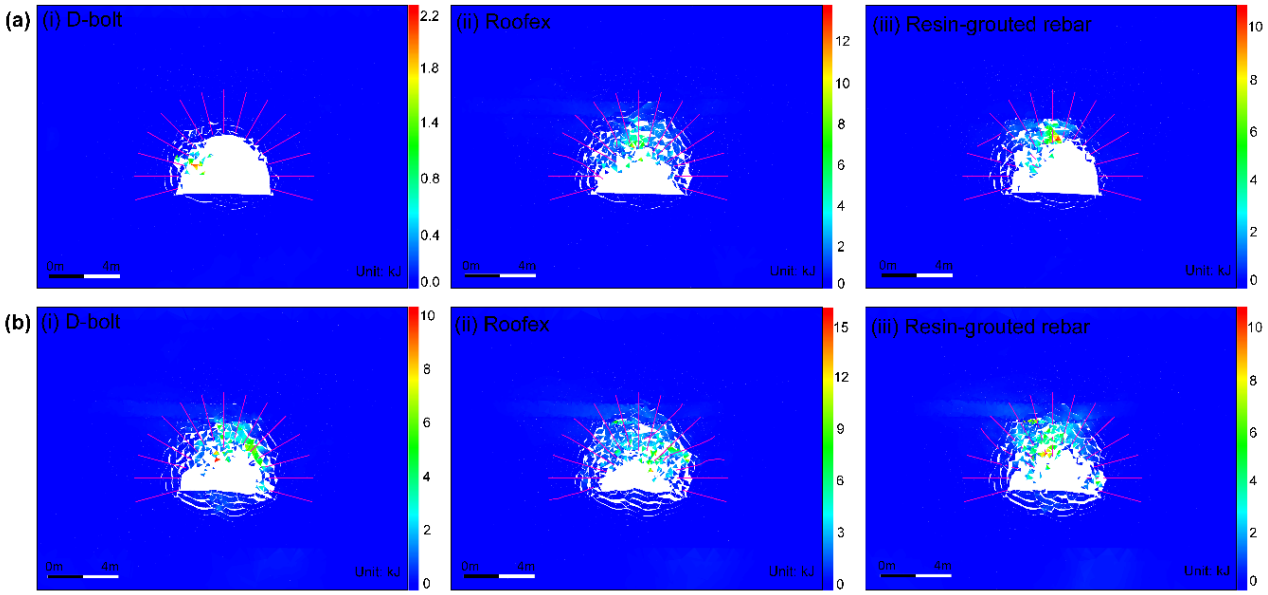

Figure 5.18 Simulated kinetic energy distribution of ejected rock blocks in the tunnel supported by different types of rockbolts. (a) PPV = 0.2 m/s. (b) PPV = 0.8 m/s.

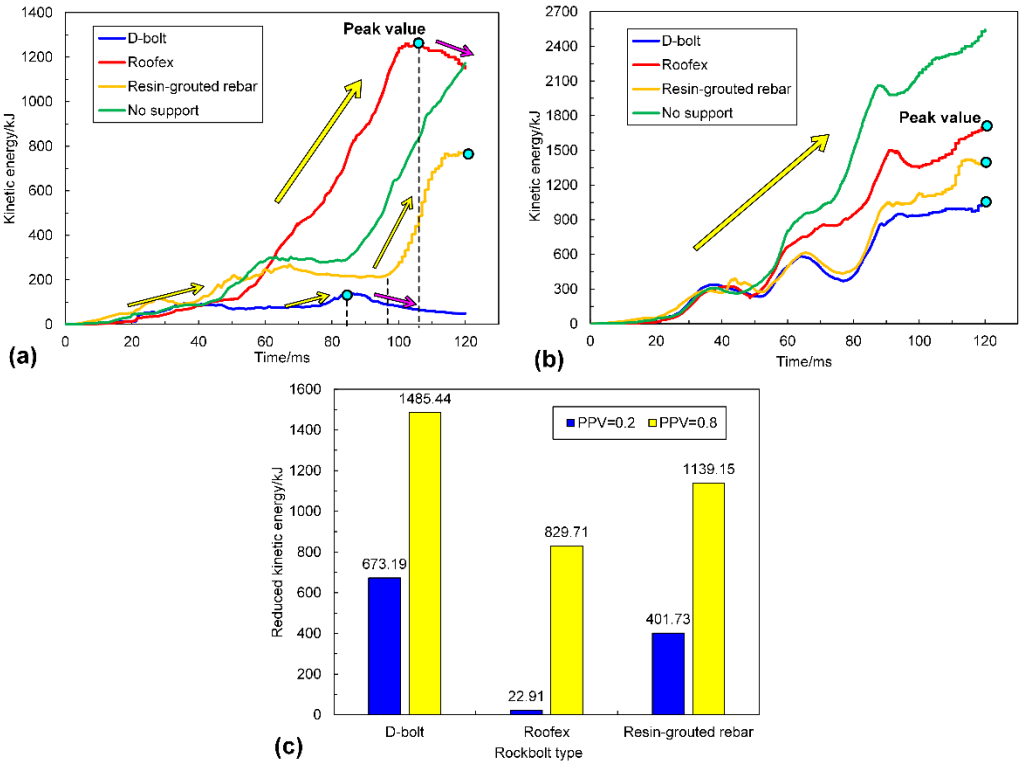

Figure 5.19 (a) and (b) are the evolution of the kinetic energy of ejected rock blocks in the tunnel when the PPVs are 0.2 and 0.8 m/s, respectively. (c) is the comparison of reduced kinetic energy of ejected rock blocks in the tunnel.

5.1.3.4 Rockbolt force analysis

The simulated axial force distribution of rockbolts in three support schemes is shown in Figure 5.20. In all three cases, the tensile axial force tends to reach the peak value at a certain distance (around 1-1.5 m) from the bolt end (head) and then gradually decreases to a low value. The simulated axial force patterns of rockbolts agree with some published experimental (Hyett et al., 1996) and numerical simulation results (Lisjak et al., 2020; Ma et al., 2014). For example, when the PPV is 0.2 m/s (Figure 5.20a), the average peak values of axial forces for three rockbolt types are 151.77 kN, 61.27 kN, and 151.05 kN, respectively. Thus, the D-bolt and resin-grouted rebar can bear the high load of rock masses, while the Roofex cannot provide sufficient resistance to control large rock deformation and rapid rock bulking during rockbursts.

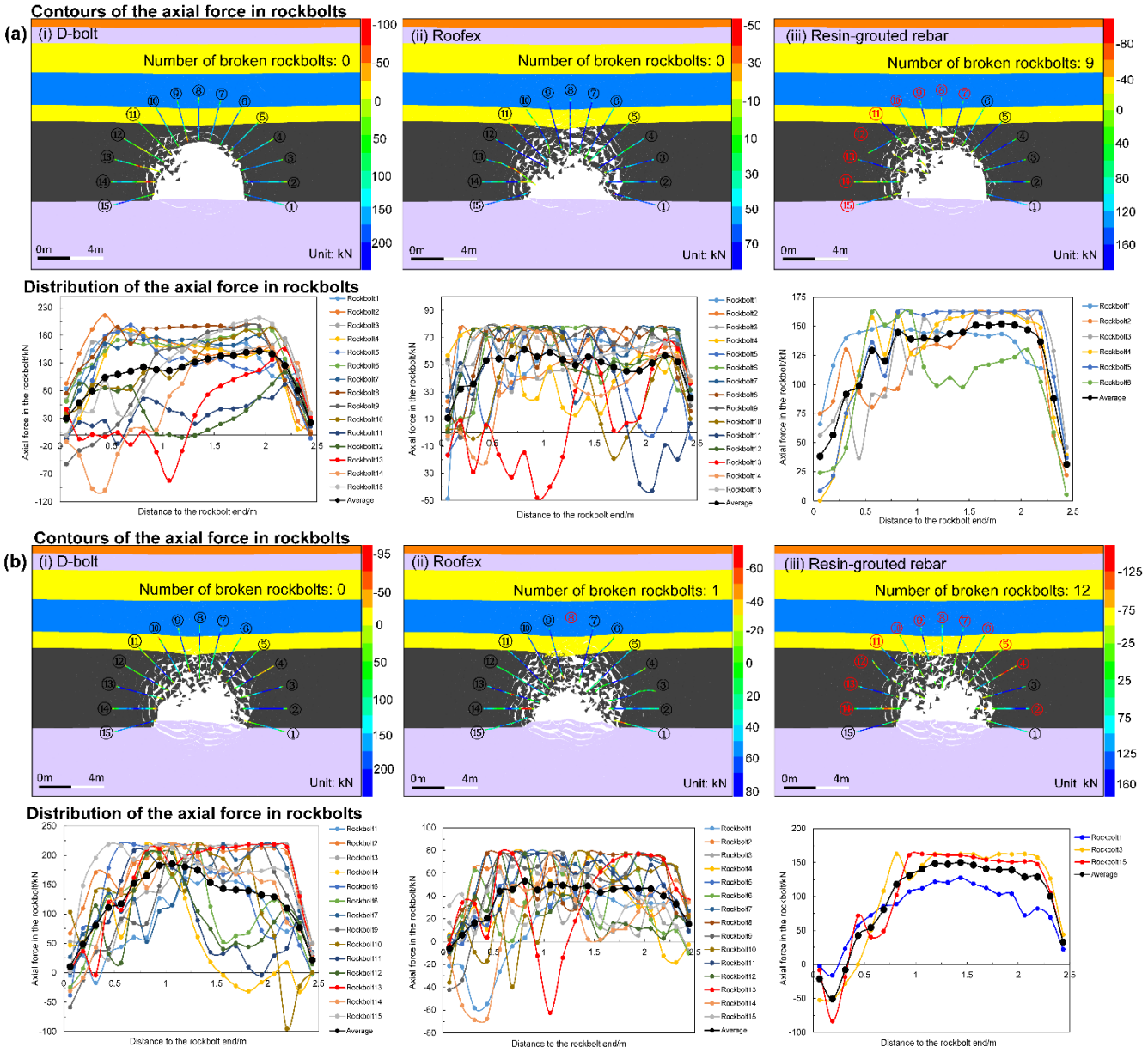

Figure 5.20 Simulated contours and distribution of the axial force in rockbolts for the tunnel supported by different rockbolts. (a) PPV = 0.2 m/s. (b) PPV = 0.8 m/s. The black and red numbers indicate intact and broken rockbolts, respectively. The positive value of axial forces represents a tensile load.

Additionally, it can be observed that nine resin-grouted rebar bolts are broken, resulting in the unsuccessful control of the rockburst. Again, this is because the resin-grouted rebar has limited deformation capacity to accommodate rapid rock bulking and relieve rock ejection (Cai, 2013; Kaiser and Cai, 2012). No broken rockbolts found for the tunnel adopting D-bolt and Roofex supporting. This finding agrees well with many in situ observations (Cai et al., 2010, 2019; Charette and Plouffe, 2007; Li, 2021).

An example is shown in Figure 5.21. When the PPV is 0.8 m/s (Figure 5.20b), the simulated axial force patterns of rockbolts resemble a weak rockburst (PPV = 0.2 m/s). The average peak values of axial forces for the three rockbolt types are 185.49 kN, 53.30 kN, and 151.17 kN, respectively. However, more rockbolts are broken due to violent rock ejection and bulking. No. 9 D-bolt in the middle roof is broken, while 12 resin-grouted rebar bolts are found to be broken in the roof and two sidewalls, with an increase of three broken bolts.

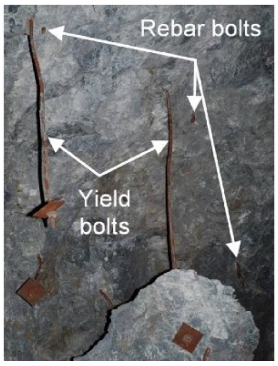

Figure 5.21 Observed performance of fully resin-grouted rebar and yielding rockbolts in a rockburst (Li, 2021).

Furthermore, it can also be observed that the location of broken rockbolts mainly depends on the rock ejection direction (Figure 5.20a (iii), b (iii)). In summary, the D-bolt and resin-grouted rebar can maintain a high axial force level during rockbursts to restrain rock ejection and bulking, but the resin-grouted rebar is prone to be broken due to a minimal elongate rate failing to mitigate rockburst damage effectively. On the other hand, Roofex's axial force is too low to control the rockburst, although it has an excellent deformation capacity over the other two rockbolt types. Besides, the axial force patterns and the intactness of D-bolt and Roofex verify the reliability and rationality of the "rockbolt" element in modeling the performance of yielding rockbolts.

5.1.4 Discussion

5.1.4.1 Effects of floor supporting

According to current simulation results and in situ observations (Mutke et al., 2009; Prusek and Masny, 2015), significant floor heaving occurs in violent rockbursts. Besides, the rockbolt supporting in roof and

sidewalls do not have notable influences on the floor response. Therefore, it is interesting to explore whether yielding rockbolts can be used to restrain floor heaving induced by rockbursts or not. Since the D-bolt performs better on controlling rockbursts than Roofex and resin-grouted rebar based on previous analyses, it was decided to simulate the tunnel supported by D-bolts with floor supporting during a violent rockburst (PPV = 0.8 m/s). The floor is supported by five D-bolts with a length of 2.5 m and row spacing of 1.4 m, while other parameters remain constant.

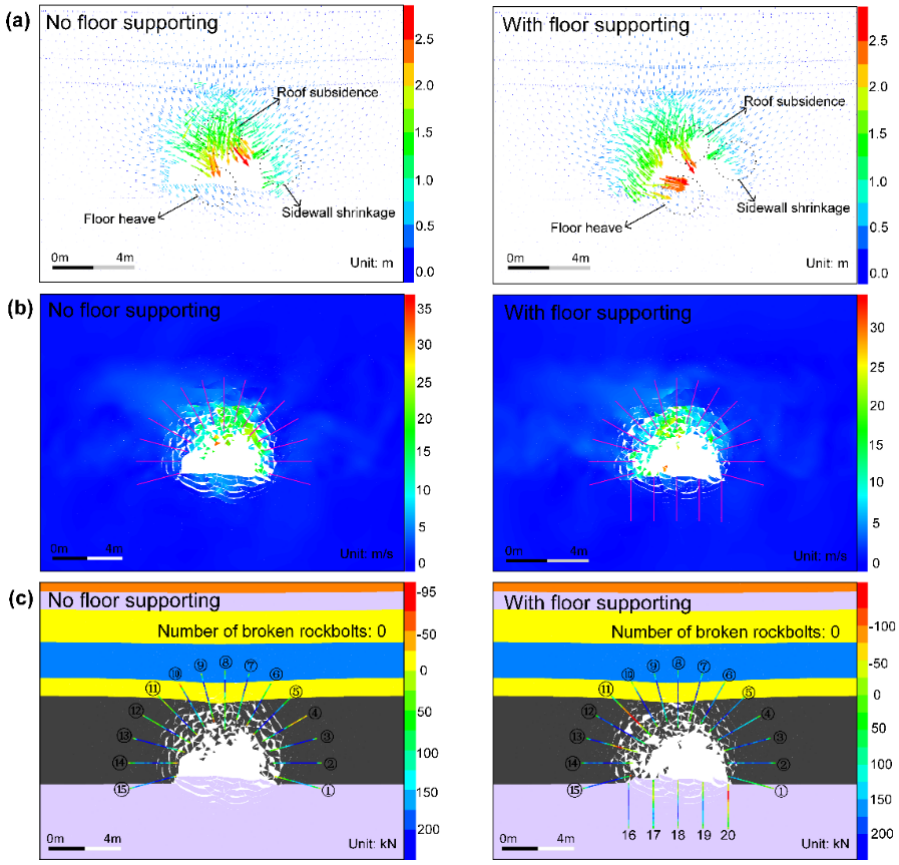

Figure 5.22 (a), (b), and (c) are simulated displacement vectors, velocity distribution, and macroscopic failure patterns of the tunnel and rockbolt axial forces.

The simulation results are shown in Figure 5.22 and Figure 5.23. It can be seen from Figure 5.22a that the floor heaving is reduced, although it still occurs when the tunnel adopts floor support. The floor heaving value is dropped from 320.5 to 148.5 mm, decreasing by 53.67 %. As shown in Figure 5.22b, the velocities of rock blocks in the floor are significantly reduced, which are lower than 3 m/s. By comparison,

the velocities can be up to 5-8 m/s when the floor is not supported. The statistical analysis results of the velocities of all detached rock blocks are illustrated in Figure 5.23a, b. As shown in Figure 5.23a, the average velocity of rock blocks in the tunnel without floor support is 8.34 m/s, while the average velocity decreases by 1.64 m/s to 6.70 m/s when the floor is supported. In addition, the velocity distributions of rock blocks in these two scenarios are all extensive.

Figure 5.23b shows that 84.8 % of rock blocks in the tunnel with floor supporting possess a velocity lower than 15 m/s, while 91.7 % of the tunnel without floor supporting are within the same velocity range. Figure 5.22c also shows that the severity of floor heaving is reduced, but rockfall and rock ejection are still observed. The variation of kinetic energy with time in two scenarios is illustrated in Figure 5.23c. The kinetic energy of ejected rock blocks almost increases linearly when the floor is not supported, although it may experience several fluctuations. In contrast, kinetic energy evolution can be divided into two stages when the floor uses D-bolts. The kinetic energy increases to the peak value from 0 to 99 ms and then gradually declines. This is because more rockbolts are deformed to absorb the kinetic energy of ejected rock blocks, which confirms the lower average velocity.

Figure 5.23d also shows that the tunnel suffers lower damage when using floor support. The volume of ejected rock blocks is decreased by 0.74 m^3 to 3.05 m^3, while the reduced kinetic energy increases to 1831.06 kJ, with a growth rate of 23.27 %. These results suggest that floor heaving and the tunnel's rockburst damage can be mitigated by floor supporting with D-bolts as the tunnel surrounding rock is an integrity system (Wang et al., 2018). However, rock blocks' average velocity and kinetic energy are still high, indicating that the new support scheme fails to control a strong rockburst.

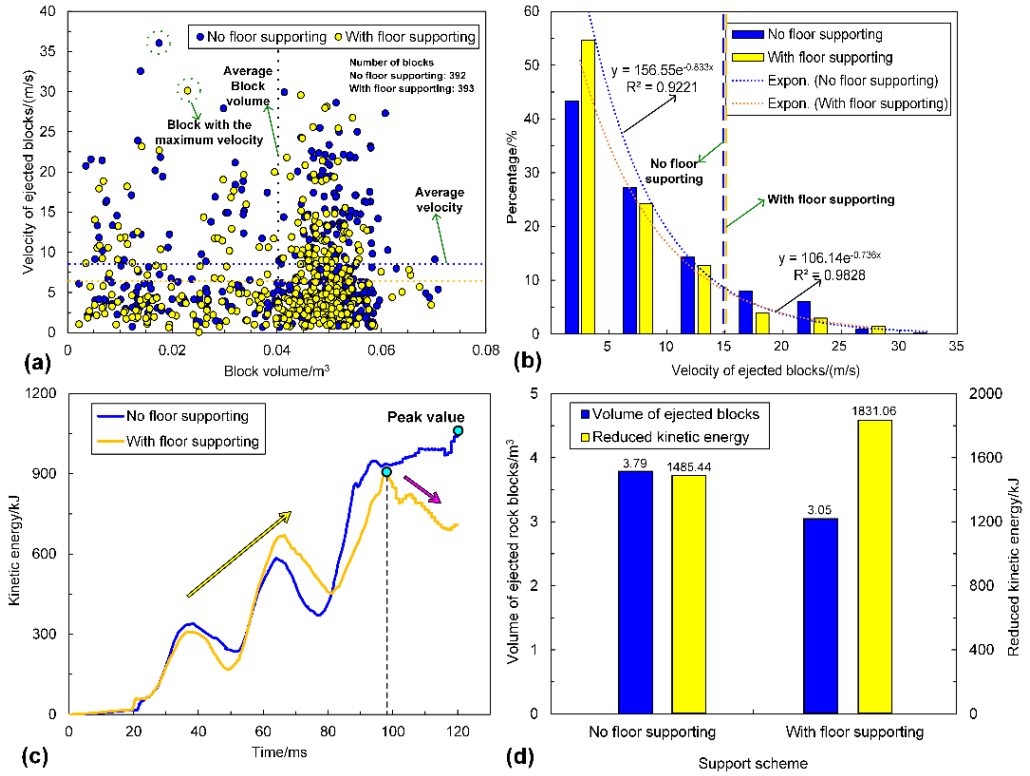

Figure 5.23 (a) is the velocity of all detached blocks versus block volume. (b) is the velocity distribution of all detached blocks. (c) is the evolution of the kinetic energy of ejected rock blocks in the tunnel. (d) is the comparison of the volume of ejected rock blocks and reduced kinetic energy.

5.1.4.2 Effects of cable bolts

Previous analyses show that supporting three types of rockbolts solely is unable to control violent rockbursts. This is because the effective support length of some rockbolts is less than the depth of the rock loose circle resulting in the instability of the tunnel (Wang et al., 2015). Therefore, it is exciting and necessary to discuss the possibility of strengthening the support system, e.g., using cable bolts. The application of cable bolts is common in many burst-prone underground tunnels (Cai, 2013). The cable bolts with high strengths and pre-stress can restrain the initiation and development of tensile and shear cracks and resist large deformation, thereby strengthening surrounding rock masses and maintaining their integrity (reinforcement function).

Furthermore, cable bolts usually have a great length, holding retaining elements and overhanging the combined arch of bolt supporting back to stable areas in depth (excavation influenced zone, Wang et al.

2015). Besides, the cable bolts also have a relatively high elongation rate (4-7 %, Kang et al., 2009) to absorb the deformation energy induced by rock bulking. Hence, the tunnel supported by D-bolts plus seven plain cable bolts during a violent rockburst (PPV = 0.8 m/s) was simulated in this research. The plain cable bolts have a length of 7.2 m and row spacing of 1.7 m, while other parameters remain constant. Therefore, the input parameters of the cable element in UDEC are adopted from Chen et al. (2016), Gao et al. (2015), and Yang et al. (2017), as listed in Table 5.7.

Table 5.7 Input parameters of the cable element (from Chen et al., 2016, Gao et al., 2015, and Yang et al., 2017)

Input parameters	Cross-sectional area (m^2)	Density (kg/m^3)	Elastic modulus (GPa)	Tensile yield strength (kN)	Grout stiffness (GN/m/m)	Grout strength (kN)
Cable	3.14×10^{-4}	7500	200	500	2	400

The simulation results are shown in Figure 5.24 and Figure 5.25. Figure 5.24a shows that the roof subsidence is reduced while sidewall shrinkage and floor heaving still occur when the tunnel adopts cable bolts. The roof subsidence magnitude is dropped from 1459.3 to 711.1 mm, decreasing 51.27 %. As shown in Figure 5.24b, the range of the region with high velocities is significantly reduced, and fewer ejected rock blocks are observed compared to the tunnel without cable support. The statistical analysis results of the velocities of all detached rock blocks are illustrated in Figure 5.25a, b. As shown in Figure 5.25a, the average velocity of rock blocks is decreased from 8.34 to 3.61 m/s when using cable bolts, with a decrease rate of 56.71 %. Besides, the velocity distributions of rock blocks in the tunnel using cable bolts are less extensive. Figure 5.25b shows that 84.8 % of rock blocks in the tunnel without cable support possess a velocity lower than 15 m/s, while 80.72 % of rock blocks are within the velocity range of 0-5 m/s for the tunnel using cable bolts. Figure 5.25c depicts that the severity of rockburst damage is remarkably reduced because the rock ejection only occurs in several local areas between rockbolts. This is mainly due to the absence of surface retaining elements (e.g., shotcrete and wire mesh). The variation of kinetic energy with time in two scenarios is illustrated in Figure 5.25c. Like the tunnel using floor support, kinetic energy evolution can be divided into two stages when the tunnel adopts cable bolts. First, the kinetic energy

increases to the peak value from 0 to 67 ms and then gradually declines and reaches a lower level. This indicates that cable bolts absorb much kinetic energy and can effectively restrain the detachment and ejection of rock blocks. A much lower average velocity can also confirm the finding.

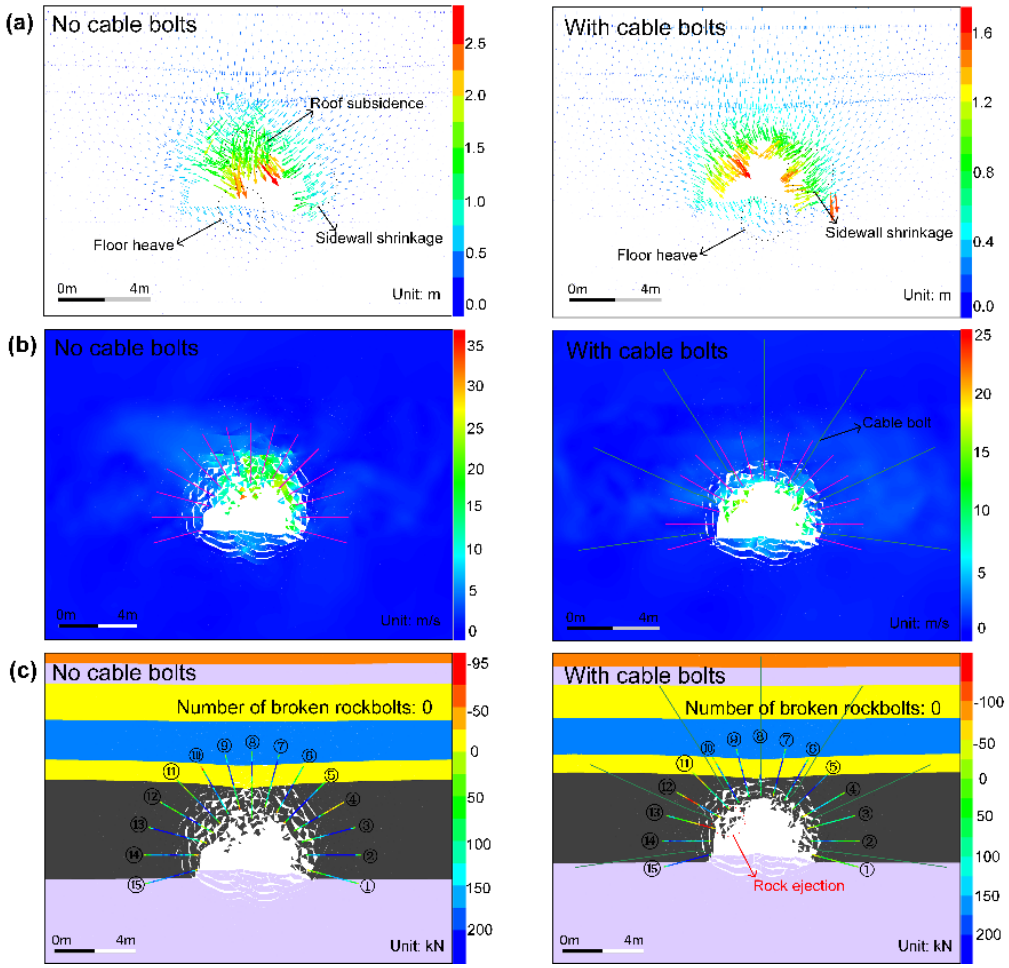

Figure 5.24 (a), (b), and (c) are simulated displacement vectors, velocity distribution, and macroscopic failure patterns of the tunnel and rockbolt axial forces.

Figure 5.25d shows that the tunnel suffers lower damage when using cable support. The volume of ejected rock blocks is decreased by 1.34 m^3 to 2.45 m^3, while the reduced kinetic energy increases to 2335.73 kJ, with a growth rate of 57.24 %. These results suggest that additional support with cable bolts can significantly reduce the rockburst damage severity. The new support scenario could also be anticipated to control violent rockbursts if rational surface retaining elements are applied.

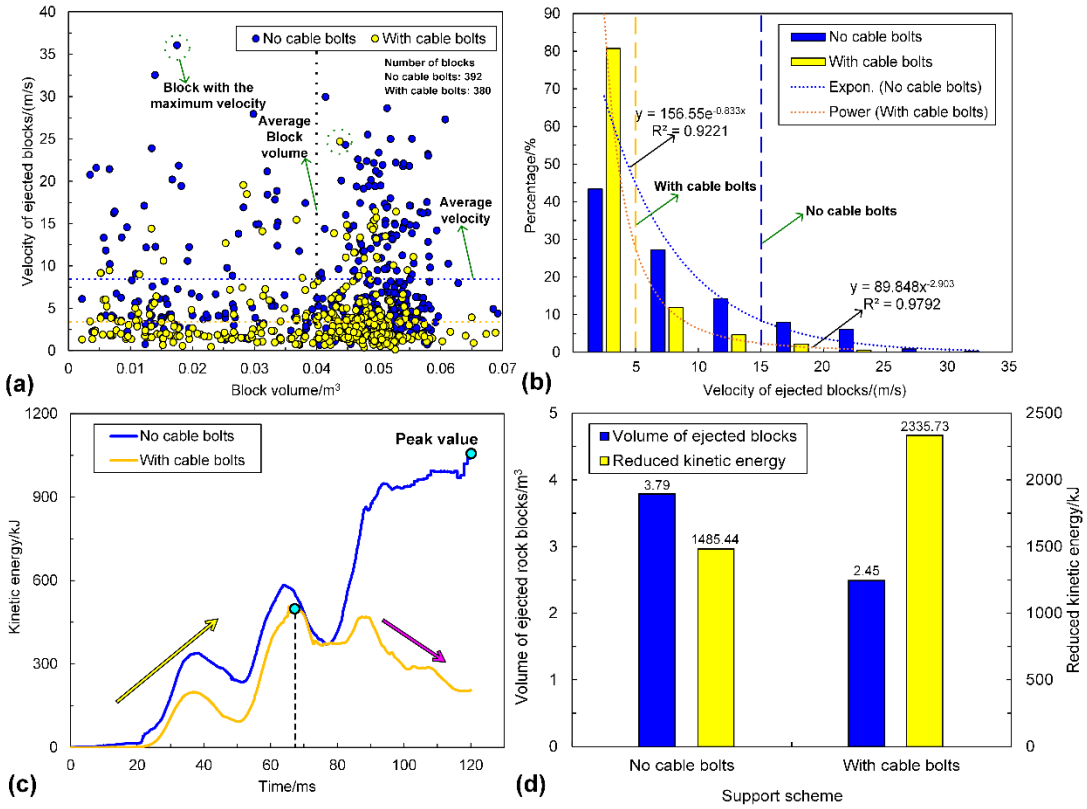

Figure 5.25 (a) is the velocity of all detached blocks versus block volume. (b) is the velocity distribution of all detached blocks. (c) is the evolution of the kinetic energy of ejected rock blocks in the tunnel. (d) is the comparison of the volume of ejected rock blocks and reduced kinetic energy.

5.1.5 Conclusions

In this part, the numerical modeling method thoroughly evaluates the performance of yielding rockbolts during rockbursts with actual seismic loading. Two types of yielding rockbolts (D-bolt and Roofex) and the fully resin-grouted rebar bolt are modelled via the "rockbolt" element in UDEC. A 2D model of a deep tunnel is built to evaluate the performance (e.g., the dynamic capacity of energy absorption and control of rock damage) of yielding and traditional rockbolts based on the simulated rockbursts. The influence of different rockburst magnitudes is also studied. The main conclusions are as follows:

(1) The "rockbolt" element in UDEC can be used to simulate the performance of yielding rockbolts. The volume of ejected rock blocks is a clear and straightforward variable to evaluate rockburst damage severity. Furthermore, the reduced kinetic energy can be accepted as a relatively rational estimation to assess the dynamic energy-absorption capacity of rockbolts.

(2) Because of its high strength and deformation capacity, the D-bolt can effectively control and mitigate rockburst damage during a weak rockburst. The Roofex is too "soft" or "smooth" to limit ejected rocks' movement and restrain the large deformation induced by rockbursts, and it has an excellent deformation capacity. The resin-grouted rebar bolt can main a high axial force level during rockbursts, but its elongation rate is very low and is easy to break during dynamic shocks, which cannot control rapid rock bulking or ejection effectively. As a result, these two types of rockbolts fail to control a weak rockburst.

(3) The rockburst is more severe when the PPV is higher. Three types of rockbolts solely fail to control the large deformation and mitigate rockburst damage during violent rockbursts. Nevertheless, the D-bolt still performs better in controlling rockbursts than the other two rockbolt types. Additional measures, e.g., using cable bolts and steel arch and/or distress drilling and blasting methods should be supplemented to control violent rockbursts.

(4) The floor heaving and the rockburst damage of the whole tunnel can be mitigated by floor support with D-bolts. Additional support with cable bolts can significantly reduce the rockburst damage severity. It could be anticipated that supporting with high-strength-yielding rockbolts and cable bolts can control violent rockbursts if rational surface retaining elements are applied.

PART TWO: EVALUATION OF THE PERFORMANCE OF YIELDING ROCKBOLTS DURING SELF-INITIATED STRAINBURSTS

This part aims to evaluate the effects of yielding rockbolts on controlling self-initiated strainbursts using DEM modeling. The rationality and capability of DEM software UDEC in modeling self-initiated strainbursts are first validated through comparison with laboratory tests. Then, two types of yielding rockbolts (Roofex and D-bolt) and the traditional rockbolt (fully resin-grouted rebar, for comparison) are modelled via the "rockbolt" element in UDEC after an exact calibration procedure. Instead of conventional drop tests, a 2D model of a deep tunnel in an underground coal mine is built to evaluate the performance fully (e.g., the dynamic capacity of energy absorption and control of rock damage) of yielding and traditional rockbolts during simulated strainbursts. The occurrence of self-initiated strainbursts is judged based on the stiffness difference between the loading system and rock masses for the first time.

5.2 Evaluation of the performance of yielding rockbolts during self-initiated strainbursts

5.2.1 Introduction

Strainburst is an unstable rock failure phenomenon at excavation boundaries of deep tunnels in mining and civil engineering projects. Generally, strainburst can be classified into two types: self-initiated and remotely triggered (Kaiser et al., 1996). The self-initiated strainburst occurs due to the concentration of excavation-induced tangential stress and the existence of a relatively "soft" loading environment in the rock mass surrounding the fracturing rock triggered (Kaiser and Cai, 2012). There is not a remote seismic event involved in self-initiated strainbursts. The remotely triggered strainburst is caused by a remote seismic event triggered by large-scale mining activities and high static stress (Mutke et al., 2015; Diederichs, 2018). Self-initiated strainburst is a more frequently encountered type of strainbursts because it happens in both mining and civil engineering projects, while remotely triggered strainburst usually occurs only in mining environments (Diederichs, 2018). This study specifically focuses on the investigation of the control of self-initiated strainbursts.

Many measures and strategies have been proposed to control and mitigate strainburst damage. For instance, distress drilling and blasting are two measures to reduce strainburst risks by transferring concentrated stresses to rock masses in-depth. Another common tactic is using yielding rockbolts. This type of rockbolts allows yielding to absorb more kinetic energy and have higher displacement capacities than conventional rockbolts (e.g., expansion-shell bolt and rebar bolt). Hence, yielding rockbolts can resist the dynamic loads and accommodate large deformation caused by rock fracturing, dilation, and ejection during strainbursts (Kaiser and Cai, 2012). In the last several decades, many different types of yielding rockbolts have been developed to control rockbursts, e.g., Cone bolt (Ortlepp, 1992), Roofex (Charette and Plouffe, 2007; Atlas Copco Construction Mining Technique, 2021) Garford bolt (Varden et al., 2008), D-Bolt (Li and Doucet, 2011; Normet, 2021), Yield-Lok (Wu et al., 2011), and He-bolt (He et al., 2012).

A critical task is to evaluate the effects (e.g., control of rock damage and the energy absorption capacity) of yielding rockbolts on controlling strainbursts before being widely used. The methodologies to study rockbolt performance mainly include field tests (Kang et al., 2009; Li, 2011; Wu et al., 2019), laboratory tests, and numerical modeling. The field test method can obtain real-time data and assess the in situ performance of rockbolts, but they are usually time-consuming, expensive, and dangerous, especially in burst-prone grounds. Compared with field tests, the experimental methods have the advantages of repeatability, safety, and flexibility (Zhang and Nordlund, 2019). At present, the evaluation of the rockbolt performance in strainburst conditions is conducted mainly using the drop test (Charette and Plouffe, 2007; Varden et al., 2008; Cai et al., 2010; Li and Doucet, 2011; Li et al., 2014; Sharifzadeh et al., 2020). The research has achieved many positive outcomes, providing excellent references for understanding the behaviour of different types of yielding rockbolts under dynamic impacts. However, the drop test is straightforward and is only a crude simulation of rockburst loading. The complex interaction between seismic waves, rockbolts, and reinforced rock masses is not considered. For instance, Bosman et al. (2018) stated that the dynamic capacity of a rockbolt is not a constant value, and the loading mode of a rockbolt will affect its dynamic capacity. Therefore, the impact loading from conventional drop tests might not represent rockburst loading. Wu et al. (2019) also pointed out that the impact load in drop tests cannot represent the impact of ground pressure load, and the existing test system generally cannot reproduce the complex ground support/rock mass interaction in an underground environment. Besides, original rock stress is not considered in tests.

With the rapid development of IT and computer equipment, various numerical methods and codes have been developed and employed to simulate complex physical phenomena in rock mechanics and rock engineering (Wang et al., 2021a, 2022a; Ji and Karlovšek, 2022a, b). The numerical simulation methods have been acknowledged as effective research and engineering design tools as it can represent the realistic

mechanical behaviour of rock masses and support elements with rational input data (e.g., excavation size and shape, material properties, and boundary conditions) and calibration procedures (Manouchehrian, 2016). Nie et al. (2014) developed rockbolt models using DDA to investigate the failure mechanism of an expansion-shell bolt, fully grouted rebar, split set, and D-bolt in simulated pull-out and drop tests. Marambio et al. (2018) modelled a laboratory-scale test via FLAC3D to study the performance of threadbar in dynamic loading. The simulation results matched well with laboratory observations. Yokota et al. (2019) assessed a self-developed deformation-controlled rockbolt (DC-bolt)'s behaviour in tunnel support via DDA simulation. Zhang and Nordlund (2019) employed the UDEC program to investigate the differences in dynamic performances of a fully grouted rebar between the simulated drop tests and seismic loading in the configuration where two slightly separated rock bars were used. Zhao et al. (2021) studied the influence of structure element position on the anchoring effect of energy-absorption bolts via simulating pull-out tests in FLAC3D.

In summary, most current work focuses on evaluating the performance of traditional rockbolts under dynamic loading, while some researchers try to simulate the dynamic behaviour of yielding rockbolts by reproducing drop tests. Few numerical studies have been reported to assess the performance of yielding rockbolts during self-initiated strainbursts with actual seismic loading. As mentioned above, the impact loading in drop tests might not represent rockburst loading, and the rock stress is also absent. Hence, the complex interaction between seismic waves, rockbolts, and reinforced rock masses during self-initiated strainbursts with explicit rock detachment and ejection (requiring the distinct element method (DEM) or DEM-related hybrid methods) needs to be further numerically investigated.

This study aims to evaluate the effects of yielding rockbolts on controlling self-initiated strainbursts using DEM modeling. The rationality and capability of DEM software UDEC in modeling self-initiated strainbursts are first validated through comparison with laboratory tests (Hu et al., 2018). Then, two types

of yielding rockbolts (Roofex and D-bolt) and the traditional rockbolt (fully resin-grouted rebar, for comparison) are modelled via the "rockbolt" element in UDEC after an exact calibration procedure. Instead of conventional drop tests, a 2D model of a deep tunnel in an underground coal mine is built to evaluate the performance fully (e.g., the dynamic capacity of energy absorption and control of rock damage) of yielding and traditional rockbolts during simulated strainbursts. The occurrence of self-initiated strainbursts is judged based on the stiffness difference between the loading system and rock masses for the first time.

5.2.2 Validation of UDEC in modeling self-initiated strainbursts

5.2.2.1 Brief introduction of the true triaxial experiments of self-initiated strainbursts

Considering that the self-initiated strainburst is a structural failure of rock masses near the excavation boundary, Su et al. (2017a, b) conducted a series of true triaxial tests of rock samples by reproducing strainbursts in a self-developed true triaxial testing facility (see Figure 5.26a,b). In tests, rock samples with the dimension of 100 mm (length) × 100 mm (width) × 200 mm (height) were used to simulate the burst volume of a representative rock element (RRE) (Figure 5.26c,d). Rock samples' cracking and ejecting processes during strainbursts were monitored by an acoustic emission (AE) system and two high-speed cameras. The tangential stress concentration and radial stress distribution of near-boundary rock masses were simulated by a loading path that keeps one face free and loads on the other faces (Figure 5.26c). The detailed test procedures are as follows: (1) maintain one face of the rock sample free (y-direction) and apply loads to the other five faces simultaneously to a pre-defined initial stress state; (2) maintain stresses in x and y directions, and increase the stress in z-direction until the strainburst occurs.

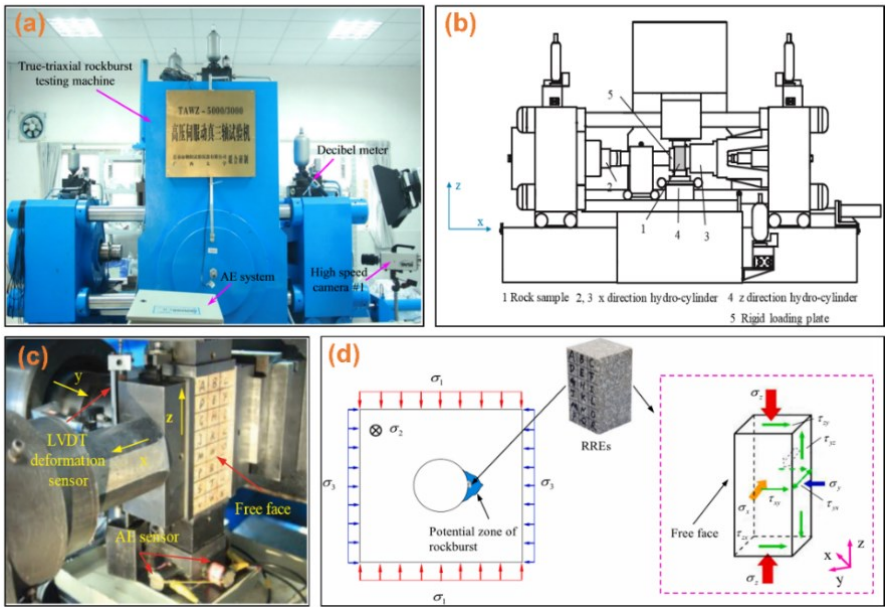

Figure 5.26 A true triaxial strainburst testing facility: (a) and (b) are the loading configuration; (c) is the stressed rock sample; (d) shows the boundary conditions and stress state of the rock sample ((a) is from Su et al., 2017b; (b)–(d) are from Hu et al., 2018).

5.2.2.2 Validation of UDEC Simulation

In order to validate the reliability and accuracy of the 2D distinct element code UDEC in modeling self-initiated strainbursts, numerical simulation results were compared with the laboratory test results from Hu et al. (2018). The model configuration, including the model dimension, block shape and size, material properties, constitutive models, and loading mode, are the same as those used by Hu et al. (2020, 2021). The only difference is that the 3D distinct element code 3DEC rather than UDEC was employed in their studies.

A Trigon approach developed by Gao et al. (2015) was used to generate blocks in the model (Figure 5.27a), as this approach is capable of reproducing the realistic fracturing processes (e.g., crack initiation, propagation, and coalescence) of rocks without adopting complicated constitutive models (Chen et al., 2016; Yang et al., 2017; Stavrou et al., 2019). In the Trigon approach, a rock or rock mass is represented as an assembly of triangular blocks bonded by contacts (Chen et al., 2016). The fracturing process can be exhibited by sliding or opening contacts. In the simulation, the blocks have an average edge length of 6 mm, sufficiently fine to simulate the failure behaviour of rocks (Hu et al., 2020, 2021). The material

properties of blocks and contacts are listed in Table 5.8. In order to trigger a strainburst (unstable failure), the top platen has a lower stiffness (4 GN/m) than the post-peak characteristic stiffness of the rock sample (4.51 GN/m), which represents a soft loading system. Accordingly, Young's modulus and length of the top platen are 40 GPa and 100 mm, respectively. The stiffness of lateral and bottom platens are 1372 GN/m and 686 GN/m, respectively, representing stiff loading systems, and thus the LSS effect can be ignored (Xu and Cai, 2017).

Table 5.8 Material properties used in the model (Hu et al., 2020, 2021)

Items	Block Properties			Contact Properties							
	ρ (kg/m^3)	K (GPa)	G (GPa)	k_n (GPa/m)	k_s (GPa/m)	c^j (MPa)	c_r^j (MPa)	φ^j (°)	φ_r^j (°)	σ_t^j (MPa)	σ_{tr}^j (MPa)
Granodiorite	2650	21.22	12.12	210,000	83,370	52	0	61.5	22	13	0
Top platen	7700	33.33	15.38				-				
Other platens	7700	171.67	79.23				-				
Interface between platens and rock sample		-		210,000	83,370	0	0	14.57	0	0	0

Note: ρ, K, and G are the bulk density, bulk modulus, and shear modulus of blocks. k_n and k_s are the normal and shear stiffness of contacts. c^j, φ^j, and σ_t^j are the cohesion force, internal friction angle, and tensile strength of contacts. c_r^j, φ_r^j, and σ_{tr}^j are the residual values of cohesion forces, internal friction angle, and tensile strength of contacts.

The simulation was implemented as following procedures: (1) A pre-defined initial stress state (σ_x = 5 MPa, σ_y = 45 MPa, and σ_z = 30 MPa) was applied to the model, and the "geostatic equilibrium" was achieved after sufficient calculation steps (Hu et al., 2020, 2021). The model boundaries were initially fixed to simulate the in situ state. (2) One lateral platen and its boundary conditions in the *x*-direction were removed, while other boundary conditions remained unchanged. A constant velocity of 0.1 m/s was applied to the surface of the top platen until the peak strength (*y*-direction) was reached. (3) The dynamic mode in UDEC was activated. The local damping ratio was set at 0.05 after a trial-and-error process. The boundary conditions (e.g., fixed boundary) used in the static stage can cause the reflection of outward propagating waves back into the model and do not allow the necessary energy radiation. Thus, the viscous boundary developed by Lysmer and Kuhlemeyer (1969) was used in the dynamic calculation.

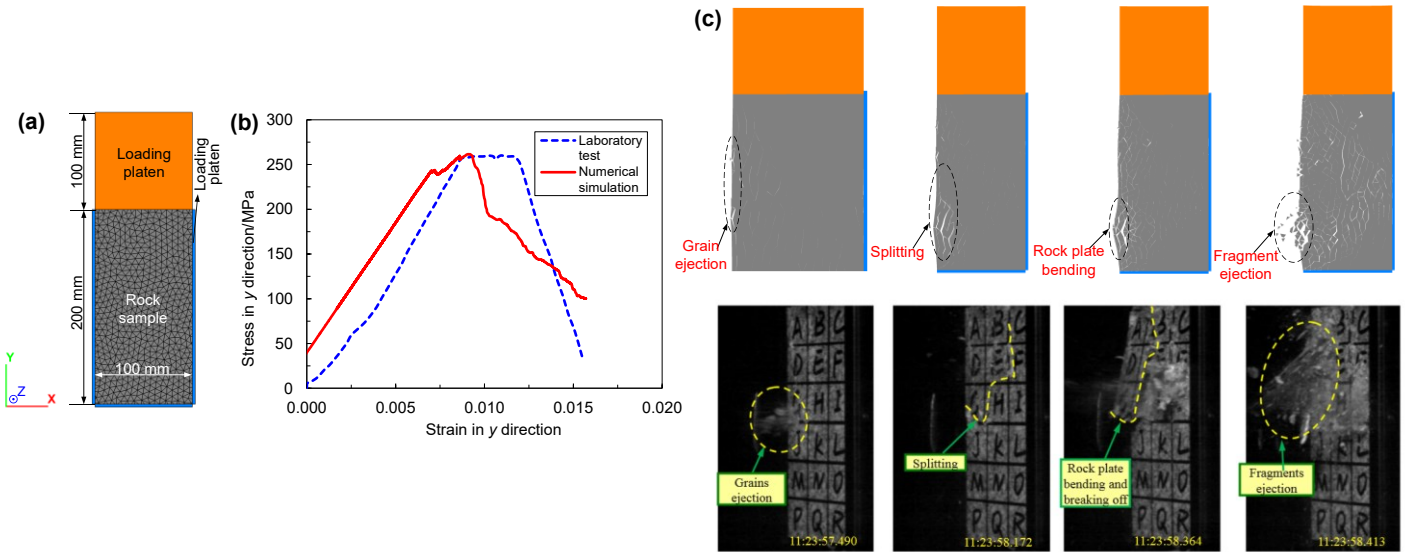

Figure 5.27 A numerical model for simulating self-initiated strainbursts and the comparison between the simulation and experimental results: (a) numerical model; (b) stress-strain curves obtained by the simulation and laboratory test (Hu et al., 2018); (c) comparison between simulated failure stages and modes, and experimental observations (Hu et al., 2018).

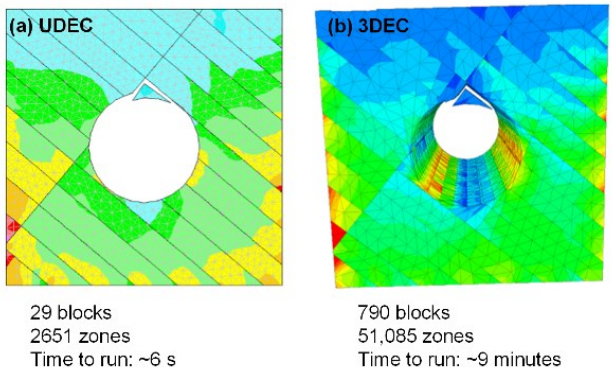

Figure 5.28 An example of the comparison of the run time between UDEC and 3DEC (Itasca, 2021).

The comparison between the simulated results and laboratory test results is shown in Figure 5.27b,c. It can be seen that the stress-strain curve, failure stages, and failure modes, including grain ejection, splitting and bending of rock plates, and fragment ejection during the strainburst test, can be realistically captured by numerical modeling. Hence, the capability and accuracy of UDEC in modeling the self-initiated strainburst are validated. Hu et al. (2020, 2021) needed to compare simulation results with laboratory test results of cuboid rock samples and investigate the influence of intermediate stress on indoor strainburst failure. Thus, the 3D program 3DEC was used in their research. As mentioned above, strainbursts usually occur at the excavation boundary of a tunnel in a high geo-stress environment. Therefore, if there are no

nearby excavations, the plane strain assumption of a 2D model would be rational. The accuracy of UDEC in modeling the self-initiated strainburst has also been verified with experimental results in this study. Besides, the employment of UDEC can significantly reduce the calculation cost compared with 3DEC. Figure 5.28 shows an example that the run time of 3DEC is around 90 times that of UDEC when dealing with the same problem, indicating that UDEC is more productive than 3DEC. Therefore, UDEC is adopted considering both reliability and efficiency.

5.2.3 Numerical Modeling

5.2.3.1. Model Setup

(a) Model Dimensions and Boundary Conditions

The simulation of the self-initiated strainburst at a laboratory scale helps understand its detailed damage mechanisms (e.g., fracturing process and failure mode). However, the complex interaction between rockbolts and reinforced rock masses during strainbursts is hard to capture in this model setup due to the size limit, which prevents the model from being a potential design tool for rockbolting in burst-prone grounds. Therefore, to analyze the performance of rockbolts more realistically and accurately, the self-initiated strainburst occurring in a deep tunnel in an underground coal mine was modelled in this research rather than simulating it at a laboratory scale as in previous studies. A widely used 2D DEM software UDEC was used to construct the numerical model. The model size is 30 m × 25 m. The shape of the tunnel cross-section is semicircular, with a width and height of 6 m and 4 m, respectively. Figure 5.29 shows the geometry of the numerical model, which is based on the lithology and designed size of a deep coal mine drift.

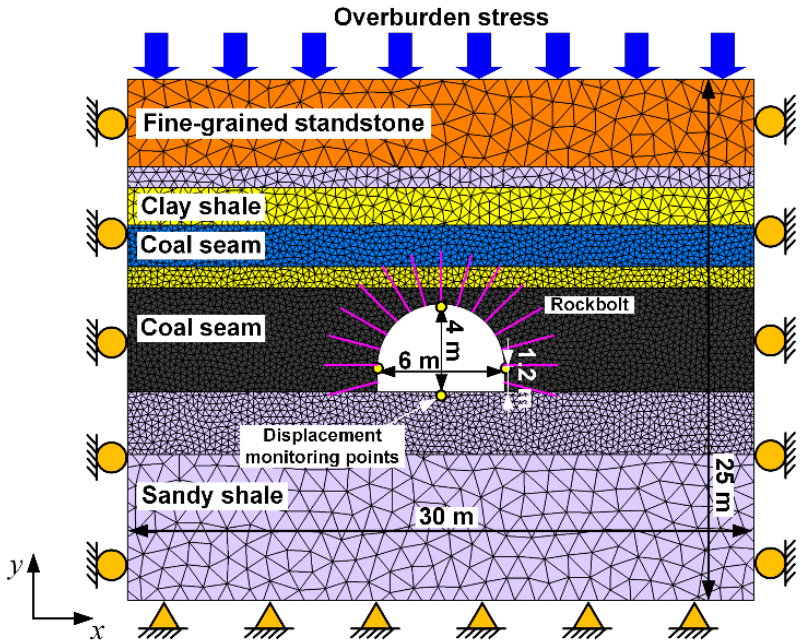

Figure 5.29 2D numerical model of a deep tunnel in an underground coal mine.

The rock masses are divided into triangular blocks using the Trigon approach (Gao et al., 2015). In the model, the average edge length of the blocks in two coal seams and nearby clay shale was set to 0.3 m. The block size with a range of 0.2–0.5 m was sufficiently acceptable to simulate the failure behaviour of surrounding rock masses for a 2D model (Gao et al., 2015; Chen et al., 2016; Yang et al., 2017). The average edge length of the blocks in the upper clay shale, sandy shale, and fine-grained sandstone was set to 0.5 m, 0.5 m, and 1 m, respectively. The average edge length of the blocks on the floor was set to 0.3 m and 1 m. A graded increasing edge length of blocks can avoid the resulting loss of simulation accuracy and enhance the calculation's reliability.

The upper boundary of the model was free and vertical stress of 24.3 MPa (assuming the unit weight of overburden is 0.027 MN/m^3 and the buried depth is 900 m) was applied to the upper boundary to simulate the overburden weight. The roller constraints were applied on lateral boundaries, and the bottom boundary was fixed during the static stage (Figure 5.29). The ratio of horizontal to vertical stress (K) was assumed since the hydrostatic stress state is a general in situ stress state in many deep excavations (Dai et al., 2021).

(b) Large-Scale Modeling Strainbursts Based on the Stiffness Theory

The loading system stiffness (also called local mine stiffness at the engineering scale) and the post-failure stiffness of rock materials can distinguish stable or unstable failure (rockburst) effectively based on the stiffness theory (Cook, 1965b). If the loading system stiffness is smaller than the post-failure stiffness, the failure will be unstable and violent because the excess energy will transfer to the kinetic energy of ejected rocks. When the research object is a rock sample (e.g., Hu et al., 2020, 2021), it is simple to obtain the loading system stiffness K_L by the following equation:

$$K_L = \frac{AE}{L} \tag{5.10}$$

where A is the cross-section area of the loading platen; E is Young's modulus of the loading platen; L is the loading platen length.

However, unlike the unstable failure of rock samples, it is hard to identify the loading system when the focus is a strainburst that usually occurs in a tunnel or roadway. Thus, the determination of local mine stiffness becomes a more difficult task. Jaiswal and Shrivastva (2012) proposed a method for calculating the local mine stiffness of a rock pillar by numerical modeling. The local mine stiffness is defined as a ratio of the load F_1 applied on the rock pillar over the distance difference ($d_1 - d_2$) with and without the modeling of the rock pillar (Figure 5.30a). This study adopted this logic to calculate the local mine stiffness for a tunnel (see Figure 5.30b). In Stage 1, the internal pressure P_1 at the planned excavation boundary equals the in situ stress P_i. In Stage 2, P_1 is reduced to zero (P_2) after excavation. Similar to the calculation method of a rock pillar, the local mine stiffness for a tunnel can be determined as follows:

$$K_L = \frac{P_1}{(d_1 - d_2)} = \frac{P_i}{U} \tag{5.11}$$

where d_1 and d_2 are the tunnel diameter before and after excavation; U is the convergence of tunnel walls after excavation. This method is the first attempt to calculate the local mine stiffness for a tunnel to the authors' knowledge. The deep coal mine drift excavation was simulated to obtain the local mine stiffness

using the proposed method in this research. The obtained local mine stiffness is 174 MPa, where the tunnel convergence has been normalized by the tunnel diameter for convenient comparison with the post-peak characteristic stiffness of rock masses.

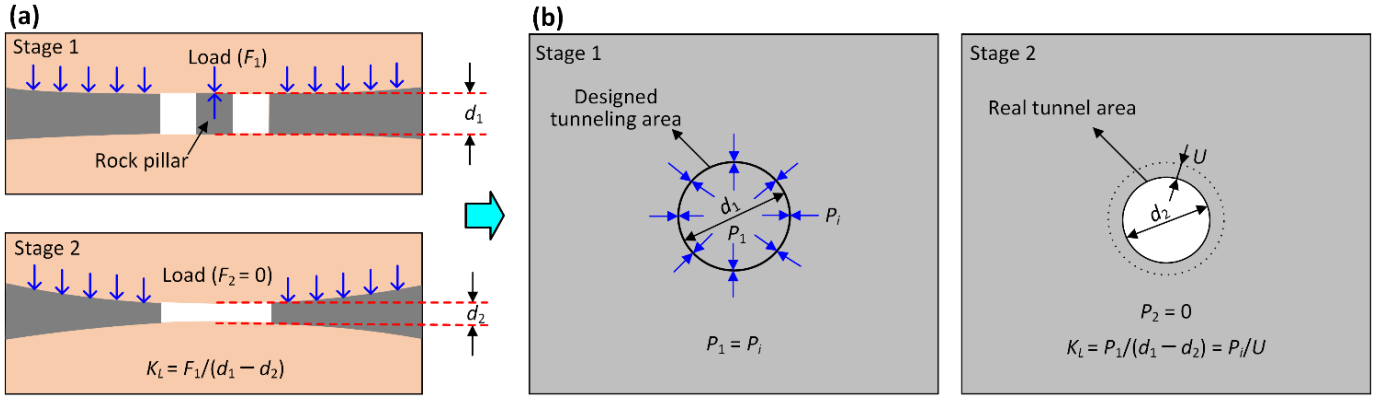

Figure 5.30 Determination of local mine stiffness by numerical modeling. (a) Local mine stiffness calculation for a rock pillar (after Jaiswal and Shrivastva, 2012). (b) Proposed calculation method of local mine stiffness for a tunnel.

Since the main surrounding rock masses are coal seam and their strength is much lower than clay shale and sandy shale, only the post-peak characteristic stiffness of coal masses is determined using simulated UCS tests. Considering that the rock mass property (e.g., strength and stiffness) is scale-dependent (Farahmand, 2018), the dimension of the rock mass model was determined based on the representative elementary volume (REV) concept (Bear, 1972). The REV refers to the minimum scale of rock masses beyond which the material property becomes independent of the sample size (see Figure 5.31a). According to Bieniawski (1968) (see Figure 5.31b), the UCS of coal masses declines gradually with increased sample side length. When the sample side length is less than 1.5 m, the UCS decreases remarkably with the growth of the specimen size. However, the UCS approaches a plateau when the sample side length exceeds 1.5 m, indicating that the scale dependency could be negligible. Thus, the REV size of the coal mass should be at least 1.5 m. In this study, the UCS model size is 4 m × 8 m, sufficient to eliminate the scale dependency. This model size is identical to Yang et al. (2017).

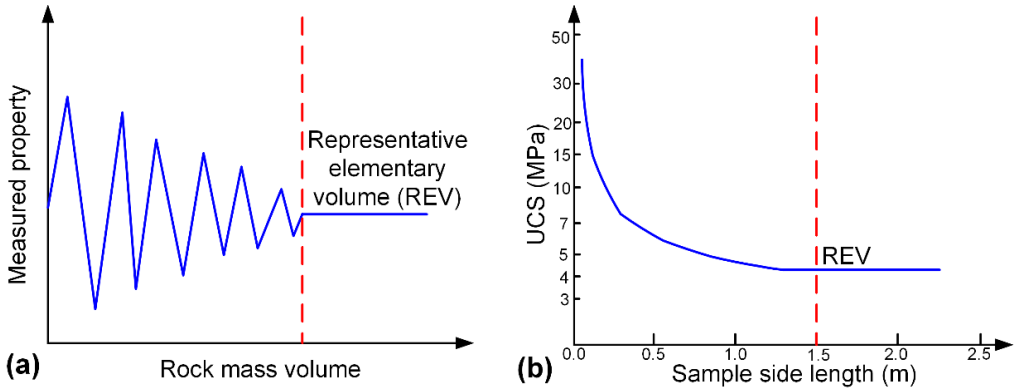

Figure 5.31 (a) Concept of the REV (after Bear, 1972). (b) The effect of sample size on the strength of coal (after Bieniawski, 1968).

Figure 5.32a shows the numerical model of UCS tests. In order to obtain the post-peak characteristic stiffness of the coal mass sample, the bulk and shear moduli of loading platens were set at an extremely high value (1000 GPa) to simulate an ideal rigid loading condition. As shown in Figure 5.32b, the obtained post-peak characteristic stiffness is 255 MPa, greater than the local mine stiffness (174 MPa). Hence, the self-initiated strainburst can happen. The material properties associated with coal masses are listed in Tables 2 and 3.

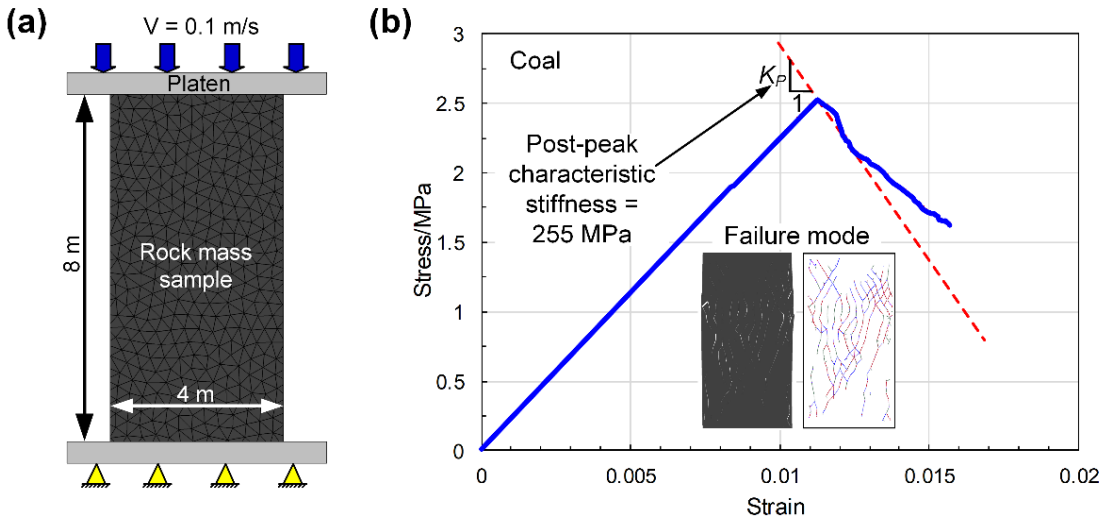

Figure 5.32 (a) UCS model. (b) Stress-strain curve of the coal mass sample under an ideal rigid loading condition. (c) Rock Mass Properties and Constitutive Model

The properties of rock masses (see Table 5.9) around the tunnel were obtained according to the laboratory tests of intact rock pieces (following ISRM recommended standards, Fairhurst and Hudson,

1999) and the generalized Hoek-Brown criterion (Marinos and Hoek, 2020) using the GSI system to evaluate rock mass qualities (Małkowski et al., 2017; Małkowski and Ostrowski, 2019; Szott et al., 2018). The UCS and deformation modulus of rock masses were estimated from the following equations (Hoek et al., 2002; Hoek and Diederichs, 2006):

$$\sigma_{cm} = \sigma_{ci} \frac{(m_b + 4s - a(m_b - 8s))\left(\frac{m_b}{4+s}\right)^{as-1}}{2(1+a)(2+a)} \tag{5.12}$$

$$E_m = E_i \left(0.02 + \frac{1 - D/2}{1 + e^{((60+15D-GSI)/11)}}\right) \tag{5.13}$$

where D is a factor that depends upon the degree of disturbance to which the rock mass has been subjected by blast damage and stress relaxation. In this study, the value of D is assumed to be zero considering that the mechanical tunnelling results in minimal disturbance to confined rock masses (Hoek et al., 2002). The calculated results of UCS and the deformation modulus of rock masses are also summarized in Table 5.9.

Table 5.9 Physical and mechanical parameters of rock masses (Małkowski et al., 2017; Szott, 2018; Małkowski and Ostrowski, 2019)

Lithology	Constant				Intact Rock				Rock Mass	
	m_i	m_b	s	a	ρ (kg/m^3)	σ_{ci} (MPa)	E_i (GPa)	v	σ_{cm} (MPa)	E_m (GPa)
Coal	17	1.729	0.0008	0.5	1300	9.3	1.86	0.30	2.50	0.23
Clay shale	9	1.327	0.0022	0.5	2500	29.0	5.62	0.31	7.93	1.26
Fine-grained sandstone	17	2.851	0.0039	0.5	2580	90.0	9.52	0.26	24.53	2.92
Sandy shale	12	1.877	0.0031	0.5	2530	26.0	5.23	0.25	7.11	1.42

Note: m_i is a material constant for intact rocks. m_b, s, and a are constants for rock masses. ρ is the bulk density of intact rocks. σ_{ci} is the UCS of intact rocks. E_i is Young's modulus of intact rocks. v is the Poisson's ratio of intact rocks. σ_{cm} is the UCS of rock masses, and E_m stands for the deformation modulus of rock masses.

The elastic constitutive model was chosen for blocks composed of finite-difference zones. The Coulomb slip model was used for contacts. The constitutive behaviour of contacts is shown in Figure 5.33. A spring-rider simulates the behaviour of contact, and the model deformation occurs when the contact stress is smaller than the contact strength, which is governed by the elastic modulus of blocks and contact stiffness; contact failure occurs when the stress exceeds its shear or tensile strength, and then blocks will slide or separate with each other (Chen et al., 2016).

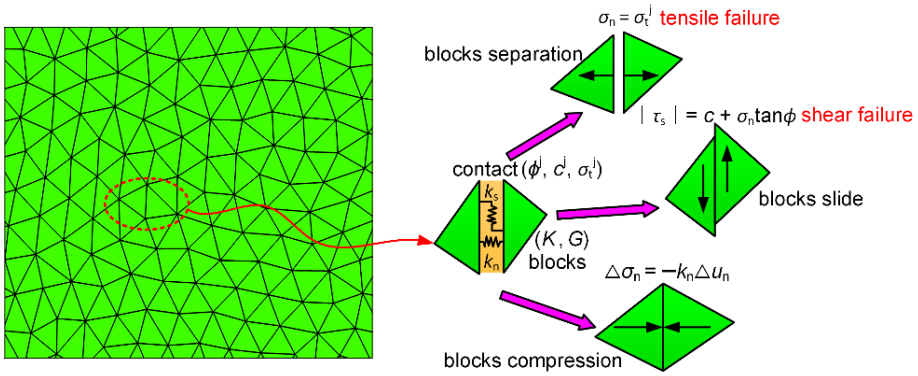

Figure 5.33 Constitutive behaviour of contacts. (K and G are the bulk and shear moduli of blocks. c^j; φ^j, and σ_t^j are the cohesion force, internal friction angle, and tensile strength of contacts. Δσn and Δun are the effective normal stress increment and normal displacement increment. Finally, σn and τs are contacts' normal and shear stresses.).

In the Trigon approach, the deformation and failure of rock masses depend on the properties of blocks and contacts (Gao et al., 2015; Chen et al., 2016). Thus, the micro parameters of blocks and contacts were calibrated against the rock mass properties (Table 5.9). Next, simulated UCS tests were conducted to calibrate the micro parameters (Gao et al., 2015). To eliminate the effect of block size on simulation accuracy, the calibration model had a large scale (4 m × 8 m) (Yang et al., 2017) and an identical block size with the tunnel model. A displacement loading mode was used in the simulation by applying a constant velocity of 0.1 m/s to the surface of the top platen, and the bottom platen was fixed. The loading rate of 0.1–0.15 m/s is slow enough to avoid the dynamic responses of models because UDEC automatically selects very small time steps (e.g., 10^{-7} s) in static analysis (Gao et al., 2019b; Hu et al., 2020). The initial micro parameters were first assumed based on the macro parameters of rock masses. Then, the modeling of UCS tests was conducted iteratively with the adjustment of micro parameters until the simulated results were consistent with the targeted material properties. The simulated failure modes and stress-strain curves of rock mass samples are shown in Figure 5.34. The main failure modes of rock mass samples are tensile (axial splitting) and tensile-shear failure, consistent with typical rock mass failure modes under no or low confining pressures (Diederichs, 2007). The calibrated micro parameters of rock masses are listed in Table 5.10. The targeted and simulated deformation modulus and UCS errors are less than 3% (Table 5.11), suggesting that the targeted values agree well with calibrated rock mass parameters.

Thus, the calibrated micro parameters in Table 5.10 could be used for further numerical analysis to evaluate the performance of yielding rockbolts during self-initiated strainbursts.

Table 5.10 Calibrated micro parameters of rock masses in the model

Lithology	Block Properties					Contact Properties				
	ρ (kg/m^3)	K (GPa)	G (GPa)	k_n (GPa/m)	k_s (GPa/m)	c^j (MPa)	c_r^j (MPa)	φ^j (°)	σ_t^j (MPa)	σ_{tr}^j (MPa)
Coal	1300	0.16	0.09	18.7	7.5	0.99	0	33	0.25	0
Clay shale	2500	0.85	0.50	108.5	40.6	2.96	0	35	0.79	0
Fine-grained sandstone	2580	1.91	1.17	69.4	27.8	8.11	0	36	2.15	0
Sandy shale	2530	0.94	0.57	113.3	45.3	2.95	0	36	0.85	0

Table 5.11 Comparison between the targeted and simulated rock mass parameters

Lithology	E_m (GPa)			UCS (MPa)		
	Target	Simulation	Error (%)	Target	Simulation	Error (%)
Coal	0.23	0.226	0.09	2.50	2.51	0.48
Clay shale	1.26	1.234	−1.82	7.93	7.91	−0.29
Fine-grained sandstone	2.92	2.852	−2.48	24.53	24.52	−0.05
Sandy shale	1.42	1.39	−2.11	7.11	7.02	−1.27

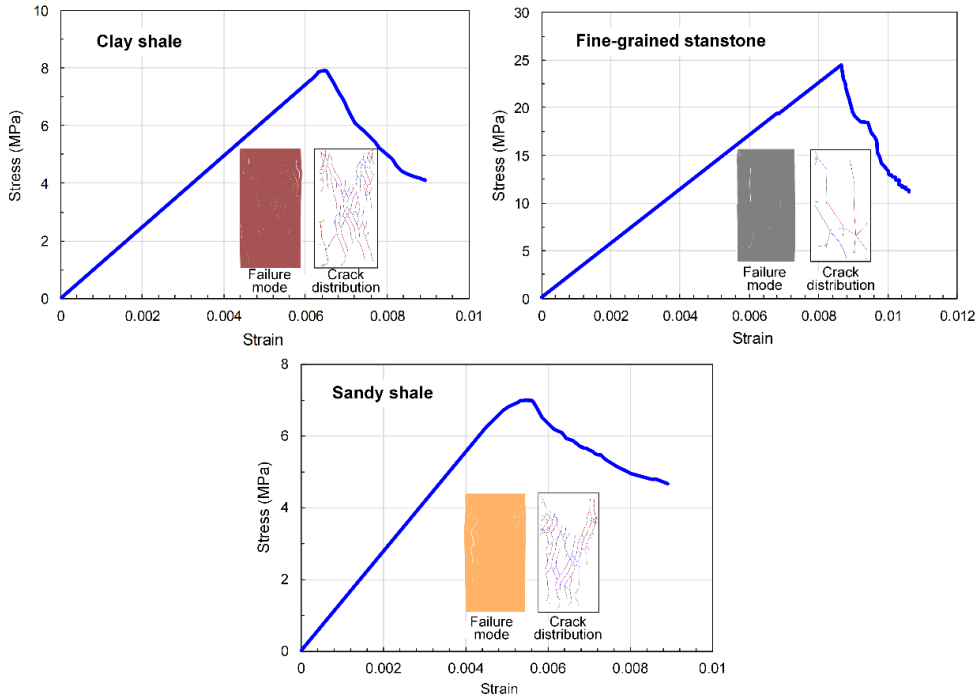

Figure 5.34 Simulated failure modes and stress-strain curves of rock mass samples.

5.2.3.2 Properties of Rockbolts

(a) Introduction of the "Rockbolt" Element

In the past, the "cable" element in UDEC was more popular used than the "rockbolt" element to model a mechanically anchored or grouted cable or rockbolt, although both elements can simulate the shearing

resistance along their length, which is provided by the shear bond between the grout and either the cable/rockbolt or the host rock (Bahrani and Hadjigeorgiou, 2017). This could be owing to more understandable input parameters and the more straightforward calibration process for using the "cable" element. Figure 5.35a shows the conceptual mechanical representation of the "rockbolt" element. It can be seen the "rockbolt" element is composed of several segments and nodal points located at segment ends. It has both shear and normal coupling springs, which are connectors that transfer forces and motion between the "rockbolt" element and the grid points associated with the block zone, while the "cable" element only has sliders (similar to shear coupling spring). Therefore, the "cable" element provides little resistance to bending, and thus it is more suitable for modeling cable bolts. In contrast, the "rockbolt" element can provide sufficient resistance for shearing and bending, appropriate for simulating rockbolts such as rebar bolts (Tomasone et al., 2020). The other strength of the "rockbolt" element is that it can explicitly model the rockbolt breakage according to a user-defined tensile failure strain limit ε_{pl} (Itasca, 2020):

$$\varepsilon_{pl} = \sum \varepsilon_{pl}^{ax} + \sum \frac{d}{2}\frac{\theta_{pl}}{L} \tag{5.14}$$

where $\varepsilon_{pl}{}^{ax}$ is the axial plastic strain of rockbolt segment elements; d is the rockbolt diameter; L is the rockbolt segment length; θ_{pl} is the average angular rotation over the rockbolt. The tensile failure strain limit provides a more accurate and realistic approach to reproducing rockbolt performances. Thus, the "rockbolt" element was used in this study to simulate the mechanical behaviour of both yielding and conventional rockbolts.

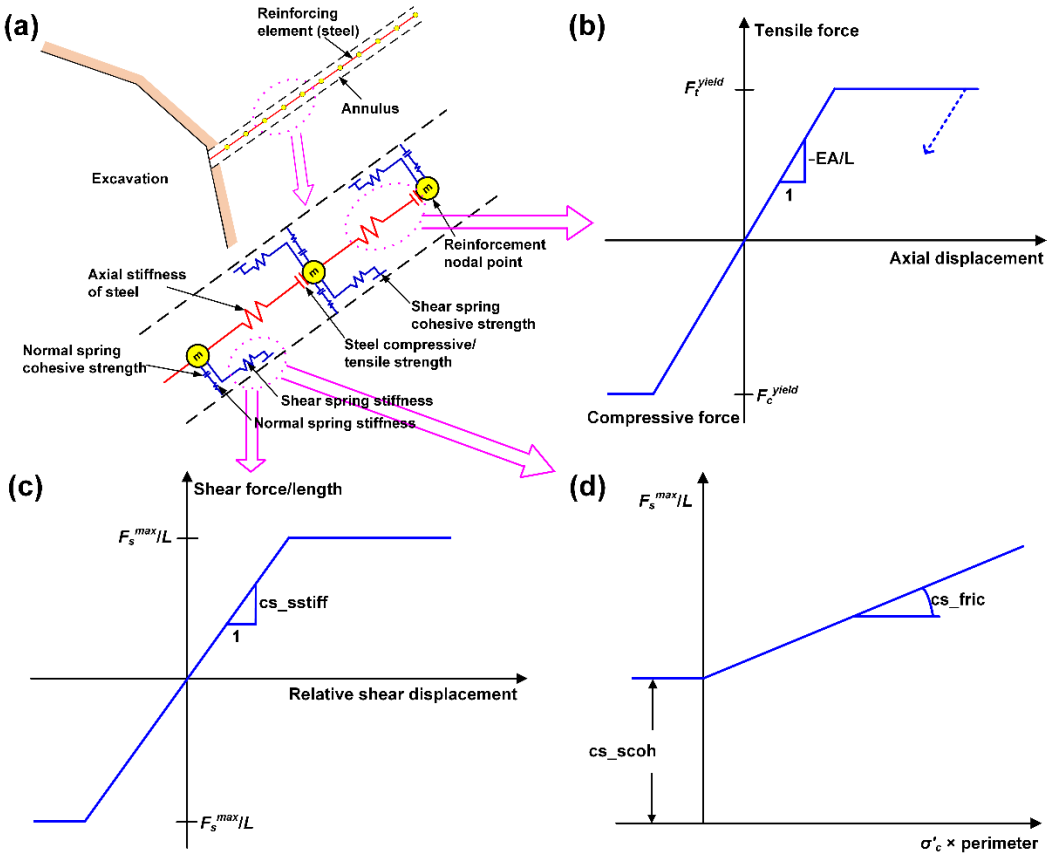

Figure 5.35 (a) Conceptual mechanical representation of the "rockbolt" element, which accounts for the shear behaviour of grout annulus and bending resistance of the reinforcement. (b) Mechanical behaviour of the "rockbolt" element in the axial direction. (c) Shear force versus displacement of the shear coupling spring. (d) The shear criterion of the shear coupling spring ((a) is modified after Itasca, 2020; (b–d) are from Itasca, 2020).

The "rockbolt" element has a linearly elastic material behaviour that it can yield in both tension and compression in the axial direction (Figure 5.35b). Therefore, the incremental axial force in a "rockbolt" element, ΔF_t, can be obtained by the calculation of the incremental axial displacement:

$$\Delta F_t = -\frac{EA}{L}\Delta u^t \tag{5.15}$$

where $\Delta u^t = \Delta u_i t_i = \Delta u_1 t_1 + \Delta u_2 t_2 = (u_1^{[b]} - u_1^{[a]})t_1 + (u_2^{[b]} - u_2^{[a]})t_2$; $u_1^{[b]}$, $u_1^{[a]}$, etc. are the displacements at the bolt nodes associated with each "rockbolt" element. Subscript 1 and 2 represent the x-direction and y-direction, respectively; the superscripts $[a]$, $[b]$ stand for bolt nodes. The direction cosines t_1, t_2 refer to the tangential (axial) direction of the "rockbolt" element.

The applied load is axial in an ideal pull-out test as simulated in this study. Thus, the parameters regarding resistance to bending (normal spring) are not discussed. The shear behavior of the "rockbolt"

element was briefly introduced in this study. The shear behaviour of the rockbolt/gridpoint interface is represented as a spring-slider system at the rockbolt nodal points. This behaviour during relative displacement can be described numerically by the coupling spring shear stiffness (cs_{sstiff} in Figure 5.35c):

$$\frac{F_s}{L} = cs_{sstiff}\left(u_p - u_m\right) \tag{5.16}$$

where F_s represents the shear force that develops in the shear coupling spring (e.g., along with the interface between the rockbolt element and the gridpoint); cs_{sstiff} is the coupling spring shear stiffness (coupling-stiffness-shear); u_p is the axial displacement of the rockbolt; u_m is the axial displacement of the medium (soil or rock); and L is the contributing element length.

The maximum shear force that can be developed along the rockbolt/gridpoint interface is a function of the cohesive strength of the interface and the stress-dependent frictional resistance along with the interface (Figure 5.35d). The following equation can be used to determine the maximum shear force per length of the rockbolt:

$$W_k = \sum \frac{1}{2} m v^2 \tag{5.17}$$

where cs_{scoh} is the cohesive strength of the shear coupling spring (coupling-cohesion-shear); σ_c' is the average effective confining stress perpendicular to the "rockbolt" element; cs_{sfric} is the friction angle of the shear coupling spring (coupling-friction-shear), and *perimeter* is the exposed perimeter of the element.

(b) Calibration of Rockbolt Properties

The pull-out test is well-recognized and can represent the static load-displacement characteristics of rockbolts before rockbursting (Skrzypkowski et al., 2020; Skrzypkowski, 2021). Besides, the performance of rockbolts during strainbursts has been initially confirmed by in situ observations (Cai et al., 2010, 2019; Charette and Plouffe, 2007; Li, 2021) and others' experimental (Hyett et al., 1996) and numerical simulation results (Lisjak et al., 2020; Ma et al., 2014) in this research. Hence, only the simulated pull-out tests were conducted to calibrate the input parameters of the "rockbolt" element with the comparison of the laboratory test results from Charette and Plouffe (2007), Stillborg (1994), and Li (2011). The model's

size is 2 m × 1 m, and the bolt length is 2 m. This model size is almost identical to Bahrani and Hadjigeorgiou (2017). The model has Young's modulus of 7.5 GPa and a Poisson's ratio of 0.25 to represent an elastic rock mass because it has been confirmed that the elastic properties of the rock mass do not influence the load-displacement response of the "rockbolt" element (Tomasone et al., 2020) which can significantly save computation time. The rockbolt was divided into 40 segments and 41 nodes to ensure that at least one node fell into each block zone (Bahrani and Hadjigeorgiou, 2017). The upper boundary of the model was free, and a vertical upward velocity of 0.08 m/s was applied to the end node of the bolt to simulate a pull action (Zhu et al., 2020). The roller constraints were applied on the side boundaries, and the bottom boundary was fixed. A function was developed using the FISH language (built-in programming package) in UDEC to monitor the axial force and displacement of the last segment of the rockbolt in the *y*-direction.

Pull-out tests were modelled iteratively to adjust input parameters (e.g., tensile yield strength, tension failure strain, shear coupling spring stiffness, and shear coupling spring cohesion, Itasca, 2020) until the simulated results were consistent with the targeted properties of rockbolts. Other input parameters (e.g., the diameter, length, density, and elastic modulus of rockbolts) are the same as those used in laboratory tests. The simulated load-displacement curves and axial force of rockbolts and the block displacement are shown in Figure 5.36. The calibrated input parameters of rockbolts are listed in Table 5.12. The applied load is axial in an ideal pull test as simulated in this study. Thus, the parameters regarding resistance to bending are not employed. The errors between the targeted and simulated ultimate load, rupture displacement, and static energy-absorption capacity of rockbolts are less than 5% (Table 5.13), indicating that the targeted values agree well with calibrated input parameters. Thus, the calibrated parameters in Table 5.12 could be used to further the numerical analysis of the performance of yielding and conventional rockbolts (Zhang and Nordlund, 2019). However, it should be noted that the sliding or extraction of

Roofex was not simulated explicitly in the pull-out test, and its energy-absorption mechanism was simplified to the deformation or stretch of bolt shanks. This equivalent approach could be regarded as a relatively good selection at this stage since the complexity of simulating bolt sliding was ignored, and the time cost was thus significantly reduced.

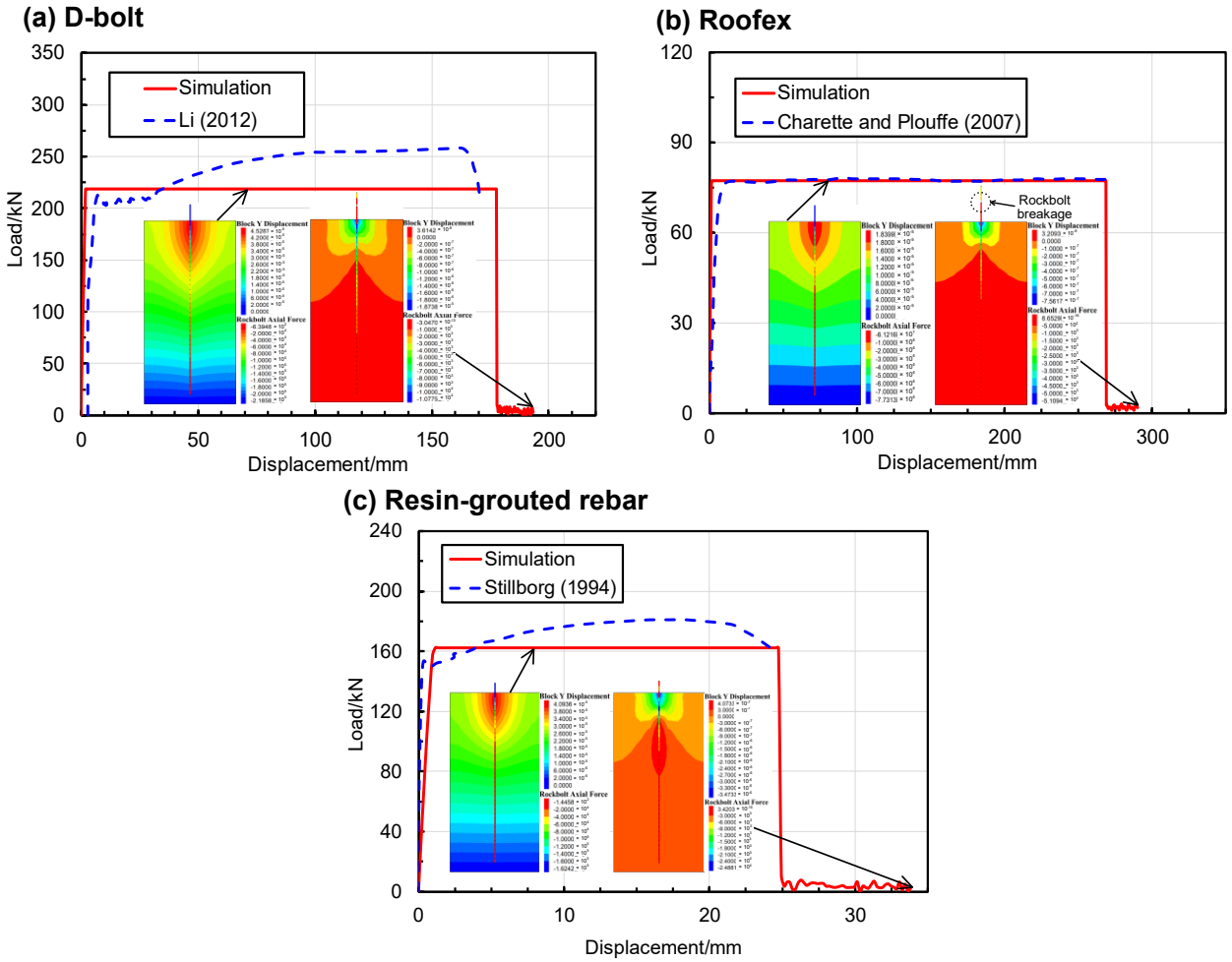

Figure 5.36 Simulated load-displacement curves and axial forces of rockbolts and deformation of rockmasses. (Rockbolt axial force in N and block Y displacement in m.)

Table 5.12 Calibrated input parameters of rockbolts.

Rockbolt Type	Cross-Sectional Area (m^2)	Moment of Inertia (m^4)	Perimeter of Borehole (m)	Density (kg/m^3)	Elastic Modulus (GPa)	Tensile Yield Strength (kN)	Tension Failure Strain	Shear Coupling Spring Stiffness (GN/m/m)	Shear Coupling Spring Cohesion (kN/m)	Shear Coupling Spring Friction Angle (°)
Resin-grouted rebar	3.14×10^{-4}	7.85×10^{-9}	0.08	7500	200	517	0.33	0.31	400	45
D-bolt	3.80×10^{-4}	1.15×10^{-8}	0.10	7500	200	575	1.36	0.29	438	45
Roofex	1.23×10^{-4}	1.20×10^{-9}	0.08	7500	200	630	1.66	0.21	353	45

Table 5.13 Comparison between the targeted and simulated rockbolt properties.

Rockbolt Type	Ultimate Load (kN)			Rupture Displacement (mm)			Static Energy-Absorption Capacity (kJ)		
	Laboratory Test	Simulation	Error /(%)	Laboratory Test	Simulation	Error /(%)	Laboratory Test	Simulation	Error /(%)
Resin-grouted rebar	162	162	0.0	24.1	24.9	3.3	4.15	3.96	−4.6
D-bolt	212	219	3.3	170	178	4.7	40.23	38.65	−3.9
Roofex	77.6	77.3	−0.4	274	269	−1.8	20.94	20.71	−1.1

5.2.3.3 Simulation Procedures and Schemes

The following stages and schemes performed modeling the effects of yielding rockbolts on controlling self-initiated strainbursts.

Stage I (static stage): The in situ stress field was applied to the model, and the geostatic equilibrium was achieved. Then, the tunnel was excavated by deleting the blocks. Adequate calculation steps were run to ensure the gradual and slow release of surrounding rock stresses (Gao et al., 2015). The installation of rockbolts was conducted immediately after the excavation of the tunnel.

Stage II (dynamic stage): The dynamic mode was activated. The local damping ratio was set 0.05. The viscous boundary (Lysmer and Kuhlemeyer 1969) was used in the dynamic calculation to avoid propagating waves' reflection and allow the necessary energy radiation. The dynamic calculation time is set to 120 ms. The pattern layout of rockbolts in the tunnel is shown in Figure 4. The roof and two ribs of the tunnel were supported by 15 rockbolts, while the floor remained unsupported, as is a common practice. The roof and rib bolts have a 2.5 m and a row spacing of 0.7 m. The spacing of rockbolts along the tunnel axis is one meter by setting the "spacing" parameter in UDEC. Besides, D-bolt, Roofex, and fully resin-grouted rebar were simulated in each scheme.

5.2.4 Analysis of Simulation Results

5.2.4.1 Displacement and Velocity Analysis

The simulated displacement patterns of the tunnel supported by different rockbolts are shown in Figure 5.37a. The large deformation only occurs in a local tunnel area that D-bolts support. In contrast,

noticeable roof subsidence and sidewall shrinkage are observed when the tunnel is supported with Roofex and resin-grouted rebar. To further investigate the effects of different rockbolts on controlling strainbursts, four monitoring points were arranged at the roof, floor, and two sidewalls of the tunnel to record the tunnel deformation (Figure 5.29). The comparison of the tunnel deformation in three support schemes is shown in Figure 5.37b. It can be seen that the tunnel supported by D-bolts suffers minor deformation (1411 mm in total). However, the total deformations of the tunnel supported with Roofex and resin-grouted rebar are 2159 mm and 2946 mm, respectively, which are 1.53 and 2.09 times that of the tunnel supported by D-bolts.

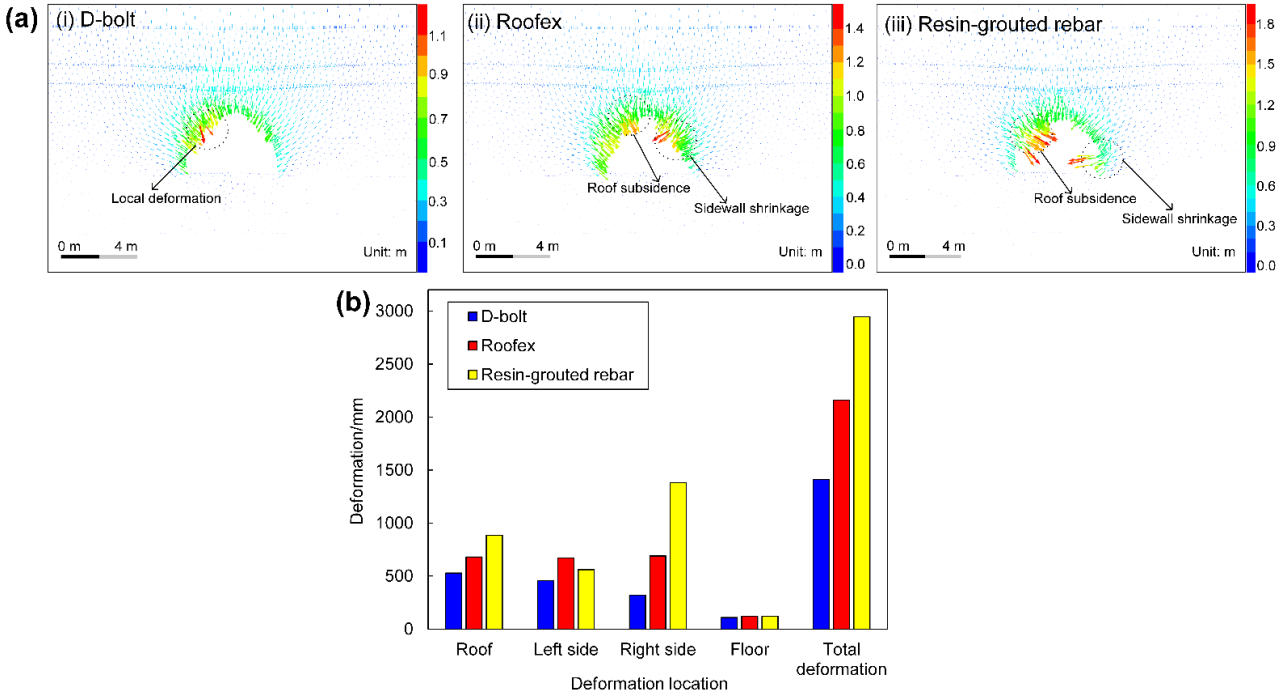

Figure 5.37 (a) Simulated displacement vectors of the surrounding rock masses along the tunnel supported by different types of rockbolts. (b). Comparison of the deformation of the tunnel supported by different types of rockbolts.

The most severe deformation is found when the resin-grouted rebar supports the tunnel. Although the resin-grouted rebar has relatively high strength (162 kN), its elongation rate is low and easy to break during dynamic shocks. As shown in Figure 5.38c, many resin-grouted rebar bolts are broken during the strainburst, and therefore they cannot control rapid rock bulking or ejection effectively. Some in situ

observations (see Figure 5.39) can confirm this phenomenon. Figure 5.39a shows that resin-grouted rebar bolts were broken in a rockburst while yielding rockbolts survive. Figure 5.39b, c also illustrates that many rebar bolts failed in rockbursts in deep tunnels. The match between simulation results and in situ observations verifies the reliability and rationality of the "rockbolt" element in modeling the performance of yielding rockbolts. Roofex also fails to restrain the large deformation because it possesses the lowest strength (77 kN) compared to D-bolt (219 kN) and resin-grouted rebar (162 kN). In summary, Roofex and resin-grouted rebar cannot effectively control the large deformation in self-initiated strainbursts.

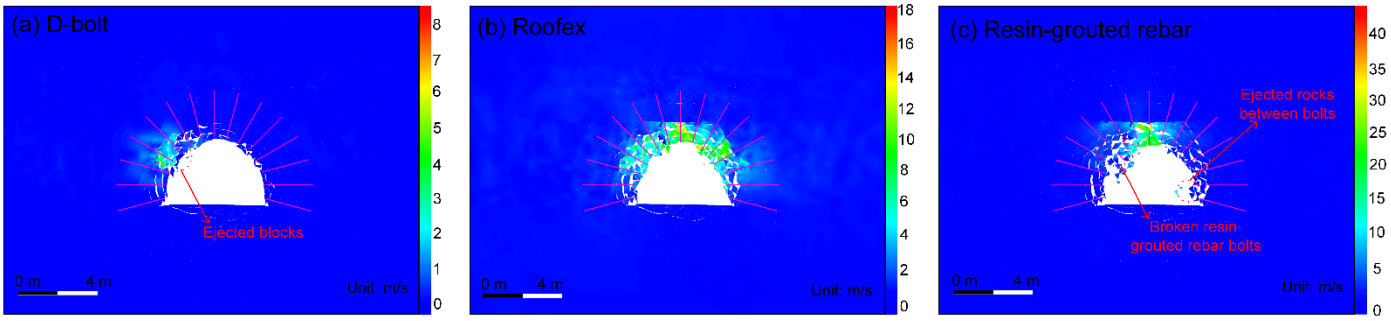

Figure 5.38 Simulated velocity distribution of the surrounding rock masses along the tunnel supported by different types of rockbolts.

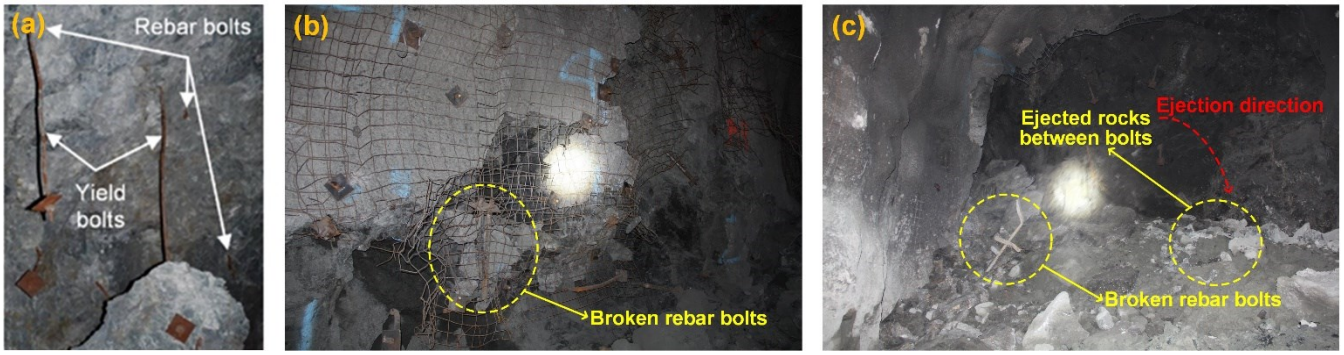

Figure 5.39 (a) Observed performance of fully resin-grouted rebar and yielding rockbolts in a rockburst (Li, 2020). (b) and (c) are in situ observations of broken rebar bolts after rockbursts in deep tunnels (photographs taken by authors).

The velocity distribution of tunnel surrounding rock masses in three support schemes is shown in Figure 5.28. It can be seen from Figure 5.28 that only a few rock blocks are ejected from a local zone when the D-bolt is adopted. For the tunnel supported by Roofex and resin-grouted rebar, much more rock blocks are ejected from the roof and sidewalls. To further study the effects of different rockbolts on

mitigating rockburst damage, a function was developed using FISH language programming in UDEC to record the velocity and volume of all the detached rock blocks in the model. The detached rock blocks were detected when blocks or clusters of blocks had no contact with normal forces on their boundaries. The statistical analysis results are illustrated in Figure 5.40. As shown in Figure 5.40a, the average velocity of detached rock blocks in the tunnel supported by D-bolts is only 0.34 m/s, although a few blocks may have a relatively high velocity (e.g., 5–10 m/s). By comparison, the average velocities of detached rock blocks in the tunnel supported with Roofex and resin-grouted rebar are 3.22 and 3.97 m/s, respectively. Besides, the velocity distributions of rock blocks in these two scenarios are more extensive than those in the tunnel using D-bolts. Figure 5.40b shows that 99.8% of rock blocks in the tunnel supported by D-bolts possess a velocity lower than 5 m/s, while the velocities of most rock blocks in the other two scenarios (95.1% for Roofex and 89.2% for resin-grouted rebar) are within the range of 0–10 m/s. In addition, many rock blocks focus on the volume range of 0.04–0.055 m^3. This is because the edge length of blocks near the tunnel was set to 0.3 m. These results suggest that the rock ejection is much more violent when the tunnel is supported by Roofex and resin-grouted rebar, which further confirms that these two types of rockbolts are unable to control strainbursts.

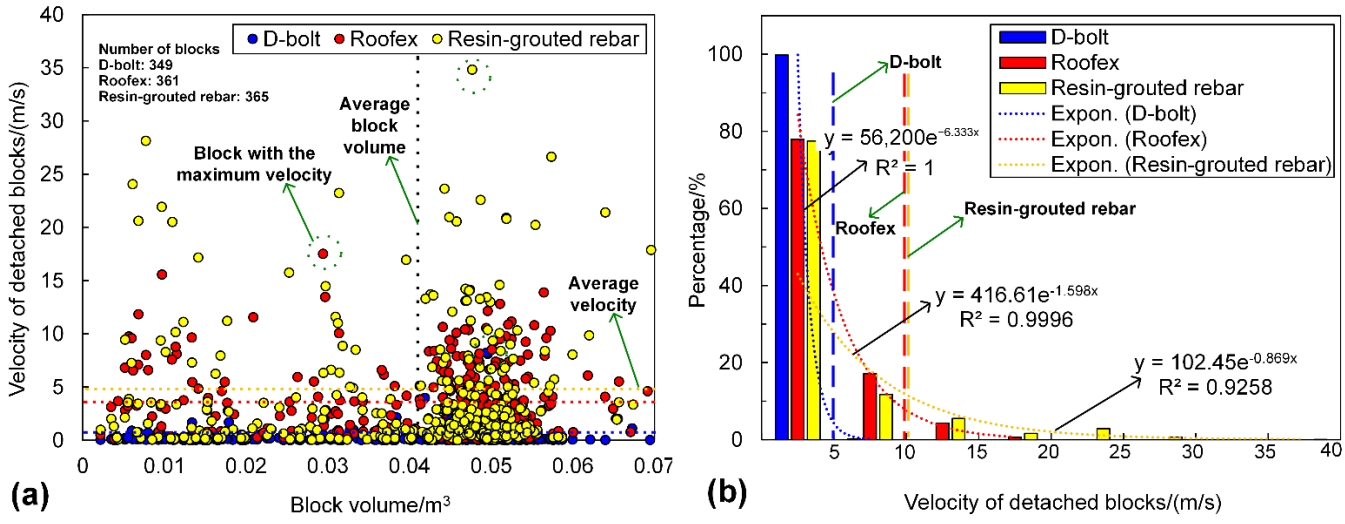

Figure 5.40 (a) is the velocity of all detached blocks versus block volume. (b) is the velocity distribution of all detached blocks. e is the Euler's number.

5.2.4.2 Rockburst Damage Analysis

In order to investigate the influences of different types of rockbolts on mitigating rockburst damage, the macroscopic failure pattern and damage degree of the tunnel induced by strainbursts were analyzed. This study evaluated the rockburst damage degree by failed rock volume (Cai, 2013). A function was developed using FISH language programming in UDEC to sum the volume of detached rock blocks. It should be noted that the volume of detached rock blocks induced by static excavation was excluded from the calculation.

Figure 5.41 shows the tunnel's macroscopic failure patterns supported by different rockbolts. As shown in Figure 5.41a, when D-bolts are adopted in the tunnel, the extent of the fractured zone is much smaller than that of the tunnel supported with Roofex and resin-grouted rebar. As a result, only a few rock blocks are ejected between bolts, and the tunnel surrounding rock masses is overall stable. However, the surrounding rock masses are fractured for the tunnel using Roofex and resin-grouted rebar, and many ejected rock blocks are observed. As a result, rockfall occurs, and the tunnel tends to be unstable.

The comparison of the volume of ejected rock blocks of the tunnel in three support schemes is shown in Figure 5.41b. The volume of ejected rock blocks is the least (1.07 m^3) when the tunnel uses D-bolt support. However, the volume of ejected rock blocks of the tunnel supported with Roofex and resin-grouted rebar is 1.54 m^3 and 1.79 m^3, respectively, which are 1.44 and 1.67 times that of the tunnel supported by D-bolts. Rockburst damage is the most serious when resin-grouted rebar supports the tunnel due to its low deformation capacity to restrain rapid rock bulking and ejection (Cai, 2013; Diederichs, 2018). This finding further verifies that the conventional rockbolts (e.g., rebar bolts) are too stiff to control rockburst damage. Besides, the volume of ejected rock blocks of the tunnel supported with Roofex is moderate. This is because Roofex has the lowest strength, and its sliding mechanism can be easily activated. Thus, it is too “soft” or “smooth” to limit ejected rocks’ movement compared to D-bolts.

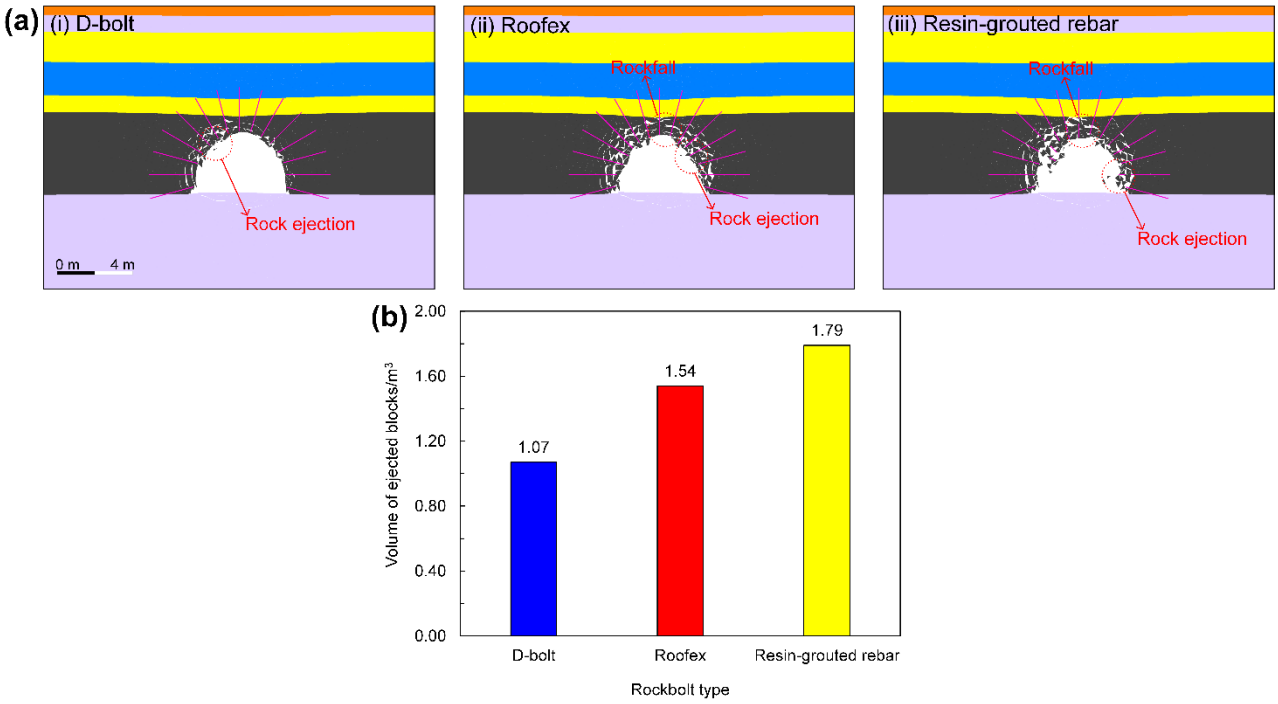

Figure 5.41 (a) Macroscopic failure patterns of the tunnel supported by different types of rockbolts. (b) is the volume of ejected rock blocks of the tunnel induced by rockbursts.

5.2.4.3 Energy Evolution Analysis

The severity of rockbursts is related to the magnitude of the kinetic energy of ejected rock materials (Cai, 2013; Zhu et al., 2020). The kinetic energy is one part of the total released energy that the supporting system (e.g., rockbolt, cable bolt, liner, and wire mesh) must absorb to reduce rockburst risks (Raffaldi, 2017). Therefore, the influences of rockbolt supporting the distribution and change of kinetic energy were investigated in this study. The kinetic energy of ejected rock blocks was captured by the FISH language programming in UDEC using the following formula:

$$W_k = \sum \frac{1}{2} m v^2 \tag{5.18}$$

where m and v are the mass and velocity of ejected rock blocks at the current time step.

The distribution of the kinetic energy of ejected rock blocks in three support schemes is shown in Figure 5.42. It can be seen that the kinetic energy pattern is very similar to that of velocity (see Figure 13). As shown in Figure 5.42a, only a few rock blocks have relatively high kinetic energy when the D-bolt is adopted. On the other hand, more rock blocks possess higher kinetic energy for the tunnel supported by

Roofex and resin-grouted rebar. The variation of kinetic energy with time influenced by different rockbolt types is illustrated in Figure 5.42b. When the tunnel is supported with D-bolts, kinetic energy evolution can be divided into two stages: the kinetic energy first increases to the peak value from 0 to 26 ms and then gradually declines to almost zero. For Roofex, the kinetic energy experiences fast growth, especially after 80 ms, and reaches the peak value at 103 ms. Then, the kinetic energy drops with time but is still high. When the tunnel is supported by resin-grouted rebar, the kinetic energy increases rapidly to the peak value from 0 to 54 ms and then suffers a sudden drop. Then, it surges again at 100 ms.

Interestingly, kinetic energy grows again. This is because the ineffectiveness of resin-grouted rebar results in the "Domino-like" failure fashion during the strainburst. In summary, D-bolts effectively absorb the kinetic energy of ejected rock blocks, and the strainburst is controlled. However, Roofex and resin-grouted rebar fail to absorb the kinetic energy of ejected rock blocks effectively and cannot control the strainburst.

To further evaluate the dynamic energy-absorption capacity of three types of rockbolts, the tunnel without adopting any supports during the strainburst was simulated. Then, a new variable was defined as the reduced kinetic energy, the difference between the kinetic energy of ejected rock blocks in the tunnel without and using rockbolts. Figure 5.42c compares the reduced kinetic energy of ejected rock blocks in the tunnel supported by different rockbolts. The reduced kinetic energy is the highest (469.30 kJ) when the tunnel uses D-bolt support. In contrast, the reduced kinetic energy is the lowest (125.19 kJ) for the tunnel supported by resin-grouted rebar, while the performance of Roofex on reducing kinetic energy (295.16 kJ) is in between the D-bolt and resin-grouted rebar. These results are not surprising because they agree that D-bolt has both high strength and excellent deformation capacity, while Roofex has low strength and resin-grouted rebar has very limited deformation capacity.

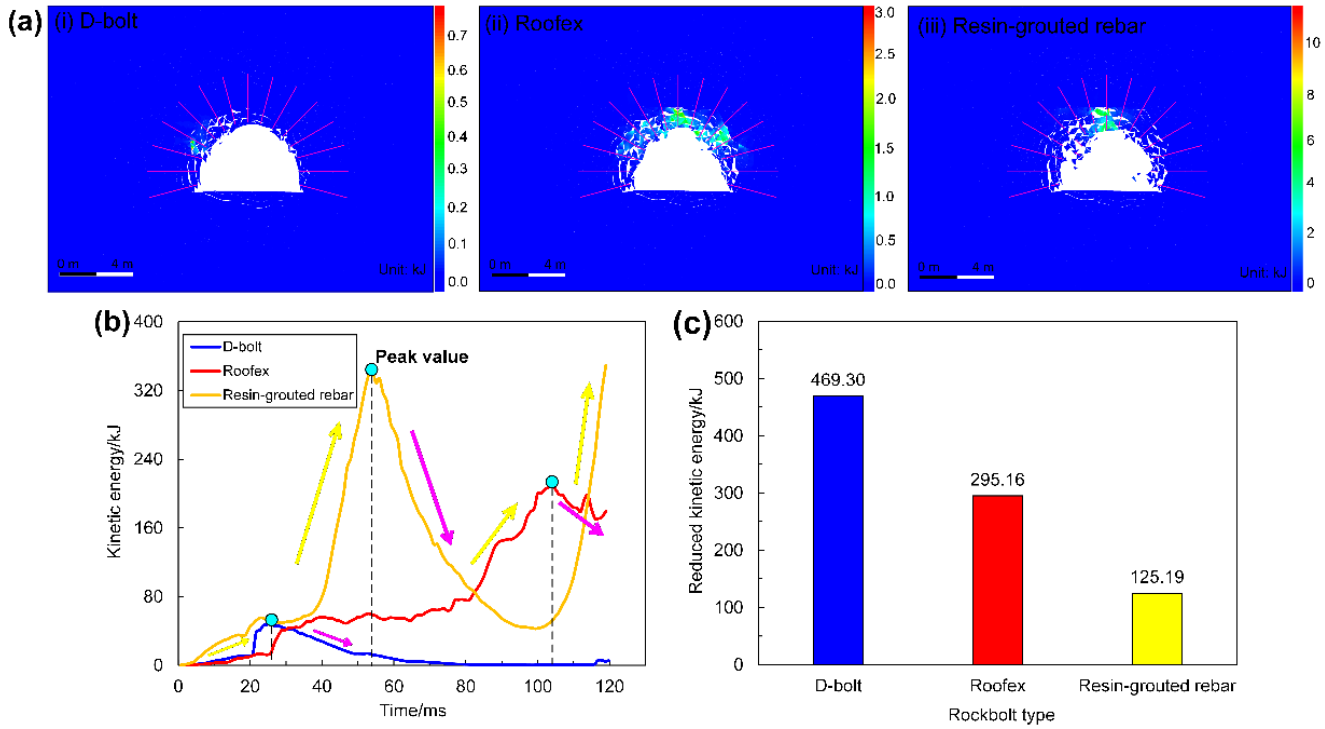

Figure 5.42 (a) Simulated kinetic energy distribution of ejected rock blocks in the tunnel supported by different types of rockbolts. (b) is the evolution of kinetic energy of ejected rock blocks. (c) is the comparison of reduced kinetic energy of ejected rock blocks.

5.2.4.4 Rockbolt Force Analysis

The simulated axial force distribution of rockbolts in three support schemes is shown in Figure 5.43. In all three cases, the tensile axial force tends to reach the peak value at a certain distance (around 1–1.5 m) from the bolt end (head) and then gradually decreases to a low value. The simulated axial force patterns of rockbolts agree with some published experimental tests (Hyett et al., 1996) and numerical simulation results (Ma et al., 2014; Lisjak, 2020). The average peak values of axial forces for the three rockbolt types are 214.87 kN, 76.99 kN, and 151.05 kN, respectively. Thus, the D-bolt and resin-grouted rebar can bear the high load of rock masses, while the Roofex cannot provide sufficient resistance to control large rock deformation and rapid rock bulking during strainbursts.

Additionally, it can be observed that 13 resin-grouted rebar bolts are broken, resulting in the unsuccessful control of the strainburst. Again, this is because the resin-grouted rebar has limited deformation capacity to accommodate rapid rock bulking and relieve rock ejection (Cai, 2013; Diederichs,

2018). No broken rockbolts were found for the tunnel adopting D-bolt and Roofex supporting. In summary, the D-bolt and resin-grouted rebar can maintain a high axial force level during the strainburst to restrain rock ejection and rock bulking, but the resin-grouted rebar is prone to be broken due to a minimal elongate rate failing to mitigate rockburst damage effectively. Roofex's axial force is too low to control strainbursts, although it has an excellent deformation capacity over the other two rockbolt types.

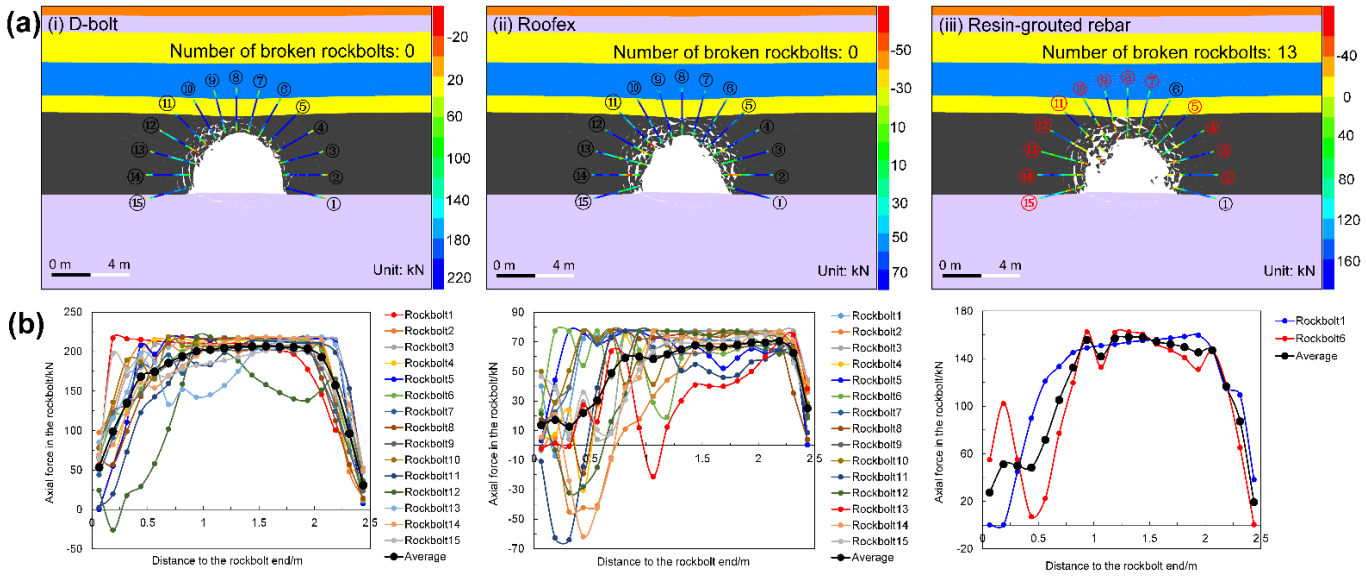

Figure 5.43 Simulated contours (a) and distribution of the axial force (b) in rockbolts for the tunnel supported by different rockbolts. The black and red numbers indicate intact and broken rockbolts, respectively. The positive value of axial forces represents a tensile load.

5.2.5. Discussion

5.2.5.1 Influence of the Bolt Number

The effects of rockbolts on controlling self-initiated strainbursts depend on rockbolt types and are also affected by other factors, e.g., bolt number, bolt length, and row spacing. Therefore, it is interesting to explore the influences of these factors on the control and mitigation of strainburst damage, which can be used for optimizing the support design in burst-prone grounds. Since the D-bolt performs better on controlling strainbursts than Roofex and resin-grouted rebar based on previous analyses, it was decided to simulate the tunnel supported by D-bolts with different bolt numbers (9, 12, 15, and 18) as an example, while other influence factors (e.g., bolt length) can also be studied in the model.

The simulation results are shown in Figures 5.44 and 5.45. It can be seen from Figure 5.44a that many rock blocks with high velocities are ejected from the roof and sidewalls when 9 D-bolts support the tunnel. A moderate number of rock blocks are ejected from a local zone when 12 D-bolts are installed. However, only a few rock blocks are ejected for the tunnel supported with 15 D-bolts, and almost no ejected rock blocks are found when the bolt number is 18. The statistical analysis results of the velocity and volume of all the detached rock blocks in the model are illustrated in Figure 5.45. As shown in Figure 20a, the average velocity of rock blocks in the tunnel supported by 9 D-bolts is 4.54 m/s. By comparison, the average velocities of rock blocks in the tunnel supported with 12, 15, 18 D-bolts are 0.48, 0.34, and 0.04 m/s, respectively. These results suggest that the rock ejection is very violent when the tunnel is supported by 9 D-bolts, which fail to control the strainburst.

Figure 5.44b shows the macroscopic failure patterns of the tunnel supported by different numbers of rockbolts. It can be seen that the extent of the fractured zone gradually decreases with the growth of bolt numbers. For the tunnel using 9 and 12 D-bolts, surrounding rock masses are very fractured, and rockfall and rock ejection are observed. The tunnel tends to be unstable. In contrast, only a few rock blocks are ejected when 15 D-bolts are installed. No obvious rockfall and rock ejection are observed, and the tunnel surrounding rock masses is very stable when the blot number is 18.

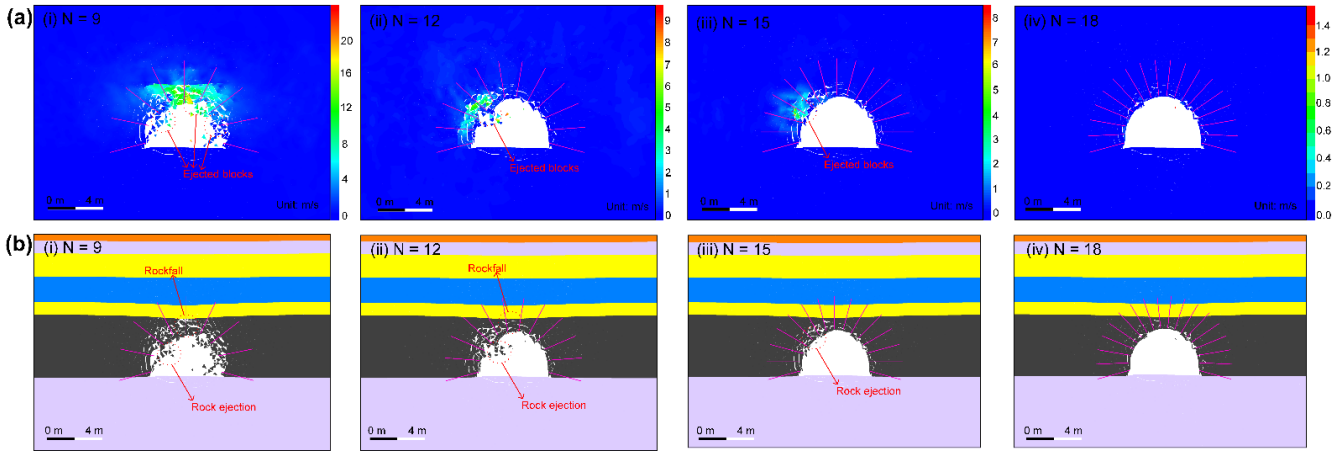

Figure 5.44 (a,b) are simulated velocity distribution and macroscopic failure patterns of the tunnel. N is the bolt number.

The variation of the kinetic energy of ejected rock blocks with time is illustrated in Figure 5.45b. When the tunnel is supported with 9 D-bolts, the kinetic energy increases from 0 to 40 ms and then experiences several fluctuations. After that, the kinetic energy grows fast, especially after 100 ms, and reaches the peak value at 117 ms. In contrast, the kinetic energy evolution trends for the tunnel using 12, 15, and 18 bolts can all be divided into two stages: the kinetic energy first increases to the peak value and then gradually declines to lower values (almost zero when using 18 bolts). This is because more rockbolts are deformed to absorb the kinetic energy of ejected rock blocks, which confirms the lower average velocity. However, the residual kinetic energy is still high (12.7 kJ) when adopting 12 D-bolts, indicating that this number is insufficient to control the strainburst. In summary, 9 and 12 D-bolts cannot control the strainburst, while 15 and 18 bolts can make the tunnel stable.

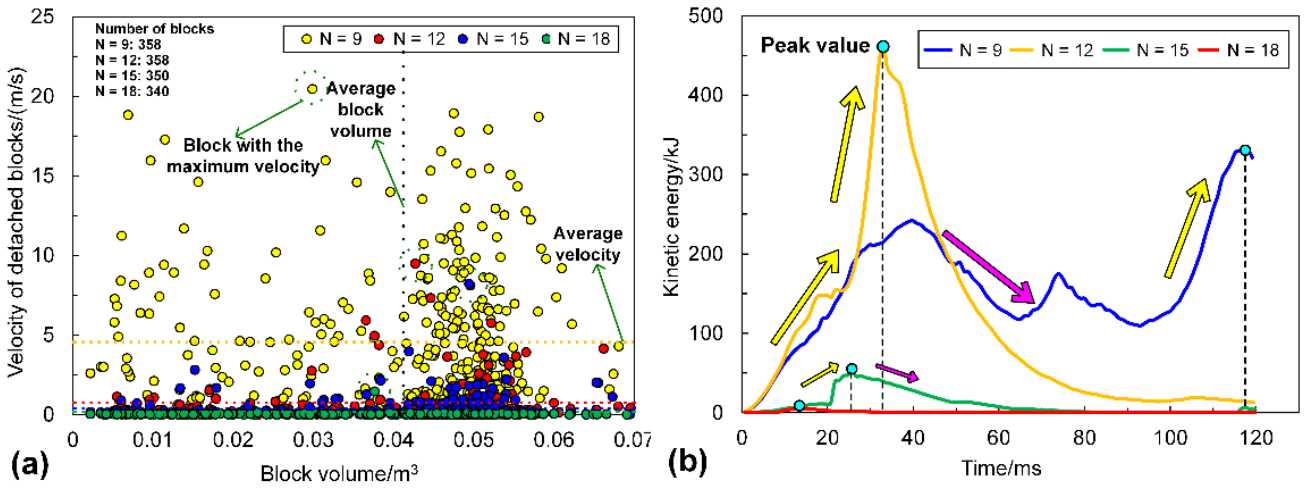

Figure 5.45 (a) is the velocity of all detached blocks versus block volume. (b) is the evolution of kinetic energy of ejected rock blocks in the tunnel. N is the bolt number.

5.2.5.2 Influence of the Surface Retaining Element

The surface retaining element (e.g., fibre-reinforced shotcrete, wire mesh, and steel arch) is an indispensable component of the support system as it can prevent the unravelling of fractured rocks between rockbolts. Therefore, the effects of combining surface retaining elements and yielding rockbolts on controlling strainbursts should be investigated. In this research, the tunnel supported with D-bolts and a steel arch was simulated to demonstrate the benefits of surface retaining elements. The beam structural

element modeled the steel arch in UDEC. The input parameters of the beam structural element are adopted from Małkowski et al. (2017), as listed in Table 5.14.

Table 5.14 Input parameters of the beam structural element (from Małkowski et al., 2017)

Input Parameter	Cross-Sectional Area (m^2)	Moment of Inertia (m^4)	Density (kg/m^3)	Poisson's Ratio	Elastic Modulus (GPa)	Tensile Yield Strength (kN)	Shear Coupling Spring Stiffness (GN/m/m)	Normal Coupling Spring Stiffness (GN/m/m)
Beam	4×10^{-3}	8.38×10^{-6}	7700	0.3	210	650	10^4	10^4

It should be noted that simulating both rockbolt and beam elements in the dynamic calculation mode in UDEC currently takes impracticable time (e.g., more than 1000 h) to approach the equilibrium state due to intrinsic difficulties in the program. Thus, the model's simulation results, only running 20 ms were analyzed. Figure 5.46 shows the macroscopic failure patterns of the tunnel with and without a steel arch. It can be seen that the detachment and ejection of rock bocks between rockbolts are well restrained by the steel arch, although the surrounding rock masses are still fractured.

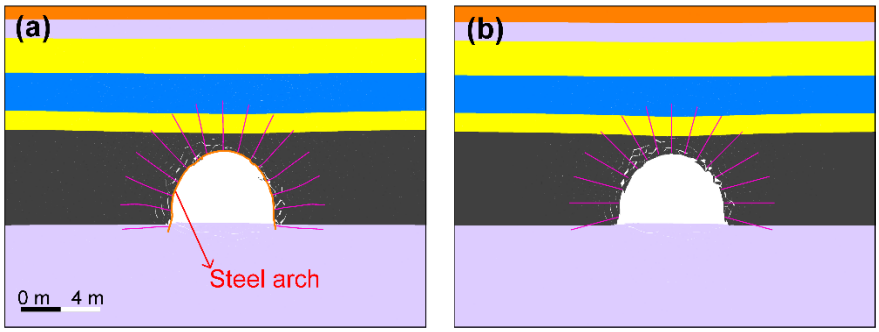

Figure 5.46 (a) and (b) are the macroscopic failure patterns of the tunnel with and without a steel arch. The dynamic calculation time is 20 ms.

5.2.5.3 Highlights and Limitations

The effects of yielding rockbolts on controlling self-initiated strainbursts were investigated using DEM. Instead of conventional drop tests, the performance of yielding rockbolts (e.g., the dynamic capacity of energy absorption and control of rock damage) is evaluated during simulated strainbursts for the first time. The results suggest that the D-bolt, as a type of high strength yielding rockbolt, can effectively control the large deformation, reduce kinetic energy, and mitigate rockburst damage, while Roofex (low strength yielding rockbolt) and resin-grouted rebar (stiff rockbolt) fail to control self-initiated strainbursts. This

finding agrees well with many others' studies. For instance, Li et al. (2014), Li (2020), and Sharifzadeh et al. (2020) suggested that the high-strength yielding rockbolt should be used to control rockbursts, because this type of rockbolt can bear high loads and displace significantly, thereby absorbing a significant amount of kinetic energy than other types of rockbolts.

This study highlights the usage of numerical modeling methods in assessing the performance of yielding rockbolts, which can be served as a promising tool to improve and optimize the design of rock supporting in burst-prone grounds following the presented modeling framework (including modeling sequence, parameter calibration method, model validation method, etc.). For example, the support scenarios with the combination of different bolt types (e.g., resin-grouted rebar and D-bolt), various bolt parameters (e.g., bolt number, bolt length, bolt strength, and row spacing), and surface retaining elements (e.g., fibre-reinforced shotcrete, wire mesh, and steel arch) can be modelled to select the optimal scheme that has best control effects and lowest cost.

The prerequisite for modeling self-initiated strainbursts is to determine whether the unstable failure will occur or not, which can be judged based on the local mine stiffness and the post-failure stiffness of rock masses. However, unlike the unstable failure of rock samples, it is hard to calculate the local mine stiffness when the focus is a strainburst that usually occurs in a tunnel or roadway. In this research, the authors first proposed a novel method to calculate the local mine stiffness of a tunnel: the ratio of the in situ stress at the designed excavation boundary to the convergence of tunnel walls. This straightforward method can be easily fulfilled in 2D and 3D numerical modeling. The proposed method fills the gap in determining the local mine stiffness of a tunnel for modeling self-initiated strainbursts and provides a tool to predict the tendency of strainbursts using the stiffness theory during the design stage of mining and civil engineering projects.

The presented study and obtained results also point out some limitations for further research work:

(1) The accuracy of simulation results can be improved if the dynamic mechanical properties of rock masses and joints and related constitutive relationships are known and used.

(2) There is no energy dissipation when two contact faces are separated. However, further studies (e.g., setting residual values of contacts or selecting more representative constitutive models) need to be conducted to consider the influences of fracture energy on simulation results.

(3) The performance of yielding rockbolts during strainbursts has been initially confirmed by in situ observations and others' experimental tests and simulation results. However, the simulation results will be more accurate and reliable if field monitoring data (e.g., dynamic strength and elongation rate) of yielding rockbolts during strainbursts are available to calibrate simulation parameters.

(4) The sliding or extraction mechanism of Roofex should be simulated explicitly to evaluate its performance during strainbursts better. Setting reasonable parameters for the bolt-grout/rock interface will be a choice.

(5) The performance of yielding rockbolts was mainly evaluated from the "macro" views of the dynamic energy-absorption capacity and the control of the deformation and damage of rock masses. Other "micro" behaviour of rockbolts, e.g., the shear force and failure of bolt-grout/rock interfaces, can be studied in future research.

5.2.6. Conclusions

In this part, a 2D DEM model of a deep tunnel in an underground coal mine is built to thoroughly evaluate the effects of yielding (D-bolt and Roofex) and the traditional rockbolt (fully resin-grouted rebar) on controlling self-initiated strainbursts. The occurrence of self-initiated strainbursts is judged based on the stiffness difference between the loading system and rock masses for the first time. The main conclusions are as follows:

(1) The total deformations of the tunnel supported with Roofex and resin-grouted rebar are 1.53 and 2.09 times that of D-bolts (1411 mm). The average velocities of detached rock blocks in the tunnel supported with Roofex and resin-grouted rebar are 3.22 and 3.97 m/s, respectively, which are much higher than that of D-bolts (0.34 m/s). 13 resin-grouted rebar bolts are broken during the strainburst, while D-bolts and Roofex survive. This phenomenon agrees well with some in situ observations(Cai et al., 2010, 2019; Charette and Plouffe, 2007; Li, 2021), verifying the reliability and rationality of the "rockbolt" element in modeling yielding rockbolts.

(2) The volume of ejected rock blocks can be obtained by the developed FISH function in the numerical model. The volume of ejected rock blocks in the tunnel supported by D-bolts is 1.07 m^3, which is the least compared with Roofex (1.54 m^3) and resin-grouted rebar (1.79 m^3).

(3) The dynamic energy-absorption capacity of rockbolts can be evaluated by a proposed variable, reduced kinetic energy. Compared with Roofex (295.16 kJ) and resin-grouted rebar (125.19 kJ), the D-bolt can reduce the most kinetic energy (469.30 kJ).

(4) The simulated axial force patterns of rockbolts agree with some published experimental (Hyett et al., 1996) and numerical simulation results (Lisjak et al., 2020; Ma et al., 2014). For example, the average peak values of axial forces for D-bolt, Roofex, and resin-grouted rebar are 214.87 kN, 76.99 kN, and 151.05 kN, respectively.

(5) The bolt number significantly influences the control effects of yielding rockbolts on strainbursts. For example, 9 and 12 D-bolts cannot control the strainburst, while 15 and 18 D-bolts can make the tunnel stable. In addition, the detachment and ejection of rocks between rockbolts can be well restrained using surface retain elements, e.g., steel arch.

In summary, D-bolt can effectively control the large deformation, reduce kinetic energy, and mitigate rockburst damage, while Roofex and resin-grouted rebar fail to control self-initiated strainbursts.

Furthermore, this study highlights the usage of numerical modeling methods in assessing the performance of yielding rockbolts, which can be served as a promising tool to improve and optimize the design of rock supporting in burst-prone grounds.

6. CHAPTER 6: PREDICTION OF STRAINBURST RISKS BASED ON THE STIFFNESS THEORY: DEVELOPMENT AND VERIFICATION OF A NEW ROCKBURST INDICATOR

*This chapter first proposes a novel method to calculate the LMS for a tunnel. Later, the LMS determined by the proposed calculation method is compared to the PCS of surrounding rock masses with different brittleness to judge strainburst occurrence, which is verified with simulated stable and unstable rock failure occurring in a calibrated deep tunnel model established by UDEC. The reliability and accuracy of the proposed LMS calculation method are further examined by comparing excess energy's analytical and numerical results. Then, a new rockburst indicator, called the strainburst stiffness factor, is proposed to predict strainburst risks based on the analysis of stiffness differences. Finally, the effectiveness of the new rockburst indicator is validated with reported strainburst cases. This study provides an effective tool to predict strainburst risks, which can further improve the safety of workers and equipment when constructing deep excavations in mining and civil engineering projects. This chapter is based on the submitted paper "**Wang, J.,** Apel, D. B., Wei, C,. Xu, H. (2022). Prediction of strainburst risks based on the stiffness theory: development and verification of a new rockburst indicator. In preparation for submission".*

6.1 Introduction

A critical task for researchers is to predict the possibility or risk of strainburst occurrence. This can help engineers improve and optimize project layouts, mining or excavation methods to avoid potential strainbursts during the design phase and adjust construction schemes or adopt distress and support measures in time during the production stage. In the last few decades, with the deeper understanding of rockburst mechanisms and the development of all aspects of rock mechanics, great achievements have been made in strainburst prediction, which are twofold. First, different research methods, including analytical, empirical, experimental, data-based, and numerical, have been developed and applied to predict the possibility, location, and severity of strainbursts (Pu et al., 2019; Zhou et al., 2018). Second, many prediction indicators of rockbursts have been proposed and developed based on various theories, e.g., strength, stiffness, energy, stability, fracture, damage, etc. (Wang et al., 2021b).

The loading system stiffness (LSS, also called local mine stiffness (LMS) at the engineering scale) and the post-peak characteristic stiffness (PCS) of rock materials can distinguish stable or unstable failure (rockburst) effectively based on the stiffness theory (Cook, 1965b; Salamon, 1970). If LSS is less than PCS, the failure will be unstable and violent due to the existence of excess energy, and vice versa. Hence, using this principle to discriminate unstable rock failure is straightforward.

Compared with analytical and experimental methods, the numerical method can provide more information (e.g., the evolution of displacement and stress field after excavation) and simulate the complex mechanical behaviour of rocks and rock masses under different conditions (Ji and Karlovšek, 2022a, b; Xu, 2021). It also has the strengths of safety, low cost, time-saving, and flexibility. Therefore, combining stiffness theory and numerical methods has become popular in predicting and evaluating rockburst risks. For example, Pen (1994) proposed a method to determine the LMS of chain pillars with non-linear material properties and used it to predict pillar bumps via three-dimensional boundary element method

(3D BEM) modeling. The effectiveness of the proposed method was verified with a case history back analysis. Wiles (2002) derived the formulas of LSS calculation and implemented them in numerical modeling to predict potential rockburst areas. The predicted results matched well with in situ observations. Kias and Ozbay (2013) employed the FLAC/PFC coupled models to predict the unstable failure of coal pillars by comparing LSS and the PCS of coal materials. Garvey (2013) investigated the influence of LMS on pillar bursts based on the analysis of maximum velocity, acceleration, shear strain rate, and excess energy in 2D and 3D models built by FLAC3D. Gu and Ozbay (2015) adopted the DEM software UDEC to study the effects of different factors, e.g., loading stiffness and in situ stress, on the stability of the shear failure of simplified rock discontinuities via calculating LMS in underground coal mines. Manouchehrian and Cai (2016) investigated the effects of LSS, height-to-width ratio, and intermediate principal stress on unstable rock failure under polyaxial unloading conditions using the explicit FEM simulation. Khademian and Ugur (2018) employed UDEC to investigate the influences of various LSS on the unstable compression and slip failure of pillars and faults from the view of radiated seismic energy. Wang and Kaunda (2019) studied the energy mechanisms of pillar bursts with different loading stiffness in DEM models by tracking the transformation of various energy components, and they concluded that a soft loading system could store more strain energy, resulting in a great amount of plastic work and released kinetic energy. Their research has achieved many fruitful outcomes, which greatly advances the development of rockburst prediction based on the stiffness theory.

In summary, the current work is mainly limited to predicting and evaluating pillar burst risks using the stiffness theory. This is because it is not hard to obtain LSS or LMS by theoretical equations, numerical modeling, and experimental tests when the research object is a rock sample or pillar with a regular shape and apparent loading and bearing systems. However, to the authors' knowledge, no studies in the literature have been reported to predict strainbursts based on the stiffness theory, which could be attributed to two

reasons. First, when the focus is a strainburst that usually occurs in a tunnel, it is much more challenging to identify the extent to which surrounding rock masses can be regarded as a loading system. Second, the LMS depends on many factors, e.g., elastic modulus, excavation geometry, and/or other rock mass properties.(Salamon, 1970; Pen, 1994) The integrated influence of these factors on calculating LMS in a tunnel configuration is still unknown. Therefore, the scientific problem of determining the LMS for a tunnel and using it to predict strainburst occurrence has confused researchers for a long time and remains unsolved.

This study aims to predict strainburst risks based on the stiffness theory. A novel method is first proposed to calculate the LMS for a tunnel. Later, the LMS determined by the proposed calculation method is compared to the PCS of surrounding rock masses with different brittleness to judge strainburst occurrence, which is verified with simulated stable and unstable rock failure occurring in a calibrated deep tunnel model established by UDEC. The reliability and accuracy of the proposed LMS calculation method are further examined by comparing excess energy's analytical and numerical results. Then, a new rockburst indicator, called the strainburst stiffness factor, is proposed to predict strainburst risks based on the analysis of stiffness differences. Finally, the effectiveness of the new rockburst indicator is validated with reported strainburst cases.

6.2 Stiffness theory and a novel method to calculate the LMS for a tunnel

6.2.1 Stiffness theory and energy balance

The recognition of the significance of stiffness in judging unstable rock failure dates back to the efforts to obtain the complete stress-strain curves of brittle rocks. At the earlier stage of rock mechanics tests, rock samples always fail suddenly and violently once the strength is attained. Hence, stress-strain curves without the post-peak stage were usually recorded. However, one might ask, is this the real property of rocks? The answer becomes a definite “no” after Cook (1965b) found that unstable rock failure is caused

by the additional energy released by soft testing machines. He proposed that rock samples would fail stably, and thus complete stress-strain curves could be obtained when using stiff testing machines because additional energy was eliminated during the post-peak stage. This important finding promotes the invention of stiff testing machines and greatly advances the development of rock mechanics. Then, Salamon (1970) generalized the LSS to an engineering scale, LMS. He developed a criterion according to the relationship between LMS and PCS and applied it to distinguish stable and unstable failure of rock pillars in room and pillar mining.

Figure 6.1 shows the concept of the stability analysis of a rock sample (pillar) based on the stiffness theory. As shown in Figure 6.1, a rock sample (pillar) is under a UCS test, which results can be illustrated as a stress-strain curve. The slope of red and blue dashed lines denotes the LSS of stiff and soft loading systems, respectively. The black sold line's slope represents the rock sample's PCS. If the LSS is less than the PCS, the rock failure will be unstable and violent because rock materials cannot fully absorb the deformation energy from the loading system. Hence, excess energy exists and is transferred to the kinetic energy of ejected rock fragments. By comparison, the loading system's deformation energy can be fully stored in rock materials and thus, failure is stable when the LSS is greater than the PCS.

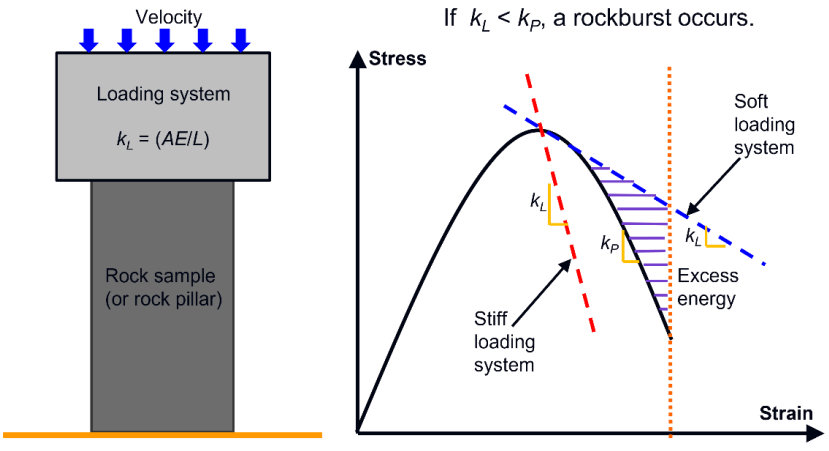

Figure 6.1 Stability analysis of a rock sample (pillar) based on the stiffness theory.

The energy balance in a rock system is shown in Figure 6.2. The total boundary loading work W supplied to the system will be converted to the stored strain energy W_e in rock materials, the dissipated energy W_j in joint shear, the plastic work W_p of intact rocks, and the released or excess energy W_r (Salamon, 1984). Hence, the released energy W_r can be obtained indirectly using the following equation:

$$W_r = W - (W_e + W_j + W_p) \tag{6.1}$$

UDEC uses a mechanical damping mechanism to reduce the unbalanced force at grid points and dissipate a great portion of kinetic energy at each timestep for making models reach an equilibrium state in a quasi-static calculation scheme (Itasca, 2020). The remaining kinetic energy approaches zero when the equilibrium state is attained. Hence, the released energy W_r can also be calculated directly:

$$W_r = W_k + W_d \tag{6.2}$$

where W_k is the total kinetic energy at the current timestep in the system; W_d is the cumulative damped energy for all timesteps. This direct calculation approach was employed in this study to calculate the released (excess) energy in the subsequent strainburst simulation.

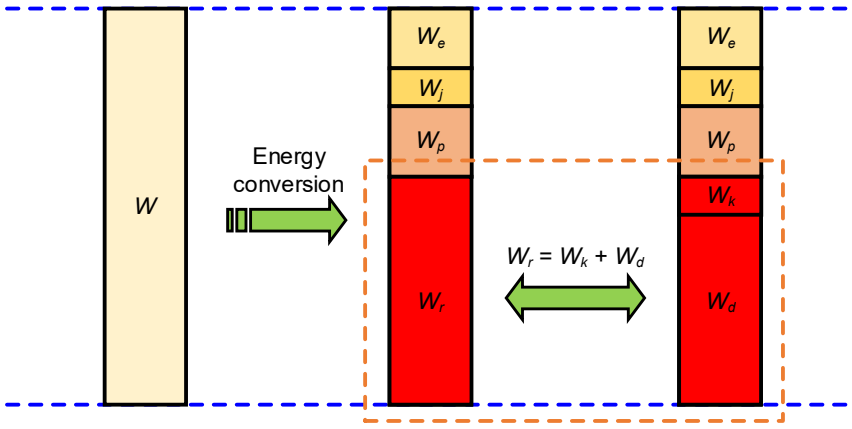

Figure 6.2 Schematic diagram of the energy balance in a rock system. The energy bar is not to scale.

6.2.2 A novel method to calculate the LMS for a tunnel

When our focus is a rock sample (pillar), it is very simple to calculate the LSS using the following formula:

$$K_L = \frac{AE}{L} \tag{6.3}$$

where K_L is LSS; A, L, and E are the loading system's cross-section area, length, and elastic modulus.

However, it is not easy to calculate K_L or LMS when the research objective is a strainburst that usually occurs in a tunnel because we even do not know the extent to which surrounding rock masses can be regarded as a loading system, unlike a UCS test that has apparent loading and bearing systems. Although we understand that LMS is not only related to elastic modulus but also a function of elastic modulus, excavation geometry, and/or other rock mass properties (Pen, 1994; Salamon, 1970), determining it quantitively is still a challenging task because of the difficulty about how to comprehensively consider these influence factors in the LMS calculation.

Jaiswal and Shrivastva (2012) proposed a method to calculate the LMS of a rock pillar via numerical modeling. As shown in Figure 6.3a, the LMS can be obtained by dividing the load F_1 applied on the rock pillar at Stage 1 with the roof-to-floor convergence (d_1-d_2) after the rock pillar is removed (Stage 2). Hauquin et al. (2018) obtained the LMS of the roof and floor by the method and calculated the released kinetic energy during pillar bursts in UDEC modeling. The results were verified by comparing analytical calculations and an empirical classification of rockbursts. Khademian and Ugur (2018, 2019) used the LMS method and then employed the graphical (analytical) approach to calculate the radiated seismic energy in pillar bursts. The theoretically calculated results agree well with numerical solutions in UDEC. Gao et al. (2019c) also adopted the method to calculate the LMS of coal pillars and compared it with PCS to judge in which excavation step the coal burst would happen using numerical modeling. Finally, a physical model experiment confirmed the simulation results. Therefore, it can be concluded that the LMS calculation method proposed by Jaiswal and Shrivastva (2012) is correct and valid for predicting pillar bursts.

These findings also motivated the authors to rethink what exactly the LMS is. Drawing on the same logic as Jaiswal and Shrivastva (2012), we proposed an innovative method to calculate the LMS for a

tunnel, as shown in Figure 6.3b. At Stage 1, the internal pressure P_1 at the designed excavation boundary equals the in situ stress P_i. At Stage 2, P_1 is reduced to zero (P_2) after excavation. Then, the LMS of a tunnel can be calculated as follows:

$$K_{LMS} = \frac{P_1}{(d_1 - d_2)} = \frac{P_i}{U} \tag{6.4}$$

where d_1 and d_2 are the tunnel diameter before and after excavation; U is the tunnel wall convergence after excavation. We can notice that Figure 6.3b and Eq. (6.4) have made the answer more and more visible that the LMS is the strength or magnitude of ground reaction induced by excavation. This hypothesis will be verified by predicting strainburst occurrence in the next section. To the authors' knowledge, the proposed method is the first attempt to calculate the LMS for a tunnel. It might be argued that the method is too simple because the tunnel excavation situation is more complex than a rock pillar loading. However, we should remember that the ground reaction strength is inherently the result of the combined effects of multiple influence factors (e.g., excavation geometry and the deformation modulus and stress-strain relationship of surrounding rock masses). Thus, this is actually an indirect method to determine the LMS where the difficulty of comprehensively considering different influence factors in the calculation and the extent of involved rock masses is bypassed.

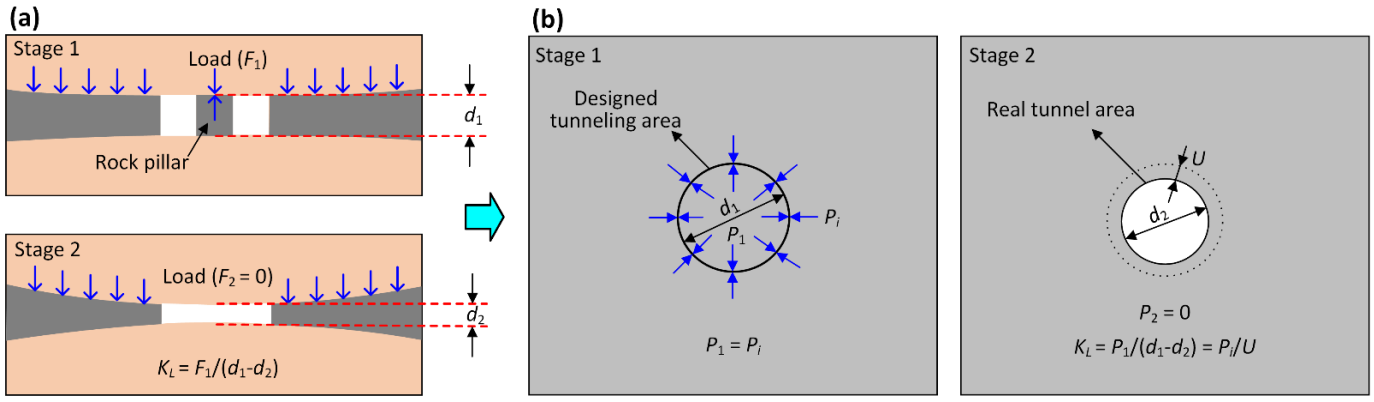

Figure 6.3 Methods to determine LMS (Wang et al., 2022b). (a) LMS calculation for a rock pillar (after Jaiswal and Shrivastva, 2012). (b) Proposed LMS calculation method for a tunnel.

6.3 Development and verification of a new indicator for strainburst prediction

6.3.1 Model setup and calibration

This study constructed a tunnel model using 2D DEM software UDEC to perform the numerical simulation employing the plane strain assumption (Wang et al., 2022b). Figure 6.4 shows the geometry of the built model. The circular tunnel has a radius of 3 m. The radius ratio of the model to the tunnel is 16.7, which is sufficiently large to eliminate boundary effects (Manouchehrian and Cai, 2018). The fixed constraints were applied on the model boundary to simulate a far-field condition. The model was first to run to a hydrostatic stress state with a magnitude of 20 MPa. Then, a SOLVE relax method was employed to slowly reduce the boundary forces on the internal boundary of the tunnel for simulating the 3D effect of a tunnel advance (Itasca, 2020), which was performed with a total of 25 stress relaxation steps.

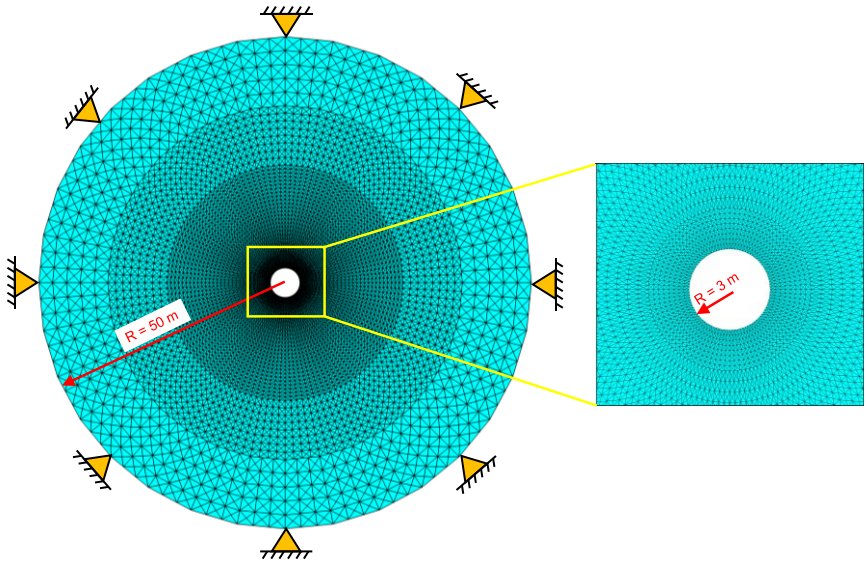

Figure 6.4 2D numerical model of a circular tunnel.

In addition to the LMS, the PCS is the other key factor controlling unstable failure. In order to obtain the PCS, accurate modeling of the post-peak responses of rocks is required. Studies have shown that the Mohr-Coulomb strain softening (MCSS) constitutive model can capture different post-peak responses by adjusting the relationship between cohesion force, tension strength, friction angle, etc. and the plastic shear strain during the post-peak stage (Hauquin et al., 2018; Khademian and Ozbay, 2019; Khademian and

Ugur, 2018; Manouchehrian and Cai, 2016, 2018). Hence, the MCSS constitutive model was adopted to simulate the mechanical behaviour of brittle and semi-brittle rock masses, while the elastic-perfectly plastic Mohr-Coulomb (EPMC) constitutive model was used for simulating ductile rock masses.

When subjected to driving forces, natural systems, e.g., rock masses, would not oscillate indefinitely because of the damping of the vibration energy within the system. The damping is partially caused by energy loss as a result of internal friction in intact materials and slippage along interfaces within the system (Itasca, 2020). Similarly, UDEC uses local damping constant to reduce the unbalanced force at gridpoints and dissipate kinetic energy to make models reach an equilibrium state in a quasi-static calculation scheme, which can be represented by the following equation(Itasca, 2020):

$$\dot{u}_i^{(t+\Delta t/2)} = \dot{u}_i^{(t-\Delta t/2)} + \left\{\sum F_i^{(t)} - \alpha\left|\sum F_i^{(t)}\right| sgn\left(\dot{u}_i^{(t-\Delta t/2)}\right)\right\}\frac{\Delta t}{m_n} \tag{6.5}$$

where t is time; $\triangle t$ is the timestep; $\dot{u}_i$ is the velocity of the gridpoint; $F_i^{(t)}$ is the resultant of all external forces applied to the gridpoint (from block contacts or otherwise) at time t; m_n is the nodal mass; α is the local damping constant. Thus, before conducting subsequent studies, the simulated radial displacement of the tunnel excavated in semi-brittle rock masses (using the MCSS constitutive model) was compared with the self-similar solution obtained by Alonso et al. (2003) for calibrating the damping constant. It should be noted that currently, there are no analytical solutions to the stress and deformation for the tunnel analyzed by the MCSS constitutive model. Therefore, damping constants from 0 to 1.0 were examined in this research. The used material properties of rock masses are adopted from Alonso et al. (2013), as listed in Table 6.1.

Table 6.1 Material properties used in the model (Alonso et al., 2003)

Constitutive model	ρ (kg/m^3)	K (GPa)	G (GPa)	c_p (MPa)	c_r (MPa)	φ_p (°)	φ_r (°)	ψ (°)
MCSS	2500	6.7	4.0	1 (ε_p = 0)	0.7 (ε_p = 0.008)	30 (ε_p = 0)	22 (ε_p = 0.008)	3.75
EPMC	2500	6.7	4.0	1	N/A	30	N/A	3.75

Note: ρ, K, and G are the bulk density, bulk modulus, and shear modulus. c_p and φ_p are the initial cohesion force and internal friction angle. c_r and φ_r are residual cohesion force and internal friction angle. ψ is the dilation angle. ε_p is the plastic shear strain. N/A: not applicable.

It should be noted that a mesh-dependent effect exists when using the MCSS constitutive model. Localization and bifurcation phenomena usually cannot be observed for large meshes models. When the mesh is refined, these phenomena occur in shear bands. The finer the mesh is, the narrower the shear bands are. However, Varas et al. (2005) have proved that localization and bifurcation phenomena do not affect the macro responses of an excavation, e.g., the ground reaction curve (GRC) of a tunnel. Therefore, similar to Khademian and Ugur (2018), the constant mesh (zone) size is used to exclude the mesh-dependent effect of the MCSS constitutive model on rock mass responses among different simulations.

Figure 6.5 shows the influence of the damping constant on the simulated tunnel deformation. It can be seen that the tunnel radial displacement decreases noticeably with the growth of the damping constant. When the damping constant is 0.6-0.9, the average difference between simulation results and the self-similar solution is 3.91 %. Hence, a local damping constant of 0.8 was employed in this research since the rationality and accuracy of using this value had been proved. Additionally, as shown in Figure 6.6a, the simulated GRC agrees well with that obtained by the self-similar solution (Alonso et al., 2003), verifying not only the chosen damping constant (0.8) but also the effectiveness of the used model configuration.

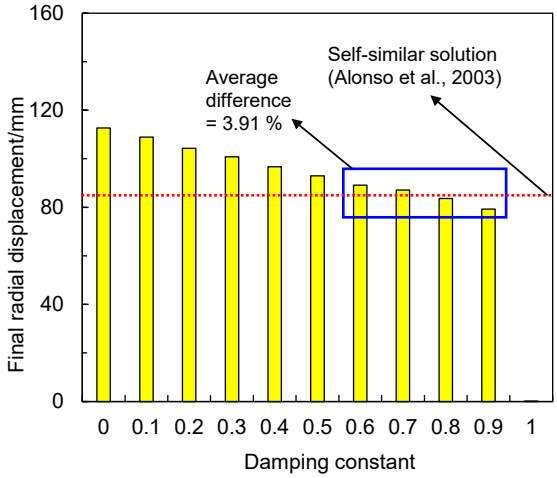

Figure 6.5 Influence of the damping constant on final tunnel radial displacement simulation results.

Since the EPMC constitutive model was also employed in this research, the tangential and radial stress distribution after tunnel excavation simulated by the EPMC constitutive model was compared with

classical analytical solutions (Salencon, 1969). The material parameters used in the EPMC constitutive model have also been listed in Table 6.1. The following equations can theoretically calculate the tangential and radial stresses within the plastic and elastic zones:

$$\begin{cases} \sigma_{\theta p} = \frac{\sigma_c}{\xi-1}\left[\xi\left(\frac{r}{r_a}\right)^{\xi-1} - 1\right] \\ \sigma_{rp} = \frac{\sigma_c}{\xi-1}\left[\left(\frac{r}{r_a}\right)^{\xi-1} - 1\right] \end{cases} \tag{6.6}$$

$$\begin{cases} \sigma_{\theta e} = p_0\left(1 + \frac{R_p^2}{r^2}\right) - \sigma_{R0}\frac{R_p^2}{r^2} \\ \sigma_{re} = p_0\left(1 - \frac{R_p^2}{r^2}\right) + \sigma_{R0}\frac{R_p^2}{r^2} \end{cases} \tag{6.7}$$

where $\sigma_{\theta p}$ are σ_{rp} are tangential, and radial stresses of a sampling point in the plastic zone; $\sigma_{\theta e}$ are σ_{re} are tangential and radial stresses of a sampling point in the elastic zone; $\xi = (1+\sin\varphi)/(1-\sin\varphi)$, φ is the internal friction angle; $\sigma_c = 2c\cos\varphi/(1-\sin\varphi)$, c is the cohesion force; r_a is the tunnel radius and r is the distance from the tunnel boundary to the sampling point; p_0 is the initial stress; σ_{R0} is the radial stress at the plastic zone radius R_p; the following equation can obtain R_p:

$$R_p = r_a\left[\frac{2p_0(\xi-1)+2\sigma_c}{\sigma_c(\xi+1)}\right]^{\frac{1}{\xi-1}} \tag{6.8}$$

Figure 6.6b compares stress distribution between analytical solutions and numerical simulation results. As shown in Figure 6.6b, the distribution law and magnitude of simulated tangential and radial stresses agree well with classical analytical solutions (Salencon, 1969). Hence, it can be concluded that the adopted damping constant and model setup are validated when using both MCSS and EPMC constitutive models, and subsequent studies can be performed based on the established numerical model.

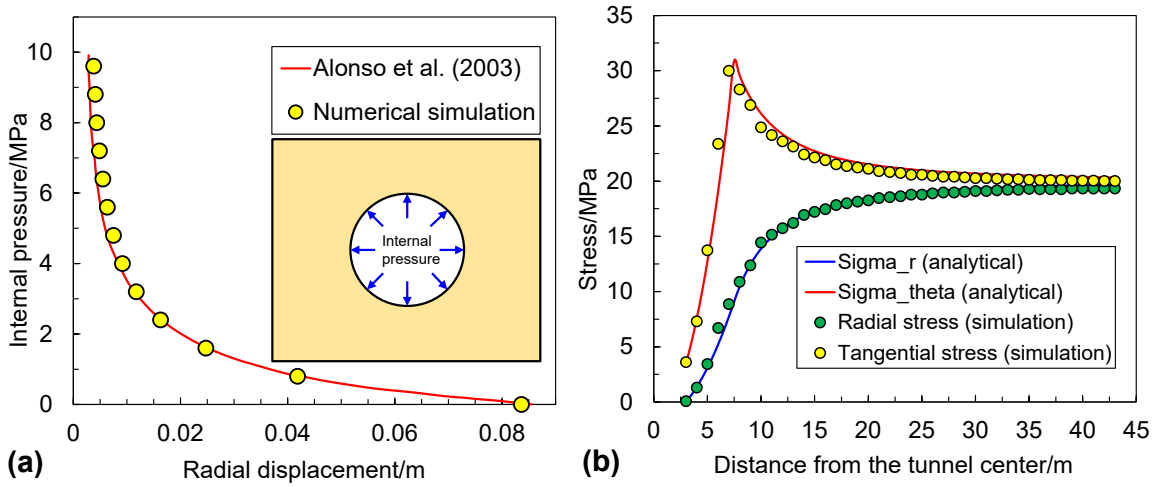

Figure 6.6 (a) Comparison of GRC between the self-similar solution (Alonso et al., 2003) and simulation results (MCSS constitutive model). (b) Comparison of stress distribution between analytical solutions (Salencon, 1969) and simulation results (EPMC constitutive model).

6.3.2 Determination of the unstable failure (strainburst) for a tunnel

To determine the unstable failure (strainburst) via the relationship between LMS and PCS, four models with the brittle, semi-brittle (#1 and #2), and ductile post-peak responses of rock masses were established. The model geometry, mesh type and size, and boundary conditions are the same as that used in Section 3.1. Case studies have shown that the unfavourable stress state (e.g., greater differences in principal stresses resulting from geology variations and major structures) is a very important contributing factor to strainburst occurrence and high-stress magnitudes (Keneti and Sainsbury, 2018). Thus, the model was first to run to a non-isotropic stress state with a horizontal-to-vertical stress ratio (K) of 0.5 before excavation to make a strainburst prone. The horizontal and vertical stresses are 30 MPa and 60 MPa, respectively. The SOLVE relax method with 25 stress relaxation steps in total was also adopted to simulate the progressive tunnel advance to avoid possible dynamic failure in zones caused by the instantaneous excavation.

The used rock mass properties (see Table 6.2) are adapted from Manouchehriana and Cai (2018), representing moderate hard rock masses. Except for the ductile rock mass, the different post-peak responses of brittle and semi-brittle rock masses are obtained by adjusting the relationship between the

cohesion force and the plastic shear strain (Hauquin et al., 2018; Khademian and Ozbay, 2019; Khademian and Ugur, 2018).

Table 6.2 Material properties of rock masses with different post-peak responses

Rock mass response	Constitutive model	ρ (kg/m^3)	K (GPa)	G (GPa)	φ (°)	c_p (MPa)	c_r (MPa)
Ductile	EPMC	2500	11.1	8.3	30	20	NA
Semi-brittle #1	MCSS	2500	11.1	8.3	30	20 (ε_p = 0)	0 (ε_p = 0.2)
Semi-brittle #2							0 (ε_p = 0.15)
Brittle							0 (ε_p = 0.001)

Unlike observing rock failure processes and characteristics directly in experimental tests, it is not straightforward to recognize stable and unstable failure in numerical modeling (Manouchehrian and Cai, 2018). A commonly used approach is to compare model responses with a base model in which failure is known to be stable. The compared model responses usually include stress-strain curve, unbalanced force, velocity, acceleration, kinetic energy, and damping energy (Garvey, 2013; Gu and Ozbay, 2015; Khademian et al., 2016; Manouchehrian and Cai, 2016). For instance, the failure induced by excavating the tunnel within ductile rock masses can be regarded as stable (base model). Then, we can compare the responses of other models using brittle and semi-brittle rock masses with the base model to judge stable or unstable failure. In this research, the velocity of zones, the volume of failed rock masses, kinetic energy, and damping energy were monitored to compare them with the base model to determine the failure mode.

6.3.2.1 Comparation of the velocity distribution of tunnel surrounding rock masses

The velocity distribution of tunnel surrounding rock masses in four scenarios is shown in Figure 6.7. It can be seen that the maximum velocity of surrounding rock masses is less than 0.05 m/s at the whole excavation stage when rock masses have the mechanical behaviour of ductile, semi-brittle #1 and #2 (Figure 6.7a, b and c), suggesting that the entire system is in a quasi-static state. However, the maximum velocity of surrounding rock masses can be up to 1.8 m/s at the last relaxation step when the tunnel is excavated in brittle rock masses, although it is less than 0.05 m/s at most relaxation steps (Figure 6.7d).

Figure 6.7e was illustrated further to investigate the velocity change at the last relaxation step. At the earlier stage of relaxation step 25 (timestep = 200000), the surrounding rock masses are static because the maximum velocity is less than 0.05 m/s. Then, the maximum velocity is increased to 1.8 m/s when the timestep is 230000. The increment of 30000 timesteps is equal to the numerical time of around 0.2 s. In addition, it is found that the rock masses at the tunnel surface possess the maximum velocity. These results indicate that rock ejection occurs suddenly when the tunnel excavation is almost done. It is also interesting that a V-shaped zone with high speeds exists. Therefore, we can expect that a V-shaped burst pit will appear if a bonded block method (BBM) allowing block detachment is used. The V-shaped burst pit has been reported in many strainburst cases (e.g., Zhang et al., 2012, 2013), further confirming the model's effectiveness.

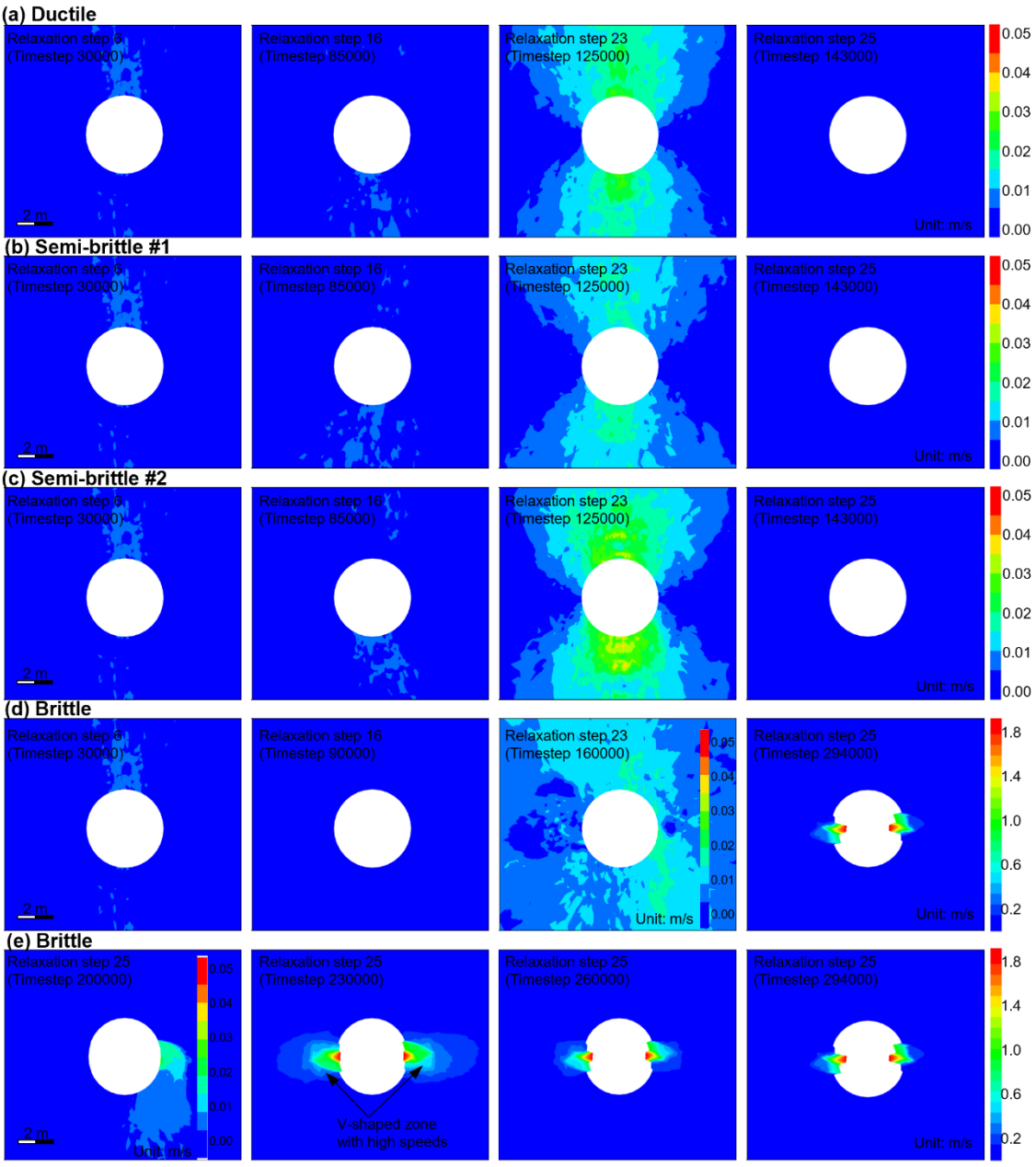

Figure 6.7 Velocity distribution in zones around the tunnel with different rock mass behaviour.

Moreover, it might be argued that the simulated maximum velocity, 1.8 m/s, appears to be low because the ejection velocity of rock fragments with an order of 10 m/s or greater is not unusual (McGarr, 1997; Ortlepp and Stacey, 1994). This is because the static calculation scheme is used; thus, most of the kinetic energy has been damped. A dynamic calculation scheme is required to obtain more realistic rock ejection velocities, which is currently beyond the scope of this research. As shown in Figure 6.7e, the range of the

V-shaped zone with high speeds decreases with the timestep, which is also due to the mechanical damping mechanism.

6.3.2.2 Comparation of the volume of failed rock masses

Figure 6.8 shows the plastic zone distribution around the tunnel with different types of rock masses. As shown in Figure 6.8a, the failure zone is concentrated in two sidewalls of the tunnel, and the maximum failure depth is 0.75 m when surrounding rock masses have the mechanical behaviour of ductile, semi-brittle #1 and #2. No failure is observed in the roof and floor. In contrast, the failure zone is much more extensive and deeper than the first three scenarios, and the maximum failure depth reaches 8.5 m when the tunnel is excavated in brittle rock masses. Failure occurs in some areas of the roof and floor. Theoretically, brittle rock masses will experience less failure than ductile and semi-brittle rock masses, which seems contrary to the current finding. This is because the rock masses are assumed to be a continuum in this research, and thus, the kinetic energy released from surrounding rock masses is consumed by plastic deformation rather than rock detachment and ejection. In order to quantitively assess the failure degree of the tunnel induced by excavation, a function was developed using FISH language programming in UDEC to calculate the volume of failed rock masses and the results are shown in Figure 6.9a. The volume of failed rock masses is the least (5.64 m^3) when the tunnel is excavated within ductile rock masses and is slightly higher (5.73 m^3) when surrounding rock masses have the mechanical behaviour of semi-brittle #1 and #2, indicating that the failure degree is low. However, the rock failure is much more serious for the tunnel excavated in brittle rock masses. The volume of failed rock masses is 125.26 m^3, 21.86 times that of the tunnel within ductile and semi-brittle rock masses.

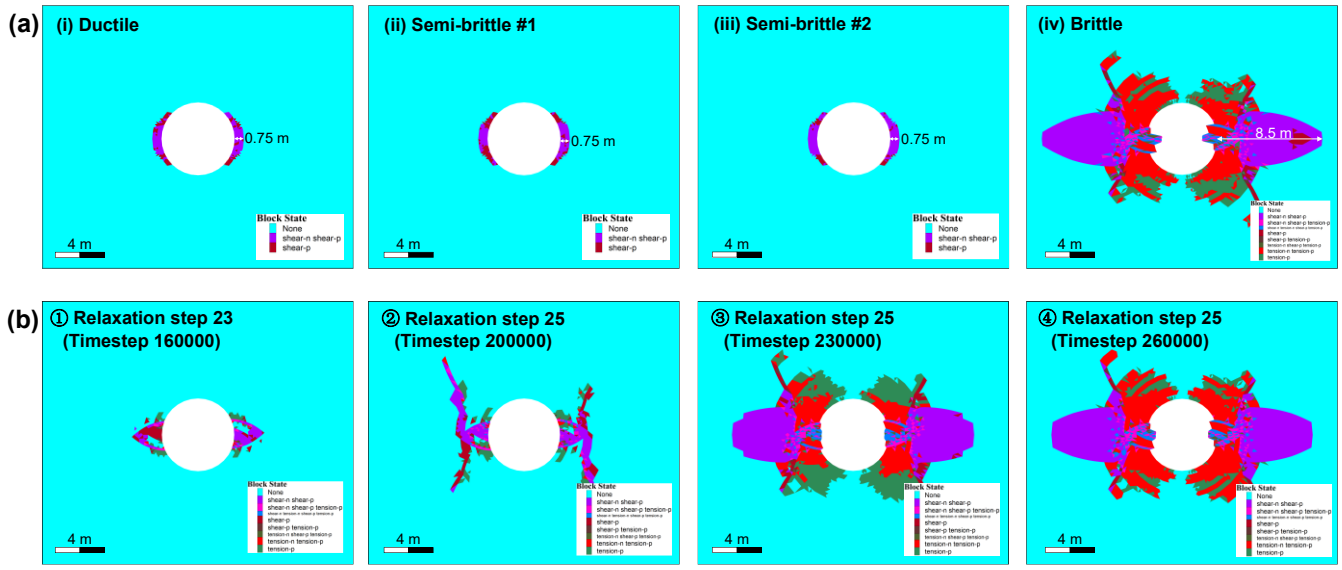

Figure 6.8 Plastic zone distribution around the tunnel: (a) Comparation between different types of rock masses and (b) Development of the plastic zone distribution in brittle rock masses.

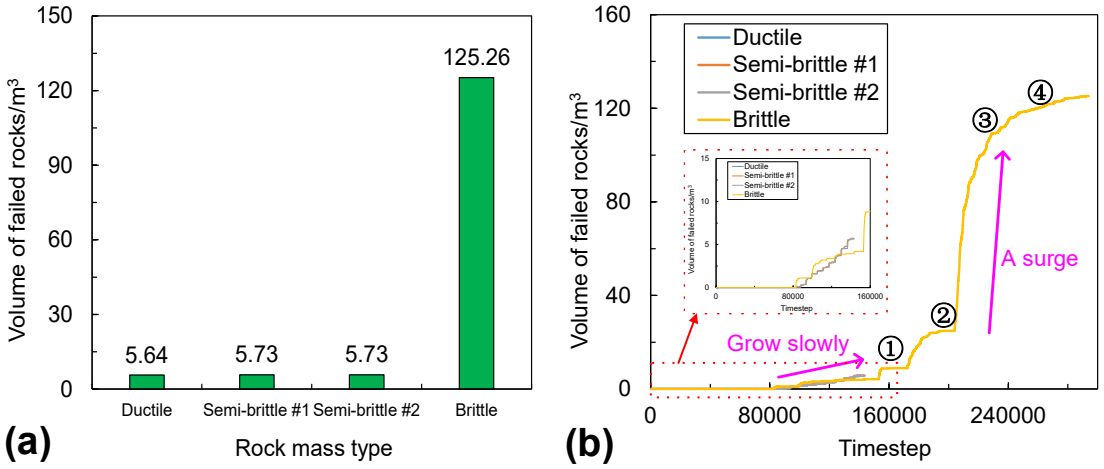

Figure 6.9 (a) Volume of failed rock masses around the tunnel with different types of rock masses and (b) Variation of the volume of failed rock masses with the timestep.

Figure 6.8b illustrates the development of the plastic zone distribution around the tunnel with brittle rock masses. A V-shaped failure zone appears in two sidewalls, and its range is limited at relaxation step 23 (timestep = 160000). At the earlier stage of relaxation step 25 (timestep = 200000), a wing-shaped failure zone occurs in deep areas of sidewalls, but the extent of the failure zone is still minor. Then, the range of the failure zone suffers a significant growth from 200000 to 230000 timesteps. After that, the change of the failure zone becomes stable due to the previously mentioned damping effects. A FISH

function was also developed to record the variation of the volume of failed rock masses with the timestep. The results are shown in Figure 6.9b. It can be seen that the volume of failed rock masses grows very slowly when the tunnel is excavated in ductile and semi-brittle rock masses and at the earlier stage of excavation (before 160000 timesteps) when surrounding rock masses are brittle. However, the volume of failed rock masses increases rapidly after 160000 timesteps and a surge from 200000 to 230000 timesteps. Thus, it can be concluded that sudden and violent rock failure (strainburst) happens at the last relaxation step.

6.3.2.3 Comparation of the kinetic and damping energy in the model

The variation of kinetic energy in the model with the timestep is shown in Figure 6.10. For stable failure, the kinetic energy in the model should be zero or close to zero. It can be seen from Figure 6.10a that the kinetic energy is less than 225 J during the entire excavation stage and becomes almost zero when the equilibrium state is reached for the first three scenarios, suggesting a stable failure mode. By comparison, the kinetic energy can be up to 43 kJ (timestep = 210400), and the final value is 4 kJ when the tunnel is excavated in brittle rock masses (Figure 6.10b). This finding agrees with previous simulation results that some zones possess a relatively high speed (e.g., 1.8 m/s).

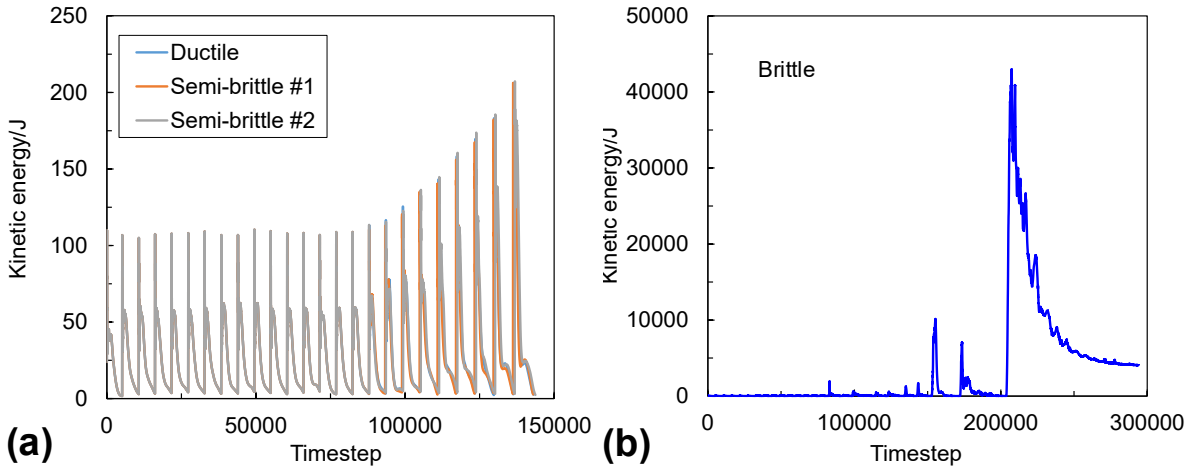

Figure 6.10 Variation of kinetic energy in the model with the timestep: (a) Ductile, semi-brittle #1 and #2 rock masses; (b) brittle rock masses.

The comparison of the damping energy in the model with different types of rock masses is shown in Figure 6.11a. It can be seen that the damping energy is the least (0.200 MJ) when the tunnel is excavated within ductile rock masses and is slightly higher (0.201 MJ) when surrounding rock masses have the mechanical behaviour of semi-brittle #1 and #2. In contrast, the damping energy reaches 6.034 MJ, around 30 times that in models with ductile and semi-brittle rock mass behaviour. The large difference in damping energy indicates that much kinetic energy has been damped, suggesting that unstable and violent failure occurs for the tunnel excavated in brittle rock masses. The variation of the damping energy with the timestep influenced by different rock mass types is shown in Figure 6.11b. The damping energy change is similar to kinetic energy (see Figure 6.10b). The damping energy grows very slowly when the tunnel is excavated in ductile and semi-brittle rock masses and at the earlier stage of excavation (before 160000 timesteps) when surrounding rock masses are brittle. However, the damping energy increases rapidly after 160000 timesteps, and a surge is also observed from 200000 to 230000. Then, the damping energy tends to be steady gradually. These findings further confirm that sudden and violent rock failure (strainburst) happens at the last relaxation step.

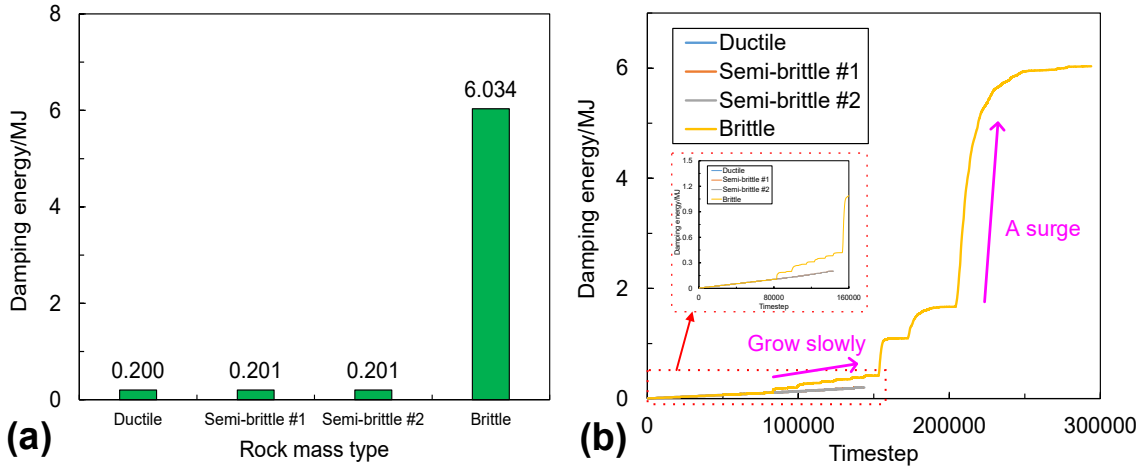

Figure 6.11 (a) Comparison of the damping energy in the model with different types of rock masses and (b) Variation of the damping energy in the model with the timestep.

In this research, the excess or seismic energy is defined as the difference in the sum of kinetic and damping energy between stable and unstable failure. The obtained seismic energy for the simulated

strainburst is 5.838 MJ. The seismic energy can be used to assess the severity of rockbursts by calculating the Richter magnitude (M_L) via the following formula (Gutenberg and Richter, 1956):

$$M_L = (\log(E) - 4.4)/1.5 \tag{6.9}$$

where E stands for seismic energy. The calculated Richter magnitude is 1.58, which falls into the category of a weak rockburst based on a classification proposed by Bieniawski (1986).

6.3.2.4 Relationship between LMS and PCS

The previous analysis demonstrates that unstable rock failure or strainburst occurs in the tunnel excavated in brittle rock masses, and failure is stable for the tunnel with ductile and semi-brittle rock mass behaviour. Now it is time to investigate whether the proposed LMS calculation method and the relationship between LMS and PCS can discriminate strainburst occurrence or not. Since the tunnel is excavated in a non-isotropic in situ stress field, non-uniform deformation is expected. Hence, the LMS was calculated using the proposed method based on the tunnel convergence in horizontal (minimum principal stress orientation) and vertical (maximum principal stress orientation) directions. The simulated UCS tests were conducted to determine the PCS of the different types of rock masses (see Figure 6.12). For a convenient and consistent comparison with the PCS of rock masses, the tunnel convergence was normalized by the tunnel diameter.

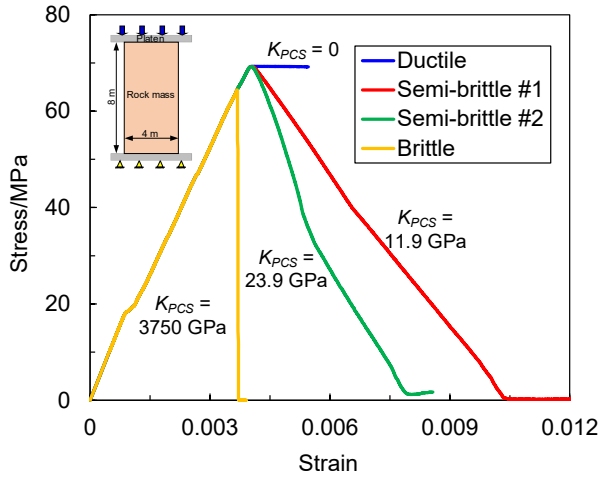

Figure 6.12 Stress-strain curve and the PCS of the different types of rock masses.

The calculated results are listed in Table 6.3. It can be seen that simulated failure modes are consistent with that determined by the relationship between LMS and PCS. For the case of semi-brittle #2, the relationships between PCS and LMS in horizontal and vertical directions judge stable and unstable failure modes, respectively. In contrast, the simulated failure mode is stable, suggesting that the PCS should be compared with the greatest LMS for distinguishing strainburst occurrence. This finding can be analogous to predicting burst potential for an isolated rock pillar. The LMS in the vertical direction is always used because it is zero in the horizontal direction due to no confinement. Hence, the PCS is compared with the maximum LMS to determine the failure mode for the rock pillar. Otherwise, the rockburst risk will be overestimated.

Table 6.3 Judging strainburst occurrence via the relationship between LMS and PCS

Rock mass response	k_{PCL} (GPa)	k_{LMS_x} (GPa)	k_{LMS_y} (GPa)	Relationship	Determined failure mode	Simulated failure mode
Ductile (base model)	0	26.5	12.4	$k_{PCL} < k_{LMS\ x}$	Stable	Stable
				$k_{PCL} < k_{LMS\_y}$	Stable	
Semi-brittle #1	11.9	26.5	12.3	$k_{PCL} < k_{LMS\_x}$	Stable	Stable
				$k_{PCL} < k_{LMS\_y}$	Stable	
Semi-brittle #2	23.9	26.5	12.4	$k_{PCL} < k_{LMS\_x}$	Stable	Stable
				$k_{PCL} > k_{LMS\_y}$	Unstable	
Brittle	3750	0.007	3.5	$k_{PCL} > k_{LMS\ x}$	Unstable	Unstable
				$k_{PCL} > k_{LMS\ y}$	Unstable	

Note: k_{PCS} is the PCS of rock masses; k_{LMS_x} and k_{LMS_y} are the LMS in horizontal and vertical directions, respectively.

To further verify the reliability and accuracy of strainburst prediction based on the stiffness theory, the calculated graphical (analytical) result of excess energy was compared with the numerical result of damping energy in UDEC.

Figure 6.13 is a schematic diagram showing a method to calculate the excess energy from a stress-strain curve of a rock mass sample under a UCS test. The excess energy at different post-peak stages can be obtained by calculating the area between the post-peak stress-strain curve and LMS line and then multiplying it by the volume of the rock mass sample. First, as listed in Table 6.3, PCL and LMS have been calculated, which can be used to derive the formulas shown in Figure 6.13. Then, these formulas

were implemented in UDEC via FISH language programming to calculate the excess energy of each failed zone and then sum it to obtain the total excess energy in the model.

Initially, the k_{LMS_y}, 3.5 GPa, was used to calculate the model's analytical result of excess energy. The obtained excess energy is 30.35 MJ, which is unrealistically high compared with the numerical result (5.838 MJ). This is because the happened strainburst significantly impacts tunnel deformations (see Figure 6.8). Hence, the calculated LMS is not real. We assumed that the LMS could be estimated from the base model (ductile rock masses) and then adopted k_{LMS_x} (26.5 GPa) to calculate the analytical result of excess energy. The obtained value is 5.180 MJ, with an 11.3% difference from the numerical result (5.838 MJ) in UDEC (see Table 6.4). This value is equal to a seismic event with a Richter magnitude of 1.54 calculated with Eq. (6.9), which is very close (2.5% relative error) to that (1.58) obtained by the numerical method. Therefore, a relatively good match between analytical and numerical results is attained, verifying that the proposed LMS calculation method and the relationship between LMS and PCS can judge strainburst occurrence.

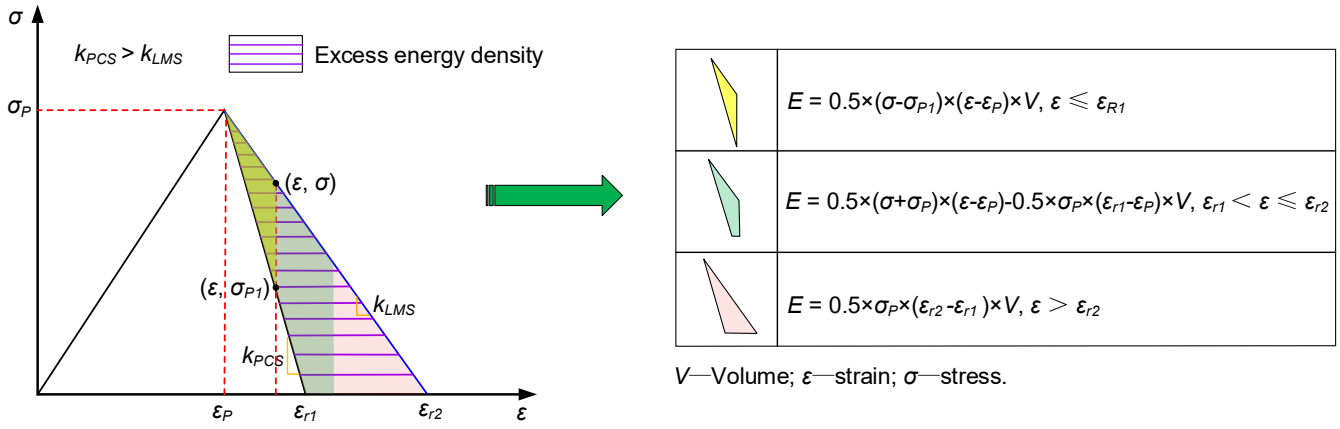

Figure 6.13 A method to calculate the excess energy from a stress-strain curve of a rock mass sample under a UCS test.

Table 6.4 Comparison of the excess energy and Richter magnitude obtained by analytical and numerical methods

Item	Analytical result	Numerical result	Difference (%)
Seismic energy (MJ)	5.180	5.838	11.3
Richter magnitude	1.54	1.58	2.5

6.3.3 Strainburst stiffness factor

After proving the effectiveness of PCS and LMS in judging strainburst occurrence, we proposed a new indicator of strainburst prediction, called strainburst stiffness factor (SSF). It is defined as the ratio between PCS and LMS, which can be calculated as follows:

$$SSF = \frac{k_{PCS}}{k_{LMS}} \tag{6.10}$$

where k_{PCS} is the PCS of surrounding rock masses; k_{LMS} is the LMS of the tunnel. A strainburst will occur if the SSF is greater than one. The greater the SSF is, the more serious the strainburst damage is.

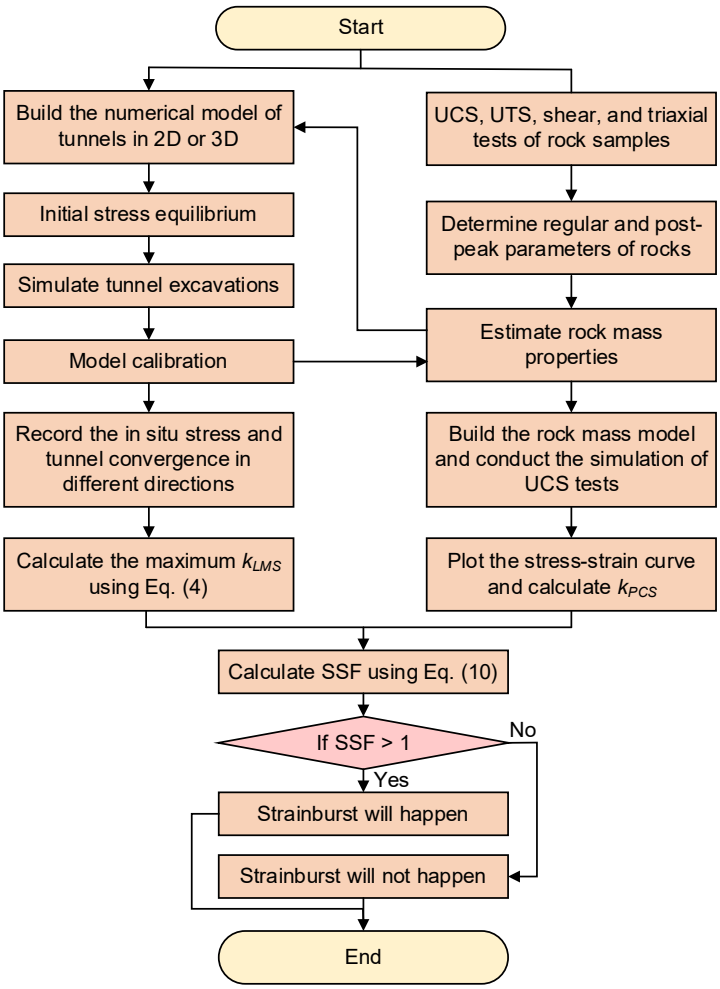

Figure 6.14 A flowchart showing the procedure to obtain and use SSF for predicting strainburst risks.

A flowchart (see Figure 6.14) was drawn to illustrate the procedure to obtain and employ SSF for predicting strainburst risks. The first step is to build the numerical model of tunnels in 2D or 3D. The

EPMC constitutive model should be used to stabilize rock failure, which avoids the influence of possible unstable failure on calculating LMS when using the MCSS constitutive model. The second step is initial stress equilibrium, followed by tunnel excavation. Calibration is required to ensure the effectiveness of the built model. The in situ stresses at excavation boundaries and tunnel convergences in different directions are then recorded to calculate the LMS using Eq. (6.4).

Another task is to calculate the PCS of rock masses. The first step is to obtain the regular (e.g., Young's modulus and internal friction angle) and post-peak parameters (e.g., the relationship between cohesion force and plastic shear strain) based on laboratory tests of rock samples. Then, these parameters are used to estimate rock mass properties. After that, a rock mass model is built to conduct the simulation of UCS tests. Then, the stress-strain curve of the rock mass sample can be plotted to calculate the PCS. Finally, the SSF is determined using Eq. (6.10) to judge whether a strainburst will occur or not.

6.4 Validation of the SSF with reported strainburst cases

In this section, the effectiveness of the SSF was validated by comparing SSF prediction results with two reported strainburst cases in an underground coal mine and a hydropower station.

6.4.1 "5.5" rockburst event in the Zofiowka Coal Mine

6.4.1.1 Engineering overview

On May 5, 2018, an incredibly intense rockburst event occurred in the intersection area of H-4 tailgate and H-10 main drift at the Zofiówka Coal Mine, Poland, as shown in Figure 6.15a. The rockburst caused significant damage to H-10 main drift, e.g., rockfall and floor heaving (see Figure 6.16) and resulted in four injuries and five fatalities.

There are two coal seams in the analyzed area: coal seams 409/3 and 409/4, with thicknesses of 1.8-2.7 m and 4.0-5.3 m, respectively. The average thickness of the interlayer between two coal seams is one meter. Coal seams' average mining depth and dip angles are 900 m and 5-10°, respectively. The roof and floor are composed of shale and sandstone (Figure 6.15b). H-4 headgate, tailgate, and H-10 main drift

were arranged in coal seam 409/4 underneath the coal seam 409/3. H-10 main drift has a semi-circular section with a width of 6 m and a height of 4 m. The panels H-4 and H-6 in coal seam 409/3 had been mined out when the rockburst occurred.

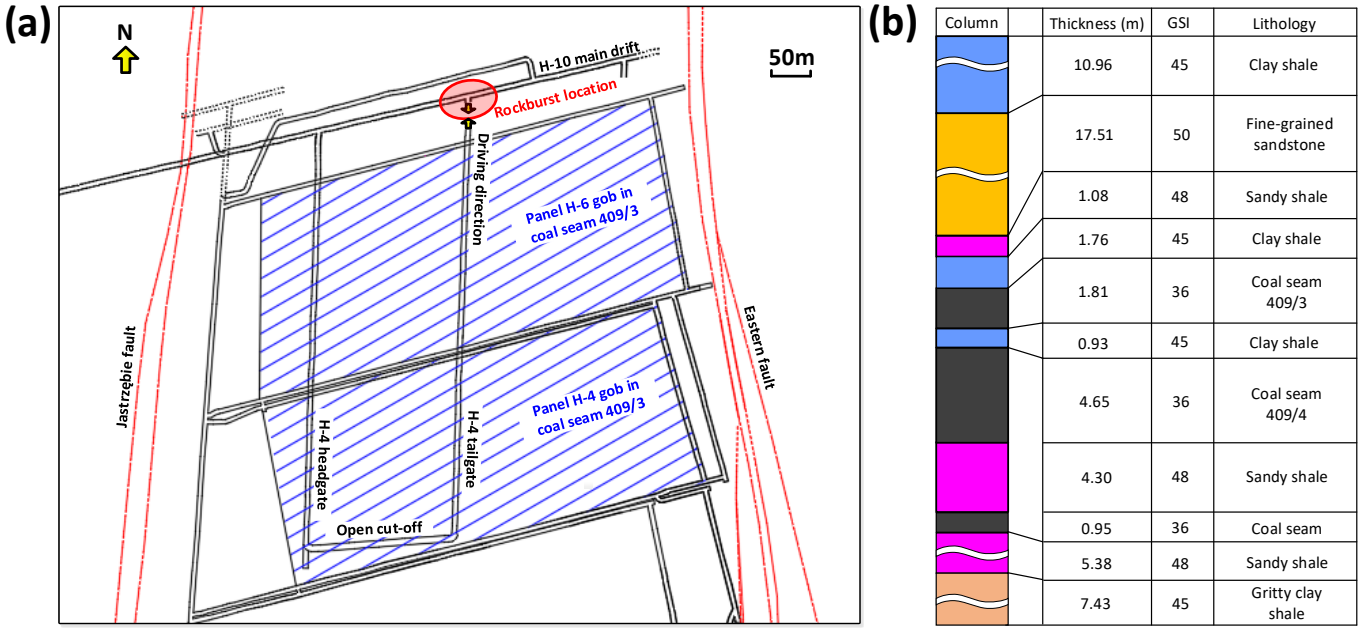

Column	Thickness (m)	GSI	Lithology
	10.96	45	Clay shale
	17.51	50	Fine-grained sandstone
	1.08	48	Sandy shale
	1.76	45	Clay shale
	1.81	36	Coal seam 409/3
	0.93	45	Clay shale
	4.65	36	Coal seam 409/4
	4.30	48	Sandy shale
	0.95	36	Coal seam
	5.38	48	Sandy shale
	7.43	45	Gritty clay shale

Figure 6.15 (a) Location of the "5.5" rockburst event and (b) Geological column of the study site (after Wang et al., 2021b)). GSI is the geological strength index.

Figure 6.16 In situ observations of rockburst damage caused by the "5.5" rockburst event (after Jastrzębska Spółka Węglowa S.A. Group, 2019).

6.4.1.2 Numerical model, prediction results, and analysis

A 2D model of H-10 main drift (Figure 6.17a) was built using UDEC to "predict" the strainburst potential. The detailed model configuration parameters, e.g., mesh size and type, boundary conditions, material properties, and model calibration, can be referred to Wang et al. (2022a, b). Coal is more prone

to failure than shale and sandstone due to its lower strength. Hence, only the PCS of coal masses was determined via the simulated UCS test, as shown in Figure 6.17b. The obtained PCS is 255 MPa (Figure 6.17c). The LMS of H-10 main drift was calculated using the proposed method in this research. The determined LMS is 174 MPa (Wang et al., 2022b); thus, the SSF is 1.47. This SSF value predicts that a strainburst event could occur, agreeing with the fact.

However, it could be argued that the obtained SSF value seems very low, which might only indicate a minor strainburst, but the reported strainburst case is undoubtedly a major rockburst according to the damage degree (Kaiser and Cai, 2012). This is because the "5.5" rockburst event is caused by seismic waves and high static stress rather than excavation-induced stresses (Wang et al., 2022a). Therefore, the authors hypothesized that seismic waves could significantly affect LMS, thereby increasing the SSF value. Furthermore, the simulated rock damage resulting from the assumed self-initiated strainburst (without considering seismic waves) in Wang et al. (2022b) is less serious than that reported in the field, confirming this hypothesis. Currently, the relationship between LMS and seismic waves is unknown and out of the scope of this research, which the authors will investigate shortly.

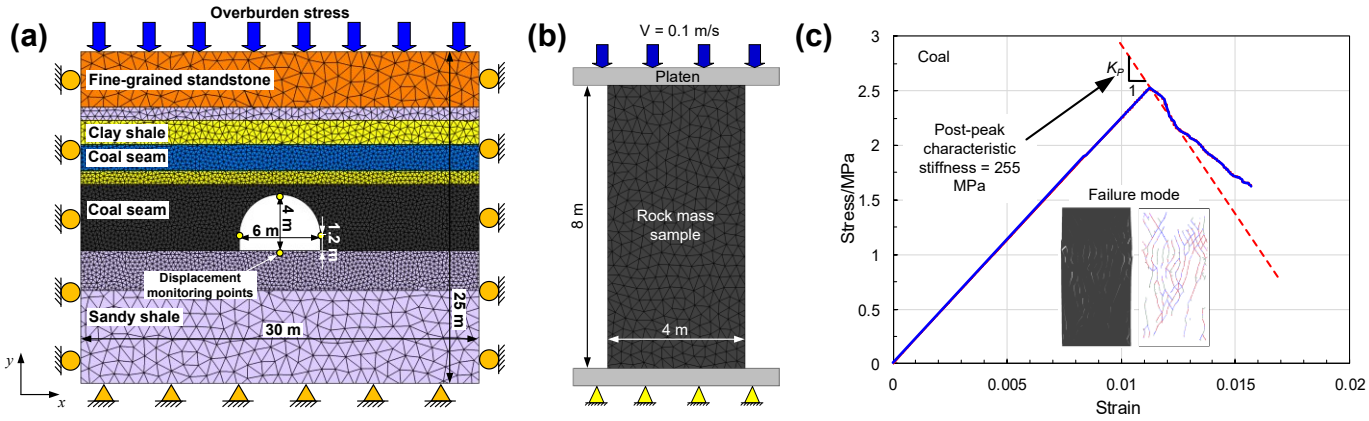

Figure 6.17 (a) 2D numerical model of H-10 main drift, (b) UCS model, and (c) Stress-strain curve and failure mode of the coal mass sample (after Wang et al., 2022b).

6.4.2 "11.28" rockburst event in the Jinping II Hydropower Station

6.4.2.1 Engineering overview

Jinping II Hydropower Station is located in southwestern China, and consisting of seven parallel tunnels: one drainage tunnel, two auxiliary tunnels, and four diversion tunnels (see Figure 6.18a). These tunnels are excavated in a mountain area with a maximum buried depth of 2525 m. The TBM method was employed to excavate the drainage tunnel and Nos. 1 and 3 diversion tunnels, while the drilling and blasting method was used to excavate the remnant tunnels. The drainage tunnel has a circular cross-section with a radius of 3.6 m.

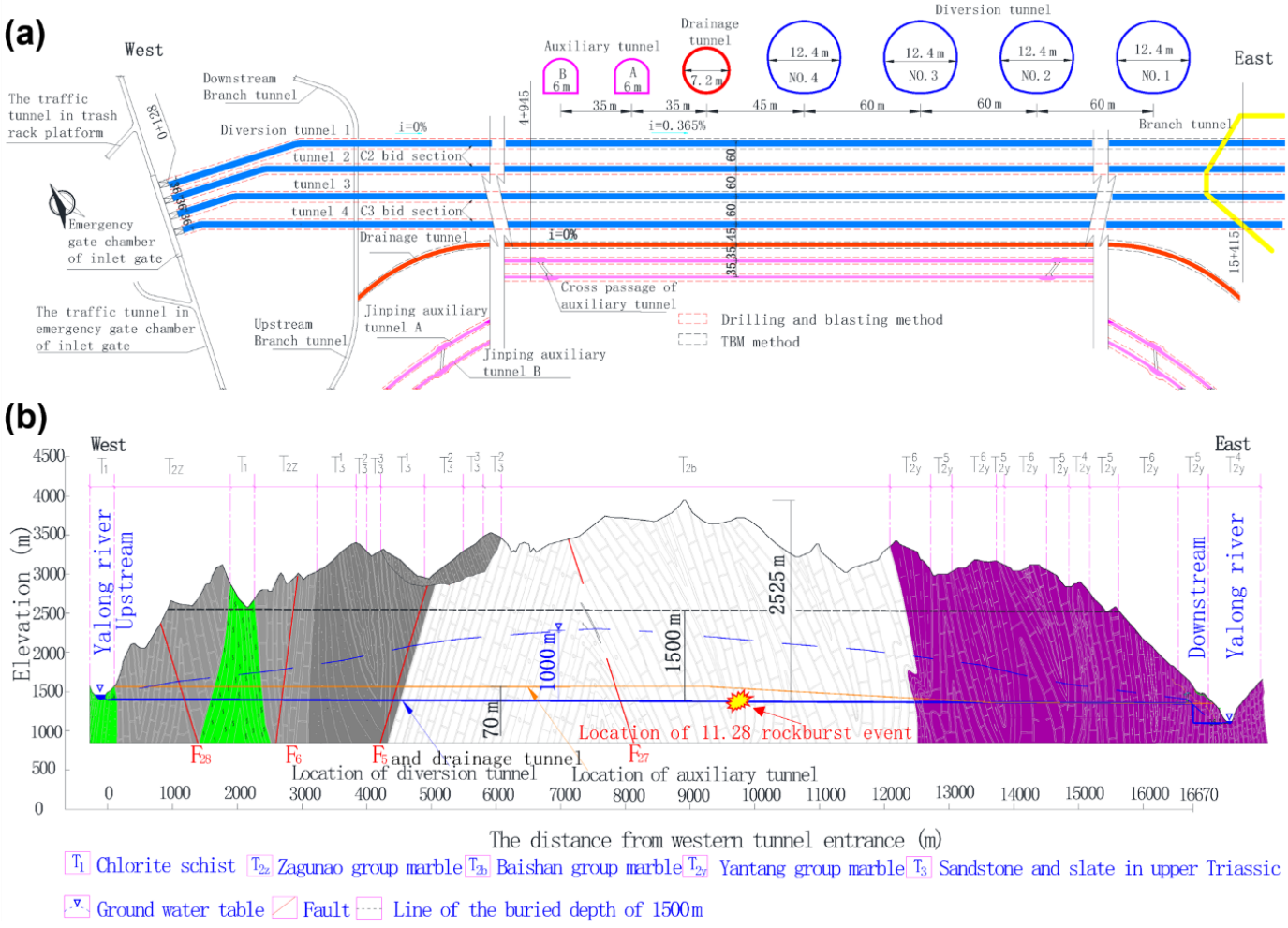

Figure 6.18 (a) Layout and (b) Geological profile of the Jinping II Hydropower Station (after Zhang et al., 2018).

On November 28, 2009, a violent rockburst event with a Richter magnitude of 2.0 occurred at Stake SK9+283–9+322 drainage tunnel. The rockburst caused a sudden expulsion and ejection of a large volume of rock masses (see Figure 6.19a), resulting in seven fatalities and one injury. In addition, a TBM was also destroyed and buried (Figure 6.19a, b).

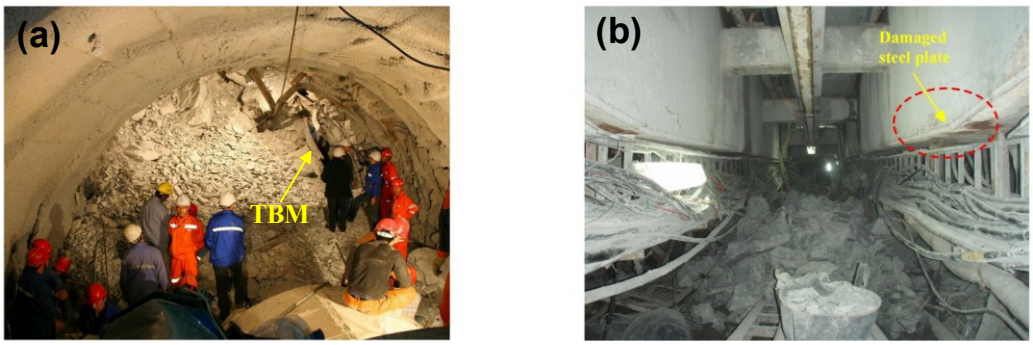

Figure 6.19 Post-event observations of the "11.28" rockburst event: (a) Rockfall and buried TBM and (b) Damaged 80 mm steel plate in the TBM (after Zhang et al., 2018).

The host rock of the drainage tunnel section where the rockburst occurred is T2b marble. The physical and mechanical properties of the rock mass are listed in Table 6.5. Post-event observations reveal a minor fault sub-parallel to the tunnel axis with a dip angle of 50°. The fault is straight and has no infillings. The rockburst is around 2330 m deep and in the core of a fold syncline, which is prone to a high local stress concentration (Figure 6.18b). The in situ stress components at the rockburst location of the drainage tunnel is listed in Table 6.6. The stress orientation has been transformed according to the coordinate system in UDEC for further usage.

Table 6.5 Material properties of T2b marble (after Zhang et al., 2013)

Rock mass response	Constitutive model	ρ (kg/m^3)	K (GPa)	G (GPa)	c_p (MPa)	c_r (MPa)	φ_p (°)	φ_r (°)	ψ (°)
Ductile	EPMC	2780	11.7	7.7	15.6	0.01	25.8		10
Brittle	MCSS	2780	11.7	7.7	15.6 (ε_p = 0)	0.01 (ε_p = 0.001)	25.8 (ε_p = 0)	39 (ε_p = 0.009)	10

Table 6.6 In situ stress components at the rockburst location of the drainage tunnel (Zhang et al., 2013)

Stress components	σ_x (MPa)	σ_y (MPa)	σ_z (MPa)	τ_{xy} (MPa)	τ_{xz} (MPa)	τ_{yz} (MPa)

Magnitude	-46.4	-61.5	-51.7	3.5	-2.4	-0.6

Note: Negative sign denotes the compressive stress.

6.4.2.2 Numerical model, prediction results, and analysis

A 2D numerical model with the plane strain assumption was established using UDEC to "predict" the strainburst risks of the drainage tunnel. The only nearby opening was auxiliary tunnel A when the rockburst event happened. The distance between the two tunnels is around 90 m, beyond the excavation disturbed zone of the two tunnels (Zhang et al., 2013). Hence, only the drainage tunnel was simulated.

Studies have shown that the reported minor fault influences the occurrence of the "11.28" rockburst event (Zhang et al., 2012; Manouchehrian and Cai 2018; Wang, 2019). Thus, the fault was included in the model. Since the fault has a dip angle of 50° causing the difficulties of generating meshes and the objective of this numerical study is to predict strainburst risks rather than reproduce realistic rock failure, the model was rotated clockwise 50° along the tunnel axis to make the fault be oriented in the *y* direction referred to Wang (2019), as shown in Figure 6.20. The in situ stress components and gravitational acceleration was then adjusted according to stress transformation rules in the new coordinate system. The transformation would not affect strainburst prediction results because the stress field is the same, and the coordinate system is the only difference.

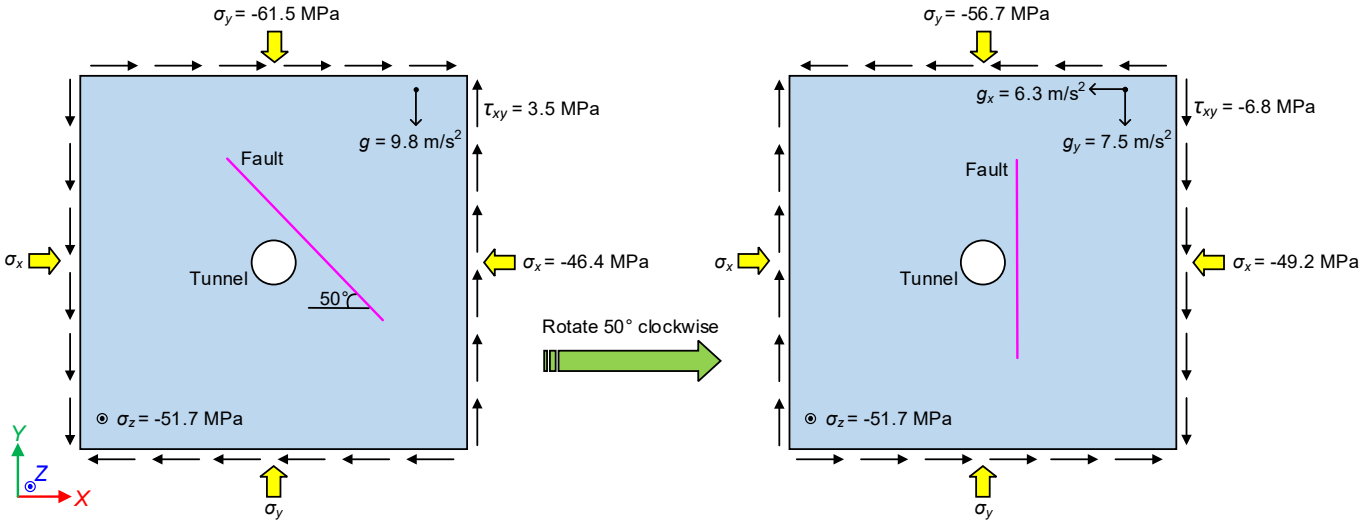

Figure 6.20 Transformation of the drainage tunnel's in situ stress field.

Figure 6.21 shows the geometry of the established model. To avoid the boundary effects, the model has a boundary length of 120 m (16.7 times the tunnel diameter 7.2 m). The fixed constraints were applied on model boundaries. The MCSS constitutive model was used to simulate the brittle behaviour of rock masses. For comparison, the response of the drainage tunnel model with ductile rock masses was also simulated via the EPMC constitutive model. The used rock mass parameters are listed in Table 6.5. The fault was modelled by the continuously yielding (CY) joint model in UDEC. Compared with the standard Mohr-Coulomb joint model, the CY model is considered more "realistic" because it could account for some nonlinear behaviour observed in physical tests (e.g., joint shearing damage, normal stiffness dependence on normal stress, and decrease in dilation angle with plastic shear displacement). More details about the CY model can be referred to Itasca (2020). Table 6.7 shows the material parameters of the simulated fault, which are adapted from Wang (2019). The fault length is assumed to be 60 m. According to post-event observations, the normal distance from the fault to the excavation boundary is within the range of 0.3-1.4 m. An average normal distance might be from 0.6 to 0.9 m. A sensitivity analysis has demonstrated that violent rock failure occurs when the distance decreases from 0.7 m to 0.6 m (Wang, 2019). Thus, a normal distance of 0.6 m was used. The model was first run to reach an initial stress equilibrium. Then, the tunnel was gradually excavated using the SOLVE relax method with 25 stress relaxation steps.

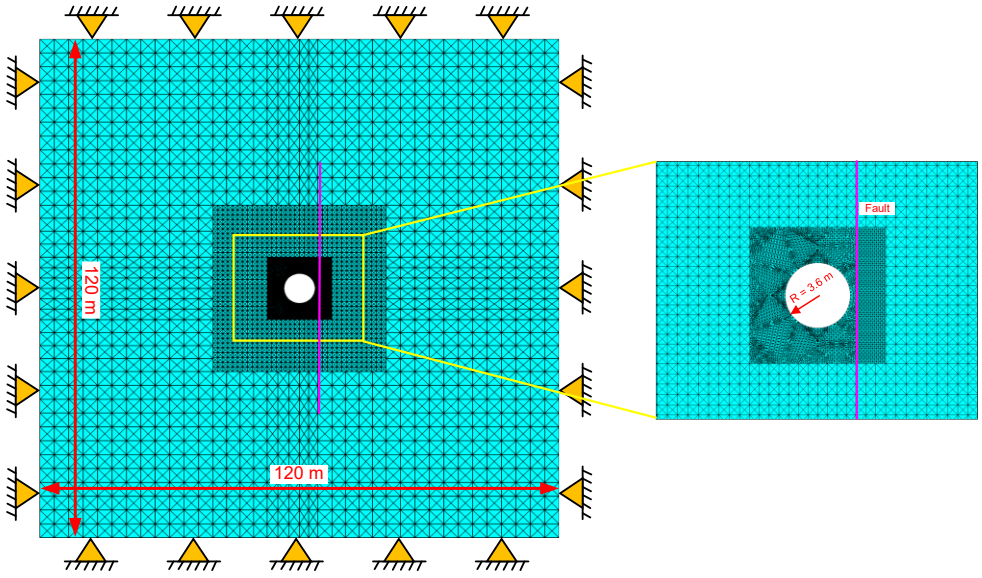

Figure 6.21 2D numerical model of the drainage tunnel.

Table 6.7 Material properties of the simulated fault (adapted from Wang, 2019)

Parameter	k_n (GPa)	k_s (GPa)	J_r (mm)	φ_p (°)	φ_r (°)
Value	500	200	0.1	25.8	39

Note: k_n and k_s are the normal and shear stiffness of joints; J_r is the joint roughness; φ_p and φ_r are the initial and residual internal friction angles.

Figure 6.22a shows the plastic zone distribution around the drainage tunnel. The failure zone is observed all around the tunnel and is extensive and deep in the top-left and bottom-right sidewalls because of the influence of the non-uniform in situ stress field. Moreover, a large separation is found in the fault zone. Thus, it can be expected that the simulated rock masses below the fault will fall if the BBM is adopted. This finding agrees that the rock masses in the footwall of the fault fell into the tunnel during the rockburst event, as shown in Figure 6.22b.

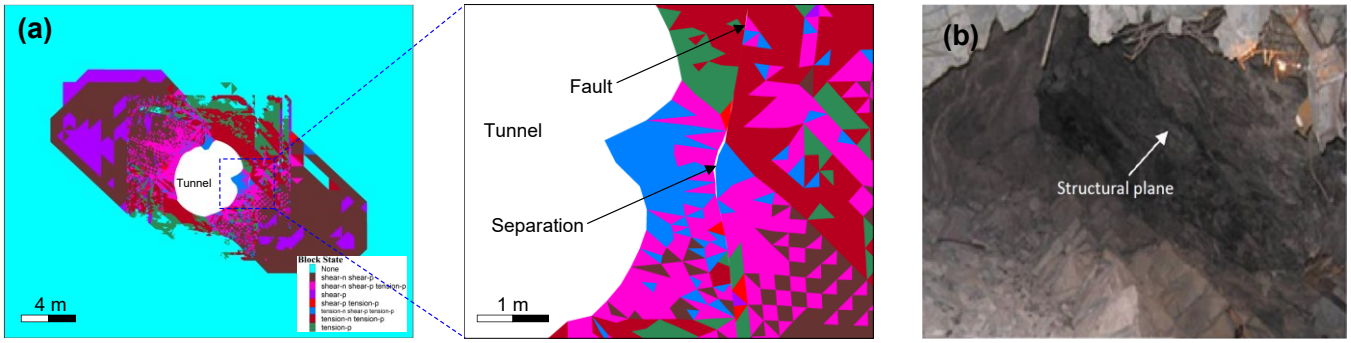

Figure 6.22 (a) Plastic zone distribution around the tunnel and (b) Revealed fault near the drainage tunnel after the "11.28" rockburst event (Feng et al., 2019c).

The variation of kinetic and damping energy in the model with the timestep is shown in Figure 6.23. The kinetic energy is less than 25 kJ before relaxation step 25 and suddenly surges to 217 kJ at the beginning of relaxation step 25. Then, the kinetic energy is decreased to almost zero due to the damping effects. The change of damping energy is similar to that of kinetic energy. The damping energy grows very slowly before relaxation step 25 and then increases rapidly at the beginning of relaxation step 25. After that, the damping energy gradually approaches a plateau. The sudden growth of kinetic and damping energy suggests that a strainburst occurs.

Furthermore, the calculated excess energy in the model is 21.65 MJ. This value is equal to a seismic event with a Richter magnitude of 1.96, which is very close to the reported magnitude (2.0) of the "11.28" rockburst event. Thus, the established model including material properties, constitutive relationships, geometry, etc., are validated.

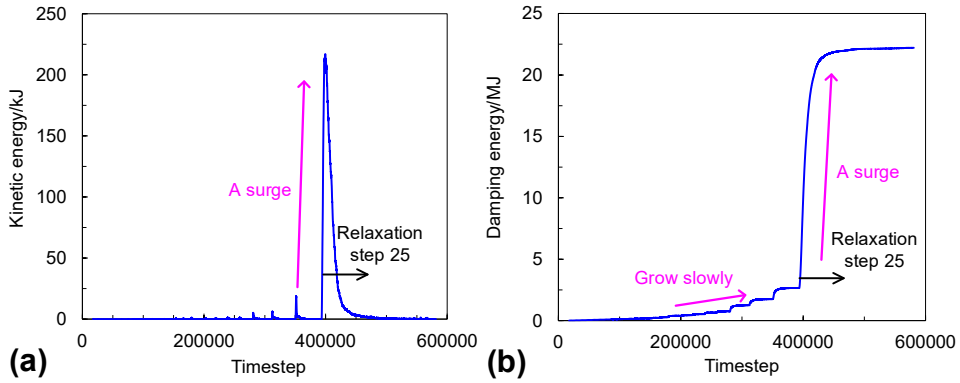

Figure 6.23 Variation of kinetic (a) and damping energy (b) in the model with the timestep.

After the model is calibrated, the simulated UCS test was conducted to determine the PCS of the surrounding rock mass. The obtained value is 1060 GPa (see Figure 6.24).

Then, the rockburst prediction method proposed in Chapter 3 was used to evaluate the rockburst potential for the case example. The first step is to evaluate the rockburst proneness of rocks based on indicators at a laboratory scale. According to the laboratory test results of intact rock samples (Zhang et al., 2012b), the σ_c and σ_t of T2b marble are around 100 MPa and 4.5 MPa, respectively. Hence, the rock

brittleness coefficient (B) is 22.2, showing that T2b marble inherently possesses a moderate rockburst proneness.

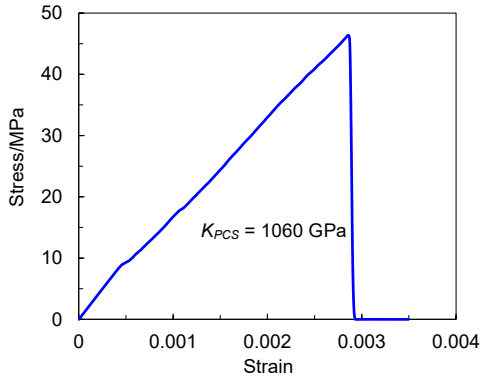

Figure 6.24 Stress-strain curve and the PCS of the surrounding rock mass.

Next, SSF was employed to predict rockburst tendency using numerical simulation. The LMS of the drainage tunnel was calculated using the proposed method in this research. The determined LMS is 11.1 GPa. Therefore, the SSF is 99.50 according to Eq. (6.9), suggesting that a very strong strainburst event could occur. This prediction result successfully matches the severity of the "11.28" rockburst event.

6.5 Discussion

This study presents a novel method to calculate LMS. The proposed method fills the gap in determining the LMS for a tunnel and using it to predict strainburst occurrence. The method is straightforward but also valid. As a result, a new rockburst indicator, SSF, is proposed and developed based on the analysis of stiffness differences. The SSF can be easily implemented in numerical modeling, which provides an effective tool to predict strainburst risks, which can further improve the safety of workers and equipment when constructing deep excavations in mining and civil engineering projects. Moreover, it is well known that the excavation geometry, nearby excavation disturbance, seismic wave, etc., influence LMS, thereby changing strainburst potential. Using this study's proposed LMS calculation method, these effects could be investigated and quantified in future studies.

This study employs the maximum LMS in different directions around the tunnel to predict strainburst risks. However, the rock masses in other directions could also release excess energy contributing to the strainburst strength, which might cause the difference between the analytical and numerical results of excess energy observed in this research. The authors will further study this hypothesis to improve the reliability and accuracy of the SSF in the future.

In addition to LMS, PCS is the other key factor controlling unstable rock failure. The PCS of rock masses depends on the relationship between cohesion force, tension strength, friction angle etc. and the plastic shear strain during the post-peak stage. This relationship can be estimated from the experimental results of rock samples. Furthermore, back-analyzing numerical simulation parameters with the field monitored data can also obtain it. However, currently, there is no uniform standard to obtain the PCS of rock masses due to the complexity of rock mass behaviour. Hence, more work needs to be done to determine PCS accurately to improve the robustness of the SSF.

6.6 Conclusions

This chapter proposes a novel method to calculate the LMS for a tunnel. The reliability and accuracy of the proposed LMS calculation method are verified and examined by comparing the prediction results with simulated rock failure and the analytical and numerical results of excess energy. A new rockburst indicator, SSF, is proposed and developed to predict strainburst risks based on the analysis of stiffness differences. The main conclusions are as follows:

(1) The damping constant has a significant influence on tunnel responses in numerical modeling. The tunnel radial displacement decreases noticeably with the growth of the damping constant. For example, when the damping constant is 0.6-0.9, the average difference between simulation results and the self-similar solution is 3.91 %. Hence, the damping constant should be calibrated first before conducting subsequent modeling.

(2) Considering the velocity of zones, the volume of failed rock masses, and the kinetic and damping energy in the model, stable failure is found for the tunnel excavated within ductile and semi-brittle rock masses, whereas unstable failure (strainburst) occurs when the surrounding rock masses are brittle. The simulation results are consistent with the prediction results determined by LMS and PCS.

(3) A method is developed to calculate the analytical result of excess energy based on LMS and PCS. The obtained excess energy is 5.180 MJ, with an 11.3% difference from the numerical result (5.838 MJ) in UDEC. The relative error is 2.5% regarding the measurement of the Richter magnitude. Therefore, a relatively good match between analytical and numerical results is attained, verifying the reliability and accuracy of the proposed LMS calculation method and the capability of LMS and PCS to discriminate strainburst occurrence.

(4) A new rockburst indicator, SSF, defined as the ratio between PCS and LMS, is proposed and developed to predict strainburst risks. The prediction results of SSF successfully match the 5.5" rockburst event in the Zofiowka Coal Mine and the "11.28" rockburst event in the Jinping II Hydropower Station, validating the effectiveness of the SSF.

7. CHAPTER 7: SUMMARY, CONCLUSIONS, AND FUTURE WORK

In this chapter, the thesis summary and research conclusions are presented. In addition, the significance and contributions of this research are discussed. Moreover, the chapter also points out future work in investigating rockburst mechanism and rockburst prediction using numerical modeling methods.

7.1 Summary of the research

Rockburst is one of the most hazardous geological disasters. Due to its sudden and violent nature, rockburst has caused thousands of injuries, fatalities, and significant economic losses to mine enterprises. To date, great efforts have been devoted to investigating rockburst problems, including the mechanisms, risk evaluation and prediction, and prevention and mitigation of rockbursts. The investigation of rockburst mechanisms can let researchers and engineers reveal the 'nature' of rockbursts and thus help engineers prevent and control rockbursts by choosing the rational location, size, and shape of openings, changing mining methods and sequences, improving and optimizing support designs, and using ground conditioning methods. Moreover, understanding rockburst mechanisms also help researchers and engineers identify different contributing factors required for rockburst occurrence, which provides a theoretical basis for the proposal of various prediction and evaluation indicators of rockbursts. The rockburst indicators can then predict possible rockburst locations and severity. This can further help engineers improve and optimize project layouts, mining or excavation methods to avoid potential rockbursts during the design phase and adjust construction schemes or adopt distress and support measures during the production stage.

This research mainly investigates rockburst mechanisms and prediction using numerical modeling methods. Compared with other methods, such as physical simulation and field tests, the numerical modeling method has the advantages of low cost, safety, time-saving, and flexibility. More importantly, it can provide more information (e.g., the evolution of displacement and stress field after excavation) and simulate the complex mechanical behaviour of rocks and rock masses under different conditions. This can visualize the "real" world in underground mining for researchers and engineers to tackle various rock mechanics problems (e.g., rockburst). Thus, this study employs numerical modeling as the primary research approach.

This study revealed rockburst mechanisms and developed a systematic method and a new stiffness-based indicator for predicting rockburst risks. Chapter 1 presents the research background, problem statement, objectives and methodologies, and outlines the organization of the thesis. Chapter 2 provides a thorough literature review of rockburst-related studies based on the objectives of this study. A systematic numerical modeling framework for studying rockburst mechanisms and other rockburst-related problems was established based on the summary and analysis of the literature. In Chapter 3, following the proposed numerical modeling framework, a 3D FDM model was established via FLAC3D using the "5.5" rockburst event in the Zofiówka Coal Mine as a case example to reveal the rockburst source mechanism of driving roadways in close-distance coal seam mining conditions. In addition, a systematic method that can reasonably select and use rockburst indicators was proposed to predict the location and magnitude of rockbursts. Chapter 4 adopted an improved global-local modeling approach to study strainburst damage mechanisms. In Chapter 5, instead of conventional drop tests, the performance of yielding rockbolts (D-bolt and Roofex) during remotely triggered and self-initiated strainbursts was systematically evaluated via building a 2D DEM model of a deep roadway using UDEC. In Chapter 6, a new rockburst indicator, called SSF, was proposed and developed to predict strainburst risks based on the analysis of stiffness differences. Chapter 7 presents the thesis summary, conclusions, research contributions, and future work. Figure 7.1 shows the visual summary of the research methods.

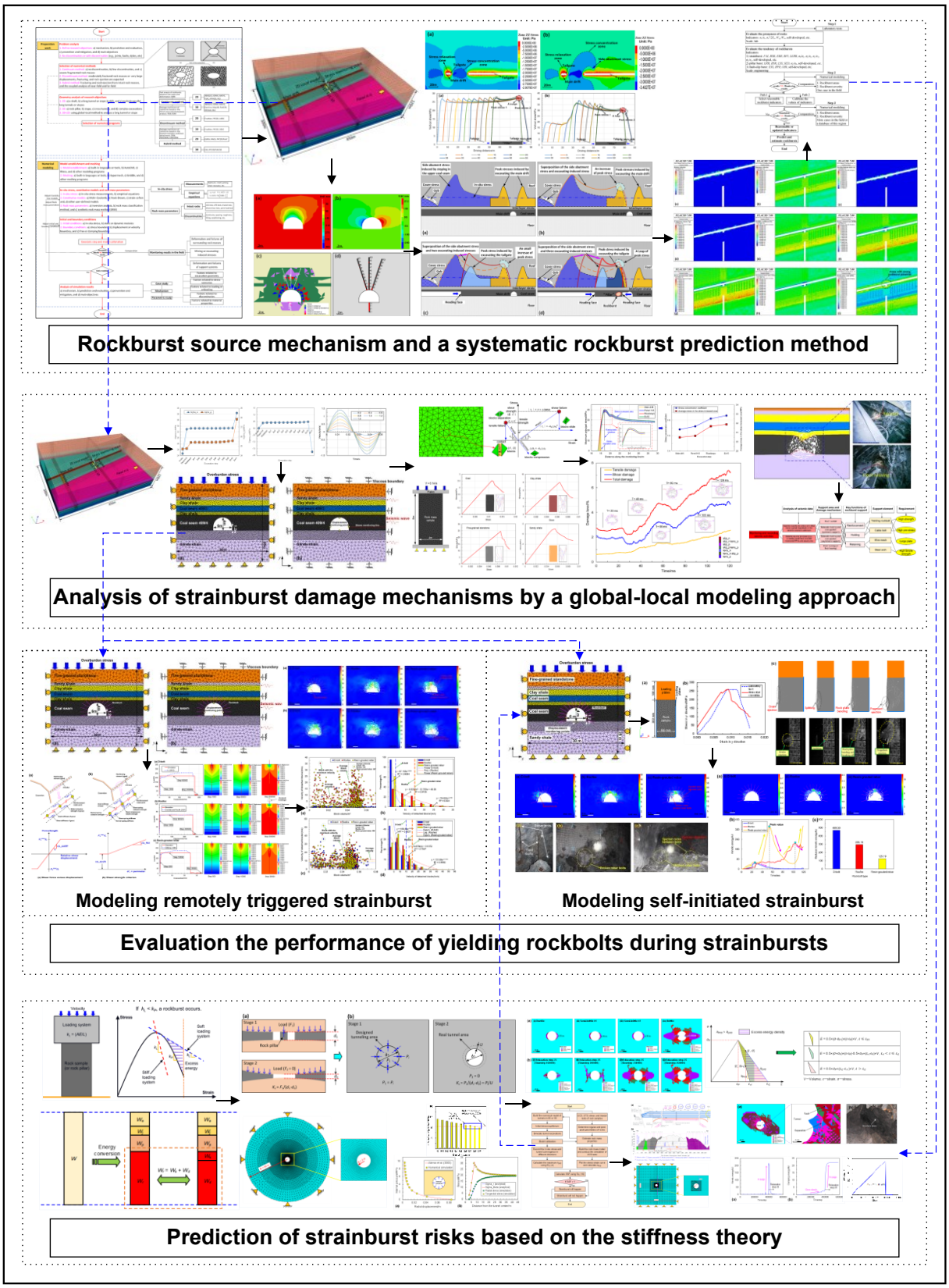

Figure 7.1 Visual summary of the research methods.

7.2 Conclusions of the research

The main conclusions of this research are summarized as follows:

(1) The rockburst source mechanism of driving roadways in close-distance coal seam mining conditions: the superposition of multiple excavation-induced stresses of roadways provides an environment for stress concentration and energy accumulation; the side abutment stress induced by mining in the upper coal seam has a "strengthening" effect to the rockburst occurrence, and the great deviatoric stress induced by complex excavating situations is another crucial exterior cause. A strict calibration procedure should be implemented before using indicators to predict rockburst potential. Thus, a systematic method that can reasonably select and use rockburst indicators is proposed to predict the location and magnitude of rockbursts.

(2) The deformation and damage level of the roadway gradually increase with the growth of surrounding rock stress caused by the superposition of mining- or excavation-induced stresses of the panel and nearby roadways. The significant increase of surrounding rock stresses will result in more accumulated strain energy in two sidewalls, providing a necessary condition for the strainburst occurrence in the dynamic stage. The strainburst damage mechanism for the study site combines three types of damage: rock ejection, rock bulking, and rockfall, which agrees well with in situ observations confirming the rationality and capability of the modeling approach. During the strainburst, tensile cracks' initiation, propagation, and development play a crucial role in controlling the macroscopic failure of surrounding rock masses, although the shear crack always accounts for the main proportion of damage levels. The deformation and damage level of the roadway during a strainburst positively correlate with the increasing PPVs. However, due to the limited energy absorption capacity, the yielding steel arch might not dissipate kinetic energy and

mitigate strainburst damage effectively. The principles to control and mitigate strainburst damage are proposed in this study.

(3) D-bolt can effectively control and mitigate rockburst damage during a weak rockburst because of its high strength and deformation capacity. The Roofex is too "soft" or "smooth" to limit the movement of ejected rocks and restrain the large deformation, although it has an excellent deformation capacity. The resin-grouted rebar bolt can maintain a high axial force level during rockbursts but is easy to break during dynamic shocks, which fails to control rapid rock bulking or ejection. Three types of rockbolts cannot control the large deformation and mitigate rockburst damage during violent rockbursts. Additional support with cable bolts can significantly reduce the rockburst damage severity.

(4) During the self-initiated strainburst, the average velocities of detached rock blocks in the tunnel supported with Roofex and resin-grouted rebar are 3.22 and 3.97 m/s, respectively, which are much higher than that of D-bolts (0.34 m/s). 13 resin-grouted rebar bolts are broken during the strainburst, while D-bolts and Roofex survive. Compared with Roofex (295.16 kJ) and resin-grouted rebar (125.19 kJ), the D-bolt can reduce the most kinetic energy (469.30 kJ). D-bolt and resin-grouted rebar can maintain high axial force levels during the strainburst. Both Roofex and resin-grouted rebar fail to control the self-initiated strainburst. The bolt number significantly influences the control effects of yielding rockbolts on the strainburst. 9 and 12 D-bolts cannot control the strainburst, while 15 and 18 D-bolts can make the tunnel stable. In addition, the detachment and ejection of rocks between rockbolts can be well restrained using surface retain elements, e.g., steel arch.

(5) A novel method is proposed to calculate the LMS for a tunnel. The LMS determined by the proposed calculation method is compared with the PCS of surrounding rock masses having

different brittleness to discriminate strainburst occurrence, which is verified with simulated stable and unstable rock failure occurring in a calibrated deep tunnel model established by UDEC. The reliability and accuracy of the proposed LMS calculation method are further examined by comparing excess energy's analytical and numerical results. The relative difference is 11.3 % and 2.5 % regarding the measurement of the Richter magnitude. As a result, a new rockburst indicator, SSF, is proposed to predict strainburst risks based on the analysis of stiffness differences. The prediction results of SSF successfully match the 5.5" rockburst event in the Zofiowka Coal Mine and the "11.28" rockburst event in the Jinping II Hydropower Station, validating the effectiveness of SSF.

7.3 Contributions of the research

The findings from this PhD study are significant in predicting and controlling rockburst risks for the underground mining industry. The main contributions are summarized as follows:

(1) A systematic and reasonable numerical modeling framework for studying rockburst mechanisms and other rockburst-related problems is established. The selection of numerical modeling approaches, numerical programs, numerical modeling sequences, material parameters, and model calibration are all included in the framework providing a clear guideline for researchers and engineers to study rockburst problems using numerical modeling.

(2) The rockburst source mechanism of driving roadways during close-distance coal seam mining is revealed thoroughly. The results suggest that the superposition of multiple excavation-induced stresses of roadways provides an environment for stress concentration and energy accumulation, and the side abutment stress induced by mining in the upper coal seam has a "strengthening" effect to the rockburst occurrence. In addition, the great deviatoric stress induced by complex excavating situations is another important exterior cause. As a result, some alternative methods are proposed

to prevent and mitigate rockburst hazards of driving roadways during close-distance coal seam mining. For instance, the rockburst hazard in the case study site could be reduced using the down-dip recovery sequence and changing the driving direction of roadways.

(3) A systematic method that can select and use rockburst indicators reasonably to predict the location and magnitude of different rockbursts is developed, providing an effective tool for engineers to combine rockburst indicators and numerical modeling for predicting and evaluating rockburst risks.

(4) An improved global-local modeling approach is novelly employed to investigate the damage mechanisms of strainbursts. The improved global-local modeling approach provides a more insightful understanding of the influences of the realistic stress loading path on strainburst occurrence and a quantitive evaluation of rockburst damage. As a result, the damage mechanisms of strainbursts can be fully revealed, which helps improve and optimize the rock support design in the burst-prone ground to control and mitigate rockburst damage.

(5) Instead of conventional drop tests, the performance of yielding rockbolts during remotely triggered and self-initiated strainbursts was systematically evaluated. The results suggest that the yielding rockbolt with high strength and deformation capacity (e.g., D-bolt) has a better performance in controlling rockburst damage. Furthermore, the support effects can be significantly improved by increasing the bolt number and supplementing cables and surface retaining elements (e.g., steel arch). These findings can also help to improve and optimize rockbolt support in burst-prone mines.

(6) A novel method is proposed to calculate the LMS for a tunnel. As a result, a new stiffness-based rockburst indicator, SSF, is proposed and developed for predicting strainburst risks. The effectiveness of SSF is verified by comparing its prediction results with reported rockburst cases. The SSF can be easily implemented in numerical modeling, which provides an effective tool for engineers to predict strainburst risks in engineering practice.

In summary, the outcomes of this PhD study can contribute to understanding rockburst mechanisms and to effectively predicting rockburst risks for improving the safety of workers and production in burst-prone mines.

7.4 Limitations and future research

Although during this research, the author was able to reveal rockburst mechanisms and develop a systematic method and a new stiffness-based indicator for predicting rockburst risks, the thesis has some limitations, and future work can be done in the following aspects to improve this work further:

(1) The reliability and accuracy of the simulation results in the 3D model could be further improved if more field monitoring data is provided.

(2) Stress relief and transfer measures (e.g., distress drilling and blasting) are alternative techniques to control and mitigate rockburst risks. The effects of these measures on controlling rockbursts should be further investigated for driving roadways during close-distance coal seam mining.

(3) Only the simplified P wave was used in this study. However, the actual dynamic disturbance is composed of P and S waves and is usually very complex. Therefore, the strainburst damage mechanisms and the performance of yielding rockbolts during rockbursts should be further examined if actual seismic data are available.

(4) The accuracy of simulation results can be improved if the dynamic mechanical properties of rock masses and joints and related constitutive relationships are known and used. There is no energy dissipation when two contact faces in UDEC models are separated. Further studies (e.g., setting residual values of contacts or selecting more representative constitutive models) need to be conducted to consider the influences of fracture energy on simulation results.

(5) The performance of yielding rockbolts was mainly evaluated from the “macro” views of the dynamic energy-absorption capacity and the control of the deformation and damage of rock masses.

Other "micro" behaviour of rockbolts, e.g., the shear force and failure of rockbolt-grout interfaces, will be studied in future research.

(6) The performance of yielding rockbolts during strainbursts has been initially confirmed by in situ observations and others' experimental tests and simulation results. However, the simulation results will be more accurate and reliable if field monitoring data (e.g., dynamic strength and elongation rate) of yielding rockbolts during strainbursts are available to calibrate simulation parameters.

(7) The sliding or extraction mechanism of Roofex should be simulated explicitly to evaluate its performance during strainbursts better. Setting reasonable parameters for the bolt-grout/rock interface will be a choice.

(8) This study employs the maximum LMS in different directions around the tunnel to predict strainburst risks. However, the rock masses in other directions could also release excess energy contributing to the strainburst strength, which might cause the difference between the analytical and numerical results of excess energy observed in this research. This hypothesis should be further studied to improve the reliability and accuracy of the SSF in the future.

(9) In addition to LMS, PCS is the other key factor controlling unstable rock failure. Currently, there is no uniform standard to obtain PCS due to the complexity of rock mass behaviour. Hence, more work needs to be done to determine PCS accurately to improve the robustness of SSF.

BIBLIOGRAPHY

Adam, M., 2018. Report of the Commission appointed by the President of the State Mining Authority in Katowice to investigate the causes and circumstances of the rock burst and the collective accident on May 5, 2018 in KWK "Borynia -Zofiówka-Jastrzębie" Ruch "Zofiówka" with / in Jastrzębie Zdrój., Katowice, Poland: State Mining Authority.

Afraei, S., Shahriar, K. and Madani, S.H., 2019. Developing intelligent classification models for rock burst prediction after recognizing significant predictor variables, Section 1: Literature review and data preprocessing procedure. Tunnelling and Underground Space Technology, 83, 324-353.

Alonso, E., Alejano, L. R., Varas, F., Fdez-Manin, G., and Carranza-Torres, C., 2003, Ground response curves for rock masses exhibiting strain-softening behaviour: International Journal for Numerical and Analytical Methods in Geomechanics, 27(13), p.1153-1185.

Ahmed, S.S., ALHeib, M., Gunzburger, Y. and Renaud, V., 2017. Pillar Burst assessment based on large-scale numerical modeling. Procedia Engineering, 191, 179-187.

Apel, D.B., 2005. Design and development of an underground hard-rock mine with the assistance of rock mechanics software. Mining Engineering, 57(9), 83-88.

Apel, Z., Vafaeian, B., Apel, D.B. and Hussain, A., 2021. Occlusal stresses in beveled versus non-beveled tooth preparation. Biomedical Engineering Advances, 2, p.100010.

Arndt S. M., Fillery B. P. and Beck D. A., 2009. Advances in Mining Simulation. 2009 SIMULIA Customer Conference, London, England.

Atlas Copco Construction Mining Technique., 2009. Roofex rock bolt. https://www.forconstructionpros.com/equipment/underground/vertical-drilling-equipment/product/10080325/atlas-copco-construction-mining-technique-usa-llc-roofex-rock-bolt. Accessed 22 May 2021

Bai, M., Kendorski F., and Van Roosendaal D., 1995. Chinese and North American high-extraction underground coal mining strata behaviour and water protection experience and guidelines. Proceedings of the 14th International Conference on Ground Control in Mining, Morgantown, 209-17.

Bahrani, N. and Hadjigeorgiou, J., 2017. Explicit reinforcement models for fully-grouted rebar rock bolts. Journal of Rock Mechanics and Geotechnical Engineering, 9(2), pp.267-280.

Bardet, J.P., 1987. Numerical Assessment of Rockbursting. Agbabian Associates El Segundo Ca. 8618(6171).

Bardet, J.P., 1990. Finite element analysis of surface instability in hypo-elastic solids. Computer Methods in Applied Mechanics and Engineering, 78(3), 273-296.

Barton, N., Lien, R., and Lunde, J., 1974. Engineering classification of rock masses for the design of tunnel support. Rock Mechanics and Rock Engineering. 6(4), 189-236.

Basarir, H., Sun, Y. and Li, G., 2019. Gateway stability analysis by global-local modeling approach. International Journal of Rock Mechanics and Mining Sciences, 113, pp.31-40.

Bear, J., 1972. Dynamics of Fluids in Porous Media. Dover Publication: New York, NY, USA.

Bennett, T.J. and Marshall, M.E., 2001. Identification of rockbursts and other mining events using regional signals at international monitoring system stations. SCIENCE APPLICATIONS INTERNATIONAL CORP MCLEAN VA. Corp Mclean VA 2001.

Bieniawski, Z.T., 1968, July. The effect of specimen size on compressive strength of coal. In International Journal of Rock Mechanics and Mining Sciences & Geomechanics Abstracts, 5(4), pp. 325-335.

Bieniawski, Z.T., 1986. Strata control in mineral engineering, John Wiley& sons, New York. 135-146.

Blake, W., 1972a. Rock-burst mechanics. Q. Colo. Sch. Mines;(United States), 67(1).

Blake, W., 1972b. Rock-burst mechanics. Doctoral dissertation, Colorado School of Mines, Golden, US.

Blake, W., and Hedley, D. G., 2003. Rockbursts: case studies from North American hard-rock mines. Littleton, Colorado: SME.

Board, M.P. and Voegele, M.D., 1981. Examination and demonstration of undercut and fill stoping for ground control in deep vein mining. Application of Rock Mechanics to Cut and Fill Mining, Sweden, 300.

Bosman, K., Cawood, M., and Berghorst, A., 2018. Relationship between energy per impulse and dynamic capacity of a rockbolt, CRC Press.

Brady, B.H. and Brown, E.T., 1993. Rock mechanics: for underground mining. Springer science & business media.

Brady, B.H.G., 1979. Boundary element methods for mine design. Doctoral dissertation, Imperial College of Science and Technology, London, UK.

Brown, E.T., 1984. Rockbursts: prediction and control. Tunnels Tunnell, 84, 17-19.

Cai, M., 2013. Principles of rock support in burst-prone ground. Tunnelling and Underground Space Technology, 36: 46–56.

Cai, M., Kaiser, P.K., Morioka, H., Minami, M., Maejima, T., Tasaka, Y. and Kurose, H., 2007. FLAC/PFC coupled numerical simulation of AE in large-scale underground excavations. International Journal of Rock Mechanics and Mining Sciences, 44(4), 550-564.

Cai, M., Champaigne, D., Kaiser, P.K., 2010. Development of a fully debonded cone bolt for rockburst support. In: Proceedings of the Fifth International Seminar on Deep and High Stress Mining. Australian Centre for Geomechanics, Santiago, pp.329-342.

Cai, M., and Champaigne, D., 2012. Influence of bolt-grout bonding on MCB conebolt performance. International Journal of Rock Mechanics and Mining Sciences, 49, 165-175.

Cai, M., 2016. Prediction and prevention of rockburst in metal mines–A case study of Sanshandao gold mine. Journal of Rock Mechanics and Geotechnical Engineering, 8(2), pp.204-211.

Cai, W., 2015. Fault Rock burst Induced by Static and Dynamic Loads Superposition and its Monitoring and Warning. PhD Thesis, China University of Mining and Technology, Xuzhou, China. (In Chinese)

Campoli A.A., Barton T.M., Dyke F., and Gauna M., 1993. Gob and gate road reaction to longwall mining in bump-prone strata. 9445. RI: Bureau of Mines, 48.

Castro, L.A.M., Bewick, R.P., and Carter, T.G., 2012. In: an overview of numerical modelling applied to deep mining. innovative numerical modelling in geomechanics. CRC Press, 393-414.

Castro L.A.M., 1996. Analysis of Stress-Induced Damage Initiation around Deep Openings Excavated in a Moderately Jointed Brittle Rock Mass, PhD Thesis, University of Toronto, Toronto, Canada.

Castro, L.A., Grabinsky, M.W. and McCreath, D.R., 1997. Damage initiation through extension fracturing in a moderately jointed brittle rock mass. International Journal of Rock Mechanics and Mining Sciences, 34(3-4), pp.110-e1.

Chamber of Mines of South Africa., 1982. Rockburst terminology: Circular No. 28/82, Johannesburg.

Charette, F. and Plouffe, M., 2007, November. Roofex®–Results of laboratory testing of a new concept of yieldable tendon. In Deep Mining 2007: Proceedings of the Fourth International Seminar on Deep and High Stress Mining (pp. 395-404). Australian Centre for Geomechanics.

Chen, B.R., Feng X.T., Ming H.J., Zhou H., Zeng X.H., Feng G.L. and Xiao Y.X., 2012. Evolution law and mechanism of rockbursts in deep tunnel：time delayed rockburst. Chinese Journal of Rock Mechanics and Engineering, 31(3), 561-569. (In Chinese)

Chen, M., Yang, S.Q., Zhang, Y.C. and Zang, C.W., 2016. Analysis of the failure mechanism and support technology for the Dongtan deep coal roadway. Geomechanics and Engineering, 11(3), pp.401-420.

Chen, W.Z., Lu, S.P., Guo, X.H. and Qiao, C.J., 2009. Research on unloading confining pressure tests and rockburst criterion based on energy theory. Chinese Journal of Rock Mechanics and Engineering, 28(8), pp.1530-1540. (In Chinese)

Cheng, Y. M., Wang, J. A., Xie, G. X. and Wei, W. B., 2010. Three-dimensional analysis of coal barrier pillars in tailgate area adjacent to the fully mechanized top caving mining face. International Journal of Rock Mechanics and Mining Sciences, 47, 1372-1383.

Cieślik, J., Burtan, Z., Chlebowski, D. and Zorychta, A., 2017. Geomechanical analysis of location and conditions for mining-induced tremors in LGOM copper mines. Journal of Sustainable Mining, 16(3), 94-103.

Coggan, J.S. & Stead, D., 2005. Numerical modelling of the effects of weak mudstone on tunnel roof behaviour. In: Proc. 58th Canadian Geotechnical Conference, Saskatoon, Canada.

Colson, C.M., 1950. Rockbursts. Masters Theses. Missouri S&T, 43-49.

Cook, N.G.W., 1965a. A note on rockbursts considered as a problem of stability. Journal of the Southern African Institute of Mining and Metallurgy, 65(8), 437-446.

Cook, N.G., 1965b. The failure of rock. International Journal of Rock Mechanics and Mining Sciences & Geomechanics Abstracts, 2, 389–403.

Cundall, P.A. and Strack, O.D.L., 1979. The development of constitutive laws for soil using the distinct element method. Numerical methods in geomechanics, 1, 289-317.

Cundall, P.A., 1971. A computer model for simulating progressive, large-scale movement in blocky rock system. In Proceedings of the International Symposium on Rock Mechanics, Nancy, France.

Cundall, P.A., 1988. Formulation of a three-dimensional distinct element model—Part I. A scheme to detect and represent contacts in a system composed of many polyhedral blocks. In International Journal of Rock Mechanics and Mining Sciences & Geomechanics Abstracts, 25(3), 107-116.

Daehnke, A., 1999, January. Stress wave and fracture propagation in rock. In 9th ISRM Congress, International Society for Rock Mechanics and Rock Engineering, Paris, France.

Dai, L., Pan, Y., Li, Z., Wang, A., Xiao, Y., Liu, F., Shi, T. and Zheng, W., 2021. Quantitative mechanism of roadway rockbursts in deep extra-thick coal seams: theory and case histories. Tunnelling and Underground Space Technology, 111, p.103861.

Dehghan, S., Shahriar, K., Maarefvand, P. and Goshtasbi, K., 2013a. 3-D modeling of rock burst in pillar No. 19 of Fetr6 chromite mine. International Journal of Mining Science and Technology, 23(2), 231-236.

Dehghan, S., Shahriar, K., Maarefvand, P. and Goshtasbi, K., 2013b. 3-D numerical modeling of Domino failure of hard rock pillars in Fetr6 Chromite Mine, Iran, and comparison with empirical methods. Journal of Central South University, 20(2), 541-549.

Demirdag, S., Tufekci, K., Kayacan, R., Yavuz, H. and Altindag, R., 2010. Dynamic mechanical behavior of some carbonate rocks. International Journal of Rock Mechanics and Mining Sciences, 47(2), 307-312.

Dammyr, Ø., 2016. Prediction of brittle failure for TBM tunnels in anisotropic rock: a case study from Northern Norway. Rock Mechanics and Rock Engineering, 49(6), pp.2131-2153.

Deng, J. and Gu, D.S., 2018. Buckling mechanism of pillar rockbursts in underground hard rock mining. Geomechanics and Geoengineering, 13(3), 168-183.

Díaz-Aguado, M.B., and González, C., 2009. Influence of the stress state in a coal bump-prone deep coalbed: a case study. International Journal of Rock Mechanics and Mining Sciences, 46(2): 333-345.

Diederichs, M.S., 1999. Instability of Hard Rock Masses: The Role of Tensile Damage and Relaxation, PhD Thesis, University of Waterloo, Waterloo, Canada.

Diederichs, M.S., 2007. The 2003 Canadian Geotechnical Colloquium: mechanistic interpretation and practical application of damage and spalling prediction criteria for deep tunnelling. Canadian Geotechnical Journal, 44(9), 1082-1116.

Doležel, V. and Procházka, P., 2007. Rock bumps due to the creation of a dislocation during deep mining. WIT Transactions on Modeling and Simulation, 46.

Durrheim, R., 2010. Mitigating the risk of rockbursts in the deep hard rock mines of South Africa: 100 years of research. Extracting the Science: a century of mining research, Brune J (eds), Society for Mining, Metallurgy, and Exploration, Inc, 156-171.

Eberhardt, E., 2012. The Hoek–Brown Failure Criterion. Rock Mechanics and Rock Engineering, 45, 981-988.

Edelbro, C., 2008. Strength, fallouts and numerical modeling of hard rock masses. PhD Thesis, Luleå tekniska universitet, Luleå, Sweden.

Edelbro, C., Sjöberg, J., Malmgren, L. and Dahnér-Lindqvist, C., 2012. Prediction and follow-up of failure and fallouts in footwall drifts in the Kiirunavaara mine. Canadian geotechnical journal, 49(5), pp.546-559.

Elmo, D., Coggan, J.S. and Pine, R.J., 2005. Characterisation of rock mass strength using a combination of discontinuity mapping and fracture mechanics modeling. Alaska Rocks 2005, The 40th US Symposium on Rock Mechanics (USRMS), American Rock Mechanics Association.

Esterhuizen, G.S., Dolinar, D.R. and Ellenberger, J.L., 2011. Pillar strength in underground stone mines in the United States. International Journal of Rock Mechanics and Mining Sciences, 48(1), pp.42-50.

Fafal R., 2017. Ruch "Zofiówka" KWK "Borynia-Zofiówka" https://www.google.com/maps/uv?pb=!1s0x471152872e7ea45b%3A0xdb7afc22d1434fb0!3m1!7e115!4shttps%3A%2F%2Flh5.googleusercontent.com%2Fp%2FAF1QipNR7dJ41poI3q3fA76MeVeS-FLFobhCC3nzpUi4%3Dw234-h176-k-no!5sZofi%C3%B3wka%20coal%20mine%20Jastrz%C4%99bie-Zdr%C3%B3j%20-%20Google%20Search!15sCgIgAQ&imagekey=!1e10!2sAF1QipOp0M3vFTCIpZQAN6kv3xuujmtPKDZMUfehapzk&hl=en&sa=X&ved=2ahUKEwib4e-nx87tAhXSJzQIHfUvC2MQoiowCnoECBcQAw

Fakhimi, A., 2009. A hybrid discrete-finite element model for numerical simulation of geomaterials. Computers and Geotechnics, 36(3), 386-395.

Fan, D., Liu, X., Tan, Y., Song, S., Gu, Q., Yan, L. and Xu, Q., 2019a. Roof cutting parameters design for gob-side entry in deep coal mine: A case study. Energies, 12(10), p.2032.

Fan, D.Y., Liu XS, Tan Y.L., Yan L., Song S.L., Ning, J.G., 2019b. An innovative approach for gob -side entry retaining in deep coal mines: A case study. Energy Science & Engineering.

Fairhurst, C.E. and Hudson, J.A., 1999. Draft ISRM suggested method for the complete stress-strain curve for intact rock in uniaxial compression. International journal of rock mechanics and mining sciences (1997), 36(3), pp.279-289.

Farahmand, K., Vazaios, I., Diederichs, M.S. and Vlachopoulos, N., 2018. Investigating the scale-dependency of the geometrical and mechanical properties of a moderately jointed rock using a synthetic rock mass (SRM) approach. Computers and Geotechnics, 95, pp.162-179.

Farrokh, E. and Rostami, J., 2009. Effect of adverse geological condition on TBM operation in Ghomroud tunnel conveyance project. Tunnelling and underground space technology, 24(4), pp.436-446.

Feng, F., Li X., Li, D., and Chen, C., 2017. Numerical analysis of failure characteristics of circular hole specimen containing pre-existing flaw based on finite/discrete elements. Rock and Soil Mechanics, 38, 337-348. (In Chinese)

Feng, G.L., Feng, X.T., Chen, B.R., Xiao, Y.X. and Zhao, Z.N., 2019c. Effects of structural planes on the microseismicity associated with rockburst development processes in deep tunnels of the Jinping-II Hydropower Station, China. Tunnelling and Underground Space Technology, 84, pp.273-280.

Feng, X.T, Xiao Y.X., Feng G.l., Yao Z.B., Chen B.R., Yang C.X. and Su G.X., 2019a. Study on the development process of rockbursts. Chinese Journal of Rock Mechanics and Engineering, 38(4), 649-673. (In Chinese)

Feng, F., Li, X., Rostami, J. and Li, D., 2019b. Modeling hard rock failure induced by structural planes around deep circular tunnels. Engineering Fracture Mechanics, 205, 152-174.

Feng, X.T., Liu, J., Chen, B., Xiao, Y., Feng, G. and Zhang, F., 2017. Monitoring, warning, and control of rockburst in deep metal mines. Engineering, 3(4), 538-545.

Gao, M.S., Dou, L.M., Yan, R.L., Han, C.L. and Guo, Y.S., 2009. Prevention mechanism of roadway supported by bolt-mesh subjected to rock burst and degree calculation. Journal of Mining & Safety Engineering, 26(4), pp.402-406.

Gao, F., 2013. Simulation of failure mechanisms around underground coal mine openings using discrete element modeling. PhD Thesis, Simon Fraser University, Vancouver, Canada.

Gao, F.Q. and Stead, D., 2014. The application of a modified Voronoi logic to brittle fracture modeling at the laboratory and field scale. International Journal of Rock Mechanics and Mining Sciences, 68, pp.1-14.

Gao, F., Stead, D. and Kang, H., 2015. Numerical simulation of squeezing failure in a coal mine roadway due to mining-induced stresses. Rock Mechanics and Rock Engineering, 48(4), pp.1635-1645.

Gao, F., 2019. Use of numerical modeling for analyzing rock mechanic problems in underground coal mine practices. Journal of Mining and Strata Control Engineering, 1(1), 013004. (In Chinese)

Gao, F., Kaiser, P.K., Stead, D., Eberhardt, E. and Elmo, D., 2019a. Numerical simulation of strainbursts using a novel initiation method. Computers and Geotechnics, 106, 117-127.

Gao, F., Kaiser, P.K., Stead, D., Eberhardt, E. and Elmo, D., 2019b. Strainburst phenomena and numerical simulation of self-initiated brittle rock failure. International Journal of Rock Mechanics and Mining Sciences, 116, 52-63.

Gao, F., Kang, H., Lou, J., Li, J. and Wang, X., 2019c. Evolution of local mine stiffness with mining process: insight from physical and numerical modeling. Rock Mechanics and Rock Engineering, 52(10), pp.3947-3958.

Garvey, R. J., 2013, A study of unstable rock failures using finite difference and discrete element methods. PhD Thesis, Colorado School of Mines, Golden, USA.

Goodman, R.E. and Shi, G.H., 1985. Block theory and its application to rock engineering.

Grisi, S., Castellanza, R., Agliardi, F., Crosta, G. and Elmo, D., 2016. Failure mechanism of a gypsum pillar by 2D and 3D FEM/DEM numerical analyses. ISRM International Symposium-EUROCK, International Society for Rock Mechanics and Rock Engineering.

Gu, R. and Ozbay, U., 2015. Numerical investigation of unstable rock failure in underground mining condition. Computers and Geotechnics, 63, pp.171-182.

Guo, Z., 1996. Practical rockmass mechanics. Beijing: Earthquake Press, 190-200. (In Chinese)

Guo, W., Gu, Q., Tan, Y. and Hu, S., 2019c. Case Studies of Rock Bursts in Tectonic Areas with Facies Change. Energies, 12(7), 1330.

Guo, W.Y., Yu, F.H., Tan, Y.L. and Zhao, T.B., 2019b. Experimental study on the failure mechanism of layer-crack structure. Energy Science & Engineering, 7(6), pp.2351-2372.

Guo, X., Zhao, Z., Gao, X., Ma, Z. and Ma, N., 2019a. The Criteria of Underground Rock Structure Failure and Its Implication on Rockburst in Roadway: A Numerical Method. Shock and Vibration, 1-12.

Gutenberg, B. and Richter, C.F., 1956. Earthquake magnitude, intensity, energy, and acceleration: (Second paper). Bulletin of the seismological society of America, 46(2), pp.105-145.

Hart, R.D., 1980, Geotechnical modeling of a cut and fill mining operation. In Proceedings of the Conference on the Application of Rock Mechanics to Cut and Fill Mining. Lulea, Sweden, 307-15.

Hauquin, T., Gunzburger, Y. and Deck, O., 2018. Predicting pillar burst by an explicit modelling of kinetic energy. International journal of rock mechanics and mining sciences, 107, 159-171.

Hazzard, J.F. and Young, R.P., 2002. Moment tensors and micromechanical models. Tectonophysics, 356(1-3), 181-197.

Hazzard J., 2020. FLAC3D version 7.0 webinar. https://www.itascacg.com/learning/webinars/learn-more-about-flac3d-7-0

He, M.C., Xie, H.P., Peng, S.P. and Jiang, Y.D., 2005. Study on rock mechanics in deep mining engineering. Yanshilixue Yu Gongcheng Xuebao/Chin. J. Rock Mech. Eng., 24(16), pp.2803-2813.

He, M., Xia, H., Jia, X., Gong, W., Zhao, F. and Liang, K., 2012. Studies on classification, criteria and control of rockbursts. Journal of Rock Mechanics and Geotechnical Engineering, 4(2), 97-114.

Heal, D., 2010. Observations and analysis of incidences of rockburst damage in underground mines. Doctoral dissertation, University of Western Australia, Perth.

Hedley, D.G.F., 1987. Catalogue of rockburst literature. Mining Res Laboratories.

Hedley, D.G.F., 1992. Rockburst handbook for Ontario hard rock mines. CANMET Special Report SP92-1E. Energy, Mines and Resources, Canada Center for Mineral and Energy Technology, Toronto, Ont.

Hoek, E. and Brown, E.T., 1980. Underground Excavation in Rock. The Institute of Mining and Metallurgy, London, 527.

Hoek, E. and Brown, E.T., 1997. Practical estimates of rock mass strength. International journal of rock mechanics and mining sciences, 34(8), pp.1165-1186.

Hoek, E., Carranza-Torres, C. and Corkum, B., 2002. Hoek-Brown failure criterion-2002 edition. In: Proceedings of NARMS-Tac. 1(1), 267–273.

Hoek, E. and Diederichs, M.S., 2006. Empirical estimation of rock mass modulus. International journal of rock mechanics and mining sciences, 43(2), 203-215.

Hosseini, O., 2016. Numerical Simulation of Rock Burst of Underground Pillars. Master Thesis, New Mexico Institute of Mining and Technology, Socorro, USA.

Hu, L., Ma, K., Liang, X., Tang, C., Wang, Z. and Yan, L., 2018. Experimental and numerical study on rockburst triggered by tangential weak cyclic dynamic disturbance under true triaxial conditions. Tunnelling and Underground Space Technology, 81, pp.602-618.

Hu, L., Liang, X., Liang, Z., Li, Y. and Zhang, Z., 2021. Influence of radial stress on strainbursts under true triaxial conditions: Insights from a distinct element modeling. International Journal of Rock Mechanics and Mining Sciences, 138, p.104577.

Hu, L., Su, G., Liang, X., Li, Y. and Yan, L., 2020. A distinct element based two-stage-structural model for investigation of the development process and failure mechanism of strainburst. Computers and Geotechnics, 118, p.103333.

Hyett, A.J., Moosavi, M. and Bawden, W.F., 1996. Load distribution along fully grouted bolts, with emphasis on cable bolt reinforcement. International Journal for Numerical and Analytical Methods in Geomechanics, 20(7), pp.517-544.

Itasca Consulting Group, 2000. FLAC (Fast Lagrangian Analysis of Continua). Itasca Consulting Group, Minneapolis, MN.

Itasca Consulting Group, 2019. FLAC3D 7.0 Documentation. Itasca Consulting Group, Minneapolis, MN.

Itasca Consulting Group, 2020. UDEC 7.0 Documentation. Itasca Consulting Group, Minneapolis, MN.

Jager, A.J. and Ryder, J.A., 1999. A handbook on rock engineering practice for tabular hard rock mines. Safety in Mines Research Advisory Committee, Johannesburg, 46.

Jaeger, J.C. and Cook, N.G.W., 1979. Fundamentals of Rock Mechanics, Chapman and Hall, London.

Jaiswal, A. and Shrivastva, B.K., 2012. Stability analysis of the proposed hybrid method of partial extraction for underground coal mining. International Journal of Rock Mechanics and Mining Sciences, 52, pp.103-111.

Ji, S., He, H. and Karlovšek, J., 2021. Application of superposition method to study the mechanical behaviour of overlying strata in longwall mining. International Journal of Rock Mechanics and Mining Sciences, 146, p.104874.

Ji, S. and Karlovšek, J., 2022a. Calibration and uniqueness analysis of microparameters for DEM cohesive granular material. International Journal of Mining Science and Technology, 32(1), pp.121-136.

Ji, S. and Karlovšek, J., 2022b. Optimized differential evolution algorithm for solving DEM material calibration problem. Engineering with Computers, pp.1-16.

Jiang F.F., Zhou H., Liu C. and Sheng J., 2019. Progress, prediction and prevention of rockbursts in underground metal mines. Chinese Journal of Rock Mechanics and Engineering, 38(5), 956-972. (In Chinese)

Jiang, F., Liu, Y., Zhai, M., Guo, X.S., Wen, J.L., Liu, X.G. and Ma, X.F., 2017b. Evaluation of rock burst hazard based on the classification of stress and surrounding rock. Chinese Journal of Rock Mechanics and Engineering, 36(5), pp.1041-1052. (In Chinese)

Jiang, J.Q., 2017. Study on strainburst in tunnel using true-triaxial test and its kinetic energy prediction. PhD Thesis, Guangxi University, Nanning, China.

Jiang, J.Q., Wang, P., Jiang, L.S., Zheng, P.Q. and Feng, F., 2018. Numerical simulation on mining effect influenced by a normal fault and its induced effect on rock burst. Geomechanics and Engineering, 14(4), 337-344.

Jiang, L.S., Wu, Q., Li, X. and Ding, N., 2017a. Numerical simulation on coupling method between mining-induced stress and goaf compression. Journal of China Coal Society, 42(8), pp.1951-1959. (In Chinese)

Jiang, Q., Feng, X.T., Xiang, T.B. and Su, G.S., 2010. Rockburst characteristics and numerical simulation based on a new energy index: a case study of a tunnel at 2,500 m depth. Bulletin of engineering geology and the environment, 69(3), pp.381-388.

Jiang, Y., Wang, H., Xue, S., Zhao, Y., Zhu, J. and Pang, X., 2012. Assessment and mitigation of coal bump risk during extraction of an island longwall panel. International Journal of Coal Geology, 95, 20-33.

Jiang, Y.D. and Zhao, Y.X., 2015. State of the art: investigation on mechanism, forecast and control of coal bumps in China. Chinese Journal of Rock Mechanics and Engineering, 34(11), 2188-2204.

Jiang, Y.D., Pan, Y.S., Jiang, F.X., Dou, L.M. and Ju, Y., 2014. State of the art review on mechanism and prevention of coal bumps in China. Journal of China Coal Society, 39(2), 205-213.

Jing, L. and Hudson, J.A., 2002. Numerical methods in rock mechanics. International Journal of Rock Mechanics and Mining Sciencaes, 39(4), 409-427.

Jing, L., 2003. A review of techniques, advances and outstanding issues in numerical modeling for rock mechanics and rock engineering. International Journal of Rock Mechanics and Mining Sciences, 40(3), 283-353.

Jastrzębska Spółka Węglowa S.A. Group., 2018. Technical report: measurement of roof quality and gateroad load and deformation.

Jastrzębska Spółka Węglowa S.A. Group., 2019. Technical presentation: A high-energy mine shock occurred on May 5, 2018 in the Zofiówka coal mine.

Kaiser, P.K., and Cai, M., 2012. Design of rock support system under rockburst condition. Journal of Rock Mechanics and Geotechnical Engineering, 2012(3), 215-227.

Kaiser, P.K., Tannant, D.D., McCreath, D.R., 1996. Canadian Rockburst Support Handbook. Geomechanics Research Centre, Laurentian University, Sudbury, Ontario, 314.

Kang, H.P., Lin, J. and Wu, Y.Z., 2009. High pretensioned stress and intensive cable bolting technology set in full section and application in entry affected by dynamic pressure. Journal of China Coal Society, 34(9), pp.1153-1159.

Keneti, A. and Sainsbury, B.A., 2018. Review of published rockburst events and their contributing factors. Engineering geology, 246, 361-373.

Khademian, Z., Poeck, E., Garvey, R. and Ozbay, U., 2016. Studies of seismicity generated by unstable failure around circular excavations. 50th US Rock Mechanics/Geomechanics Symposium. American Rock Mechanics Association.

Khademian, Z. and Ugur, O., 2018. Computational framework for simulating rock burst in shear and compression. International Journal of Rock Mechanics and Mining Sciences, 110, pp.279-290.

Khademian, Z. and Ozbay, U., 2019. Modeling violent rock failures in tunneling and shaft boring based on energy balance calculations. Tunnelling and Underground Space Technology, 90, pp.62-75.

Kias, E.M.C. and Ozbay, U., 2013, January. Modeling unstable failure of coal pillars in underground mining using the discrete element method. 47th US Rock Mechanics/Geomechanics Symposium. American Rock Mechanics Association.

Kidybiński, A., 1981, August. Bursting liability indices of coal. In International Journal of Rock Mechanics and Mining Sciences & Geomechanics Abstracts, 18(4), pp. 295-304.

Konicek, P., Saharan, M.R., and Mitri, H., 2011. Destress blasting in coal mining State-of-the-art review. Procedia Engineering, 26: 179-194.

Konicek, P., Soucek, K., Stas, L. and Singh, R., 2013. Long-hole destress blasting for rockburst control during deep underground coal mining. International Journal of Rock Mechanics and Mining Sciences, 61, pp.141-153.

Kose H., Cebi Y., 1988. Investigation the stresses forming during production of thick coal seam. In: Proceedings of the 6th Coal Congress of Turkey, Zonguldak. 371–383. (In Turkish with English abstract)

Kong, P., Jiang, L., Jiang, J., Wu, Y., Chen, L. and Ning, J., 2019. Numerical analysis of roadway rock-burst hazard under superposed dynamic and static loads. Energies, 12(19), p.3761.

Kang, H.P., Lin, J. and Wu, Y.Z., 2009. High pretensioned stress and intensive cable bolting technology set in full section and application in entry affected by dynamic pressure. Journal of China Coal Society, 9. (In Chinese)

Kusui, A., Villaescusa, E. and Funatsu, T., 2016. Mechanical behaviour of scaled-down unsupported tunnel walls in hard rock under high stress. Tunnelling and Underground Space Technology, 60, 30-40.

Kwasniewski, M., and Wang, J., 1999. 3D numerical modeling and study of mine tremors induced by coal mining in the vicinity of major faults-A case study. In FLAC and Numerical modeling in geomechanics, pp. 379-388.

Kwasniewski, M., Szutkowski, I. and Wang, J.A., 1994. Study of ability of coal from seam 510 for storing elastic energy in the aspect of assessment of hazard in Porabka-Klimontow Colliery. Sci. Rept. Silesian Technical University.

Lemos, J., Hart, R. and Lorig, L., 1987. Dynamic analysis of discontinua using the distinct element method. In 6th ISRM Congress, International Society for Rock Mechanics and Rock Engineering, 1079-1084.

Lenhardt, W.A., 1992. Seismicity associated with deep-level mining at Western Deep Levels Limited. Journal of the Southern African Institute of Mining and Metallurgy, 92(5), 113-120.

Leveille, P., Sepehri, M. and Apel, D.B., 2017. Rockbursting potential of kimberlite: A case study of Diavik diamond mine. Rock Mechanics and Rock Engineering, 50(12), 3223-3231.

Li, C.C., 2011. Performance of D-bolts under static loading. Rock Mechanics and Rock Engineering, 45(2), pp.183-192.

Li, C.C., Stjern, G. and Myrvang, A., 2014. A review on the performance of conventional and energy-absorbing rockbolts. Journal of Rock Mechanics and Geotechnical Engineering, 6(4), pp.315-327.

Li, C.C., 2021. Principles and methods of rock support for rockburst control. Journal of Rock Mechanics and Geotechnical Engineering, 13(1), pp.46-59.

Li, C.C., 2018. Rockburst conditions and rockburst support. Chinese Journal of Rock Mechanics and Engineering, 38(4), 674-682. (In Chinese)

Li, C.C. and Doucet, C., 2012. Performance of D-bolts under dynamic loading. Rock Mechanics and Rock Engineering, 45(2), pp.193-204.

Li, X.B, Chen S. R., and Gu D.S., 1994. Dynamic strength of rock under impulse loads with different stress waveforms and durations. Journal of Central South Institute of Mining and Metallurgy. 25(3), 301-4.

Li, X.B, Gu D.S., and Li H.H., 1993. On the reasonable loading stress waveforms determined by dynamic stress-strain curves of rocks by SHPB. Explosion and Shock Waves, 13(2), 125-130.

Li, D.J., Qi, H. and Feng, J.L., 2015. Granite burst under loading conditions and its characteristics of energy dissipation: implementation by fdem method and laboratory experiments. 13th ISRM International Congress of Rock Mechanics, International Society for Rock Mechanics and Rock Engineering.

Li, G., Zhou, C., Zhang, Y., Xu, H., Gao, Y. and Zhang, R., 2013. Review of rockburst in underground engineering. Advances in Science and Technology of Water Resources, 33(3), 77-83, 94. (In Chinese)

Li, Q., Chen, L., Sui, Z., Wang, L. and Dong, J., 2019. Dynamic analysis and criterion evaluation on rockburst considering the fractured dissipative energy. Advances in Mechanical Engineering, 11(3), 1-12.

Li, T.B., Xiao, X.P., Shi, Y.C., 2008. Comprehensively integrated methods of rockburst prediction in underground engineering. Advance in Earth Science, 23 (5), 533–540.

Li, X., Li, C., Cao, W. and Tao, M., 2018. Dynamic stress concentration and energy evolution of deep-buried tunnels under blasting loads. International Journal of Rock Mechanics and Mining Sciences, 104, 131-146.

Li, Z.L., He, X.Q., Dou, L.M., Song, D.Z. and Wang, G.F., 2018. Numerical investigation of load shedding and rockburst reduction effects of top-coal caving mining in thick coal seams. International Journal of Rock Mechanics and Mining Sciences, 110, 266-278.

Lightfoot, N., 1993. The use of numerical modelling in rockburst control. Rockbursts and Seismicity, 93, 355.

Linkov A.V., 1992. Dynamic phenomena in mines and the problem of stability, University of Minnesota, USA.

Lisjak, A., Young-Schultz, T., Li, B., He, L., Tatone, B.S.A. and Mahabadi, O.K., 2020. A novel rockbolt formulation for a GPU-accelerated, finite-discrete element method code and its application to underground excavations. International Journal of Rock Mechanics and Mining Sciences, 134, p.104410.

Liu, C.Y., Huang, B.X., Meng, X.J., Yang, P.J. and Chen, L.G., 2007. Research on abutment pressure distribution law of overlength isolated fully-mechanized top coal caving face. Chin J Rock Mech Eng, 26(S1), pp.2761-2766. (In Chinese)

Liu, E., Huang, R. and He, S., 2012. Effects of frequency on the dynamic properties of intact rock samples subjected to cyclic loading under confining pressure conditions. Rock mechanics and rock engineering, 45(1), 89-102.

Liu, G., Karakus, M. and Mu, Z., 2019. Propagation and attenuation characteristics of rockburst-induced shock waves in coal-rock medium. Arabian Journal of Geosciences, 12(4), 113.

Liu, J. X., Tang C.A., and Wang S.H., 2003. Numerical simulation to excavation of thick coal seam. The Chinese Journal of Nonferrous Metals, 13(2), 754-759.

Liu, X.S., Tan, J., Tan, Y.L. and Hu, S.C., 2015. Pattern recognition of signals for the fault-slip type of rock burst in coal mines. Shock and Vibration, 2015.

Liu, X., 2017. Study on the mechanism and control of rockburst in roadways under dynamic loads. PhD Thesis, Shandong University of Science and Technology, Qingdao, China.

Liu, X., Xu, G., Zhang, C., Kong, B., Qian, J., Zhu, D. and Wei, M., 2017. Time effect of water injection on the mechanical properties of coal and its application in rockburst prevention in mining. Energies, 10(11), p.1783.

Liu, X., Fan, D., Tan, Y., Song, S., Li, X., Ning, J., Gu, Q. and Ma, Q., 2021a. Failure evolution and instability mechanism of surrounding rock for close-distance parallel chambers with super-large section in deep coal mines. International Journal of Geomechanics, 21(5), p.04021049.

Liu, X., Fan, D., Tan, Y., Ning, J., Song, S., Wang, H. and Li, X., 2021b. New detecting method on the connecting fractured zone above the coal face and a case study. Rock Mechanics and Rock Engineering, 54(8), pp.4379-4391.

Liu, X., Song, S., Tan, Y., Fan, D., Ning, J., Li, X. and Yin, Y., 2021c. Similar simulation study on the deformation and failure of surrounding rock of a large section chamber group under dynamic loading. International Journal of Mining Science and Technology, 31(3), pp.495-505.

Lu, C.P., Liu, G.J., Liu, Y. and Zhang, H., 2019. Mechanisms of rockburst triggered by slip and fracture of coal–parting–coal structure discontinuities. Rock Mechanics and Rock Engineering, 52(9), pp.3279-3292.

Lysmer, J. and Kuhlemeyer, R.L., 1969. Finite dynamic model for infinite media. Journal of the engineering mechanics division, 95(4), pp.859-878.

Ma, C., Li, T., Zhang, H., Jiang, Y. and Song, T., 2019. A method for numerical simulation based on microseismic information and the interpretation of hard rock fracture. Journal of Applied Geophysics, 164, 214-224.

Ma, S., Nemcik, J. and Aziz, N., 2014. Simulation of fully grouted rockbolts in underground roadways using FLAC2D. Canadian Geotechnical Journal, 51(8), pp.911-920.

Ma, Y., Liu, C., Wu, F. and Li, X., 2018. Rockburst Characteristics and Mechanisms during Steeply Inclined Thin Veins Mining: A Case Study in Zhazixi Antimony Mine, China. Shock and Vibration, 1-16.

McGarr, A., 1997. A mechanism for high wall-rock velocities in rockbursts. Pure and Applied Geophysics, 150(3), pp.381-391.

Małkowski P., Ostrowski Ł., and Bachanek P., 2017. Modelling the Small Throw Fault Effect on the Stability of a Mining Roadway and Its Verification by In Situ Investigation. Energies, 10.

Małkowski, P. and Ostrowski, Ł., 2019. Convergence monitoring as a basis for numerical analysis of changes of rock-mass quality and Hoek-Brown failure criterion parameters due to longwall excavation. Archives of Mining Sciences, 64(1).

Marinos, P. and Hoek, E., 2000, November. GSI: a geologically friendly tool for rock mass strength estimation. In ISRM international symposium. International Society for Rock Mechanics and Rock Engineering.

Mahabadi, O.K., Lisjak, A., Munjiza, A. and Grasselli, G., 2012. Y-Geo: new combined finite-discrete element numerical code for geomechanical applications. International Journal of Geomechanics, 12(6), 676-688.

Manouchehrian, A. and Cai, M., 2018. Numerical modeling of rockburst near fault zones in deep tunnels. Tunnelling and Underground Space Technology, 80, 164-180.

Manouchehrian, S.M.A., 2016. Numerical modeling of unstable rock failure. PhD Thesis, Laurentian University, Sudbury, Canada.

Marambio, E., Vallejos, J.A., Burgos, L., Gonzalez, C., Castro, L., Saure, J.P. and Urzúa, J., 2018. Numerical modelling of dynamic testing for rock reinforcement used in underground excavations, in Y Potvin & J Jakubec (eds), Proceedings of the Fourth International Symposium on Block and Sublevel Caving, Australian Centre for Geomechanics, Perth, 767-780.

Martin, C.D., Kaiser, P.K. and McCreath, D.R., 1999. Hoek-Brown parameters for predicting the depth of brittle failure around tunnels. Canadian Geotechnical Journal, 36(1), pp.136-151.

Masny, W., Prusek, S. and Mutke, G., 2017. Numerical Modeling of the Dynamic Load Changes Exerted on the Support in the Stress Concentration Zones. Procedia engineering, 191, 894-899.

Mazaira, A. and Konicek, P., 2015. Intense rockburst impacts in deep underground construction and their prevention. Canadian Geotechnical Journal, 52(10), 1426-1439.

Mine Safety and Health Administration, 1984. Hearing on Proposed Standards for Ground Control Metal/Nonmetal Mines. United States Department of Labor, Spokane, WA June.

Mi, C., Zuo, J., Sun, Y. and Zhao, S., 2022. Investigation on Rockburst Mechanism Due to Inclined Coal Seam Combined Mining and its Control by Reducing Stress Concentration. Natural Resources Research, pp.1-24.

Miranda, E.E., 1972. Deformation and fracture of concrete under uniaxial impact loading. PhD Thesis, University of Missouri Rolla, Rolla, USA.

Miao, S.J., Cai, M.F., Guo, Q.F. and Huang, Z.J., 2016. Rock burst prediction based on in-situ stress and energy accumulation theory. International Journal of Rock Mechanics and Mining Sciences, 83, pp.86-94.

Mitri, H, Tang B., and Simon R., 1999. FE modeling of mining-induced energy release and storage rates. Journal of the South African Institute of Mining and Metallurgy, 99(2):103-10.

Mitri, H.S. 2000. Practitioner's guide to destress blasting in hard rock mines. Technical report. McGill University, Montréal, Canada.

Mortazavi, A. and Alavi, F.T., 2013. A numerical study of the behavior of fully grouted rockbolts under dynamic loading. Soil Dynamics and Earthquake Engineering, 54, 66-72.

Müller, W., 1991. Numerical simulation of rock bursts. Mining science and technology, 12(1), 27-42.

Munjiza, A., Bangash, T. and John, N.W.M., 2004. The combined finite–discrete element method for structural failure and collapse. Engineering fracture mechanics, 71(4-6), 469-483.

Mutke, G., 2008. Stability of the underground mine workings in the near-field zone of seismic events. In 21st World Mining Congress, 89-97.

Mutke, G., Lurka, A. and Dubiński, J., 2009, January. Seismic monitoring and rock burst hazard assessment in Deep Polish Coal Mines–Case study of rock burst on April 16, 2008 in Wujek-Slask Coal Mine. In 7th International Symposium on Rockburst and Seismicity in Mines (RASiM 7): Controlling Seismic Hazard and Sustainable Development of Deep Mines. CA Tang (ed.). Rinton Press, pp. 1413-1424.

Mutke, G., Dubiński, J. and Lurka, A., 2015. New criteria to assess seismic and rock burst hazard in coal mines. Archives of Mining Sciences, 60.

Mutke, G., Masny, W. and Prusek, S., 2016. Peak particle velocity as an indicator of the dynamic load exerted on the support of underground workings. Acta Geodynamica et Geomaterialia, 13(4), 367-378.

Myrvang, A.M. and Grimstad, E., 1983. Rockburst problems in Norwegian highway tunnels—recent case histories. In Rockbursts: prediction and control. Symposium, 133-139.

Naji, A.M., Rehman, H., Emad, M.Z. and Yoo, H., 2018. Impact of shear zone on rockburst in the deep neelum-jehlum hydropower tunnel: A numerical modeling approach. Energies, 11(8), 1935.

Napier, J.A.L. and Stephansen, S.J., 1987. Analysis of deep-level mine design problems using the MINSIM-D boundary element program. In Proceedings of the 20th International Symposium on the Application of Computers and Mathematics in the Mineral Industries, 1, 3-19.

Neyman, B., Szecowka, Z. and Zuberek, W., 1972, August. Effective methods for fighting rock burst in Polish collieries. In Proceedings of the 5th international strata control conference, 23, 1-9.

Nie, W., Zhao, Z.Y., Ning, Y.J. and Guo, W., 2014. Numerical studies on rockbolts mechanism using 2D discontinuous deformation analysis. Tunnelling and Underground Space Technology, 41, 223-233.

Normet., 2021. Normet D-Bolt® – Dynamic rock bolt. https://www.normet.com/product/d-bolt/. Accessed 22 May 2021

Qin, H. and Mao, X.B., 2008. Numerical simulation of stress wave induced rock burst. Journal of Mining & Safety Engineering, 25(2), pp.127-131. (In Chinese)

Ortlepp, W.D., 1978. The mechanism of a rockbust. 19th US Symposium on Rock Mechanics (USRMS). American Rock Mechanics Association.

Ortlepp, W.D., 1992. The design of support for the containment of rockburst damage in tunnels—an engineering approach. In: Kaiser, P.K. and McCreath, D.R., Eds., Rock Support in Mining and Underground Construction, Balkema, Rotterdam, 593-609.

Ortlepp, W.D., 1997. Rock fracture and rockbursts, an illustrative study. Johannesburg, SAIMM Monogr. Ser. M9, 98.

Ortlepp, W.D., 2001. The behaviour of tunnels at great depth under large static and dynamic pressures. Tunnelling and Underground Space Technology, 16(1), 41-48.

Ortlepp, W.D., and Stacey, T.R., 1994. Rockburst mechanisms in tunnels and shafts. Tunnelling and Underground Space Technology, 9(1), 59-65.

Palmström, A., 1995. Characterizing rockburst and squeezing by the rock mass index. In: Int. Conf. on Design and Construction of Underground Structures; New Delhi, India, 10.

Park, H.D., 1995. Tensile rock strength and related behavior revealed by hoop tests. PhD Thesis, University of London, London, UK.

Pande, G., Beer, G. and Williams, J., 1990. Numerical methods in rock mechanics. United States: N. p., 1990.

Pen, Y., 1994, Chain pillar design in longwall mining for bump-prone seams. PhD Thesis, Univeristy of Alberta, Edmonotn, Canada.

Peng, Z., Wang, Y.H., Li, T.J., 1996. Griffith theory and rock burst of criterion. Chinese Journal of Rock Mechanics and Engineering, 15 (Suppl.), 491-495. (In Chinese)

Peng S.S., Chiang H.S., 1984. Longwall mining. New York: Wiley, 708.

Pechmann, J.C., Arabasz, W.J., Pankow, K.L., Burlacu, R. and McCarter, M.K., 2008. Seismological report on the 6 August 2007 Crandall Canyon mine collapse in Utah. Seismological Research Letters, 79(5), pp.620-636.

Pu, Y., Apel, D.B., Liu, V. and Mitri, H., 2019. Machine learning methods for rockburst prediction-state-of-the-art review. International Journal of Mining Science and Technology, 29(4), 565-570.

Pu, Y., Apel, D.B. and Hall, R., 2020. Using machine learning approach for microseismic events recognition in underground excavations: Comparison of ten frequently-used models. Engineering Geology, p.105519.

Prusek, S. and Masny, W., 2015. Analysis of damage to underground workings and their supports caused by dynamic phenomena. Journal of Mining Science, 51(1), pp.63-72.

Qi, Q.X., Chen S.B., Wang H.X., Mao D.B, and Wang YX., 2003. Study on the relations among coal bump, rockburst and mining tremor with numerical simulation. Chinese Journal of Rock Mechanics and Engineering, 22(11), 1852-1857. (In Chinese)

Qian, Q.H., 2011. Simplified analysis of rockburst mechanism and considerations of determinative parameters. Academic Department, China Association for Science and Technology ed. Explore Rockburst Mechanism. Beijing: China Science and Technology Press, 3-13. (In Chinese)

Qian, Q.H., 2014. Definition, mechanism, classification and quantitative forecast model for rockburst and pressure bump. Rock and Soil Mechanics, 35(1), 1-6. (In Chinese)

Qiu, P., Wang, J., Ning, J., Liu, X., Hu, S. and Gu, Q., 2019. Rock burst criteria of deep residual coal pillars in an underground coal mine: a case study. Geomechanics and Engineering, 19(6), p.499.

Russenes, B.F., 1974, Analysis of rock spalling for tunnels in steep valley sides. M.Sc. thesis, Norwegian Institute of Technology, Trondheim, Department of Geology, 247p. (In Norwegian)

Raffaldi, M.J., Chambers, D.J.A. and Johnson, J.C., 2017, March. Numerical study of the relationship between seismic wave parameters and remotely triggered rockburst damage in hard rock tunnels. In Proceedings of the Eighth International Conference on Deep and High Stress Mining, Australian Centre for Geomechanics, pp. 373-386.

Raffaldi, M., Loken, M., 2016. Framework for simulating fracture, ejection, and restraint of rock around a mine drift subjected to seismic loading. In: 50th US Rock Mechanics/Geomechanics Symposium. American Rock Mechanics Association.

Ryder, J.A., 1988. Excess shear stress in the assessment of geologically hazardous situations. Journal of the South African Institute of Mining and Metallurgy, 88 (1), 27–39.

Roth, A., Ranta-Korpi, R., Volkwein, A. and Wendeler, C., 2007, January. Numerical modeling and dynamic simulation of high-tensile steel wire mesh for ground support under rockburst loading. In 1st Canada-US Rock Mechanics Symposium. American Rock Mechanics Association.

Rocscience., 2015. RS2 Modeler Version 9.008. RocScience Inc., Toronto, Canada.

Sainoki, A., 2014. Dynamic modeling of mining-induced fault-slip. PhD Thesis, McGill University, Montreal, Canada.

Sainoki, A. and Mitri, H.S., 2014a. Dynamic modelling of fault-slip with Barton's shear strength model. International Journal of Rock Mechanics and Mining Sciences, 67, 155-163.

Sainoki, A. and Mitri, H.S., 2014b. Simulating intense shock pulses due to asperities during fault-slip. Journal of Applied Geophysics., 103, 71–81.

Sainoki, A. and Mitri, H.S., 2015. Evaluation of fault-slip potential due to shearing of fault asperities. Canadian Geotechnical Journal, 52(10), 1417-1425.

Sainoki, A., Emad, M.Z. and Mitri, H.S., 2016. Study on the efficiency of destress blasting in deep mine drift development. Canadian Geotechnical Journal, 54(4), 518-528.

Salamon, M.D.G., 1964. Elastic analysis of displacements and stresses induced by the mining of seam or reef deposits: Part II: Practical methods of determining displacement, strain and stress components from a given mining geometry. Journal of the Southern African Institute of Mining and Metallurgy, 64(6), 197-218.

Salamon, M.D.G., 1970, November. Stability, instability and design of pillar workings. International journal of rock mechanics and mining sciences & geomechanics abstracts, 7(6), pp. 613-631).

Salamon, M., 1993. Keynote address: Some applications of geomechanical modeling in rockburst and related research. Paper presented at the Proceedings of the 3rd International Symposium on Rockbursts and Seismicity in Mines, 297-309.

Salamon, M.D.G., 1984. Energy considerations in rock mechanics, fundamental results. Journal of the South African Institute of Mining and Metallurgy. 84 (8), 233-246.

Salamon, M.D.G., 1990. Mechanism of caving in longwall coal mining. In Rock mechanics contributions and challenges. US symposium. 31, pp. 161-168.

Salencon, J., 1969. Contraction quasi-statique d'une cavite a symetrie spherique ou cylindrique dans un milieu elastoplastique, in Proceedings Annales des ponts et chaussées, 4, p. 231-236.

Sengani, F., 2018. The performance of bolt-reinforced and shotcreted in-stope pillar in a rockburst prone areas. International Journal of Mining and Geo-Engineering, 52(2), 105-117.

Sepehri M., 2016. Finite element analysis model for determination of in-situ and mining induced stresses as a function of two different mining methods used at Diavik Diamond Mine. PhD Thesis, University of Alberta, Edmonton, Canada.

Sepehri, M., Apel, D.B., Adeeb, S., Leveille, P. and Hall, R.A., 2020. Evaluation of mining-induced energy and rockburst prediction at a diamond mine in Canada using a full 3D elastoplastic finite element model. Engineering Geology, 266, 105457.

Sharifzadeh, M., Lou, J. and Crompton, B., 2020. Dynamic performance of energy-absorbing rockbolts based on laboratory test results. Part I: Evolution, deformation mechanisms, dynamic performance and classification. Tunnelling and Underground Space Technology, 105, p.103510.

Shabanimashcool, M. and Li, C. C., 2012. Numerical modelling of longwall mining and stability analysis of the gates in a coal mine. International Journal of Rock Mechanics and Mining Sciences, 51, 24-34.

Shen, W., Dou, L.M., He, H. and Zhu, G.A., 2017. Rock burst assessment in multi-seam mining: a case study. Arabian Journal of Geosciences, 10(8), pp.1-11.

Shi G., 1991. Manifold method of material analysis. Trans. Ninth Army Conference on Applied Mathematics and Computing, Minneapolis, MN, 57-76.

Skrzypkowski, K., 2021. An experimental investigation into the stress-strain characteristic under static and quasi-static loading for partially embedded rock bolts. Energies, 14(5), p.1483.

Skrzypkowski, K., Korzeniowski, W., Zagórski, K. and Zagórska, A., 2020. Modified rock bolt support for mining method with controlled roof bending. Energies, 13(8), p.1868.

Singh, A.K., Singh, R., Maiti, J., Kumar, R. and Mandal, P.K., 2011. Assessment of mining induced stress development over coal pillars during depillaring. International Journal of Rock Mechanics and Mining Sciences, 48(5), pp.805-818.

Simon, R., 1999. Analysis of Fault-Slip Mechanisms in Hard Rock Mining. PhD Thesis, McGill University, Montreal, Canada.

Song, D., Wang, E., Liu, Z., Liu, X. and Shen, R., 2014. Numerical simulation of rock-burst relief and prevention by water-jet cutting. International Journal of Rock Mechanics and Mining Sciences, 70, 318-331.

Stacey, T.R., 2013. Dynamic rock failure and its containment-a Gordian knot design problem. First International Conference on Rock Dynamics and Applications (RocDyn 1)-State of the Art. CRC press/Balkema, 57-70.

Stacey, T.R. and Rojas, E., 2013. A potential method of containing rockburst damage and enhancing safety using a sacrificial layer. Journal of the Southern African Institute of Mining and Metallurgy, 113(7), pp.565-573.

Stavrou, A., Vazaios, I., Murphy, W. and Vlachopoulos, N., 2019. Refined Approaches for Estimating the Strength of Rock Blocks. Geotechnical and Geological Engineering, 37(6), pp.5409-5439.

Stead, D., Coggan, J.S. and Eberhardt, E., 2004. Realistic simulation of rock slope failure mechanisms: The need to incorporate principles of fracture mechanics. SINOROCK 2004: Special Issue of Int. Journal of Rock Mechanics. 41(3), 6.

Stillborg, B., 1994, Professional Users Handbook for RockBolting, Germany, Trans Tech Publications.

Stjern, G., 1995. Practical performance of rock bolts. PhD thesis, University of Trondheim, Trondheim, Norway.

Su, G., Jiang, J., Zhai, S. and Zhang, G., 2017a. Influence of tunnel axis stress on strainburst: an experimental study. Rock Mechanics and Rock Engineering, 50(6), pp.1551-1567.

Su, G., Zhai, S., Jiang, J., Zhang, G. and Yan, L., 2017b. Influence of radial stress gradient on strainbursts: an experimental study. Rock Mechanics and Rock Engineering, 50(10), pp.2659-2676.

Sun, J.S., Zhu, Q.H. and LU, W.B., 2007. Numerical simulation of rock burst in circular tunnels under unloading conditions. Journal of China University of Mining and Technology, 17(4), 552-556.

Suchowerska, A.M., Merifield, R.S. and Carter, J.P., 2013. Vertical stress changes in multi-seam mining under supercritical longwall panels. International Journal of Rock Mechanics and Mining Sciences, 61, pp.306-320.

Sweby, G., 2007. Kambalda Nickel Operations-Miningin high stress, seismically active conditions. In: Challenges in Deep and High Stress Mining, ACG. Australian Centre for Geomechanic, Perth, 192 007.

Szott, W., Słota-Valim, M., Gołąbek, A., Sowiżdżał, K. & Łętkowski, P., 2018. Numerical studies of improved methane drainage technologies by stimulating coal seams in multi-seam mining layouts. International Journal of Rock Mechanics and Mining Sciences, 108, 157-168.

Tan, X., and Konietzky, H., 2014. Brazilian split tests and numerical simulation by discrete element method for heterogeneous gneiss with bedding structure. Chinese Journal of Rock Mechanics and Engineering, 33(5), pp.938-946. (In Chinese)

Tan, Y.A., 1991. Characteristics of rockburst and structural effect on rock mass. Science China, B9, 985-987. (In Chinese)

Tan, Y.L, Zhang Z. and Ma C., 2012. Rock burst disaster induced by mining abutment pressure. Disaster Advances, 5(4), 378-382.

Tan, Y.L., Guo W.Y., Xin H.Q, Zhao T.B., Yu F.H. and Liu X.S., 2019. Key technology of rock burst monitoring and control in deep coal mining. Journal of China Coal Society, 44(1), 160-172. (In Chinese)

Tang, L., Wang W., 2002. New rock burst proneness index. Chinese Journal of Rock Mechanics and Engineering, 6. (In Chinese)

Tan, Y.L., Liu, X.S., Shen, B., Ning, J.G. and Gu, Q.H., 2018. New approaches to testing and evaluating the impact capability of coal seam with hard roof and/or floor in coal mines. Geomechanics and Engineering, 14(4), 367-376.

Tang C.A., 2004. Fracture, instability and rockburst of rocks. In: Wang SJ, Yang ZF, Fu BJ, eds. Centurial Achievement of Rock Mechanics and Engineering in China. Nanjing: Hohai University Press. (In Chinese)

Tang, B.Y., 2000. Rock burst control using distress blasting, PhD Thesis, McGill University, Montreal, Canada.

Tao, Z.Y., 1988. Support design of tunnels subjected to rockbursting. In: Romana (ed.), Rock Mechanics and Power Plants, 407-411.

Tomasone, P., Bahrani, N. and Hadjigeorgiou, J., 2020. Practical considerations in the modeling of resin-grouted rockbolts. Journal of the Southern African Institute of Mining and Metallurgy, 120(6), pp.385-392.

Tsesarsky, M., Gal, E. and Machlav, E., 2013. 3-D global–local finite element analysis of shallow underground caverns in soft sedimentary rock. International Journal of Rock Mechanics and Mining Sciences, 57, 89-99.

Turchaninov, I.A., Markov, G.A., Gzovsky, M.V., Kazikayev, D.M., Frenze, U.K., Batugin, S.A., Chabdarova, U.I., 1972. State of stress in the upper part of the Earth's crust based on direct measurements in mines and on tectonophysical and seismological studies. Phys. Earth Planet. Inter. 6, 229–234.

Varas, F., Alonso, E., Alejano, L.R. and Manín, G.F., 2005. Study of bifurcation in the problem of unloading a circular excavation in a strain-softening material. Tunnelling and Underground Space Technology, 20(4), pp.311-322.

Varden, R., Lachenicht, R., Player, J., Thompson, A. and Villaescusa, E., 2008. Development and Implementation of the Garford Dynamic Bolt at the Kanowna Belle Mine. 10th Underground Operators' Conference, Launceston, 95-102.

Vazaios, I., 2018. Modeling of Hard Rockmasses with Non-Persistent Joints to Assess the Stress Induced Damage of Deep Excavations. PhD Thesis, Queen's University, Kinston, Canada.

Vazaios, I., Diederichs, M.S. and Vlachopoulos, N., 2019. Assessment of strain bursting in deep tunnelling by using the finite-discrete element method. Journal of Rock Mechanics and Geotechnical Engineering, 11(1), 12-37.

Vennes, I. and Mitri, H., 2017. Geomechanical effects of stress shadow created by large-scale destress blasting. Journal of Rock Mechanics and Geotechnical Engineering, 9(6), 1085-1093.

Wagner, H., 2019. Deep Mining: A Rock Engineering Challenge. Rock Mechanics and Rock Engineering, 52(5), 1417-1446.

Wang, F., 2019, A numerical study of rockburst damage around excavations induced by fault-slip. PhD Thesis, Colorado School of Mines, Golden, Canada.

Wang, F. and Kaunda, R., 2019. Assessment of rockburst hazard by quantifying the consequence with plastic strain work and released energy in numerical models. International Journal of Mining Science and Technology, 29(1), pp.93-97.

Wang, H., Jiang, Y., Zhao, Y., Zhu, J. and Liu, S., 2013. Numerical investigation of the dynamic mechanical state of a coal pillar during longwall mining panel extraction. Rock Mechanics and Rock Engineering, 46(5), pp.1211-1221.

Wang, H., Jiang, Y., Xue, S., Pang, X., Lin, Z. and Deng, D., 2017. Investigation of intrinsic and external factors contributing to the occurrence of coal bumps in the mining area of Western Beijing, China. Rock Mechanics and Rock Engineering, 50(4), pp.1033-1047.

Wang, J., Apel, D.B., Pu, Y., Hall, R., Wei, C. and Sepehri, M., 2021a. Numerical modeling for rockbursts: A state-of-the-art review. Journal of Rock Mechanics and Geotechnical Engineering, 13(2), 457-478.

Wang, J., Apel, D.B., Dyczko, A., Walentek, A., Prusek, S., Xu, H. and Wei, C., 2021b. Investigation of the rockburst mechanism of driving roadways in close-distance coal seam mining using numerical modeling method. Mining, Metallurgy & Exploration, 38(5), pp.1899-1921.

Wang, J., Apel, D.B., Dyczko, A., Walentek, A., Prusek, S., Xu, H. and Wei, C., 2022a. Analysis of the damage mechanism of strainbursts by a global-local modeling approach. Journal of Rock Mechanics and Geotechnical Engineering.

Wang, J., Apel, D.B., Xu, H., Wei, C. and Skrzypkowski, K., 2022b. Evaluation of the Effects of Yielding Rockbolts on Controlling Self-Initiated Strainbursts: A Numerical Study. Energies, 15(7), p.2574.

Wang, J., Qiu, P., Ning, J., Zhuang, L. and Yang, S., 2020. A numerical study of the mining-induced energy redistribution in a coal seam adjacent to an extracted coal panel during longwall face mining: A case study. Energy Science & Engineering, 8(3), pp.817-835.

Wang, Q., Jiang, B., Pan, R., Li, S.C., He, M.C., Sun, H.B., Qin, Q., Yu, H.C. and Luan, Y.C., 2018. Failure mechanism of surrounding rock with high stress and confined concrete support system. International Journal of Rock Mechanics and Mining Sciences, 102, pp.89-100.

Wang, P., Jiang, L., Jiang, J., Zheng, P. and Li, W., 2017. Strata behaviors and rock burst–inducing mechanism under the coupling effect of a hard, thick stratum and a normal fault. International Journal of Geomechanics, 18(2), 04017135.

Wang, P., Xu, J., Liu, S., Wang, H. and Liu, S., 2016. Static and dynamic mechanical properties of sedimentary rock after freeze-thaw or thermal shock weathering. Engineering geology, 210, 148-157.

Wang S.Y., Tang C.A., and Xu T., 2003. Numerical simulation on acoustic emission during pillar rock burst. The Chinese Journal of Nonferrous Metals, 13(2), 754-759. (In Chinese)

Wang, S.Y., Lam, K.C., Au, S.K., Tang, C.A., Zhu, W.C. and Yang, T.H., 2006. Analytical and numerical study on the pillar rockbursts mechanism. Rock Mechanics and Rock Engineering, 39(5), 445-467.

Wang, X. and Cai, M., 2017. Coupled numerical analysis of ground motion near excavation boundaries in underground mines. Rock and Soil Mechanics, 38(11), pp.3347-3354. (In Chinese)

Wang, Z., Dou, L., Li, J., Kang, K. and Feng, L., 2017. Numerical investigation of damage risks of roadway surrounding rocks under oblique incident dynamic loads. Shock and Vibration, 1-13.

Wattimena, R.K., Sirait, B., Widodo, N.P., Matsui, K., 2012. Evaluation of rockburst potential in a cut-and-fill mine using energy balance. International Journal of the JCRM, 8(1), 19-23.

Wei, C., Zhang, C., Canbulat, I., Cao, A. and Dou, L., 2018. Evaluation of current coal burst control techniques and development of a coal burst management framework. Tunnelling and Underground Space Technology, 81, 129-143.

Wei, L. and Hudson, J.A., 1998. A hybrid discrete-continuum approach to model hydro-mechanical behaviour of jointed rocks. Engineering geology, 49(3-4), 317-325.

Wei, L., 1992. Numerical studies of the hydromechanical behaviour of jointed rocks. PhD Thesis, Imperial College of Science and Technology, University of London, London, UK.

Whyatt, J.K. and Board, M.P., 1991. Numerical exploration of shear-fracture-related rock bursts using a strain-softening constitutive law, United States Department of the Interior.

Wiles, T.D., 2002. Loading system stiffness-a parameter to evaluate rockburst potential. In: First International Seminar on Deep and High Stress Mining, Australian Centre for Geomechanics, Perth, Australia.

Wilson, A.H., and Carr, F., 1982. A new approach to the design of multientry developments of retreat longwall mining. In: Proceedings of the 2nd International Conference on Ground Control in Mining. Morgantown, WV, 1–21.

Wu, R., Oldsen, J. and Campoli, A., 2011. Application of Yield-Lok Bolt for Bursting and Convergence Grounds in Mines. 30th International Conference on Ground Control in Mining, Morgantown, 1-6.

Wu, B., Wang, X., Bai, J., Wu, W., Zhu, X. and Li, G., 2019. Study on crack evolution mechanism of roadside backfill body in gob-side entry retaining based on UDEC trigon model. Rock Mechanics and Rock Engineering, 52(9), pp.3385-3399.

Wu, Y., Gao, F., Chen, J. and He, J., 2019. Experimental study on the performance of rock bolts in coal burst-prone mines. Rock Mechanics and Rock Engineering, 52(10), 3959-3970.

Xu, H., 2021, Stoping sequence optimization based on stope stability assessment using finite element modeling method. PhD Thesis, University of Alberta, Edmonton, Canada.

Xu, Y.H. and Cai, M., 2017. Influence of loading system stiffness on post-peak stress–strain curve of stable rock failures. Rock Mechanics and Rock Engineering, 50(9), pp.2255-2275.

Xu L.S., and Wang, L.S., 1996. Study on the rockburst type classification. Journal of Geological Hazards and Environment Preservation, 11(3), 245-247.

Xue, Y., Cao, Z., Du, F. and Zhu, L., 2018. The influence of the backfilling roadway driving sequence on the rockburst risk of a coal pillar based on an energy density criterion. Sustainability, 10(8), 1-21.

Yang Y.Q., and Xiang M.Z., 2018. Discussion on rockbursts. Safety Popular Science, 13(11), 62-63. (In Chinese)

Yang F.J., Zhou H., Lu J. J., Zhang C.Q and Hu D.W., 2015. An energy criterion in process of rockburst. Chinese Journal of Rock Mechanics and Engineering, 34(s1), 2706-2714. (In Chinese)

Yang, J., Chen, W., Tan, X. and Yang, D., 2018. Analytical estimation of stress distribution in interbedded layers and its implication to rockburst in strong layer. Tunnelling and Underground Space Technology, 81, 289-295.

Yang, S.Q., Chen, M., Jing, H.W., Chen, K.F. and Meng, B., 2017. A case study on large deformation failure mechanism of deep soft rock roadway in Xin'An coal mine, China. Engineering Geology, 217, pp.89-101.

Yavuz, H., 2004. An estimation method for cover pressure re-establishment distance and pressure distribution in the goaf of longwall coal mines. International Journal of Rock Mechanics and Mining Sciences, 41, 193-205.

Yokota, Y., Zhao, Z., Nie, W., Date, K., Iwano, K., Koizumi, Y. and Okada, Y., 2019. Development of a new deformation-controlled rockbolt: numerical modeling and laboratory verification. Proceedings of the Ninth International Symposium on Ground Support in Mining and Underground Construction, Australian Centre for Geomechanics, 545-556.

Yu, W., Wang, W., Chen, X. and Du, S., 2015. Field investigations of high stress soft surrounding rocks and deformation control. Journal of Rock Mechanics and Geotechnical Engineering, 7(4), pp.421-433.

Zhang, C., Canbulat, I., Tahmasebinia, F. and Hebblewhite, B., 2017. Assessment of energy release mechanisms contributing to coal burst. International Journal of Mining Science and Technology, 27(1), 43-47.

Zhang, C., Feng, X.T., Zhou, H., Qiu, S. and Wu, W., 2012a. Case histories of four extremely intense rockbursts in deep tunnels. Rock mechanics and rock engineering, 45(3), 275-288.

Zhang, C., Feng, X., Zhou, H., Qiu, S. and Wu, W., 2012b. A top pilot tunnel preconditioning method for the prevention of extremely intense rockbursts in deep tunnels excavated by TBMs. Rock Mechanics and Rock Engineering, 45(3), 289-309.

Zhang, C.Q., Zhou, H. and Feng, X.T., 2011. An index for estimating the stability of brittle surrounding rock mass: FAI and its engineering application. Rock Mechanics and Rock Engineering, 44(4), 401.

Zhang, C., Feng, X.T., Zhou, H., Qiu, S. and Wu, W., 2013. Rockmass damage development following two extremely intense rockbursts in deep tunnels at Jinping II hydropower station, southwestern China. Bulletin of engineering geology and the environment, 72(2), pp.237-247.

Zhang, H., Chen, L., Chen, S., Sun, J. and Yang, J., 2018. The spatiotemporal distribution law of microseismic events and rockburst characteristics of the deeply buried tunnel group. Energies, 11(12), 3257.

Zhang, J. and Fu, B., 2008. Rockburst and its criteria and control. Chinese Journal of Rock Mechanics and Engineering, 27(10), 2034-2042. (In Chinese)

Zhao, H. and Kaunda, R., 2018. Numerical assessment of the influences of gas pressure on coal burst liability. Energies, 11(2), 260.

Zhang, P. and Nordlund, E., 2019. Numerical investigation of dynamic response of a rockbolt under drop testing and simulated seismic loading conditions. In: Proceedings of the Ninth International Symposium on Ground Support in Mining and Underground Construction. Australian Centre for Geomechanics, Perth, Australia, pp.387-398.

Zhang, W., Guo, J., Xie, K., Wang, J., Chen, L., Hu, W. and Xu, J., 2021. Comprehensive technical support for safe mining in ultra-close coal seams: a case study. Energy Exploration & Exploitation, 39(4), pp.1195-1214.

Zhao, T.B., Guo, W.Y., Tan, Y.L., Yin, Y.C., Cai, L.S. and Pan, J.F., 2018. Case studies of rock bursts under complicated geological conditions during multi-seam mining at a depth of 800 m. Rock Mechanics and Rock Engineering, 51(5), pp.1539-1564.

Zhao, T.B., Xing, M.L., Guo, W.Y., Wang, C.W. and Wang, B., 2021. Anchoring effect and energy-absorbing support mechanism of large deformation bolt. Journal of Central South University, 28(2), pp.572-581.

Zhou, G., Xu, M. and Fan, T., 2018. Numerical simulation of combined water injection in deep coal seam and its field application for dust suppression and de-stressing: A case study at dongtan coal mine, China. Geotechnical and Geological Engineering, 36(1), pp.283-291.

Zhou, J., Li, X. and Mitri, H.S., 2018. Evaluation method of rockburst: state-of-the-art literature review. Tunnelling and Underground Space Technology, 81, 632-659.

Zhu, D., Wu, Y., Liu, Z., Dong, X. and Yu, J., 2020. Failure mechanism and safety control strategy for laminated roof of wide-span roadway. Engineering Failure Analysis, 111, p.104489.

Zhu, S., Feng, Y., Jiang, F. and Liu, J., 2018. Mechanism and risk assessment of overall-instability-induced rockbursts in deep island longwall panels. International Journal of Rock Mechanics and Mining Sciences, 106, pp.342-349.

Zhu, Q.H., Lu, W.B., Sun, J.S., Yi, L.U.O. and Ming, C.H.E.N., 2009. Prevention of rockburst by guide holes based on numerical simulations. Mining Science and Technology (China), 19(3), 346-351.

Zhu, W.C., Li, Z.H., Zhu, L. and Tang, C.A., 2010. Numerical simulation on rockburst of underground opening triggered by dynamic disturbance. Tunnelling and Underground Space Technology, 25(5), 587-599.

Zang, C., Chen, M., Zhang, G., Wang, K. and Gu, D., 2020. Research on the failure process and stability control technology in a deep roadway: numerical simulation and field test. Energy Science & Engineering.

Zienkiewicz, O.C., Kelly, D.W. and Bettess, P., 1977. The coupling of the finite element method and boundary solution procedures. International journal for numerical methods in engineering, 11(2), 355-375.

Zubelewicz, A. and Mroz, Z., 1983. Numerical simulation of rock burst processes treated as problems of dynamic instability. Rock Mechanics and Rock Engineering, 16(4), 253-274.